Development of high-resolution cavity beam position monitors for use in low-latency feedback systems

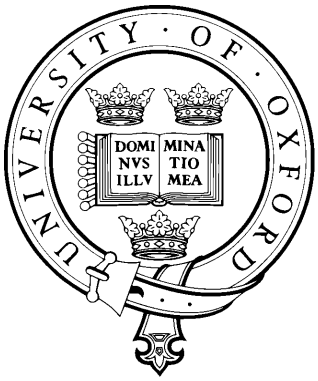

Talitha Bromwich

Magdalen College, Oxford

Thesis submitted in fulfilment of the requirements for the degree of Doctor of Philosophy at the University of Oxford

Hilary Term, 2018

Abstract

The FONT beam-based, intra-train feedback system has been designed to provide beam position stabilisation in single-pass accelerators. A FONT feedback system utilising position information from three high-resolution cavity beam position monitors (BPMs) has been commissioned at the interaction point (IP) of the Accelerator Test Facility 2 (ATF2) at KEK, Japan. The ultimate goal of the feedback in the IP region is to stabilise the low-emittance electron beam to the nanometre level. The operation, optimisation and resolution performance of this IP system forms the subject of this thesis.

The IP feedback system makes use of beam position measurements from the BPMs to drive an upstream kicker and provide a local correction. The BPMs have a fast decay time of $\sim$25 ns to allow bunches within the beam train to be resolved. The operation of the IP BPMs, the noise floor, and position sensitivity to phase are discussed in detail. Attempts are made to diagnose an unwanted $\sim$60 MHz oscillation in the cavity signals, which is bunch charge-dependent and thus likely beam generated.

The BPM resolution estimate was notably improved from 50 nm to 20 nm using waveform integration in analysis of the BPM signals. A multi-parameter fit was used to address inaccurate calibrations and charge-dependencies to achieve more consistent resolution performance and produce a best-ever resolution estimate for the BPMs of 17.5 $\pm$ 0.4 nm.

A novel mode of IP beam position stabilisation using two BPMs as input to the feedback has been successfully demonstrated. The beam position was stabilised to 57 $\pm$ 4 nm, as measured at an independent BPM. Feedback performance was improved to this level by sampling the waveform to optimise bunch-to-bunch correlation. Analysis suggests correction capability could be enhanced by firmware waveform integration to achieve a measurable beam stabilisation of $\sim$40 nm in the future.

Acknowledgements

I am grateful to Professor Philip Burrows and everyone in the FONT group past and present, particularly Neven Blaskovic Kraljevic, Ryan Bodenstein, Glenn Christian, Colin Perry and Rebecca Ramjiawan; you were a joy to work with and learn from. Many thanks to the KEK staff and my wonderful colleagues and friends in the ATF2 collaboration for their guidance and support, the STFC and FMB Oxford for sponsoring my research, and Magdalen College for taking such good care of me.

Contents

Chapter 1

Introduction

1.1 Particle physics

Particle physics is the study of the fundamental particles that make up the universe and the forces that determine how those particles interact. Researchers in the field try to understand the laws that govern these interactions in a coherent mathematical scheme, known as the Standard Model [1]. This model incorporates a system of fermions which constitute the basic units of matter, and force-carrying gauge bosons, which mediate their interactions. The Standard Model fermions and bosons are detailed in Tables 1.1 and 1.2 respectively.

Fermions come in two types: quarks and leptons, each with three generations which increase in mass with each generation. The charged leptons have an integer -1 unit of elementary charge, and each has an associated neutrino with no charge. The quarks have fractional charges of $+\frac{2}{3}$ or $-\frac{1}{3}$ and are always found bound together, usually into pairs (mesons) or triplets (baryons) by the strong force. These composite particles are known collectively as hadrons and examples include the protons and neutrons found in atomic nuclei. All stable matter in the universe is comprised of the first generation of particles. In addition, every particle in the Standard Model has an associated anti-particle, with the same mass but opposite electric charge.

The fermions interact with each other via the electromagnetic, weak and strong forces, which are mediated by their associated bosons (Table 1.2). Quarks interact via all three forces, charged leptons via the electromagnetic and weak forces, and neutrinos by the weak force only. The final component of the model is the Higgs field, which gives particles their masses via the mediating Higgs boson [2]. The Higgs is the most recent experimentally-detected Standard Model particle whose observation was made in 2012 at the Large Hadron Collider (LHC) at CERN in Geneva, Switzerland [3, 4].

Table 1.1: Fundamental fermions of the Standard Model.

	Leptons		Quarks	
Generation	Charged Leptons	Neutrinos	Up-type	Down-type
1	Electron (e)	Electron neutrino (ν_e)	Up (u)	Down (d)
2	Muon (μ)	Muon neutrino (ν_μ)	Charm (c)	Strange (s)
3	Tau (τ)	Tau neutrino (ν_τ)	Top (t)	Bottom (b)
Electric Charge	-1	0	$+\frac{2}{3}$	$-\frac{1}{3}$

Table 1.2: Gauge bosons of the Standard Model and the interactions they mediate.

Boson	Interaction
Photon (γ)	Electromagnetic force
$W^\pm$ and Z^0	Weak force
Gluon (g)	Strong force
Higgs (H^0)	Higgs field

1.2 Colliders

One of the tools used by physicists to explore new particles and forces are particle colliders. A collider experiment involves two beams of charged particles being accelerated to very high energies and brought into collision with each other. High energies are achieved by accelerating particles through longitudinal electric fields inside a sequence of radio frequency (RF) cavities, which incrementally increase the particles' energy as they pass through.

The two beams are focussed and steered into collision using strong magnets. Sophisticated particle detectors surround the interaction point (IP) to observe the collision and the resulting particles that are produced. The energy with which the particles collide will determine which interactions occur and what kinds of particles can be created in the collision.

The rate at which a certain particle interaction, X, can occur, is given by:

$$R(X) = L\,\sigma(X), \tag{1.1}$$

where $\sigma(X)$ is the cross-section of the particular interaction (typically in femtobarns, where 1 fb $\equiv 10^{-43}$ m^2). The cross-section can be calculated using the Standard Model and

includes energy dependencies that determine how likely an interaction is to occur; rare interactions will have smaller cross-sections. L is the luminosity of the colliding beams (typically quoted in units of $\mathrm{cm}^{-2}\ \mathrm{s}^{-1}$), and is given by:

$$L = H\frac{f\,N^2}{4\,\pi\,\sigma_x^*\,\sigma_y^*}, \tag{1.2}$$

where f is the frequency with which particle bunches collide, N is the number of particles in each bunch, σ_x^* and σ_y^* are the horizontal and vertical rms beam sizes, and H is a factor that depends on the electromagnetic interaction of the beams close to the collision point. To maximise the likelihood of a certain interaction occurring, the accelerated bunches need to occupy the smallest possible space in the transverse x-y plane, be densely populated and collide with a high frequency. Along with high energies, a high luminosity at the point of collision is one of the most important properties of a particle collider.

1.2.1 Accelerator beam dynamics

The ensemble of particles in an accelerator pass through a repeating magnetic structure of focusing and defocusing magnets separated by drifts, known as a "FODO" lattice. The lattice is responsible for maintaining the envelope of the beam and preventing the particles from dispersing. This sequence of alternating focusing and defocusing causes the beam's transverse position to oscillate as it propagates in the longitudinal z direction. The transverse motion the particles experience is known as a betatron oscillation [5]:

$$y = \sqrt{\beta(z)\,\epsilon}\cos(\mu(z) + \mu_0). \tag{1.3}$$

Here $\beta(z)$ is known as the beta function, which modulates the amplitude of the beam along the beamline. $\beta(z)$ will be maximal at a focusing magnet and minimal at a defocusing magnet (Fig. 1.1.a) and can be used to identify the location of the beam waist (i.e. the point of focus where the transverse beam size is smallest). The phase advance, $\mu(z)$, describes the phase of the oscillation, which will be set by the distribution of the magnetic elements. The μ_0 term accounts for the initial phase at $z = 0$.

The emittance, ϵ, in Eq. 1.3 is a measure of the spread of the particles in a bunch in the transverse y position and momentum phase space (Fig. 1.1.b). The phase space ellipse is typically defined to encircle one standard deviation of a Gaussian beam [6]. The emittance is a conserved quantity unless the particles lose energy. For a high-luminosity machine, a low-emittance beam is vital.

To achieve a low-emittance beam, accelerators make use of a damping ring stage whereby the charged particles are intentionally bent in a circle by strong magnetic dipole fields in order to emit synchrotron radiation [7] and reduce the emittance.

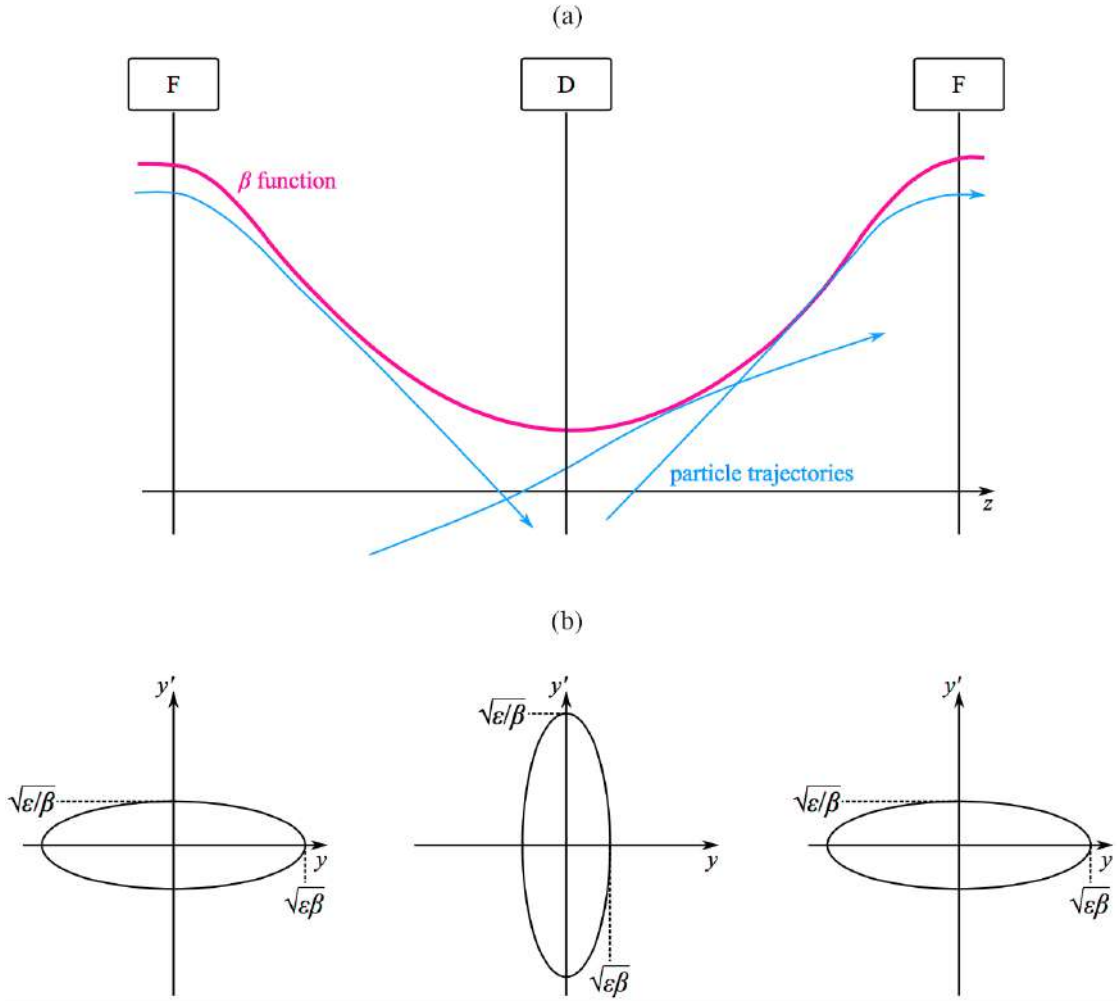

Figure 1.1: Illustrations of (a) the beta function $\beta(z)$ (pink) and particle trajectories (blue) versus longitudinal distance z in a FODO lattice of focusing (F) and defocusing (D) quadrupoles; (b) y' versus y phase space ellipses at each quadrupole [8, 9].

In the longitudinal z plane the particles are accelerated through the machine by radio frequency (RF) cavities, which will be supplied by a sinusoidal voltage. As a consequence of this, the particles do not form a continuous stream, but a train of bunches separated at a frequency determined by the RF frequency of the accelerating fields. This frequency is phase locked across all the accelerating cavities in the machine.

A particle that is synchronous with the RF voltage will receive the same energy at every cavity it passes through. Particles that arrive early will receive more energy, and those that are late will receive less (Fig. 1.2). This results in a longitudinal oscillation of the bunches in a train as they pass around a damping ring. These oscillations are known as synchrotron oscillations [9], and they impact the exact arrival time of bunches at different locations in the accelerator.

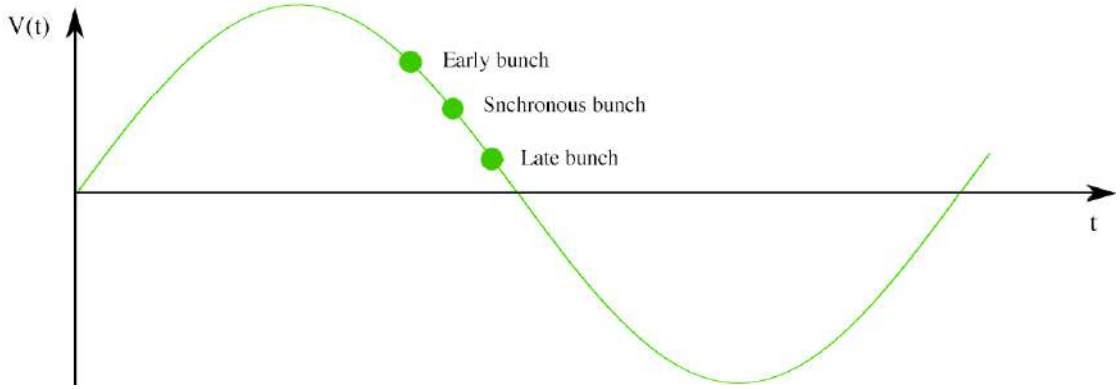

Figure 1.2: Illustration of the accelerating voltage, $V(t)$, versus time, t, and the relative timing of early, late, and synchronous electron bunches.

1.2.2 Linear and circular colliders

Particle accelerators which provide the beams for collider experiments can be circular or linear. In a linear accelerator the particles are injected and pass once through the accelerating RF cavities before being brought into collision with the opposing beam. The single-pass nature of a linear accelerator means the particles can only be used once, so the collision frequency is lower than for a circular machine. Linear machines must compensate for this to achieve good luminosities by focusing the beams to very small sizes. The maximum achievable energy is then dictated by the length of the accelerator and the accelerating gradients of the RF cavities.

A circular accelerator uses strong magnetic dipoles to bend the trajectory of the particles, allowing them to circulate through the accelerating RF fields many times, gaining more energy with each rotation. The beams are then brought into collision at specified interaction points around the ring once they have reached their maximum energy. Circular machines can achieve very high bunch crossing frequencies but are limited in energy by the size of the radius of the ring and the dipole magnetic field strength. The strength of the dipole fields must be increased synchronously with the particles' increasing energy to maintain the circular trajectory. Circular accelerators that synchronise the magnetic field strength and the beam energy in this way are given the name synchrotrons [10].

Charged particles which are bent in a magnetic field will emit synchrotron radiation, which is useful in a damping ring to reduce the emittance but can have unwanted consequences in circular accelerators. The power radiated, P, depends on the bending radius, ρ, the particle energy, E, and rest mass, m_0, [9]:

$$P \propto \frac{1}{\rho^2}\frac{E^4}{m_0^4}. \tag{1.4}$$

This means that to achieve an overall increase in energy with each turn in the accelerator, the power the accelerating RF fields supply to the particles must be greater than the power lost to synchrotron radiation. This becomes more and more challenging as the energy of the particles increases and for the acceleration of lower-mass particles.

1.2.3 Hadron and lepton colliders

Colliders can accelerate either charged hadrons or leptons and typically use either protons or electrons (and/or their anti-particles). The LHC, for example, is a proton synchrotron with a centre-of-mass energy of 13 TeV [11]. However, protons and other hadrons are not fundamental, being composed of quarks and the strong-force mediating gluons. The precise energy of each quark and gluon at the point of collision will not be known, leading to uncertainties in the expected products of the interaction. Additionally, the quarks and gluons interact very strongly and will produce a profusion of background collision events in a detector, making the tracking of specific particles of interest more difficult.

Electrons, as far as we know, are fundamental, so the initial energies of an electron (or electron-positron) collision are more well defined. This means the centre of mass energy can be tuned to the interaction of interest, increasing the cross-section and interaction rate [12]. In addition, leptons do not experience the strong force, so background events will be lower, resulting in cleaner collisions. However, electrons are ∼2000 times lighter than protons, so incur massive synchrotron radiation losses from the $\frac{1}{m_0^4}$ ratio (Eq. 1.4). For example, the Large Electron-Positron Collider (LEP) that previously occupied the LHC tunnel was only capable of achieving centre of mass energies up to ∼200 GeV [13]. The only realistic means of reaching higher energies for lepton colliders is to opt for a linear accelerating structure.

1.2.4 Future linear colliders

In recent years the Higgs Boson has been measured to have a mass of 124.98 ± 0.28 GeV [14], and the top quark 172.44 ± 0.13 GeV [15]. It is now desirable to study their properties in detail with a higher precision linear electron-positron collider that can be energy-tuned to access the peak cross sections with high reaction rates for channels of interest (for examples, see Fig. 1.3). Higher energy frontiers beyond the 1 TeV scale are also of interest for the study of rarer Higgs processes, and for searching for new physics. There are currently two linear electron-positron collider designs in development for this purpose: the Compact Linear Collider (CLIC) at CERN and the International Linear Collider (ILC), which is hoped to be built in Japan. Some key parameters of both designs are given in Table 1.3.

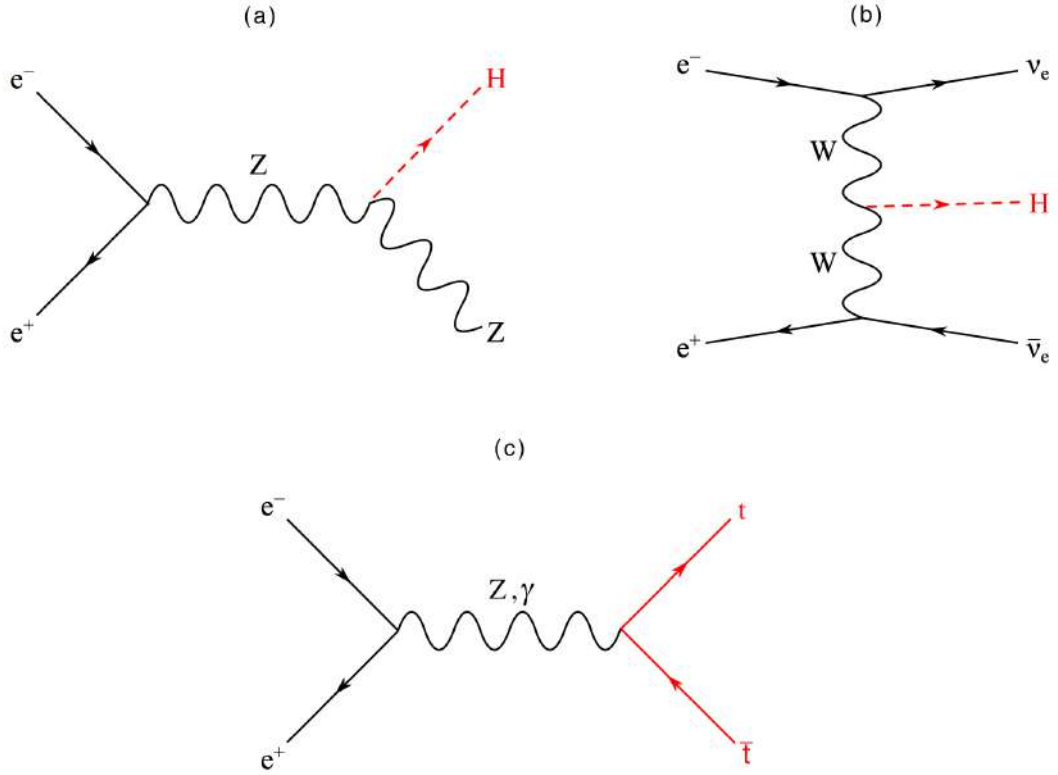

Figure 1.3: Feynman diagrams for production of Higgs Bosons via (a) Higgs-strahlung and (b) WW fusion through electron-position annihilation [16], and (c) the leading order diagram for top quark production via electron-position annihilation [17].

Table 1.3: Design parameters for the ILC [19] and CLIC [18].

Parameter	Units	ILC	CLIC
Beam energy	[GeV]	500	3000
Number of bunches	[bunches/train]	1312	312
Intensity	[10^{10} electrons/bunch]	2.0	0.372
Bunch separation	[ns]	554	0.5
Repetition rate	[Hz]	5	50
Main linac average gradient	[MV/m]	31.5	100
Horizontal rms beam size at the IP (σ_x^*)	[nm]	474	40
Vertical rms beam size at the IP (σ_y^*)	[nm]	5.9	1
Luminosity (L)	[10^{34} cm^{-2} s^{-1}]	1.8	5.9
Site length	[km]	31	48.4

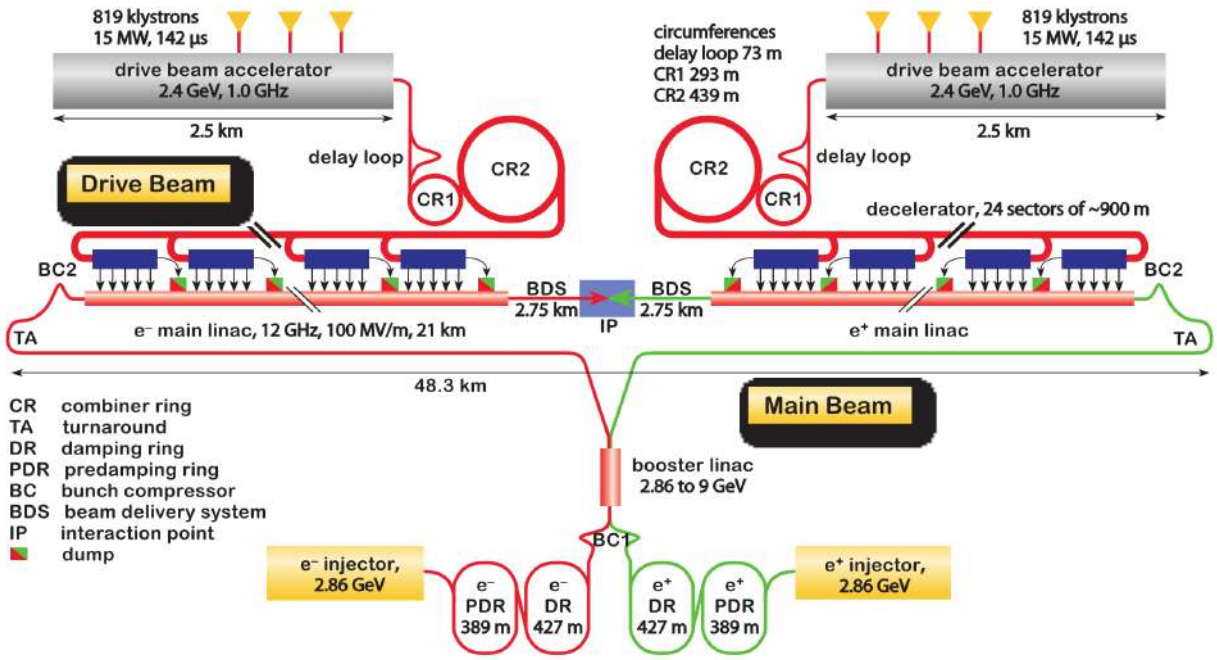

Figure 1.4: Schematic layout of the CLIC design [18].

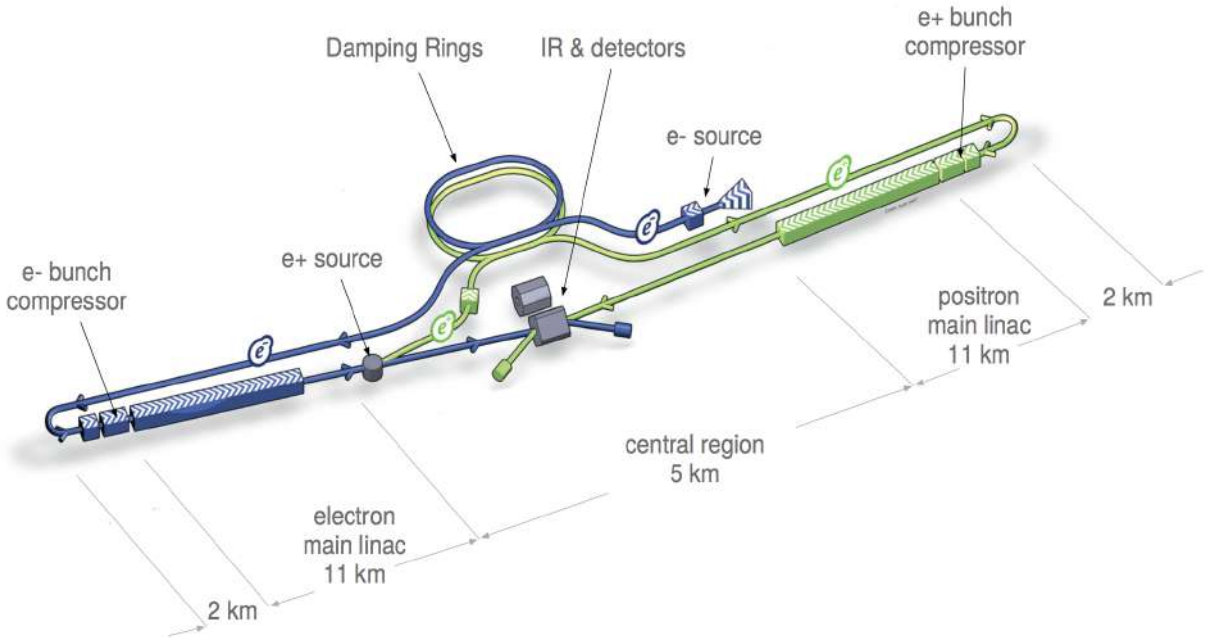

Figure 1.5: Schematic layout of the ILC design [19].

The Compact Linear Collider (CLIC)

The CLIC design (Fig. 1.4) features a novel drive beam acceleration scheme that will enable unprecedentedly high accelerating gradients, culminating in a 3 TeV collision energy and luminosity of 5.9×10^{34} cm^{-2}s^{-1} [18]. This "compact" drive beam technique will keep the machine length to ∼48.4 km. In this scheme, two drive beams are initially accelerated using normal conducting RF cavities. A delay loop and two combiner rings compress the bunch train and the resulting high-intensity beam is decelerated through a series of Power Extraction and Transfer Structures (PETS). The extracted power is used to generate the 100 MV/m accelerating gradients for the main beams. The plan is to build in stages, beginning with a 380 GeV centre-of-mass energy, followed by 1.5 TeV and 3 TeV [20]. A complete technical description of the initial 380 GeV stage is currently in progress, as well as preparation for a future technical design report phase [21].

The International Linear Collider (ILC)

The ILC (Fig. 1.5) is designed to have a tuneable centre-of-mass energy between 200 and 500 GeV (upgradable to 1 TeV) with a peak luminosity of 1.8×10^{34} cm^{-2}s^{-1}. The completed 500 GeV energy-reach machine will be approximately ∼31 km in length. The accelerating structures will be based on superconducting RF niobium cavities, providing an average accelerating gradient of 31.5 MV/m. The ILC has a less ambitious energy reach than CLIC, but is in a more advanced stage of development, with a technical design report published in 2013 [19] and proposed construction sites in Japan. The possibility of a staging approach to construction starting with a 250 GeV centre-of-mass energy (with the possibility of future upgrades to 500 GeV) is currently under consideration [22] to lower initial costs.

Test Facilities

Several test facilities have been used to study the feasibility of achieving the design parameters of these proposed machines (Table 1.3), which demand exceptionally small vertical beam sizes on the nanometre scale, nanosecond bunch separations (∼500 ns at the ILC and 0.5 ns at CLIC) and high accelerating gradients. These facilities have included the Final Focus Test Beam (FFTB) at SLAC which demonstrated a 70 ± 7 nm vertical beam size [23, 24], and the CLIC Test Facility 3 (CTF3) at CERN, which trialled the high-intensity drive beam acceleration concept [25, 26]. All the experiments presented in this thesis were conducted at The Accelerator Test Facility 2 (ATF2) at the High Energy Accelerator Research Organisation (KEK) [27] in Tsukuba, Japan.

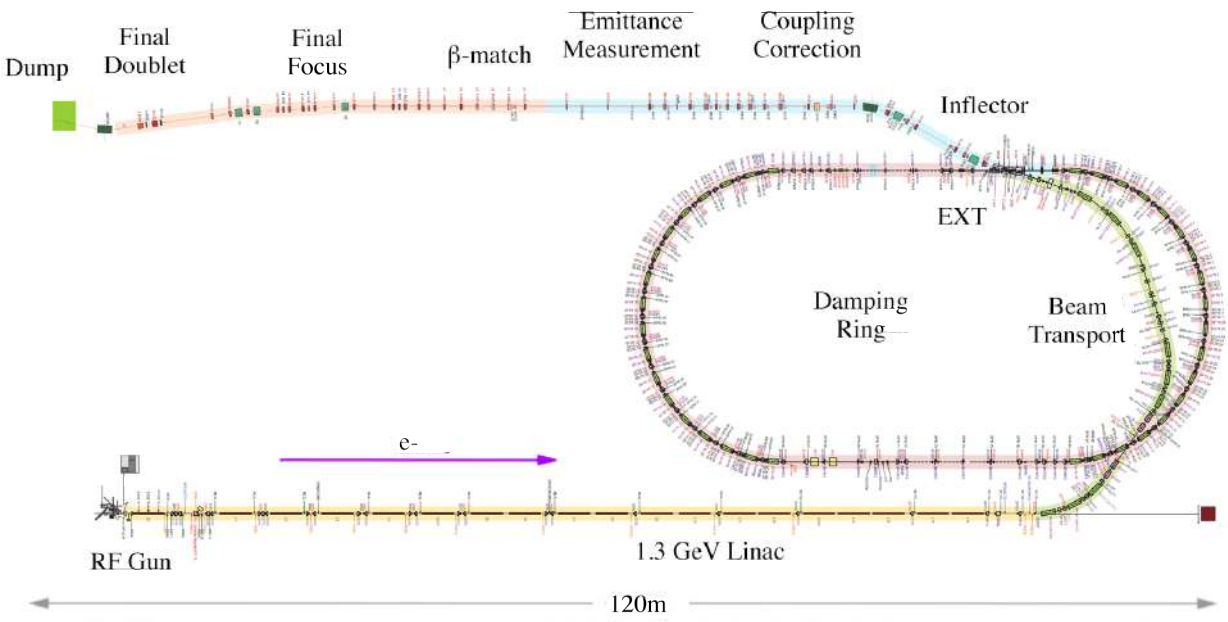

Figure 1.6: Schematic layout of the ATF2 [28].

1.3 The Accelerator Test Facility 2 (ATF2)

The ATF2 is a linear electron accelerator designed to test the feasibility of technologies and beam dynamics required for the next generation of linear colliders, particularly for application at the ILC [29]. Beam operation began in 1997 as the "ATF" with the initial goal of achieving an extremely low vertical emittance beam similar to those required for the ILC. The design parameters were achieved in 2001 [30] [31]. The facility was then upgraded in 2008 to the ATF2 [32] to address the challenges of focusing beams to nanometer sizes. The existing low-emittance ATF machine was extended to include a 100m beam delivery system with an extraction line and energy-scaled version of the final focus system design for the ILC [33]. The main design parameters for the ATF2 are detailed in Table. 1.4 and the layout is shown in Fig. 1.6.

An S-band RF gun with a cesium-telluride photocathode driven by a multi-bunch UV laser generates electron bunches of up to 1×10^{10} particles per bunch at a bunch frequency of 3.12 Hz. The bunch intensity can be varied by choosing a suitable sequence of laser pulses. The bunches are then accelerated to 1.3 GeV along an 88 m linac [34] using room temperature RF cavities.

The bunches pass through a transfer line, and are injected into a race-track shaped 138.6 m circumference damping ring, where they are stored for over 100 ms [34]. The beam emittance is reduced in the ring via synchrotron radiation. The longitudinal momentum is restored by accelerating 714 MHz RF cavities, maintaining the 1.3 GeV beam energy

Table 1.4: ATF2 design parameters [35] [36].

Parameter	Units	ATF2 design
Beam energy	[GeV]	1.3
RMS energy spread	[%]	[0.06, 0.08]
Intensity	[electrons/bunch]	1×10^{10}
Repetition rate	[Hz]	3.12
Horizontal emittance (ϵ_x)	[nm rad]	2
Vertical emittance (ϵ_y)	[pm rad]	12
Horizontal β function at the IP (β_x^*)	[mm]	4
Vertical β function at the IP (β_y^*)	[mm]	0.10
Horizontal RMS beam size at the IP ($\hat{x}^*$)	[µm]	2.8
Vertical RMS beam size at the IP ($\hat{y}^*$)	[nm]	37

[37]. A best-achieved vertical normalised emittance of 1.5×10^{-8} m (6 pm of geometrical emittance) was measured in 2004 for a bunch intensity of 1×10^{10} electrons per bunch [31]. For typical operation, the horizontal and vertical geometrical emittance are < 2 nm and $<$ 10 pm, respectively [38].

The electron bunches are extracted from the damping ring by a pulsed magnetic kicker [39], sending a single bunch down the extraction line. For trains of more than one bunch, the linac injects bunches into the damping ring at the usual frequency, and they are stored in the ring before being extracted. Once all the desired bunches have been damped, a single extraction kicker pulse extracts them to produce the multi-bunch train in the extraction line. The ATF2 is designed to be capable of extracting bunches with an ILC-like bunch separation of a few hundred nanoseconds. The maximum train length is restricted by the 300 ns extraction kicker pulse [40], but its timing can be adjusted to ensure all bunches are extracted successfully.

An inflector section of dipole magnets offsets the beam from the damping ring and brings it in parallel to the damping ring straights (see Fig. 1.6) [41], followed by a coupling correction section of skew-quadrupoles. This is followed by an emittance diagnostic section including Optical Transition Radiation monitors, which enable transverse beam size measurements and emittance reconstruction [42]. The β functions are adjusted before the final focus system minimises the beam size via a sequence of strong dipole, quadrupole, and sextupole magnets [38]. This focusing culminates in the final doublet quadrupoles, which

squeeze the beam to a very small size beam waist at the IP [35]. The IP is named to correspond to the interaction point of a collider, but there is only one beam at the ATF2, so there is no collision there.

The goals of the ATF2 are: (1) to achieve and maintain a 37 nm vertical beam size at the IP and, (2) to stabilise the IP beam position to the nanometer level [32]. Goal 1 represents an energy-scaled equivalent of the 6 nm vertical beam size required at the ILC IP. Significant progress has been made towards this goal, achieving a measured beam size of 41 nm as of 2016 [43]. Goal 2 involves the use of an intra-train beam position feedback system and forms the primary focus of the studies contained in this thesis.

1.4 Feedback On Nanosecond Timescales

It is notable that future linear colliders, such as the ILC and CLIC, plan to produce flat beams with $\sigma_x^* \gg \sigma_y^*$ and vertical beam sizes on the order of nanometres (see Table 1.3). This beam shape is reflected in the ATF2 beam sizes (Table. 1.4) and is motivated by beam-beam effects at the collision point, where the charged particles are deflected by the opposing beam's electromagnetic field as they reach collision. The forced curved trajectory causes the particles to emit beamstrahlung radiation [44], resulting in an undesirable energy spread, δ_{BS}, in the particle bunch:

$$\delta_{BS} \propto \frac{1}{(\sigma_x^* + \sigma_y^*)^2}. \tag{1.5}$$

To achieve the maximum possible luminosity, L (Eq. 1.2), it is desirable to minimise δ_{BS} simultaneously by using flat beams, and to ensure maximum beam-beam overlap for successful collisions.

Any energy and intensity jitter in hardware, beamline component vibrations or ground motion at a frequency comparable to the accelerator operation frequencies will compromise the luminosity of the experiment [45]. For example, ground motion on the order of tens of nanometres is expected at the train repetition frequency of the ILC [46]. The Feedback On Nanosecond Timescales (FONT) intra-train feedback system was conceived to counteract these instabilities to achieve and maintain the luminosity at the collision point [47].

An example of such a feedback system is illustrated in Fig. 1.7, showing the two incoming beams at the IP crossing point. If the bunches are not perfectly aligned in the transverse plane, they will deflect each other. A beam position monitor (BPM) in the path of one of the outgoing bunches can measure its deflection and use it to calculate the degree of misalignment. A corrective feedback signal is generated and amplified in time for a kick to

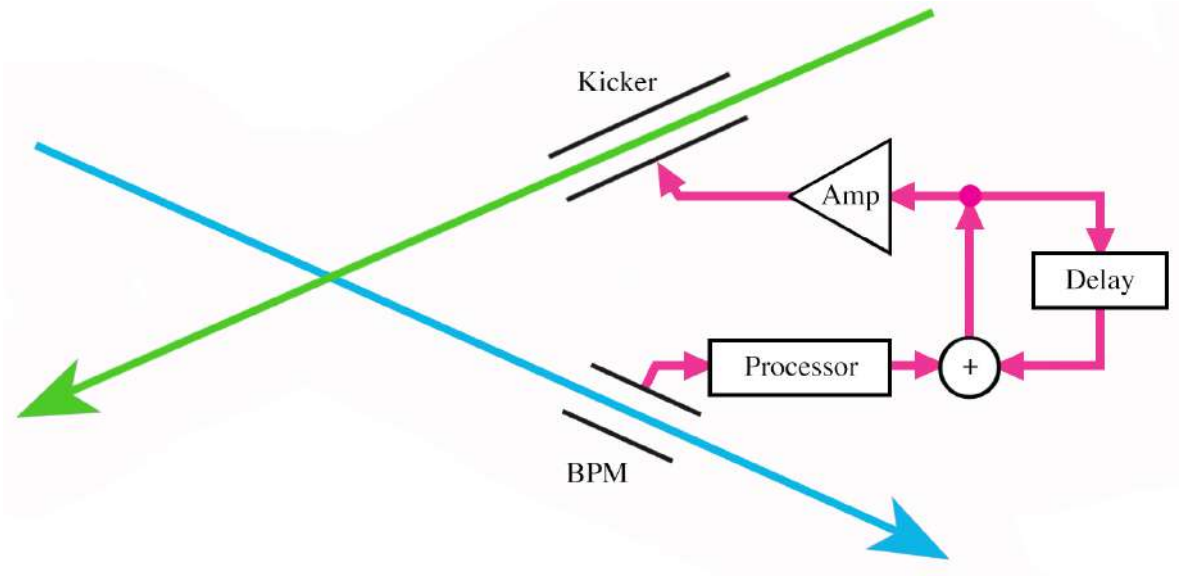

Figure 1.7: Schematic of an IP intra-train feedback system for an interaction region in the horizontal plane [48].

be applied to the next bunch of the other incoming beam. A delay loop stores the correction and ensures the necessary kick is applied to all subsequent bunches, so the correction is maintained and refined with each bunch measurement. In this way, the feedback system can stabilise the collision point for every subsequent bunch in a multi-bunch train after the first bunch and achieve maximal beam-beam overlap.

Early versions of the FONT system were analogue systems designed to optimise feedback latency, achieving a closed feedback loop of just 23 ns [49] with a feedback system early in the ATF2 extraction line. Later iterations adopted a digital feedback board for increased flexibility in firmware design, which increased processing time to ∼160 ns [50], but still within the requirements of ILC bunch spacing. Beam misalignments of the order of a fraction of a nanometre at the ILC will result in micron-level beam-beam deflections [51]. This BPM resolution and the required latency for intra-train feedback at the ILC have all been successfully demonstrated with the FONT system [52].

FONT studies have shifted in recent years to extending feedback capabilities in the context of the ATF2 IP region and the goal 2 objective. The digital design of more recent FONT systems have also enabled more sophisticated feedback modes, with inputs from up to three separate BPMs. Former FONT students have characterised the initial IP feedback system set-up and explored more advanced feedback modes with the ATF2 upstream feedback system [53, 8]. The studies presented here will build on their work with a focus on the application of feedback in the ATF2 IP.

The ATF2 only has one beam, so the feedback system has to measure and apply corrections to the same beam. For example, in a two-bunch train, the bunch 1 vertical position could be measured by a BPM, and the information used to "correct" bunch 2 before it arrives at that same BPM, where it is then also measured to observe the effect of the feedback. Measuring the beam position rather than the beam deflection puts much tougher demands on the BPM resolution performance, especially in the ATF2 IP region where nanometre-level stabilisation in the vertical plane will require nanometre-level position resolution. Consequently, most of the studies presented here focus on optimisation of the IP BPM system and analysis techniques to quantify and improve resolution capabilities.

1.5 Thesis outline

The work in this thesis is a contribution towards successful beam position stabilisation in single-pass accelerators. The experiments were all performed in the context of the ATF2 goal 2: aiming to achieve nanometre level stabilisation at the IP using an intra-train feedback system. In Chapter 2 the IP BPM system is described, including the high-resolution cavity BPMs; the signal processing, position calibration and digitisation set-ups. In Chapter 3 studies are presented on ways of calculating and optimising the position resolution of IP system both in hardware and through different approaches to analysis. In Chapter 4 studies are reported on the potential IP position measurement sensitivities to phase jitter. In Chapter 5 a novel mode of IP feedback is presented using two BPMs as input to the feedback algorithm and correcting at an intermediate location. This mode provides the first independent witness to the feedback process and has achieved the best IP position stabilisation results to date. The thesis closes with a conclusion and some suggestions for further study.

Chapter 2

IP BPM system

When a bunch of charged particles travels through a cavity, the cavity acts as a waveguide and oscillating electromagnetic fields are generated. Certain resonant modes couple strongly to the position offset of the bunch relative to the cavity's electrical centre. These modes can be used to monitor the transverse position of the beam. The FONT system in the IP region of the ATF2 has utilised three cavity BPMs for studies of beam-based feedback with the ultimate aim of stabilising the beam position to the nanometre level.

In this chapter, the theory of cavity BPMs and how position-dependent modes are isolated is explored. The three ATF2 IP cavity BPMs and their signal processing electronics are detailed, along with a set-up utilising a FONT board for signal digitisation. The position calibration method is explained. The results of studies that attempted to quantify the electronic noise floor of the IP system are explained, and the necessity for a mixer pedestal subtraction is introduced. Detailed studies of the output signals are presented, with an emphasis on troubleshooting unwanted parasitic pulse features.

2.1 Theory of cavity BPMs

The electromagnetic fields in a resonant cavity BPM are defined by their eigenmodes. These are represented in terms of integers m, n and l, which specify modes along the Cartesian x, y, and z axes respectively. If the bunch trajectory is in the z direction, an EM field with an electric field component along that axis will be excited. These eigenmodes are known as transverse magnetic (TM) modes because there is no magnetic field along the direction of propagation. The modes utilised in cavity BPMs are also selected to be independent of z (i.e. $l = 0$).

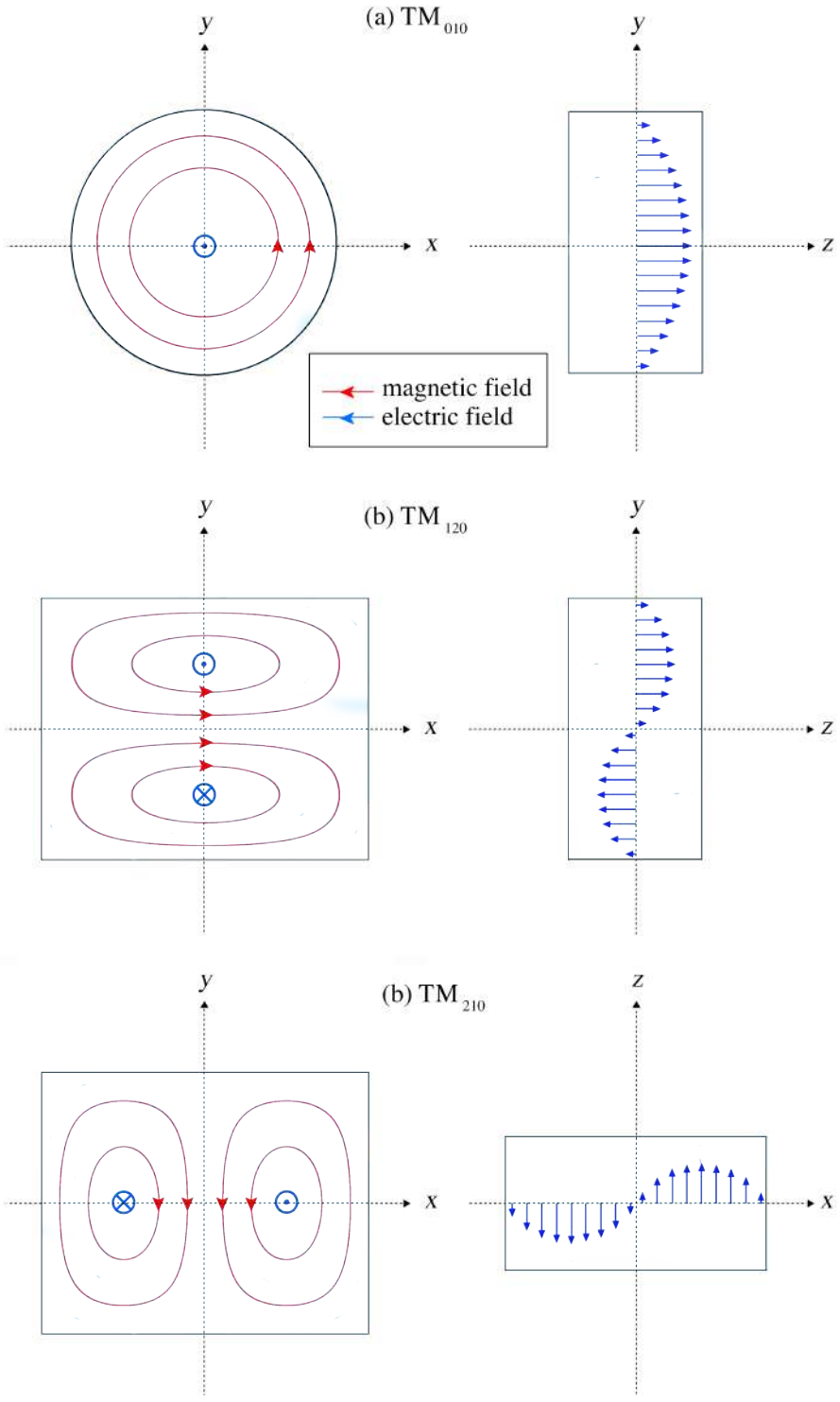

Figure 2.1: (a) Illustration of the TM_{010} monopole mode in a cylindrical BPM cavity, (b) the TM_{120} mode, and (c) the TM_{210} mode in rectangular BPM cavities. Magnetic field lines are shown in red, and electric field lines in blue. The length of the blue electric field lines in the right-hand plots indicates the amplitude of the electric field for different offsets from the electrical centre of the cavity.

Monopole mode

Fig. 2.1.a shows representations of electric and magnetic fields of the first monopole mode TM_{010} in a cylindrical cavity. The electric field is spatially rotationally symmetric and will be proportional to the charge of the bunch. In a particle accelerator, the bunches will typically pass close to the electrical centre of the cavity with small position offsets in the transverse plane where the signal amplitude is independent of position. The monopole mode is therefore used in a "reference" cavity to generate a signal that couples linearly to beam charge. The ATF2 IP system had two reference cavity BPMs; one for the x plane and one for y. The signal does not depend on x or y, and the two measurements can be used to verify each other.

Dipole modes

Figs. 2.1 (b) and (c) illustrate the first dipole modes TM_{120} and TM_{210} in rectangular cavities. The electric field of the dipole mode is spatially anti-symmetric. If the beam travels exactly through the centre, the dipole mode will not be excited. At position offsets close to the electrical centre, the strength of the TM_{120} and TM_{210} modes will be proportional to offsets in the x and y planes respectively. These modes are therefore used for determining the beam position. The strength of the dipole modes will also depend on the bunch charge, but the position dependence alone can be isolated in analysis. There are three dipole cavity BPMs in the ATF2 IP region to monitor transverse bunch position offsets.

Frequency and Quality Factor

The resonant frequencies of these modes are determined by the dimensions of the cavity. If the cavity boundaries are defined as $-\frac{a}{2} \leq x \leq \frac{a}{2}$ and $-\frac{b}{2} \leq y \leq \frac{b}{2}$, and the bunch is travelling with a velocity v, the frequency of the mode is [54]:

$$f_{mn} = \frac{v}{2}\sqrt{\left(\frac{m}{a}\right)^2 + \left(\frac{n}{b}\right)^2}. \tag{2.1}$$

For beamline cavities, a and b are typically of the order of centimetres, and the particles will be relativistic, so most cavity BPMs operate at resonant frequencies at the GHz scale.

The electromagnetic field oscillations decay exponentially as energy dissipates from the cavity, with a characteristic decay time, τ. A cavity's ability to "store" different frequency modes over time can be quantified using the quality factor, Q, defined as [55]:

$$Q_{mn} = 2\pi f_{mn} \frac{\text{energy stored}}{\text{energy lost per second}}. \tag{2.2}$$

If a cavity has a high Q value the resonant field decay time will be longer.

2.2 Signal extraction

The energy in the resonant fields can be extracted and used for diagnostic purposes. When coupling out signals it is vital to read out the required modes only. For a reference cavity the dominant monopole mode is the eigenmode of interest, so signal extraction is achieved via a coaxial electrical antenna introduced straight into the cavity.

For position-dependent dipole mode cavities the fundamental monopole mode will also be strongly present, with a wide frequency spread and often a larger amplitude than the desired dipole signals. The monopole mode, therefore, needs to be suppressed in coupling out the dipole mode signals. It is also necessary to separate the two dipole modes from each other, to distinguish x and y position information.

Spatial filtering

Mode isolation in dipole cavities is achieved through spatial filtering using waveguides [56]. Fig. 2.2 shows the design of a rectangular cavity BPM that utilises this technique, with thin coupling slots in the transverse surface of the main cavity that lead to waveguides. These slots are arranged to run parallel to the magnetic field lines of the TM_{210} or TM_{120} modes. The TM_{210} mode is used as an example in Fig. 2.2, with the magnetic fields being successfully transmitted through two vertical coupling slots to a pair of vertical waveguides.

An equivalent pair of horizontal slots and waveguides (not pictured in Fig. 2.2) are used to couple out the magnetic fields of the TM_{120} mode, whose magnetic fields are orthogonal to the TM_{210}. This arrangement (with a total of four slots leading to a vertical and horizontal pair of waveguides) results in the two modes excited by offsets in the x and y plane both being successfully transmitted from the main cavity but into separate pairs of waveguides.

The monopole mode's magnetic field lines would pass perpendicular to all four coupling slots, preventing transmission. In addition, the waveguides are designed to be small enough to support only frequencies equal to or greater than the dipole-mode frequencies, further suppressing the lower-frequency monopole mode.

Once the magnetic field has been coupled out of the cavity, it excites an electric field in the waveguide. The TM_{210} waveguide field distributions are shown in Fig. 2.2. The two antennas are positioned at anti-nodes of the fields in the pairs of waveguides, so the two signals will be π out of phase with one another. These signals are combined immediately after the cavity using a 180° hybrid, cancelling any residual components of symmetric modes and doubling the size of the output signal.

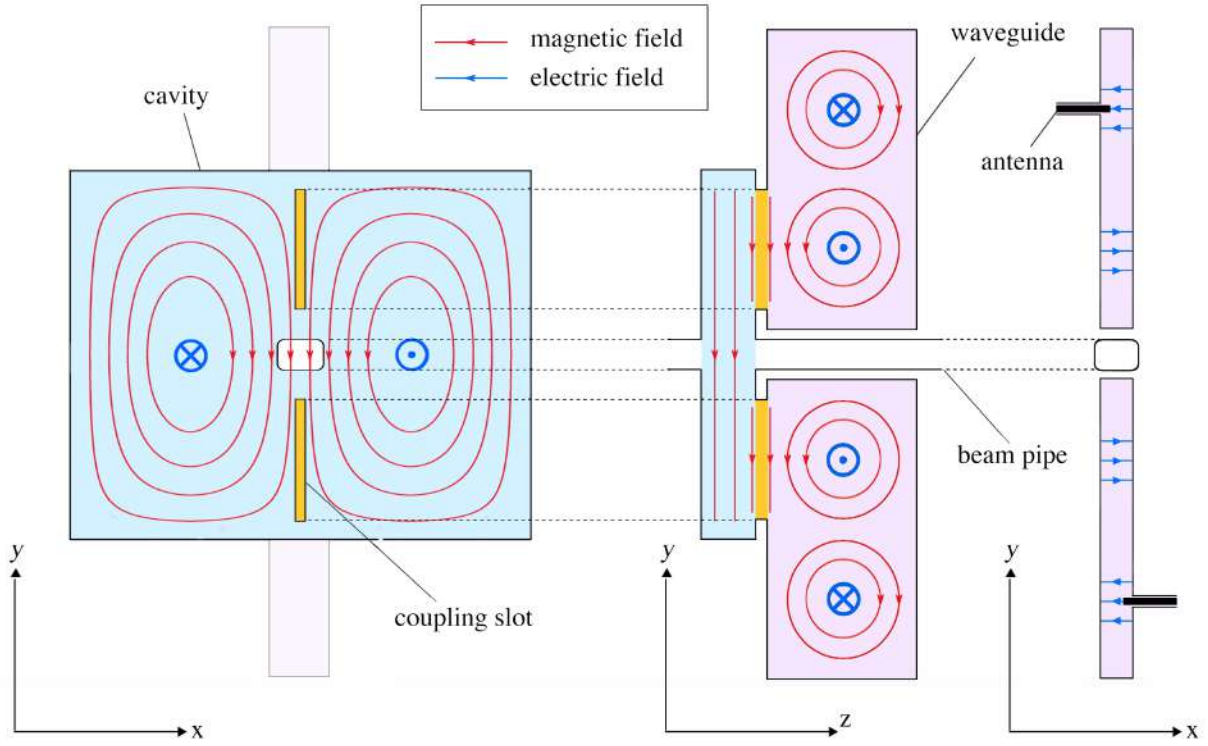

Figure 2.2: Schematic of a rectangular cavity BPM and a TM_{210} mode. Magnetic and electric field line patterns are shown in the x-y-z projections face-on (left), side-on including the waveguides (centre), and face-on showing the antenna (right). The pair of waveguides that couple to the perpendicular TM_{120} mode are not shown.

2.3 ATF2 IP BPM design and specifications

A schematic of the beamline elements in the ATF2 IP area after the final focus magnets is shown in Fig. 2.3. Two rectangular dipole cavity BPMs, IPA and IPB, are upstream and the third, IPC, is downstream of the nominal beam waist location. This allows reconstruction of the bunch position and angle in the IP. The BPMs were enclosed in a vacuum chamber, along with a beam size monitor (BSM) known as the Shintake Monitor [57]. The BSM used laser interference fringe patterns to measure the electron bunch size [58]. Upstream is the stripline kicker IPK, which was used to provide beam position kicks in FONT experiments. Downstream x and y monopole reference cavities are used to measure the bunch charge.

Dipole cavities

The original IP BPM system comprised brazed-copper cavity BPMs with a high quality factor that produced decay times of ∼30 ns [59]. This BPM design was subsequently re-fabricated in aluminium [60]. The different material enabled a low mass of ∼1 kg for each

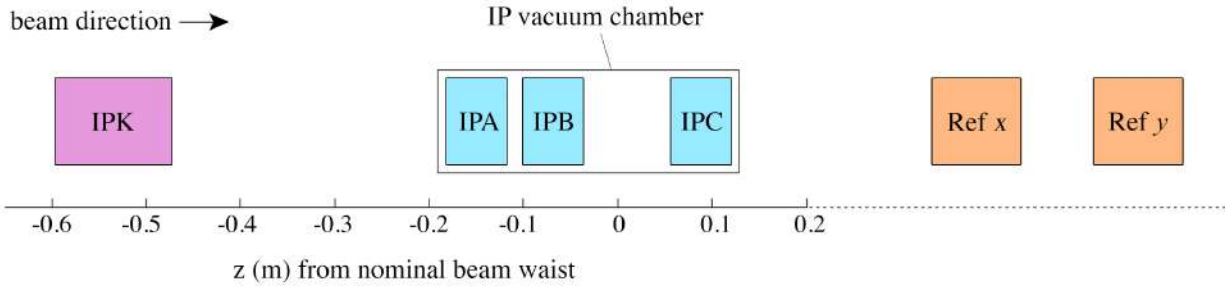

Figure 2.3: Relative longitudinal locations of beamline elements in the ATF2 IP region [8]; the kicker, (IPK), dipole cavity BPMs, (IPA, IPB and IPC) inside the vacuum chamber, and reference cavities (Ref x and Ref y) are shown schematically.

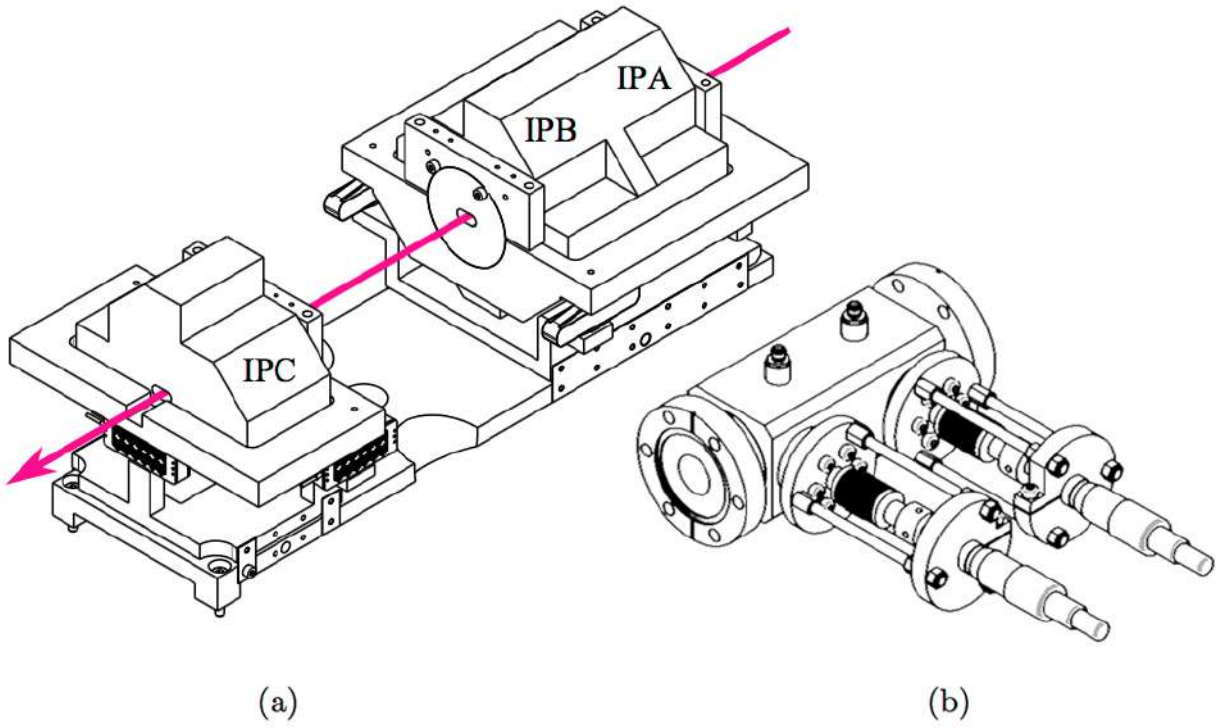

Figure 2.4: Technical drawings of (a) the dipole cavity block containing IPA, IPB and IPC [61], and (b) the reference cavity block containing the x and y reference cavities [62].

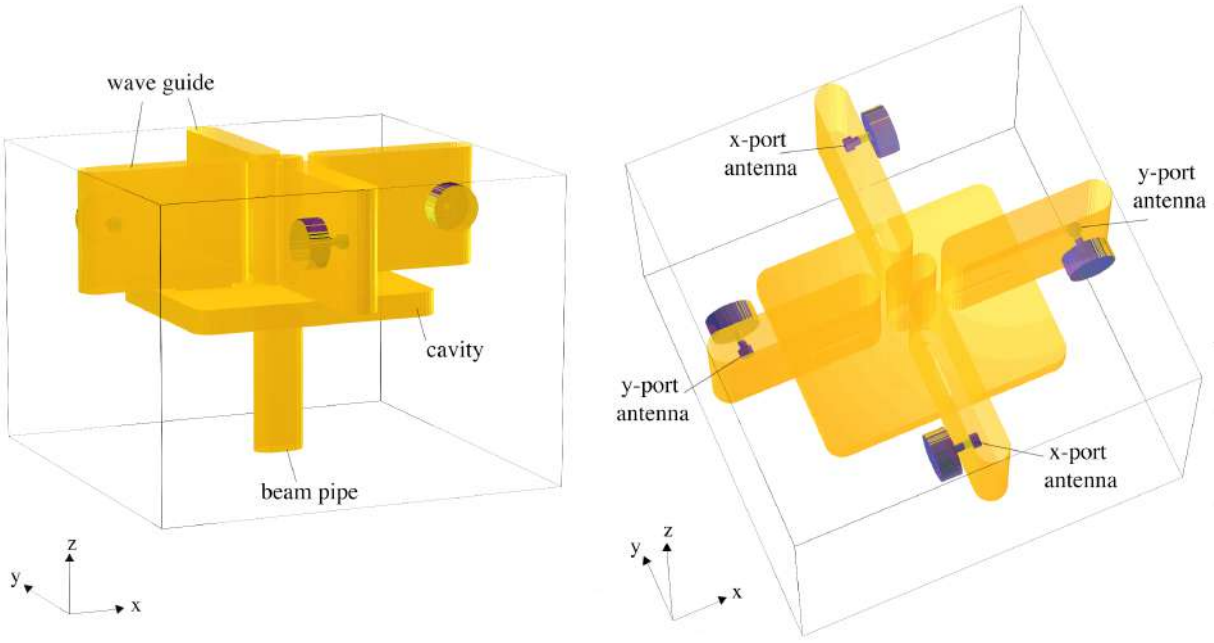

Figure 2.5: Model of the ATF2 IP dipole cavity BPMs generated in GdfidL [63].

BPM [64] so the cavities could be mounted on a customised piezo-driven mover system [65]. Fig. 2.4.a shows the three dipole BPMs on the mover system mounting table. IPA and IPB were constructed from a single block. The distances between the centres of the dipole BPMs in situ are given in Table 2.1.

Table 2.1: Longitudinal separations between the centres of the BPMs [65]. The uncertainties are derived from fabrication tolerances.

	Longitudinal distance (mm)
IPA to IPB	80.8 ± 0.1
IPB to IPC	174.2 ± 0.14

The aluminium BPMs, illustrated in Fig. 2.5, had a cross section of 11 × 11 cm^2. Unlike the original monolithic copper cavities, the aluminium versions were built from pieces. They were designed to match the resonant frequencies of the original copper BPMs so the existing ATF2 processing electronics would be compatible. The frequency matching was achieved in the new aluminium cavities, but they demonstrated lower quality factors than in design. These very short signals, with decay times of ∼10 ns, reduced signal contamination between pulses when measuring multi-bunch trains, but also resulted in reduced sensitivity to position offsets. The relative alignment of the BPMs was also not adequate for purpose, particularly between the IPA and IPB cavities.

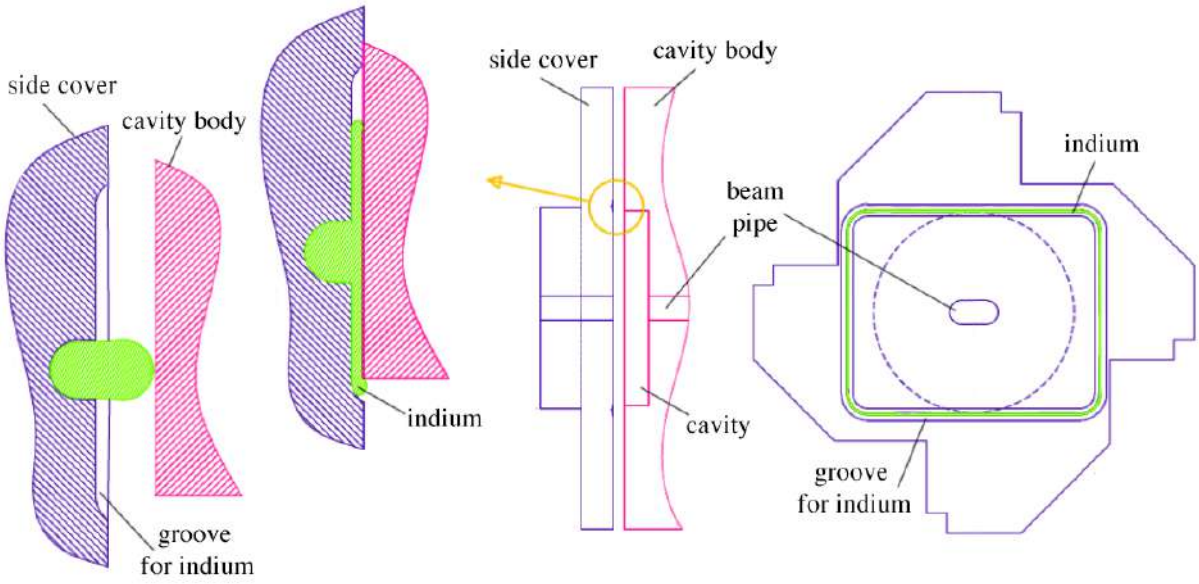

Figure 2.6: Diagrams of the groove in the BPM side plate for an indium seal [66].

Consequently, the BPMs were re-manufactured with stricter tolerances to improve the relative alignment. The cavity side covers were also re-machined in April 2017, with a groove to incorporate a good-contact indium seal between the components [66], shown in Fig. 2.6. This modification, combined with adding spacers under the antennae feedthroughs to reduce the external coupling, yielded decay times more comparable with the original copper BPMs (Table 2.2).

Reference cavities

Fig. 2.4.b shows a technical drawing of the reference cavity. These BPMs were cylindrical, with a 42.95 (38.65) mm diameter for the x (y) cavity respectively [64]. They were constructed from stainless steel with vertical tuning pins that allow the frequency of the resonant monopole mode to be adjusted within a range of $\pm$ 35 MHz to match the average frequency of the dipole cavity x and y ports [67]. The design frequencies and frequency measurements following re-tuning are listed in Table 2.2.

Mover system

The dipole cavities were mounted inside the vacuum chamber on two independent mover blocks, the first containing IPA and IPB, the second IPC. Each mover block consisted of three vertical sub-movers and one horizontal mover, enabling the vertical and lateral position and pitch to be adjusted. The movers for the IPA-IPB block were manufactured by Cedrat Technologies with a full range of 248 µm, and the movers for the IPC block by

Table 2.2: Design [60] [68] and measured frequencies [69] and decay times for the three IP BPM dipole y and x ports and the two reference cavities in y and x.

BPM cavity	Design frequency (GHz)	Measured frequency (GHz)	Decay time (ns)
IPA y-port	6.426	6.428	26
IPB y-port	6.426	6.427	22
IPC y-port	6.426	6.428	21
IPA x-port	5.712	5.705	25
IPB x-port	5.712	5.706	25
IPC x-port	5.712	5.704	23
Reference y	6.415	6.428	14
Reference x	5.711	5.705	14

the company PI with a full range of 300 µm [65]. The main limitation of this system was that IPA and IPB could not be adjusted separately, as they were mounted on the same block. All the sub-movers had feedback systems to ensure that once the position and angle had been set, the blocks remained stable to ±2nm or better [65].

For the majority of the data presented in this thesis one of the vertical sub-movers on the Cedrat IPA-IPB block was not functioning correctly. This initially presented itself as non-linear readback behaviour, and later by a complete lack of response [70]. Since access to the mover system required breaking the vacuum in the IP chamber, it was necessary to operate without full functionality on many beam shifts so as not to interrupt beam operation.

Fortunately, the sub-movers were powered independently, so the faulty one was disabled, and full use of the other two vertical sub-movers was retained. It was still possible to adjust the horizontal position and pitch of the IPA-IPB block. The major consequence was that the IP BPM mover system could not be used to calibrate the BPMs.

Signal outputs

Figure 2.7 shows an electron bunch passing through an accelerator. The vertical offset y, bunch angle, y', and bunch tilt, α, of the trajectory (along with the bunch charge, q) will impact the amplitude of the dipole mode voltage signal, V, that is coupled to the waveguide antennae [59] [71]. For a rectangular dipole cavity with a design frequency of f_{dipole} and decay constant τ_{dipole} the output signals in the limit when both y' and $\alpha << 1$, will evolve

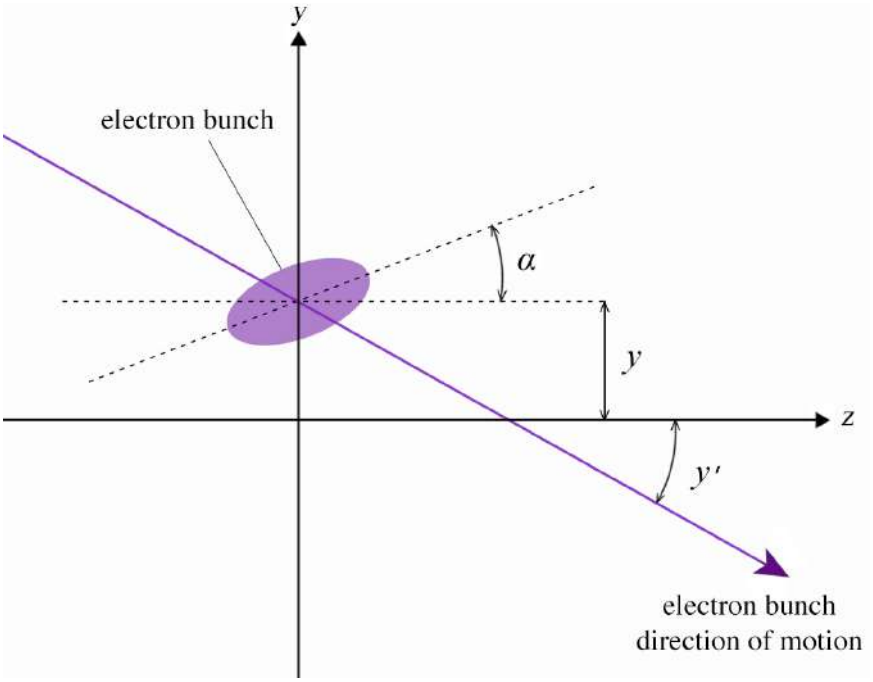

Figure 2.7: Representation of a travelling electron bunch with a vertical displacement y, a pitch angle y' and a tilt α.

with time, t, [72] as:

$$\mathrm{V}_y(y,q,t) \propto y\,q\,\mathrm{e}^{-\frac{t}{2\,\tau_{\mathrm{dipole}}}}\,\sin\Big(2\pi f_{\mathrm{dipole}}\,t\Big), \tag{2.3}$$

$$\mathrm{V}_{y'}(y',q,t) \propto y'\,q\,\mathrm{e}^{-\frac{t}{2\,\tau_{\mathrm{dipole}}}}\,\cos\Big(2\pi f_{\mathrm{dipole}}\,t\Big), \tag{2.4}$$

$$\mathrm{V}_{\alpha}(\alpha,q,t) \propto -\alpha\,q\,\mathrm{e}^{-\frac{t}{2\,\tau_{\mathrm{dipole}}}}\,\cos\Big(2\pi f_{\mathrm{dipole}}\,t\Big). \tag{2.5}$$

The total output voltage of the dipole cavity, $\mathrm{V}_{\mathrm{dipole}}$, is:

$$\mathrm{V}_{\mathrm{dipole}}(y,y',\alpha,q,t) = \mathrm{V}_y + \mathrm{V}_{y'} + \mathrm{V}_{\alpha}. \tag{2.6}$$

The position component, V_y, of this signal is 90° out of phase with the angular, $V_{y'}$, and bunch tilt, V_α, contributions.

The monopole reference cavity signal output, $\mathrm{V}_{\mathrm{ref}}$, is independent of position, angle, and tilt, depending only on the bunch charge as it evolves with time:

$$\mathrm{V}_{\mathrm{ref}}(q,t) \propto q\,\mathrm{e}^{-\frac{t}{2\,\tau_{\mathrm{ref}}}}\,\sin\Big(2\pi f_{\mathrm{ref}}\,t\Big), \tag{2.7}$$

where f_{ref} is the reference cavity monopole mode resonant frequency, and τ_{ref} is the decay constant of the cavity.

2.4 Processing electronics

The ATF2 IP BPM signal processing system developed at KEK in 2008 [59] featured two stages. First, the high-frequency signals were mixed with an external local oscillator (LO) signal to produce an intermediate frequency output. The down-mixed dipole and reference signals were then mixed in a second stage to produce baseband signals for digitisation. Fig. 2.8 shows a simplified schematic of the electronics. The output signals, I, Q, and q can then be combined to produce a signal proportional to the beam position.

Initial signals

Before entering the first down-mixing stage, the two signals (Fig. 2.2) from the dipole cavities were combined using a 180° hybrid. This was followed by 10 dB-step variable attenuators to allow control of the amplitude of the signals entering the processing electronics. The signals then passed through ±700 MHz BPFs, which were centred around the desired resonant mode frequencies, f_{dipole} and f_{ref}. This filtering removed any residual unwanted modes.

The dipole and reference cavity signals entering the first stage mixer take the form:

$$\mathrm{V}_{\text{dipole}}(y, y', \alpha, q, t) = \Big[A_y\, y \sin(2\pi f_{\text{dipole}}\, t) + (A_{y'}\, y' \,-\, A_\alpha\, \alpha) \cos(2\pi f_{\text{dipole}}\, t)\Big]\, q\, \mathrm{e}^{-\frac{t}{2\,\tau_{\text{dipole}}}}, \tag{2.8}$$

$$\mathrm{V}_{\text{ref}}(q, t) = A_{\text{ref}} \sin(2\pi f_{\text{ref}}\, t)\, q\, \mathrm{e}^{-\frac{t}{2\,\tau_{\text{ref}}}}, \tag{2.9}$$

where A_y, $A_{y'}$, A_α, and A_{ref} are constants.

First-stage processing

The cavity signals were then mixed independently with externally-provided sinusoidal LO signals with constant amplitudes, A_{LO}, and frequencies, f_{LO}:

$$\mathrm{V}_{\text{LO(dipole)}}(t) = A_{\text{LO(dipole)}} \sin(2\pi f_{\text{LO(dipole)}}\, t + \Delta\phi_{\text{LO(dipole)}}), \tag{2.10}$$

$$\mathrm{V}_{\text{LO(ref)}}(t) = A_{\text{LO(ref)}} \sin(2\pi f_{\text{LO(ref)}}\, t + \Delta\phi_{\text{LO(ref)}}), \tag{2.11}$$

where the $\Delta\phi_{\text{LO(dipole)}}$ and $\Delta\phi_{\text{LO(ref)}}$ terms are the phases of the LO signals relative to the respective dipole and reference cavity signals.

Both LO signals were derived from the damping ring (DR) 714 MHz master oscillator, which was frequency multiplied to produce signals which were 714 MHz away from the design frequencies of the BPM cavities. The frequencies at the different stages of the processing electronics in the x and y ports are listed in Table 2.3.

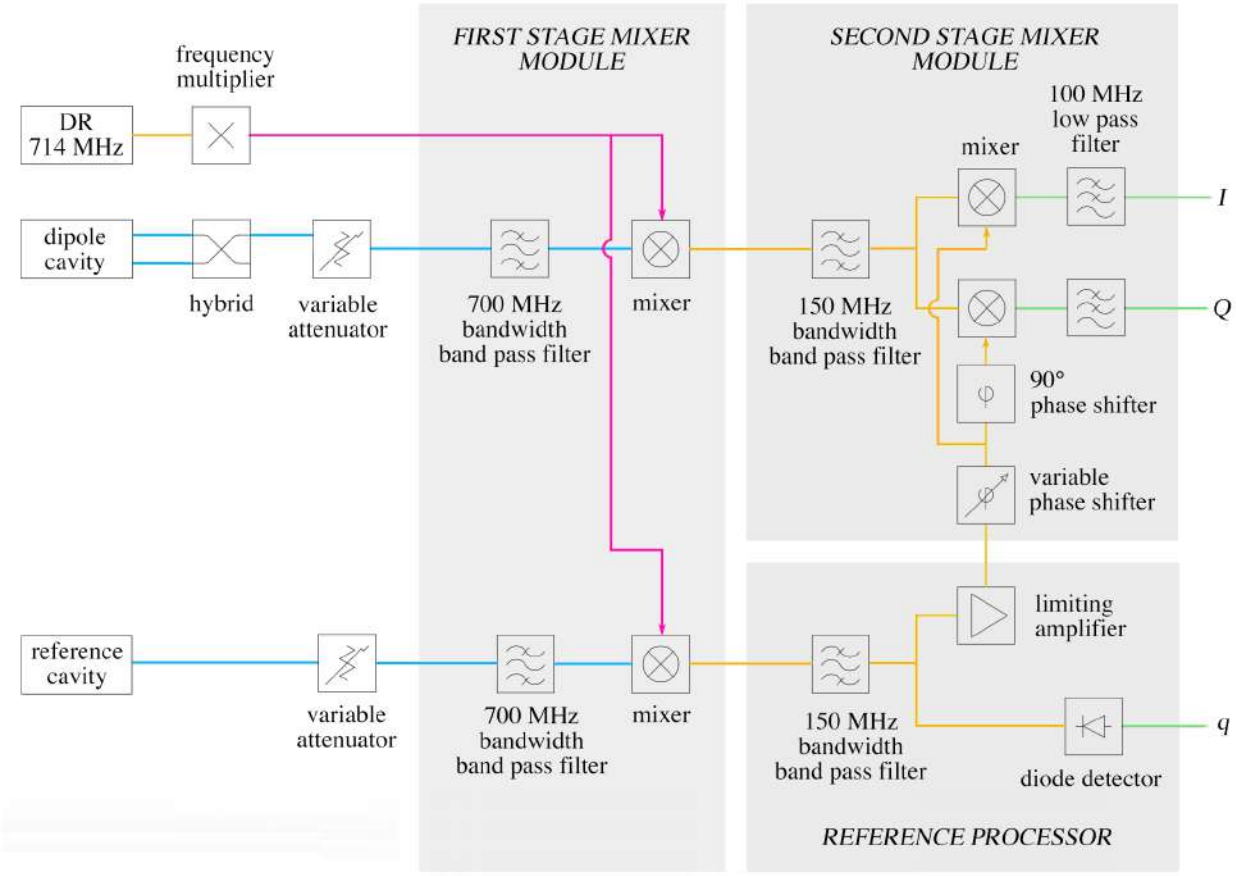

Figure 2.8: Simplified block diagram of the two-stage processing electronics for down-mixing the GHz-frequency cavity outputs to baseband. GHz-frequency (pink and blue), 714 MHz (orange), and baseband (green) paths are indicated. The IP system features two copies of this system to down-mix the x and y signals with different frequency multipliers. The specific frequencies at each stage are given in Table 2.3.

Table 2.3: Design frequencies of the x and y signals at different stages of the down-mixing. Colours indicate the different down-mixing stages illustrated in Fig. 2.8.

		Frequency (MHz)	
Colour	Stage of down-mixing	x signal	y signal
Blue	Cavity output signals	5712	6426
Pink	LO signals for first mixer	6426	5712
Orange	DR and cavity signals after first mixer	714	714
Green	Output signals after second mixer	0	0

The trigonometric formalism of mixing the LO signals with the cavity signals produced low frequency (e.g. $f_{\rm dipole} - f_{\rm LO}$) and high frequency (e.g. $f_{\rm dipole} + f_{\rm LO}$) components. A $\pm$150 MHz band pass filter (BPF) before the second mixer removed the high frequency component, leaving the two signals:

$$\mathrm{V}_{\rm dipole \otimes LO(dipole)}(y, y', \alpha, q, t) = A_{\rm LO(dipole)} \frac{1}{2} \Big\{ A_y \, y \cos\Big[2\pi (f_{\rm dipole} - f_{\rm LO(dipole)})\, t - \Delta\phi_{\rm LO(dipole)}\Big] - (A_{y'}\, y' \, - \, A_\alpha \, \alpha) \sin\Big[2\pi (f_{\rm dipole} - f_{\rm LO(dipole)})\, t - \Delta\phi_{\rm LO(dipole)}\Big] \Big\} \, q \, \mathrm{e}^{-\frac{t}{2\,\tau_{\rm dipole}}}, \tag{2.12}$$

$$\mathrm{V}_{\rm ref \otimes LO(ref)}(q, t) = A_{\rm ref} \, A_{\rm LO(ref)} \frac{1}{2} \cos\Big[2\pi (f_{\rm ref} - f_{\rm LO(ref)})\, t - \Delta\phi_{\rm LO(ref)}\Big] \, q \, \mathrm{e}^{-\frac{t}{2\,\tau_{\rm ref}}}. \tag{2.13}$$

Both outputs had a nominal frequency of 714 MHz, due to the 714 MHz difference between the $f_{\rm LO(dipole)}$ and $f_{\rm dipole}$, and $f_{\rm LO(ref)}$ and $f_{\rm ref}$, terms.

Reference limiter

The down-mixed reference signal was then split in two in the reference processor module (Fig. 2.8). One of these outputs was entered into a diode detector to produce a baseband pulse to monitor the bunch charge. The second output passed through a limiting amplifier. This produced a fixed-amplitude signal output, which still oscillated with a phase that was locked to the bunch arrival but was no longer dependent on bunch charge. The amplitude was set by the voltage level of the limiter. The time over which the reference signal remained limited depended on the size of the input signal, i.e., if the signal amplitude into the limiter was larger, it would exceed the limiting voltage level for a longer period of time. This time could, therefore, be adjusted using the variable attenuator immediately after the reference cavity. For successful mixing, the reference needed to be limited for the duration of the dipole signal.

The phase shifter following the limiting amplifier allowed the reference phase to be set relative to the dipole signal, introducing a $\Delta\phi$ term. The resulting reference signal output before entering the second-stage of the processing electronics (see Fig. 2.8), took the form:

$$\mathrm{V}_{\rm ref \otimes LO(ref)}(q, t) = A_{\rm ref} \, A_{\rm LO(ref)} \frac{1}{2} \cos\Big[2\pi (f_{\rm ref} - f_{\rm LO(ref)})\, t + \Delta\phi - \Delta\phi_{\rm LO(ref)}\Big]. \tag{2.14}$$

The different paths the reference cavity signal and dipole cavity signals took as a consequence of this reference limiter section had implications for the signal arrival times at the second-stage processor (see Section 2.8).

Second-stage processing

The second step in the down-mixing processing consisted of two mixers, which combined the dipole signal with the reference signal, and the dipole signal with the reference signal shifted by 90°. This resulted in two baseband signals known as I ("in" phase) and Q ("quadrature" phase). For the purposes of analysis, the position-dependent dipole signal terms in Eq. 2.12, V_y, are explored first. The dipole signal entering the I mixer was:

$$\mathrm{V}_y(y,q,t) = A_{\mathrm{LO(dipole)}}\,\frac{1}{2}A_y\,y\cos\Big[2\pi(f_{\mathrm{dipole}}-f_{\mathrm{LO(dipole)}})\,t-\Delta\phi_{\mathrm{LO(dipole)}}\Big]\,q\,\mathrm{e}^{-\frac{t}{2\,\tau_{\mathrm{dipole}}}}. \quad (2.15)$$

Once again, the mixer output had a low frequency and high frequency component. A low-pass filter immediately following the mixer removed the high frequency waveforms, leaving the signal:

$$\mathrm{V}_{yI}(y,q,t) = A_y\,A_{\mathrm{ref}}\,A_{\mathrm{LO(dipole)}}\,A_{\mathrm{LO(ref)}}\,y\,\frac{1}{8}\cos\Big[2\pi(f_{\mathrm{dipole}}-f_{\mathrm{LO(dipole)}}-f_{\mathrm{ref}}+f_{\mathrm{LO(ref)}})\,t - \Delta\phi_{\mathrm{LO(dipole)}}+\Delta\phi-\Delta\phi_{\mathrm{LO(ref)}}\Big]\,q\,\mathrm{e}^{-\frac{t}{2\,\tau_{\mathrm{dipole}}}}. \quad (2.16)$$

The frequencies and phase differences are combined and the output simplified to

$$\mathrm{V}_{yI}(y,q,t) = A_y\,A_{\mathrm{ref}}\,A_{\mathrm{LO(dipole)}}\,A_{\mathrm{LO(ref)}}\,y\,\frac{1}{8}\cos\theta_{IQ}\,q\,\mathrm{e}^{-\frac{t}{2\,\tau_{\mathrm{dipole}}}}, \quad (2.17)$$

where the θ_{IQ} term is defined as:

$$\theta_{IQ}(t) = 2\pi(f_{\mathrm{dipole}}-f_{\mathrm{LO(dipole)}}-f_{\mathrm{ref}}+f_{\mathrm{LO(ref)}})\,t-\Delta\phi_{\mathrm{LO(dipole)}}+\Delta\phi-\Delta\phi_{\mathrm{LO(ref)}}. \quad (2.18)$$

The LO signals were both frequency multiplied versions of the same source signal, removing any dependence of θ_{IQ} on the LO signal frequency or phase relative to the dipole cavities.

The bunch angle and tilt terms in Eq. 2.12 were treated similarly and combined with Eq. 2.17 to give a total V_I output signal from the second stage down-mixing of:

$$\mathrm{V}_I(y,y',\alpha,q,t) = A_{\mathrm{ref}}\,A_{\mathrm{LO(dipole)}}\,A_{\mathrm{LO(ref)}}\,\frac{1}{8}\Big[A_y\,y\cos\theta_{IQ}-(A_{y'}\,y'-A_\alpha\,\alpha)\sin\theta_{IQ}\Big]\,q\,\mathrm{e}^{-\frac{t}{2\,\tau_{\mathrm{dipole}}}}. \quad (2.19)$$

The reference signal was rotated 90° before the Q-mixer, so a similar expression to Eq. 2.19 is easily obtained for the output signal V_Q using $\Delta\phi+\pi/2$:

$$\mathrm{V}_Q(y,y',\alpha,q,t) = A_{\mathrm{ref}}\,A_{\mathrm{LO(dipole)}}\,A_{\mathrm{LO(ref)}}\,\frac{1}{8}\Big[A_y\,y\sin\theta_{IQ}+(A_{y'}\,y'-A_\alpha\,\alpha)\cos\theta_{IQ}\Big]\,q\,\mathrm{e}^{-\frac{t}{2\,\tau_{\mathrm{dipole}}}}. \quad (2.20)$$

If the variable phase shifter on the reference signal in Fig. 2.8 is appropriately set to allow $\theta_{IQ}=0$, then V_I loses any dependence on the angular terms. Similarly, the V_Q signal

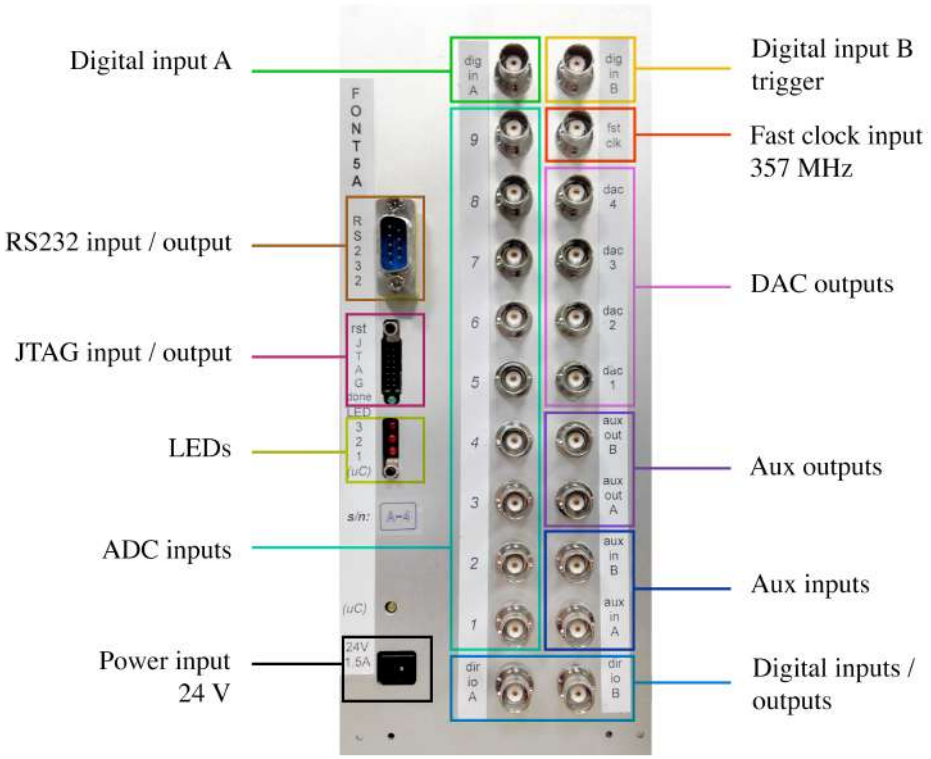

Figure 2.9: Front panel of the FONT board showing all available inputs and outputs.

would no longer be dependent on the position. If it is not possible to set the phase shifter so that $\theta_{IQ} = 0$, a position only-dependent signal I' and angle only-dependent signal Q' can be determined in analysis using linear combinations of Eq. 2.19 and Eq. 2.20:

$$\mathrm{V}_{I'}(y,q,t) = V_I \cos\theta_{IQ} + V_Q \sin\theta_{IQ} = A_{\mathrm{ref}}\, A_{\mathrm{LO(dipole)}}\, A_{\mathrm{LO(ref)}}\, \frac{1}{8}\, A_y\, y\, q\, \mathrm{e}^{-\frac{t}{2\,\tau_{\mathrm{dipole}}}}, \qquad (2.21)$$

$$\mathrm{V}_{Q'}(y',\alpha,q,t) = -V_I \sin\theta_{IQ} + V_Q \cos\theta_{IQ} = A_{\mathrm{ref}}\, A_{\mathrm{LO(dipole)}}\, A_{\mathrm{LO(ref)}}\, (A_{y'}\, y' - A_\alpha\, \alpha)\, \frac{1}{8}\, q\, \mathrm{e}^{-\frac{t}{2\,\tau_{\mathrm{dipole}}}}. \qquad (2.22)$$

2.5 The FONT board

The output baseband signals from the processing electronics were digitised using FONT boards, which were designed and produced in Oxford. The boards were built around a Xilinx Virtex-5 field-programmable gate array (FPGA) [73], featuring arrays of interconnected logic blocks which could be reconfigured and controlled in an editable hardware description language known as "firmware". Fig. 2.9 shows the front interface panel of the FONT digital board. A simplified block diagram of the board is shown in Fig. 2.10.

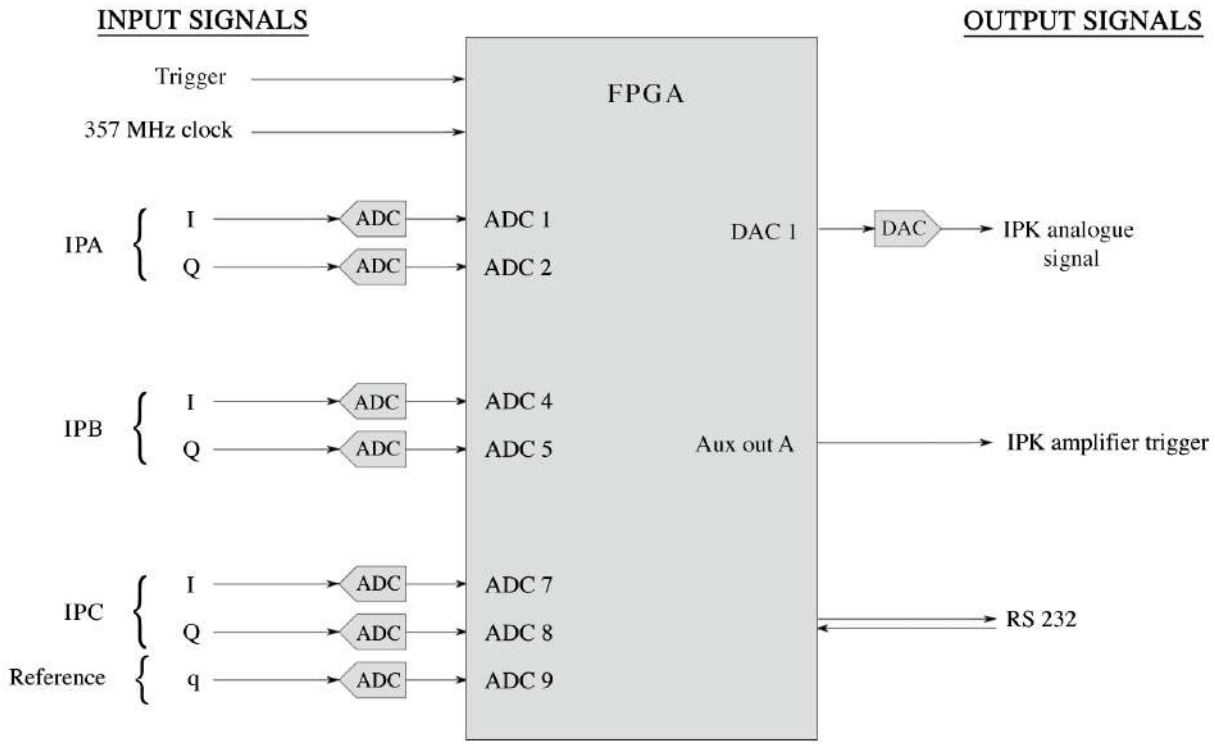

Figure 2.10: Block diagram of the FONT digital board indicating the inputs and outputs typically utilised for feedback in the ATF2 IP region.

Synchronisation and clocking

An on-board crystal oscillator, referred to as the slow clock, clocked all the underlying ancillary FPGA logic at a frequency of 40 MHz. The time-critical logic was clocked using an external 357 MHz signal referred to as the fast clock, which had a specifically assigned digital input on the board. At the ATF2 the fast clock was sourced from a frequency divided version of the damping ring 714 MHz master oscillator, which was phase locked to the RF cavity of the damping ring. This synchronised the board timing with that of the electron bunches as they were extracted from the damping ring.

As well as clocking the logic, the fast clock was copied three times and sent to three analogue-to-digital converter (ADC) banks. The FONT board has nine 14-bit ADCs arranged in groups of three, with each group sharing a common clock. Their voltage measurement range is ± 0.5 V, and the digitised sampling window could be set with a precision of 70 ps within a window of adjustable size up to a maximum of 1000 samples. For the IP region, these ADCs received the I, Q and q output signals from their respective processing electronics. The channel assignments were arbitrarily chosen, but those shown in Fig. 2.10 are typical for IP operation, with the signals from each IP BPM allocated to a different ADC bank, and the reference cavity signal on the final channel.

The board ADC logic begins running as soon as an external trigger is received. At the ATF2 the trigger was routed from the damping ring extraction kicker via digital input B (Fig. 2.9). The board also had an internal delay which could be used to set the start of the ADC sampling window relative to the trigger. The sampling window was 164 samples long with a sampling rate of 357 MHz set by the fast clock, i.e., long enough to digitise a two-bunch train with a typical bunch-to-bunch separation of 280 ns and allow both bunch signals time to decay. The RS-232 port allowed communication with the board via the FONT data acquisition software [50]. It operated at a speed of 460 kbits per second and was driven by the 40 MHz slow clock.

Feedback outputs

The FONT board had four 14-bit DAC outputs with a maximum clock speed of 210 MHz, and a maximum output of ±0.5 V. The first DAC was used to send an analogue signal to the IPK kicker amplifier to apply corrective kicks to the beam during feedback operation. One of the auxiliary outputs was used to send a trigger to the amplifier in advance of the bunch arrival. The ATF2 kicker amplifiers were developed by TMD technologies [74] to provide ±30 A of drive current and an output pulse length of up to 10 µs. The amplifier had a rapid rise-time of 35 ns from the time of receiving the input signal to reaching 90% of its peak output to enable intra-train feedback. The feedback process and how the corrective signal was calculated will be explained in Chapter 5.

Digitised signals

Example I and Q waveforms are shown in Fig. 2.11 for a single-bunch train measured at IPB, along with an example reference-cavity q signal. The sample separation was 2.8 ns, corresponding to the digitisation frequency of 357 MHz. The reference cavity q signal demonstrates the exponentially decaying pulse of Eq. 2.13. The envelope of the dipole cavity signals follows the forms of Eq. 2.19 and 2.20, but a higher-frequency parasitic signal of unknown origin is evident. The nature and potential sources of this unwanted signal will be investigated subsequently (see Section 2.10). All cavity signals decay quickly compared to the ∼200 ns (∼70 sample) bunch separation in a typical multi-bunch train mode. This was vital to prevent signals from multiple bunches overlapping each other.

To analyse these digitised pulses a single sample was selected within the digitiser window. Optimal sample number choices and the potential of waveform sample integration for improving resolution will be explored in detail in Chapter 3. The electronics processing and cabling were well matched for the I and Q signal paths to ensure the outputs arrived at the same time (see Section 2.8).

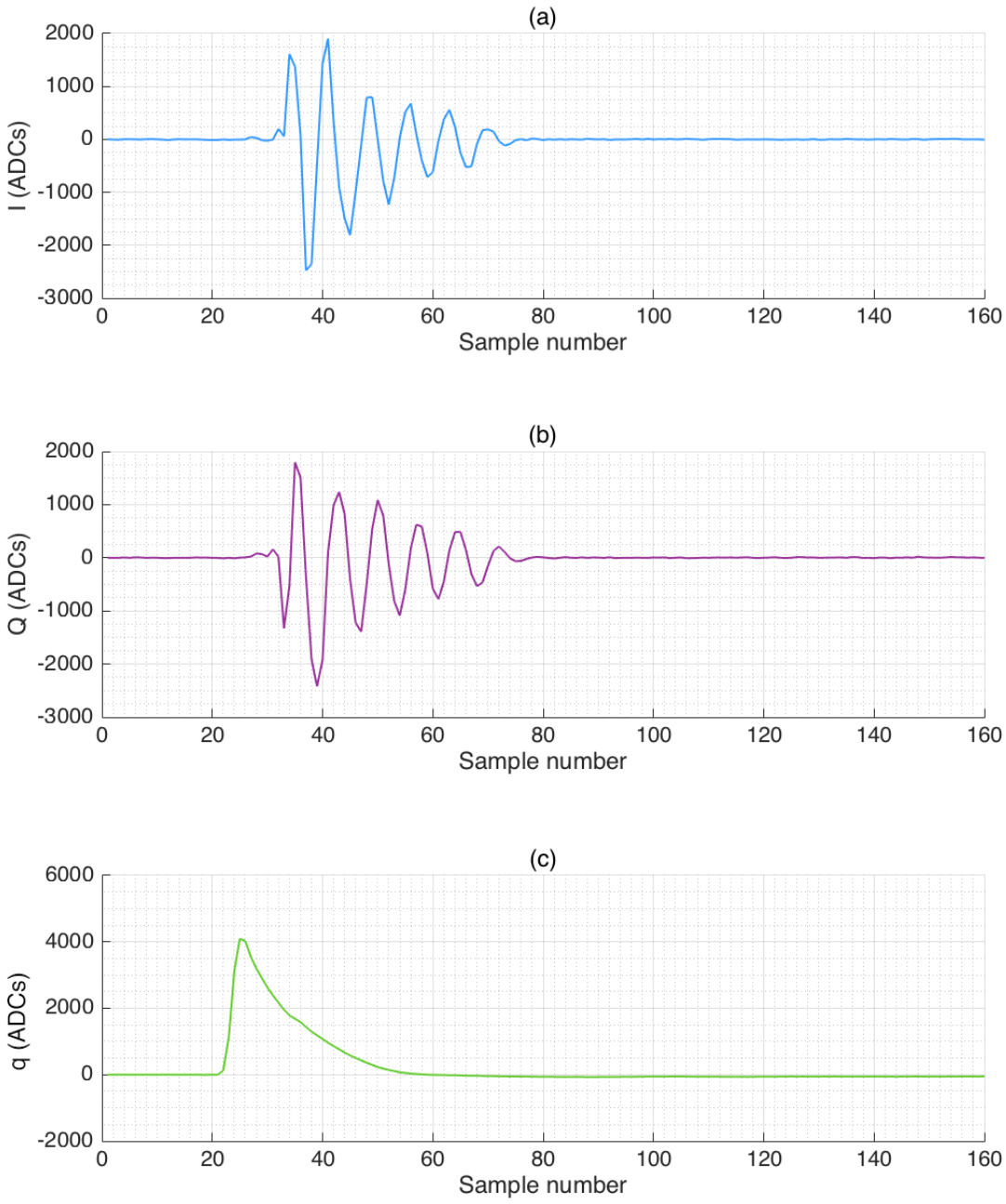

Figure 2.11: Digitised ADC counts versus sample number for (a) the I signal, (b) the Q signal, and (c) the q signal. The waveforms correspond to a single bunch measured using IPB. The data were gathered with 10 dB attenuation on the dipole and 50 dB on the reference signals at a vertical position offset of approximately 2 µm from the electrical centre of the dipole cavity and a bunch charge of $\sim 0.5 \times 10^{10}$ electrons.

2.6 Position calibration

The θ_{IQ} rotation

To derive position information it was necessary to determine the θ_{IQ} of Eq. 2.21. This could be found from the digitised I and Q signals, which are proportional to the voltage signals V_I and V_Q. At a single sample point these equations reduce to:

$$I = (k\, y \cos\theta_{IQ} - k_\epsilon\, \epsilon\, \sin\theta_{IQ})q, \tag{2.23}$$

$$Q = (k\, y \sin\theta_{IQ} + k_\epsilon\, \epsilon\, \cos\theta_{IQ})q, \tag{2.24}$$

where the angular terms have been replaced with $\epsilon = (A_{y'}\, y' - A_\alpha\, \alpha)$, and the two coefficients k and k_ϵ are constants. These two simultaneous equations were combined to define a relationship between the I and Q signals, normalised by the q signal:

$$\frac{Q}{q} = \frac{I}{q}\tan\theta_{IQ} + \frac{k_\epsilon\, \epsilon}{\cos\theta_{IQ}}. \tag{2.25}$$

Thus θ_{IQ} was determined from the inverse tangent of the gradient of a straight line fit to a $\frac{Q}{q}$ versus $\frac{I}{q}$ plot.

Varying position for calibration

To obtain this plot, the I and Q values needed to be varied by changing the beam position offset inside each cavity. Due to the aforementioned issues with one of the IP BPM sub-movers, calibrations were performed by steering the beam a known amount through the IP region. The beam was moved along the x and y axes by changing the positions of the final focus magnets QD1FF and QD0FF respectively.

The downstream beam displacement for a given magnet offset depended on the strength of the field in the magnet. Conversion factors to change QD0FF vertical position offsets into beam position offsets were calculated using the ATF2 MAD model [75]. The conversion factors for beam position measurements at IPA, IPB and IPC and are plotted in Fig. 2.12. The QD0FF currents plotted range between 120 A and 150 A, corresponding to placing the beam waist at IPC and IPA respectively. A fit has been applied to calculate the conversion factor for any magnet current within this range.

An example of a calibration data set is shown in Fig. 2.13. The I, Q and q values were recorded at a chosen sample point. This process was repeated for five successive QD0FF position values. Fig. 2.13.a shows the $\frac{I}{q}$ and $\frac{Q}{q}$ values for all recorded triggers plotted sequentially. The steps between the different magnet position settings are visible as the position and angle of trajectory of the beam through the cavity changes. Fig. 2.13.b shows

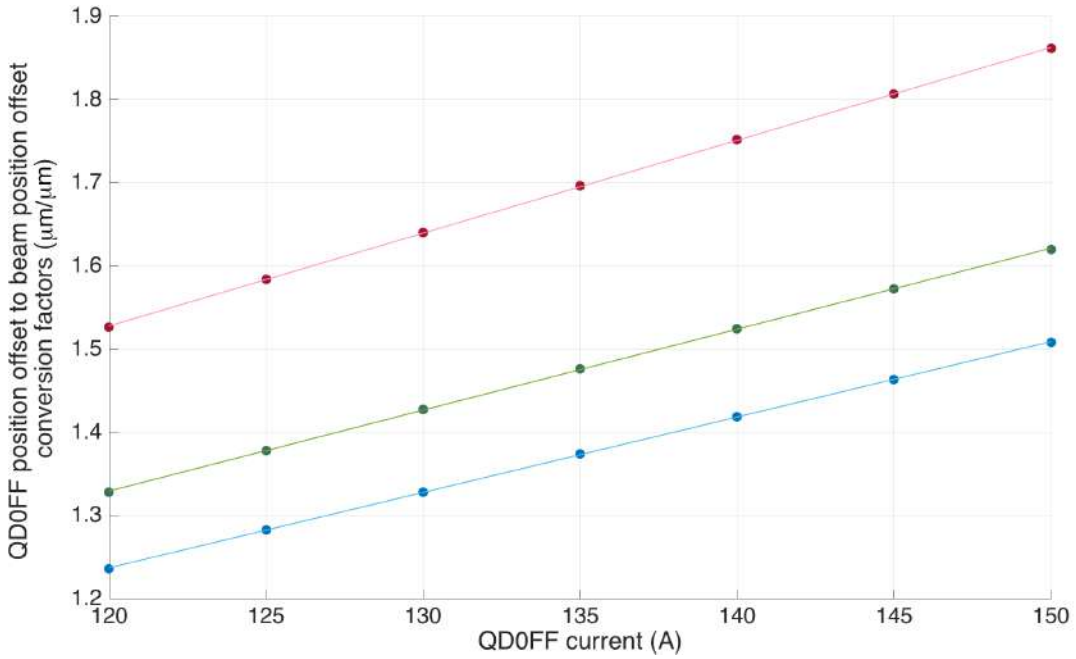

Figure 2.12: Conversion factors versus QD0FF magnet current setting to transform QD0FF position offsets to beam position offsets, calculated for IPA (blue), IPB (green) and IPC (red). The lines represent linear fits to the data.

the $\frac{Q}{q}$ versus $\frac{I}{q}$ plot, with a fitted line. The inverse tangent of the gradient of this line is θ_{IQ}, which for this calibration run is $19.4 \pm 0.2°$. The statistical uncertainty on this angle was calculated from the error on the fit.

Calibration scale factor, k

With θ_{IQ} established it was possible to perform the rotation into the I' axes derived in Eq. 2.21, which in terms of the I, Q and q signals sampled in ADCs took the form:

$$I' = I\cos\theta_{IQ} + Q\sin\theta_{IQ} = k\,q\,y, \tag{2.26}$$

and

$$y = \frac{1}{k}\Big(\frac{I}{q}\cos\theta_{IQ} + \frac{Q}{q}\sin\theta_{IQ}\Big) = \frac{1}{k}\frac{I'}{q}. \tag{2.27}$$

Fig. 2.13.c shows the $\frac{I'}{q}$ values plotted against QD0FF magnet position offsets. The scale factor k was determined from the fit gradient, which was then transformed into position units at the BPM in question using the required conversion factor from Fig. 2.12. This gave $k = 0.0287 \pm 0.0002$ (ADC/ADC)/μm for this calibration. The statistical uncertainty on k was calculated from the error on the fit.

With k and θ_{IQ} it was then possible to use I, Q and q signals to determine the beam position offset from the electrical centre of the cavity, as defined in Eq. 2.27.

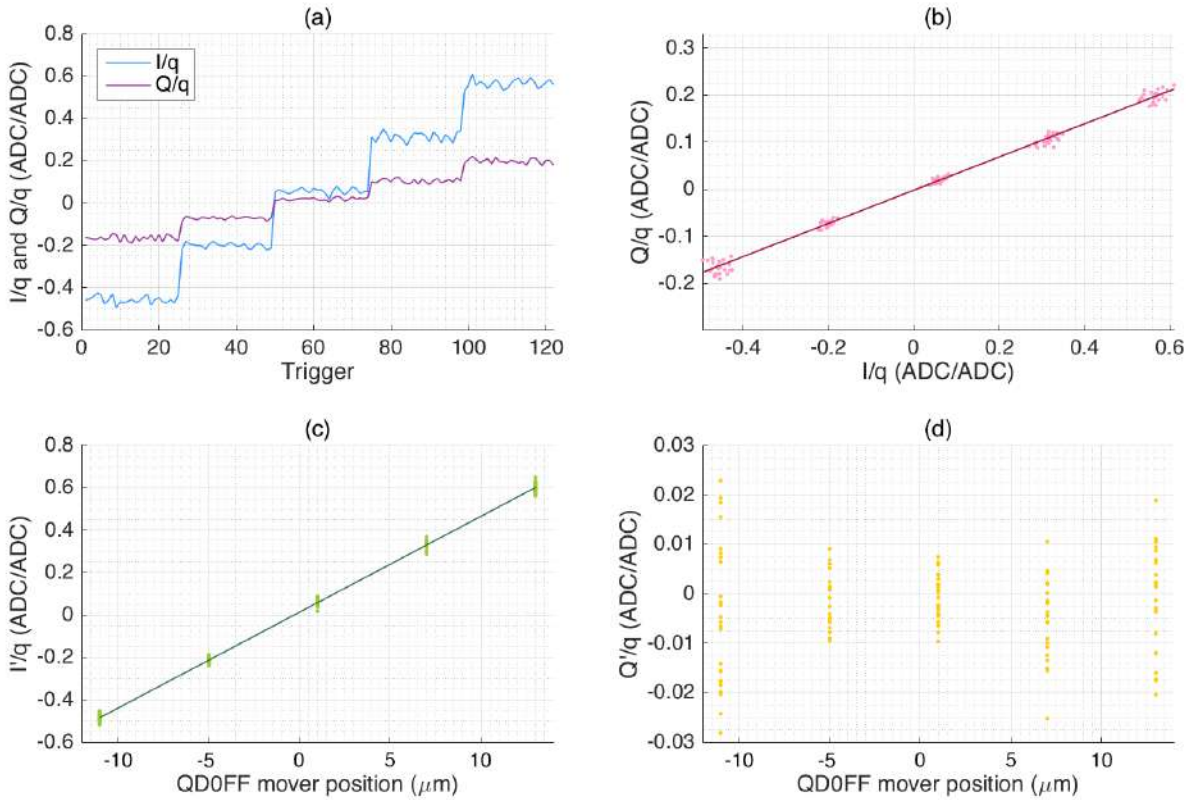

Figure 2.13: Vertical calibration of IPB: (a) $\frac{I}{q}$ and $\frac{Q}{q}$ at a single sample number versus trigger number; (b) $\frac{Q}{q}$ versus $\frac{I}{q}$, the straight line is a fit to determine θ_{IQ}; (c) $\frac{I'}{q}$ versus QD0FF mover position, the straight line is a fit to determine k; (d) $\frac{Q'}{q}$ versus QD0FF mover position. This calibration was performed with a QD0FF current of 129.5 A using signals from IPB with 20 dB attenuation at a bunch charge of $\sim 0.43 \times 10^{10}$ electrons. There were 25 triggers recorded per step.

Similar analysis was applied to find Q' using

$$Q' = -I \sin\theta_{IQ} + Q \cos\theta_{IQ}. \tag{2.28}$$

Fig. 2.13.d shows $\frac{Q'}{q}$ against vertical position offset. The $\sim$0 gradient indicates the angle of the beam through the BPM was not being significantly altered in the calibration scan.

Calibrations needed to be repeated when there was a change to the beam optics, the beam charge (see Section 3.9), the attenuation on the cavity signals, or if any of the BPMs were moved relative to the beam using their mover system. Calibrations were determined for set sampling points within the digitiser window and were applicable only if those same sample numbers were used throughout analysis. Whenever the sampling method changed, the calibration scale factor, k and rotation angle θ_{IQ} needed to be re-calculated.

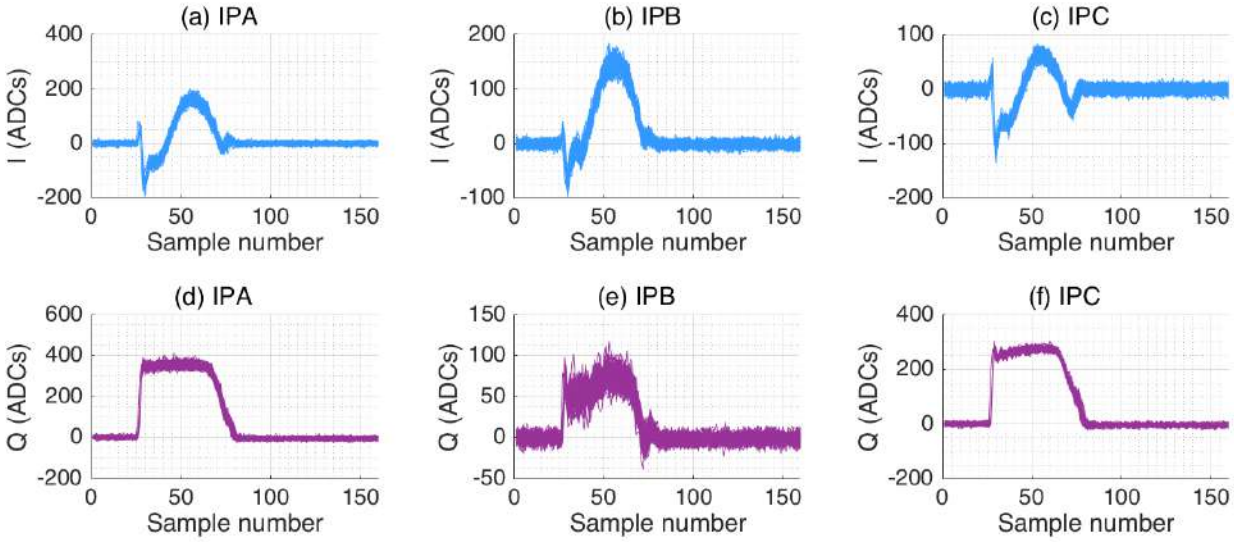

Figure 2.14: IP BPM waveform signals for an ensemble of triggers with 70 dB attenuation on the dipole cavities in ADCs versus sample number in the FONT digitiser window; (a) IPA I, (b) IPB I, (c) IPC I, (d) IPA Q, (e) IPB Q, (f) IPC Q.

2.7 Mixer pedestal subtraction

Most contemporary diode mixers utilise a ring of four diodes arranged so the overall DC output cancels out. This relies on the diodes (and everything else in the electronics) being perfectly matched. Imperfections mean the DC output will not be exactly zero. In addition, a pedestal will be introduced by the FONT board ADCs. The ADC pedestal was removed by zeroing the mean of the baseline in the absence of any BPM signal in the data acquisition system. However, the DC mixer pedestal was only introduced when the mixer was driven, and was always present in the output I and Q signals, although it was typically small relative to the overlaying dipole signals.

The mixer pedestal could be made visible on the digitised I and Q output channels by placing 70 dB attenuation on the dipole cavity signals. The mixer was driven by the reference signal's arrival, but the dipole cavity signals were essentially suppressed. Examples of the I and Q mixer pedestal signals are shown in Fig. 2.14. There are different mixers to process the different BPM signals, so there are slight differences in the absolute levels of this pedestal on the channels. It is also notable that the I signal pedestal is not a flat DC offset. The cause of this shape in the I processor pedestal has not been identified.

A data run with 70 dB attenuation on the dipole cavities was systematically taken before running experiments so the pedestal could be subtracted from subsequent waveforms.

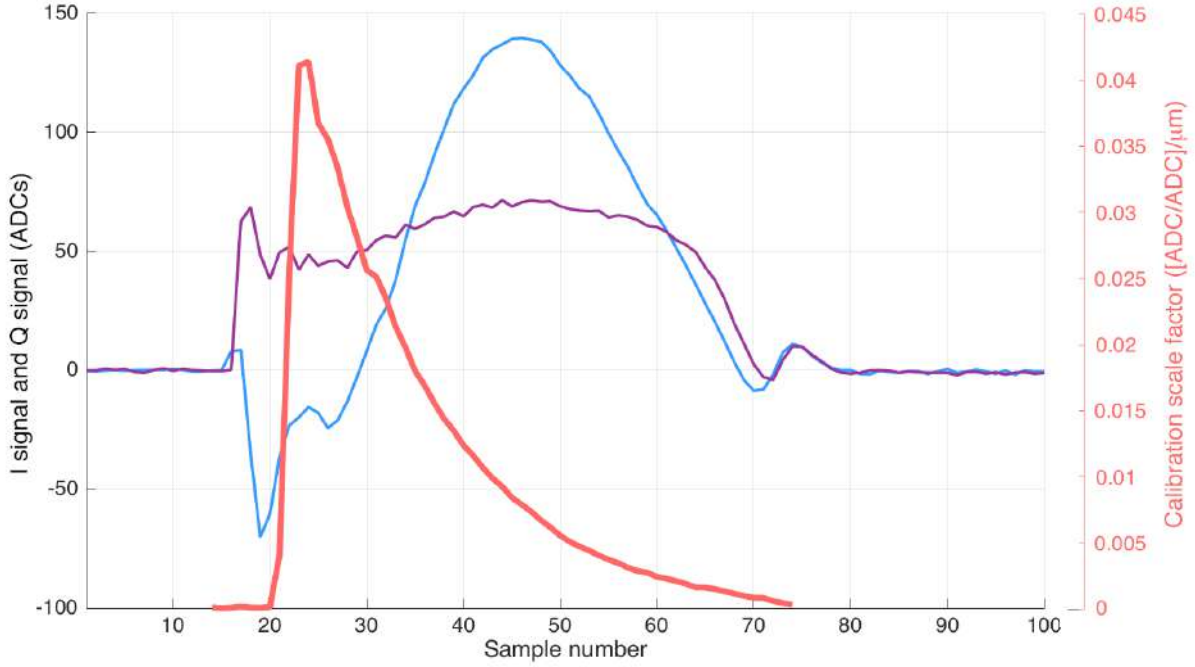

Figure 2.15: I (blue) and Q (purple) waveforms versus sample number measured at IPB with 70 dB dipole attenuation on the dipole cavities (left-hand scale), overlaid with the scale factor, k, (orange) versus sample number (right-hand scale). Recorded at a charge of 0.15×10^{10} electrons per bunch with 27 dB attenuation on the reference cavity signals.

2.8 Electronics timing

It was vital that the second stage of the processing electronics received the limited reference signal when the dipole signal arrived so the two could be successfully mixed. The 70 dB dipole attenuated data run was useful for this purpose, as the pedestal indicated when the limited reference was arriving at the mixer. Fig. 2.15 shows a plot of the I and Q 70 dB-attenuated signals overlaid with a plot of the calibration scale factor k, calculated at successive sample numbers. The scale factor provides a good measure of where the dipole signal would be in the sampling window if it were not attenuated.

The timing of the dipole and reference signal arrival times were adjusted using 14 ns and 28 ns delay cables (five and ten digitised sample numbers respectively) on the reference signal input to the second stage. Fig. 2.15 demonstrates the arrival times at the second stage processor are in good agreement.

The amplitude of the reference signal determined the length of time for which the second stage mixer was successfully driven. A variable attenuator with 1dB-increment steps was installed on the reference channel and systematically varied. The length of the pedestal

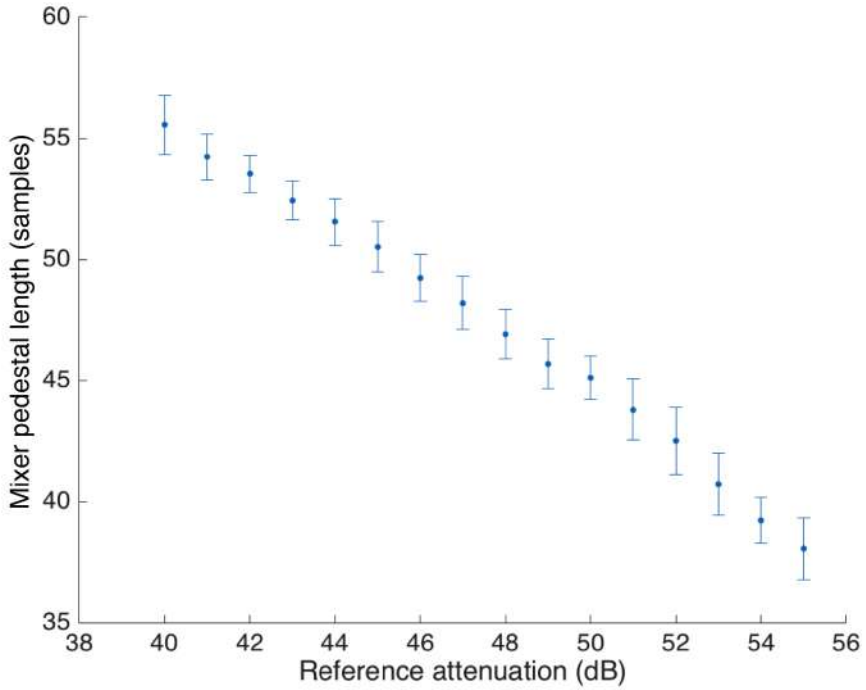

Figure 2.16: Mixer pedestal length versus reference cavity signal attenuation at a charge of 0.5×10^{10} electrons per bunch. Error bars represent the standard deviation of the pedestal length over the 100 triggers measured for each attenuation setting.

signal was averaged over 100 triggers per attenuator setting using the Q signal with 70 dB attenuation. This confirmed that the mean mixer drive time demonstrates a clear dependence on reference attenuation, as shown in Fig. 2.16. The smaller-step variable attenuator was left in place in the IP system set-up so the amplitude could be finely tuned.

2.9 Noise floor

The electronic noise floor of the processing system was estimated from the standard deviation (or "jitter") of the baseline 70 dB-attenuated mixer pedestal signals. Fig. 2.17 shows the jitter on the I and Q signal mixer pedestals for each IP BPM measured at $\sim 0.4 \times 10^{10}$ electrons per bunch. The noise floor was $\sim$11 ADC counts on all channels in the region where the peak of the pulse would be if there were no attenuation.

A calibration at IPA at a charge of 0.44×10^{10} electrons per bunch was used to convert the mixer jitter in ADCs on I and Q into a position noise floor in nanometers. The mixer jitter corresponded to 21 ± 2 nm when using a single sample of the waveforms for analysis. When the waveform was integrated across 8 samples in analysis, this result reduced to 13 ± 1 nm. The benefits of waveform integration are explored in more depth in Chapter 3.

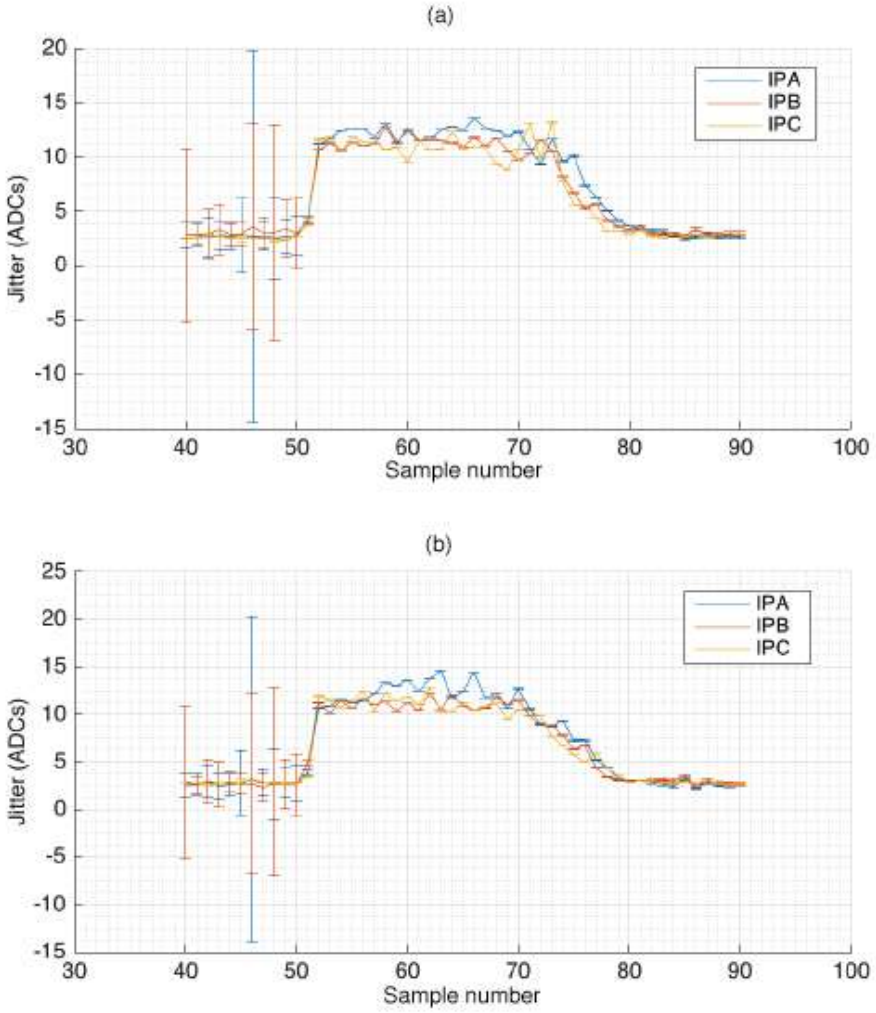

Figure 2.17: (a) Jitter on the I signal mixer pedestal versus sample number, (b) jitter on the Q signal mixer pedestal versus sample number. Jitters are calculated using the standard deviation of 100 sequential triggers at a charge of $\sim 0.4 \times 10^{10}$. Lines connect the data points. Error bars indicate the uncertainty on the standard deviation.

A previous FONT IP BPM noise floor study was performed where dipole cavity signals were split into two sets of processing electronics [8]. The comparison of the two outputs at a charge of $\sim 0.5 \times 10^{10}$ found a noise floor limit of 23.0 ± 0.7 nm using a single sample mode of analysis. This result is in agreement with the noise floor estimate found here. These jitters can be treated as characteristic of the baseline electronic noise floor for any given data run.

2.10 Waveform troubleshooting

Signals from all the IP dipole cavity BPMs contained an unwanted parasitic waveform of unknown origin, see e.g. Fig. 2.11. Fast Fourier transform (FFT) analysis of the cavity outputs, shown in Fig. 2.18 using the IPB I channel, found it to be ∼60 MHz in frequency. This result was consistent with analysis using the other two BPMs. Comprehensive tests of the two mixer stages indicated they were all functioning as expected, so diagnostic tests were performed to attempt to isolate the source.

BPM port cable mismatches

Time-domain reflectometer (TDR) measurements showed a mismatching in the pairs of BPM port cables connecting the cavities to the outside of the IP vacuum chamber. The mismatches were up to 10% of the signal wavelength for the y ports and 31% for the x ports. Insufficient cable matching from the two ports could prevent effective cancellation of unwanted cavity modes. The IP cables were also noticed to be quite worn since their initial installation in 2014. The cables were replaced in October 2016 and matched in pairs to better than 2% of the signal wavelength for the y ports, and better than 3% for the x ports. The unwanted waveform remained unaltered by this improvement to the hardware.

Signal reflections

Matched 5.5 m (28 ns) delay cables were introduced on both ports of IPBY and the reference cavity to test for reflections inside the chamber. The set-up is shown in Fig. 2.19. If the parasitic waveform originated from reflected signals, it would be expected to shift location for the I and Q signal outputs. The parasitic signal location did not change, so is unlikely to be caused by reflections inside the cavity.

Symmetric mode study

The IP BPM hybrids (see Fig. 2.19) were replaced with splitters in the processing electronics to cancel the dipole modes and instead combine all the symmetric mode outputs from the cavities. A simplified block diagram of the set-up is shown in Fig. 2.20. The parasitic waveform was then studied in the absence of any position-dependent signal. The symmetric mode outputs on the I and Q channels were recorded for all three cavity BPMs and averaged over 100 triggers to produce one trace for each channel. All channels featured the parasitic waveform. FFT analysis was applied to every channel, and all were characterised by a peak centred around ∼63 MHz.

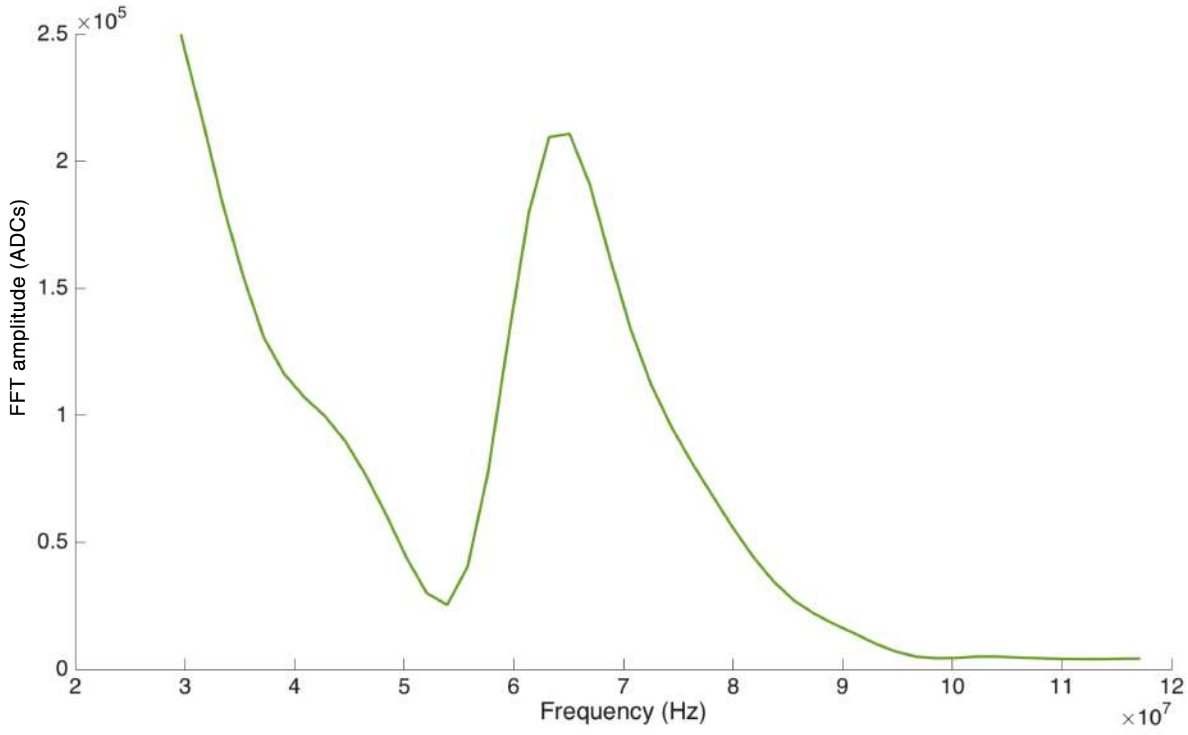

Figure 2.18: FFT amplitude versus frequency for fast Fourier transform analysis of the IPB processing electronics I channel output, showing a peak centred at 63 MHz.

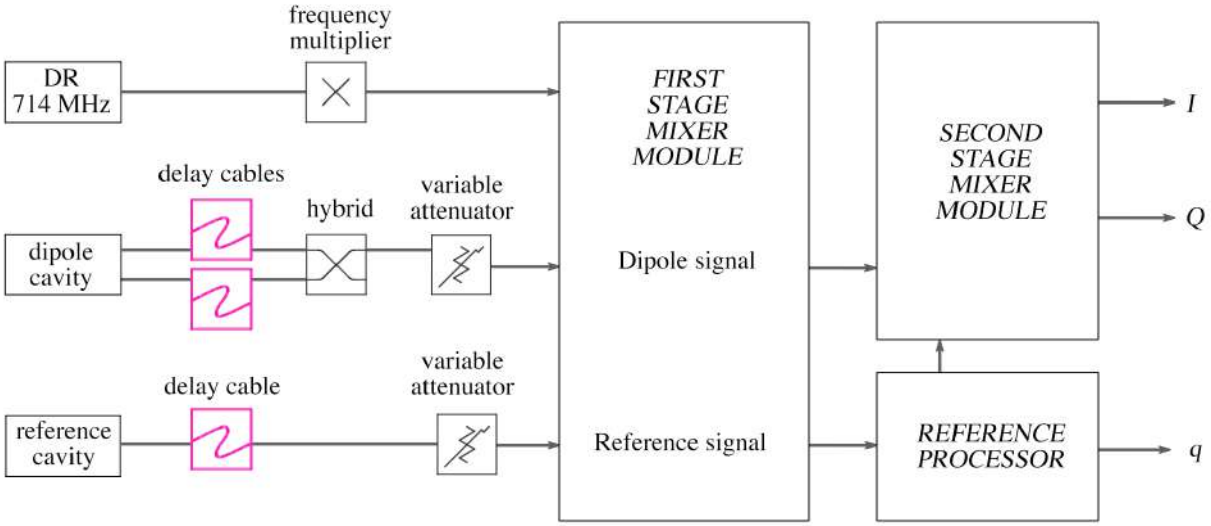

Figure 2.19: Simplified block diagram of the processing electronics with three matched 5.5 m delay cables installed on both ports of the dipole cavity and the reference cavity.

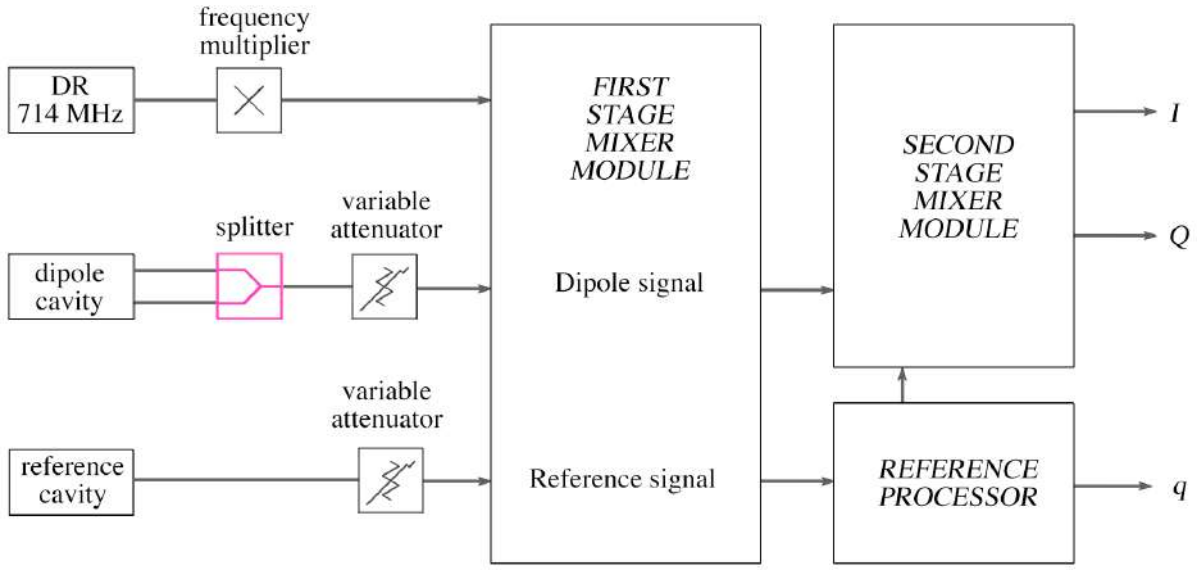

Figure 2.20: Simplified block diagram of the processing electronics in a symmetric mode setup where the hybrid in the IP BPM processing electronics is replaced with a splitter to cancel dipole modes and remove position-dependent signals.

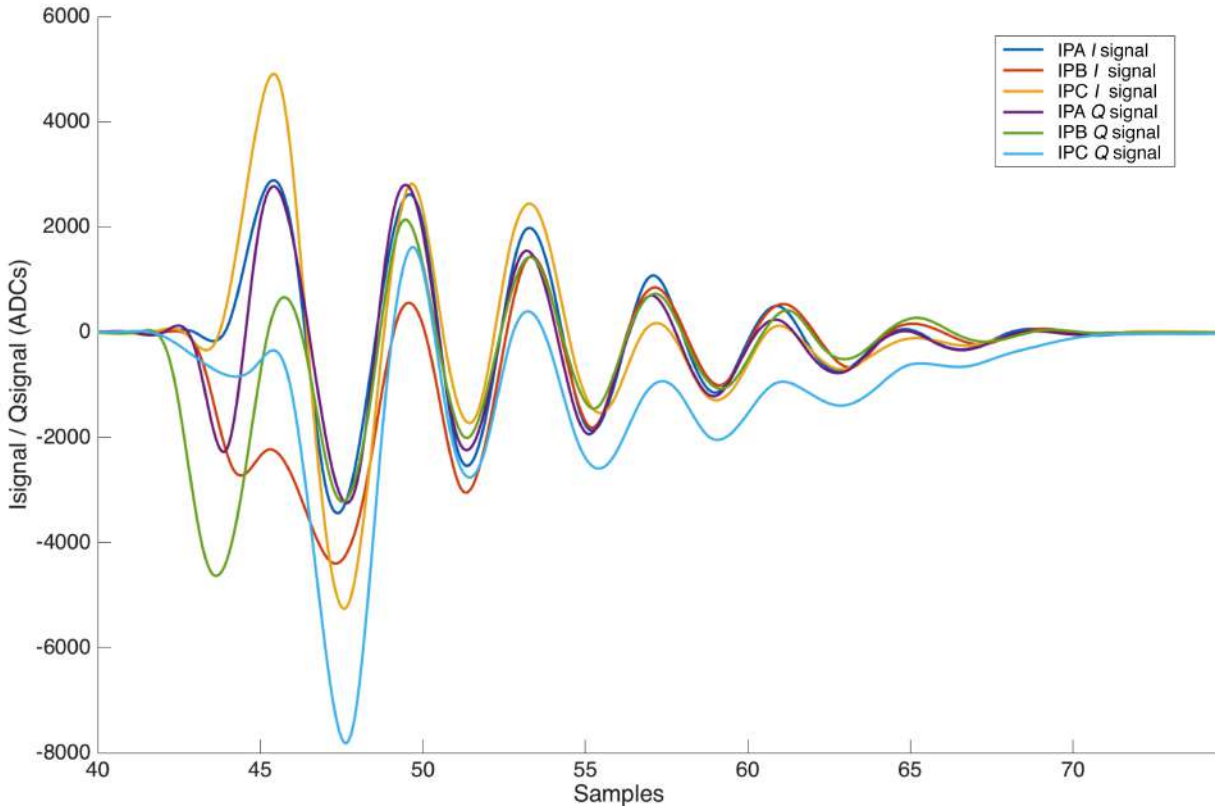

Figure 2.21: I and Q symmetric mode signal amplitude versus sample number with all IP BPM channels overlaid.

An interpolation was applied to increase the sampling frequency and smooth the digitised waveforms. Then all channels were artificially shifted horizontally and varied in amplitude to try and overlay the signals. The results of this analysis are shown in Fig. 2.21. The agreement across channels in these symmetric mode studies suggests that the source of the parasitic waveform is common to all channels.

Charge dependence

The amplitude of the parasitic waveform FFT analysis pulse in the symmetric mode set-up was compared at different bunch charges. Each accelerator charge setting was subject to a certain amount of charge jitter, so the charge level was determined for each trigger from the integral of the reference signal pulse in ADC counts, with 100 triggers taken at each charge step. Fig. 2.22 shows the results measured using IPA, demonstrating a reasonably linear relationship between bunch charge and the amplitude of the unwanted parasitic signal. Similar results were obtained by repeating this analysis using IPB and IPC. The linear relationship with charge suggests the parasitic oscillation is most likely to be caused by unwanted modes in the cavities.

Band pass filters

A 6.7 GHz low-pass filter was placed on the y-port dipole cavity output immediately after the splitter in the symmetric mode set-up, shown in Fig. 2.23. The filter had no impact on the amplitude of the parasitic waveform FFT peak. If the waveform were a result of higher-frequency LO harmonic mixing the amplitude should have been significantly attenuated by the addition of this filter.

A BPF of 6.4 GHz $\pm$ 100 MHz was then placed on the y-port dipole cavity output, again immediately after the splitter in the symmetric mode set-up. The parasitic waveform was not removed or changed. This indicates that if the signal originates from another mode in the dipole cavity, it is within 100 MH of the resonant design frequency.

Two sets of narrower-band BPFs were subsequently custom fabricated to mitigate the effects of the unwanted waveform in the I and Q signals [76]. The BPFs were built to allow frequencies of 6.401 to 6.451 GHz for the y-port and 5.687 to 5.737 GHz for the x-port. Example I and Q waveforms with these BPFs installed on the dipole cavities after the hybrid (which was reinstalled in place of the splitter, so position-dependent signals are again visible) are shown in Fig. 2.24.

Compared with Fig. 2.11 the unwanted parasitic waveform was noticeably smoothed. The waveform overall was also slightly attenuated and smeared out in the digitiser window.

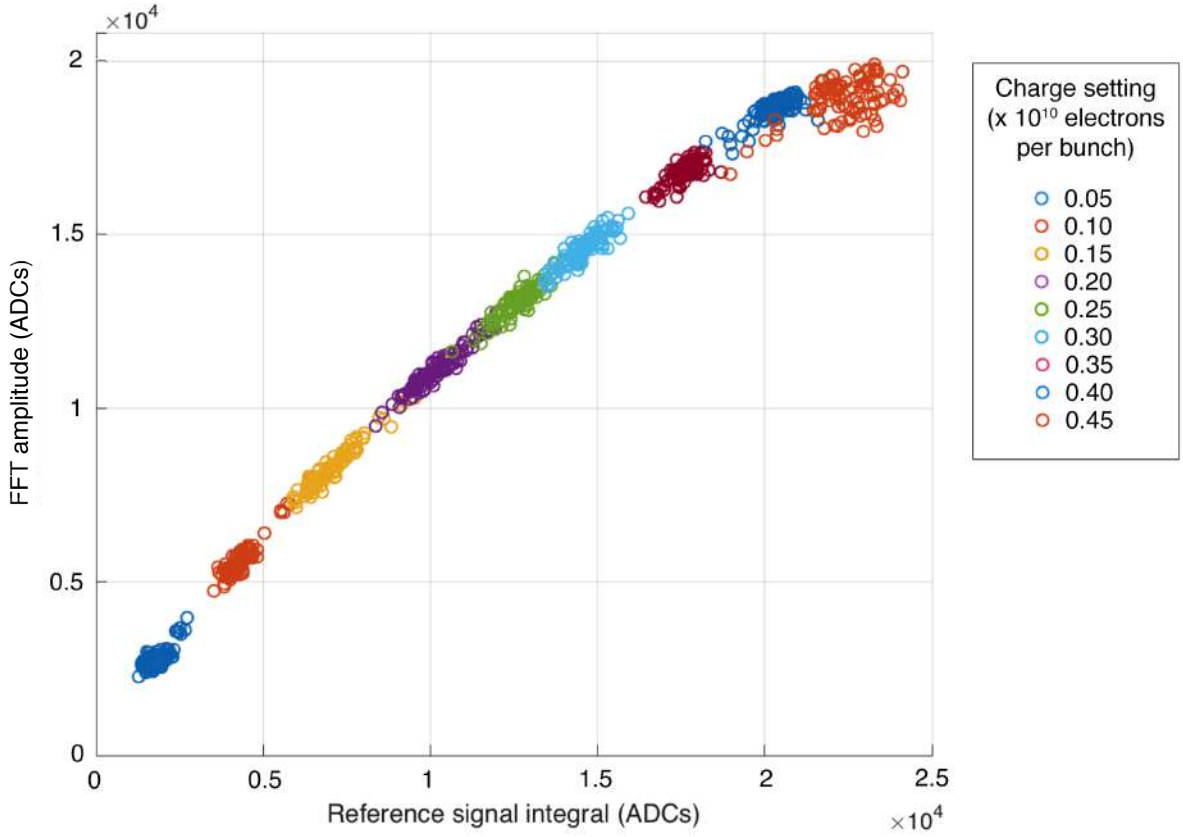

Figure 2.22: Amplitude of the peak in the FFT analysis of the parasitic waveform versus an integral of the reference pulse as a measure of the charge. Data were taken at charges of 0.05 to 0.45 $\times$ 10^{10} in steps of 0.05 with 100 triggers per step.

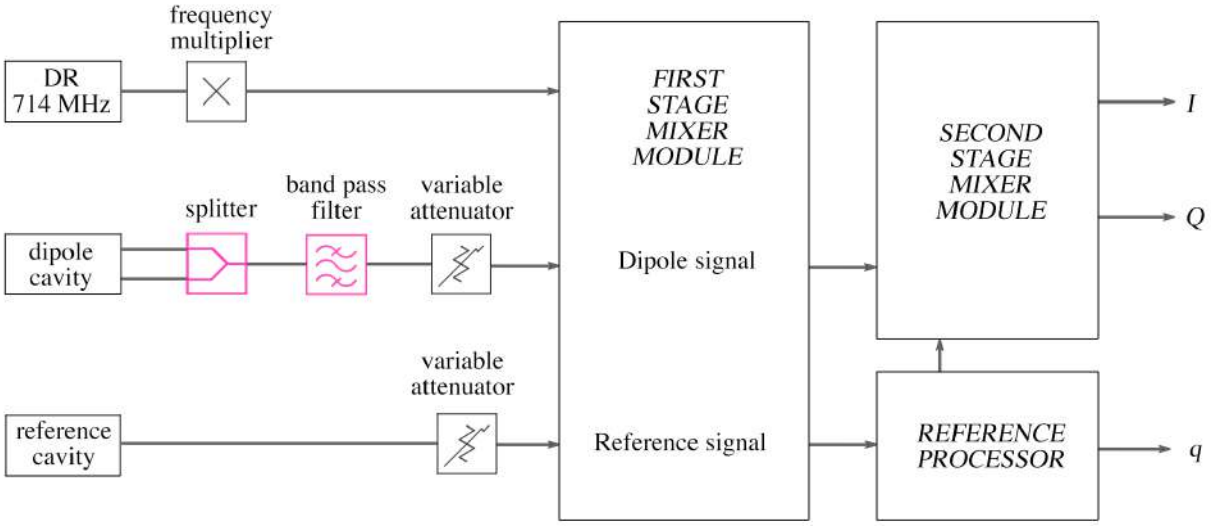

Figure 2.23: Simplified block diagram of the processing electronics in a symmetric mode setup with a BPF on the dipole cavity. The hybrid has replaced with a splitter to cancel dipole modes and remove position-dependent signals.

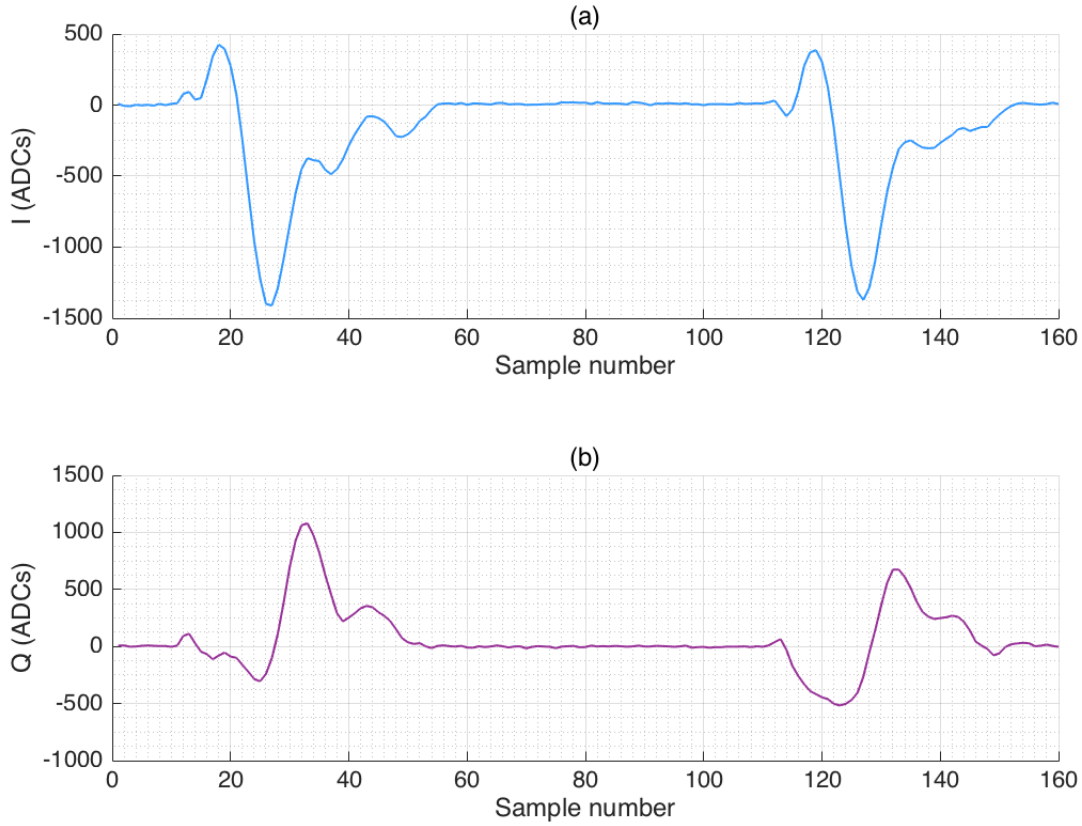

Figure 2.24: Digitised ADC counts versus sample number for (a) the I signal and (b) the Q signal. The waveforms correspond to a single trigger measured using IPB in a two-bunch train mode. These data were taken with 0 dB attenuation on the dipole variable attenuator at a vertical position offset of approximately 2 µm from the electrical centre of the cavity and a bunch charge of $\sim 0.55 \times 10^{10}$ electrons per bunch.

For operational purposes having the BPFs in place on the dipole cavity signals reduced the likelihood of saturation at lower attenuations, making it feasible to operate at higher bunch charges where resolution performance was improved. A cleaner pulse shape also made it more straightforward to centre the BPM signals in the cavities and to identify the peak of the waveforms by eye. The impact of the BPFs on resolution performance will be discussed in Section 3.11.

2.11 Summary

This chapter has introduced the IP BPM system and its associated processing electronics. The theory of cavity BPMs has been presented, along with how different resonant modes are coupled into external signals and separated through spatial filtering. The electronic processing has been detailed, along with how the signals are downmixed from a GHz range using an external LO signal. Position-dependent modes were isolated in the signal output through

the mixing of the position-dependent dipole cavity signal with the position-independent reference cavity signal. The three dipole cavity BPMs, reference cavities and other beamline components in the IP region have been introduced, including the FONT board used to digitise the BPM signals.

The position calibration method of steering the beam using the final quadrupole magnet QD0FF was explained. Signal timing requirements and the necessity for a mixer pedestal subtraction were also detailed. The electronic noise floor of the IP system was quantified as ∼11 ADC counts on all BPM channels. A calibration at IPA was used to convert this ADC noise into nanometers, and was found to correspond to 21 ± 2 nm using a single sample of the digitised waveform and 13 ± 1 nm integrating across 8 samples. These results are in agreement with previous noise floor estimates, and are considered representative of the resolution limit for position measurements with the IP BPM system.

Finally, the unwanted parasitic waveform in the dipole cavity BPM pulses was investigated. It was found to be ∼63 MHz in frequency, bunch charge-dependent and stable in the IQ-space. This implies that the unwanted pulse features are beam generated. The parasitic waveform was not attenuated by a low-pass filter (ruling out higher-frequency LO harmonic mixing), or removed by a ±100 MHz BPF. To mitigate the impact of the parasitic waveform on operation of the IP BPMs, two narrow-BPFs were installed on the dipole cavity outputs to smooth the waveform.

Chapter 3

Three-BPM resolution

The resolution of the cavity BPMs is the dominant limitation for feedback in the ATF2 IP, as the ability to know the beam position limits the ability to correct it. Therefore accurately quantifying the resolution of the BPMs and identifying ways to improve their performance is vital. With all the optimisations of the previous chapter implemented, the different methods of estimating the resolution of the IP BPM system and analysis techniques to improve resolution capability are detailed in this chapter.

Having three cavity BPMs deployed in the IP region with no intermediary magnetic components meant it was possible to estimate the resolution directly. The measured position at two BPMs was used to predict the position at the third using a linear transport model. The residual difference between the predicted and measured results at the third BPM for an ensemble of data was then used to estimate the resolution of the BPM system, assuming all three BPMs are the same.

The FONT group has previously employed a resolution estimate that makes use of the known separations of the BPMs. A simple linear fit applied to the measured position signals has also been utilised to corroborate the geometry-based method [8]. It is also possible to use more complex fits, quantifying how other parameters could be contributing to the resolution. The mathematical substance of these methods and the different estimates of the vertical position resolution obtained for the ATF2 IP cavity BPMs are detailed here.

In the past, the IP BPM signals have predominantly been analysed using a single sample in the window digitised by the FONT board, as this is how the feedback firmware currently samples the waveforms [77]. Building on experiments with a multi-sample averaging approach to analysis [8], this chapter explores how resolution varied with sample number and the potential of sample integration. This technique made a notable improvement to the

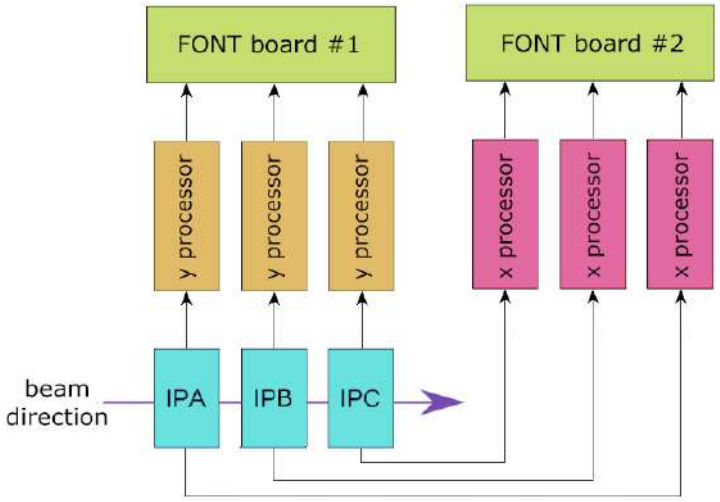

Figure 3.1: Block diagram of the IP feedback system for resolution studies utilising two FONT boards to digitise vertical and horizontal information from the cavity BPMs.

resolution estimates. The results of different integration windows are presented, with the aim of optimising the sampling for best resolution performance.

Studies are detailed of how the resolution varied as a function of dipole signal attenuation, bunch charge, beam position, and with signal filtering. The difficulties in reproducing resolution results are then addressed with a rolling resolution analysis.

3.1 Experimental set-up

Resolution studies were performed in a single-bunch train mode using two FONT boards to digitise the three IP BPMs' y and x-axis signals, as shown in Fig. 3.1. The y-axis BPM data were the primary interest for these studies, but some analysis presented also made use of the x BPM information, which was digitised simultaneously. The data gathered with the two boards were synchronised using a step signal generated internally on board 1 and sent to board 2 via the auxiliary outputs and inputs. A detailed diagram of the IP electronics set-up for processing y information is shown in Fig. 3.2. The "aux out" synchronisation signal is shown connected to a duplicate of this system for processing the x data.

For a direct resolution estimate, it was necessary to ensure the beam could pass through the linear operating range of all three BPMs. This was never possible in the past, as offsets in the relative vertical alignment of the BPMs were larger than the extremes of the BPM mover ranges. Careful iterative alignment studies [78] and adjustments to the IP chamber have now culminated in a BPM alignment that makes this study possible.

The IP processing electronics detailed in Chapter 2 were designed to have a very high

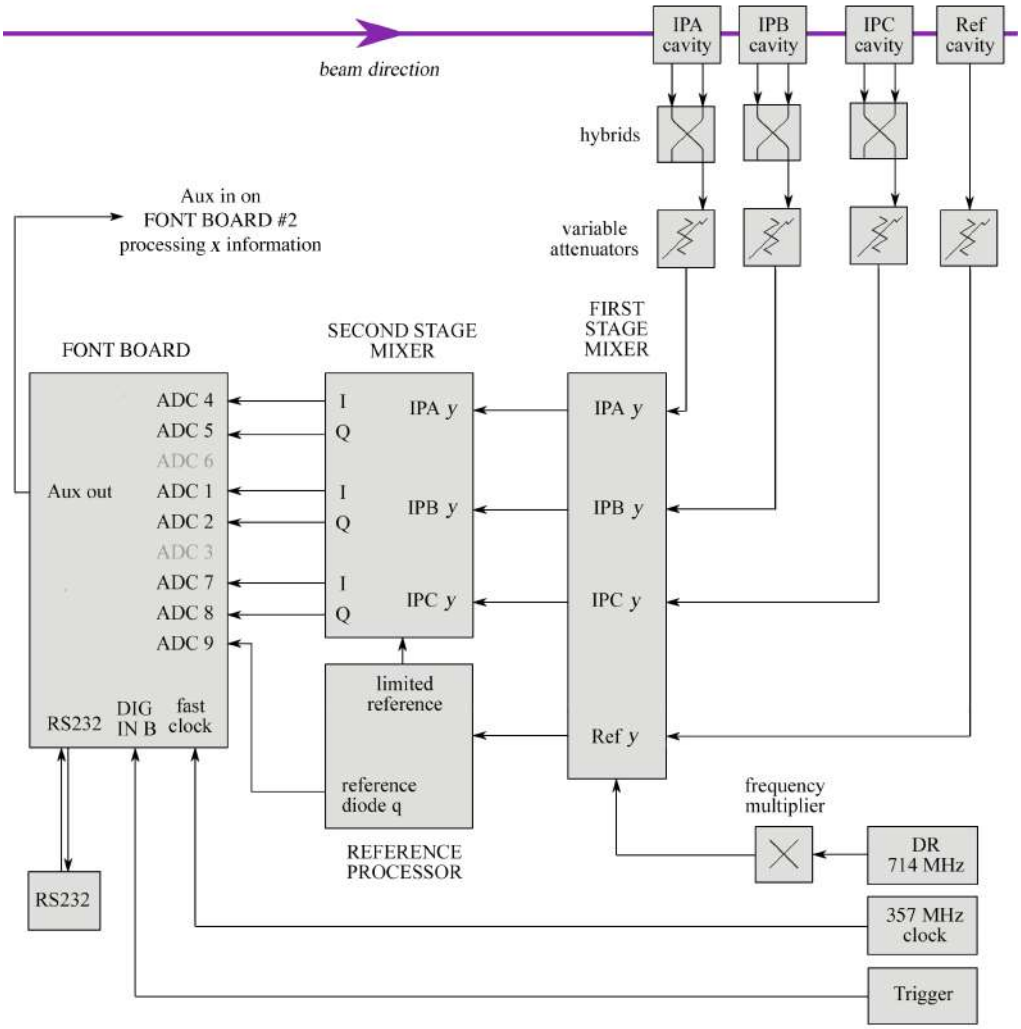

Figure 3.2: Detailed block diagram of the hardware and two-stage processing electronics set-up for digitising IP BPM cavity information in the vertical plane for resolution studies.

gain. As a consequence, their estimated linear range corresponded to only ∼5 µm around the centre of the BPM [59]. Operationally, staying within this range was calculated to correspond to ensuring BPM digitised signal peaks were always minimised to within approximately ±2500 ADC counts on the FONT board [79]. The variable attenuators in front of the down-mixing electronics were used to reduce the sensitivity and increase the dynamic range whenever the beam positions in the beam line were larger than this range.

With nominal IP optics, the standard deviation of the beam positions (known as the position "jitter") either side of the tuned waist was much larger than the dynamic range at the BPMs furthest from the IP (i.e. IPA and IPC) unless large attenuations were applied. Consequently, the optics used for resolution studies utilised a β_y^* that was 1000 times larger than the ATF2 nominal optics. This optics resulted in a much lower divergence of the

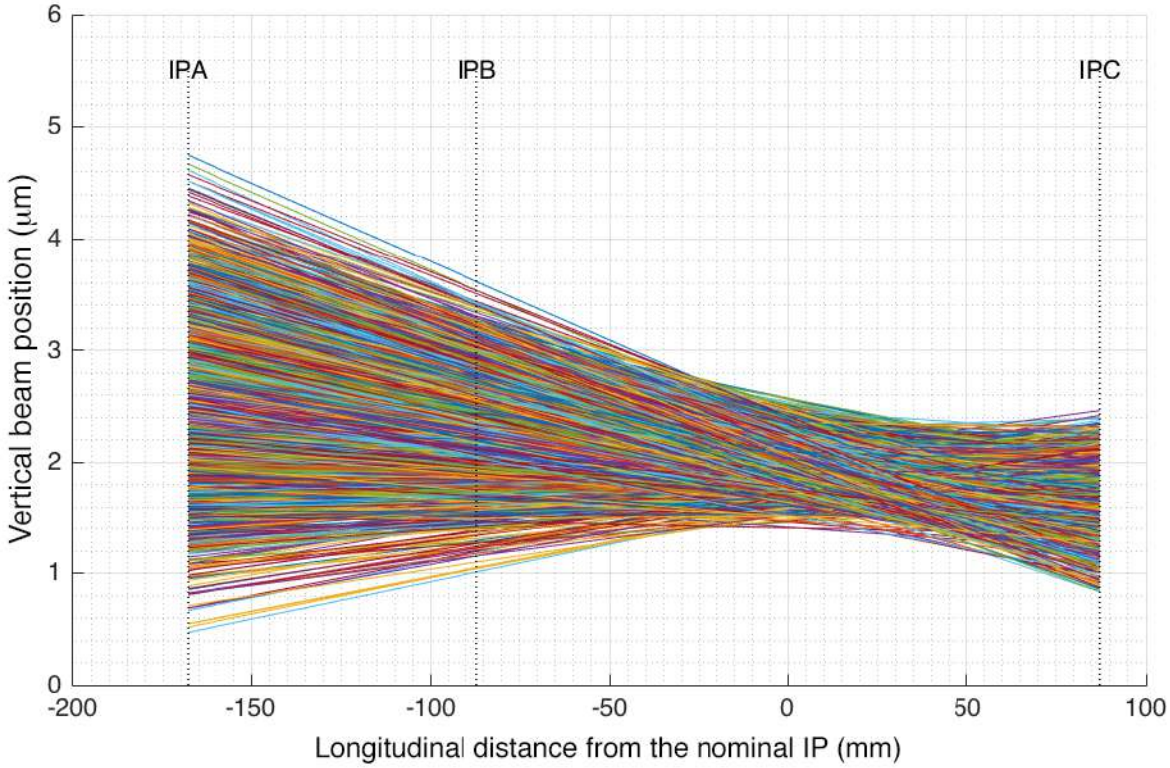

Figure 3.3: Vertical beam position versus longitudinal distance from the nominal IP for 2000 sequential triggers. Each coloured line represents the beam path of a different trigger. The locations of IPA, IPB, and IPC BPMs are indicated. The beam paths are obtained from a linear interpolation of the measured positions at IPA and IPC.

beam around the IP [80] and smaller jitters at the BPMs. Fig. 3.3 shows the beam path interpolated in the y axis between IPA and IPC for 2000 sequential measurements with just 10 dB attenuation on the dipole signals. The position jitter as a function of the longitudinal distance from the nominal IP location is shown in Fig. 3.4. The measured jitter at the IP BPMs has been reduced to the sub-micron level, as detailed in Table 3.1.

Table 3.1: Vertical position jitter measured at the three IP BPMs for the data presented in Fig. 3.4 with a high-beta optics set-up.

BPM position jitter (μm)		
IPA	IPB	IPC
0.74 ± 0.01	0.47 ± 0.01	0.28 ± 0.01

Example BPM I and Q waveforms are shown in Fig. 3.5. As discussed in Chapter 2, the higher-frequency oscillatory waveform seen in these pulses were problematic for operation of the IP system, due to large signal peaks saturating the electronics. The waveforms show that with 10 dB attenuation on the dipole signals operating at a charge of $\sim 0.5 \times 10^{10}$

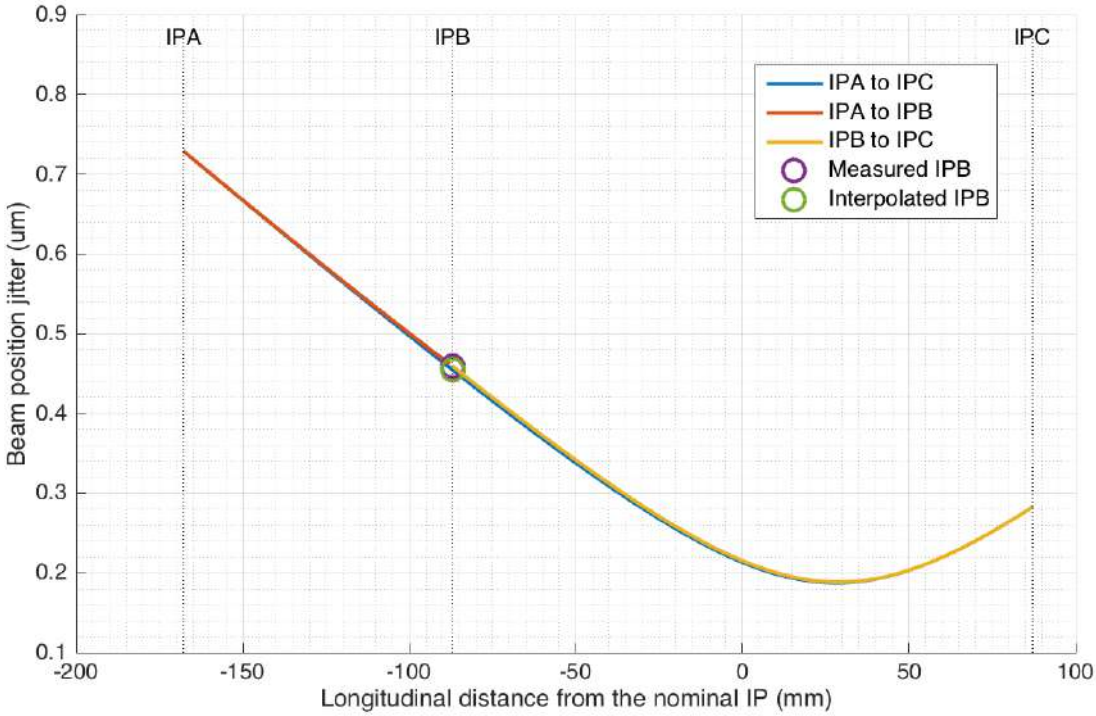

Figure 3.4: Interpolated beam position jitter versus longitudinal distance from the nominal IP. Separate interpolations between IPA and IPC (blue), IPA and IPB (red) and between IPB and IPC (yellow) are plotted. The purple circle indicates the jitter measured at IPB, and the green circle the jitter interpolated at IPB. The results are difficult to distinguish on the plot, as the different methods are in very good agreement.

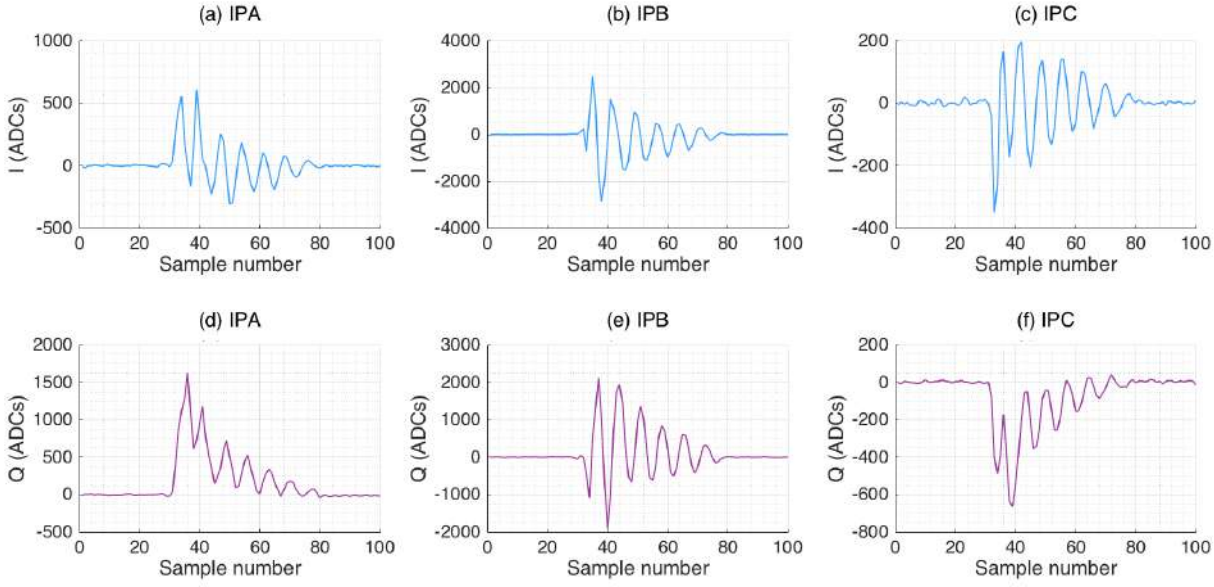

Figure 3.5: IP BPM signals in ADCs versus sample number for one example waveform in y; (a) IPA I, (b) IPB I, (c) IPC I, (d) IPA Q, (e) IPB Q, (f) IPC Q.

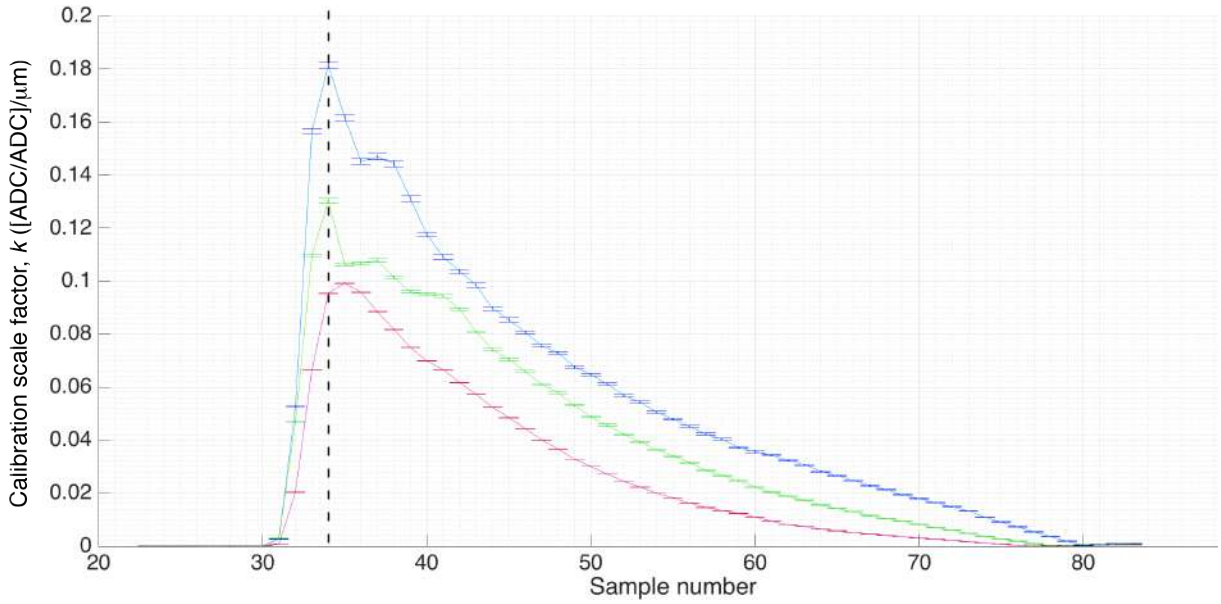

Figure 3.6: Calibration scale factor, k, versus sample number, measured at IPA (blue), IPB (green) and IPC (pink). The lines join the data points, with error bars indicating the statistical uncertainties on k. Optimal sample 34 is indicated by the dashed line.

electrons per bunch, it was possible to keep signals within the ±2500 ADC count range. This charge setting was typical for FONT experiments utilising the IP BPM system, as it was easily obtainable at the ATF2.

Fig. 3.6 shows the calibration scale factor, k, as a function of sample number. For the best signal-to-noise ratio, it was desirable to sample at the maximum k value within the digitised window. The peak k corresponds to sample 34, which was hence used for preliminary analysis of these data sets.

3.2 Resolution calculation

The predicted position at one of the IP BPMs, $\hat{y}_i$, can be calculated from a linear combination of the measured positions at the other two BPMs, y_j and y_k,

$$\hat{y}_i = C_{ij} y_j + C_{ik} y_k, \tag{3.1}$$

where the coefficients C_{ij} and C_{ik} are constants. The residual, $\Delta_i = y_i - \hat{y}_i$, between the measured and predicted results is

$$\Delta_i = y_i - (C_{ij} y_j + C_{ik} y_k).$$

Any beam position measurement, y_i, will be a combination of both the true beam

position, y_i^T and additional random measurement error, ϵ_i,

$$y_i = y_i^T + \epsilon_i. \tag{3.2}$$

Hence,

$$\begin{aligned}\Delta_i &= (y_i^T - C_{ij}y_j^T - C_{ik}y_k^T) + (\epsilon_i - C_{ij}\epsilon_j - C_{ik}\epsilon_k,) \\ &= \epsilon_i - C_{ij}\epsilon_j - C_{ik}\epsilon_k.\end{aligned} \tag{3.3}$$

For an ensemble of bunch trains these residuals are assumed to be normally distributed, with a variance given by

$$\mathrm{std}(\Delta_i)^2 = \sigma_i^2 + C_{ij}^2\sigma_j^2 + C_{ik}^2\sigma_k^2, \tag{3.4}$$

where the errors on the three BPM measurements ϵ_i, ϵ_j and ϵ_k are assumed to be uncorrelated, with normal distributions with standard deviation σ_i, σ_j and σ_k. If the BPMs are identical, their measurement error distributions will be the same, i.e., $\sigma_i = \sigma_j = \sigma_k = \sigma_{\mathrm{BPM}}$. Hence,

$$\mathrm{std}(\Delta_i)^2 = \sigma_{\mathrm{BPM}}^2(1 + C_{ij}^2 + C_{ik}^2), \tag{3.5}$$

and

$$\sigma_{\mathrm{BPM}} = \frac{\mathrm{std}(\Delta_i)}{\sqrt{1 + C_{ij}^2 + C_{ik}^2}}. \tag{3.6}$$

3.3 The geometric method

A geometric approach to the resolution calculation makes use of the known information about the relative longitudinal positions of the three BPMs. For this example the predicted position in the y axis at BPM 2, $\hat{y}_2$, is calculated based on the measured y-axis positions at BPM 1, y_1, and BPM 3, y_3, using the BPM locations s_1, s_2 and s_3, as shown in Fig. 3.7. From geometric considerations, the predicted position $\hat{y}_2$ is given by

$$\begin{aligned}\frac{\hat{y}_2 - y_1}{s_2 - s_1} &= \frac{(y_3 - y_1)}{s_3 - s_1}, \\ \hat{y}_2 &= y_1\left(1 - \frac{s_2 - s_1}{s_3 - s_1}\right) + y_3\left(\frac{s_2 - s_1}{s_3 - s_1}\right).\end{aligned} \tag{3.7}$$

Hence,

$$\sigma_{\mathrm{BPM}} = \frac{\mathrm{std}(\Delta_{y_2})}{\sqrt{\left(\frac{s_2 - s_3}{s_3 - s_1}\right)^2 + 1 + \left(\frac{s_2 - s_1}{s_3 - s_1}\right)^2}}. \tag{3.8}$$

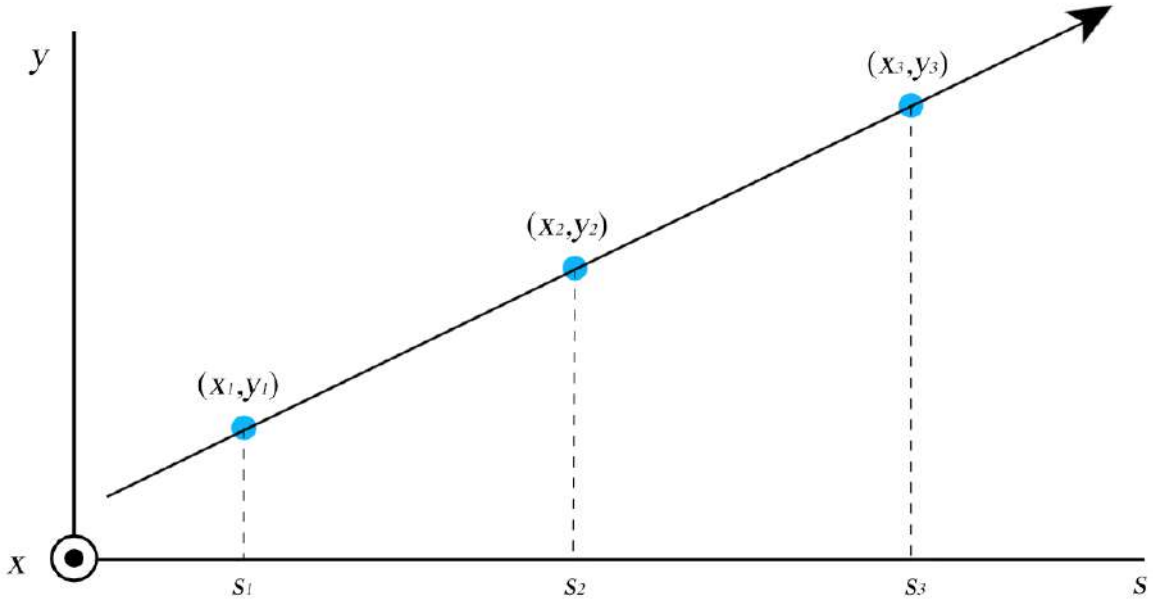

Figure 3.7: Schematic of the experimental set-up with three cavity BPMs at different locations, s_i, along the beam pipe. The blue dots mark the x and y coordinates of the beam as it passes through the three BPMs [81].

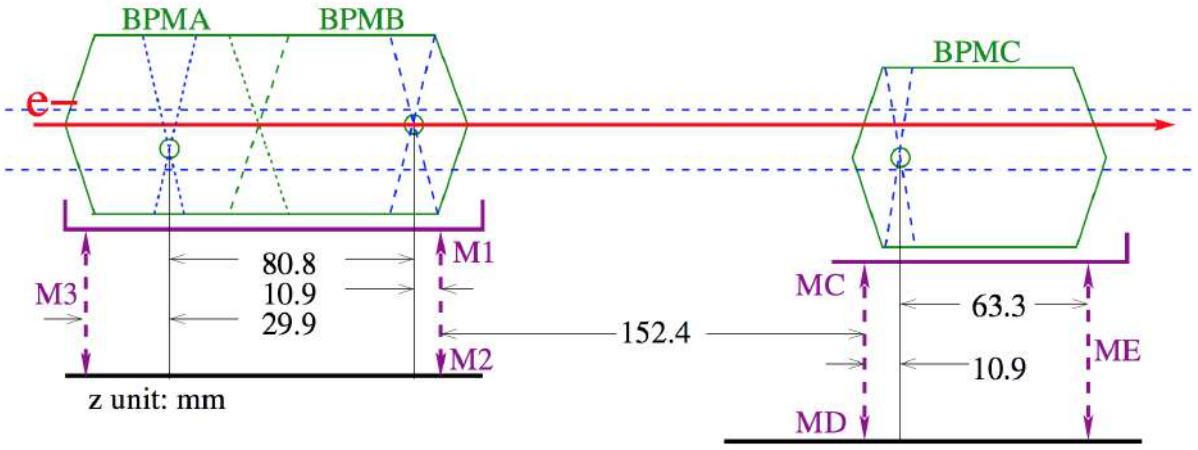

Figure 3.8: Longitudinal position of the IP BPMs within the IP mover system [82].

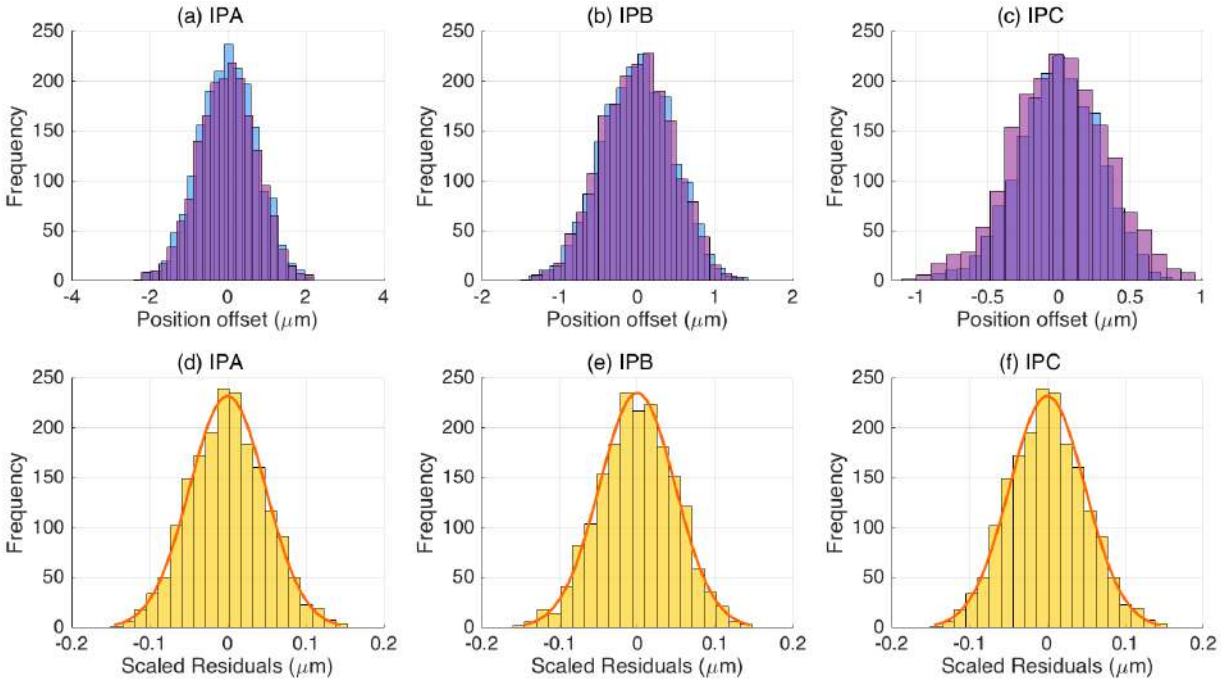

Figure 3.9: Distributions of the measured y positions (blue) and the predicted y positions obtained using the geometric method (purple) at BPMs (a) IPA, (b) IPB and (c) IPC; and distributions of the corresponding scaled position residuals at BPMs (d) IPA, (e) IPB and (f) IPC. The orange lines indicate Gaussian fits to the data.

These distances are determined from measurements of the BPM locations within the mover system mounting table, shown in Fig. 3.8, and detailed in Table 2.1.

There are three versions of the equation for the vertical BPM beam position resolution, depending on which BPM is used for prediction,

$$\sigma_{\mathrm{BPM}} = \frac{\mathrm{std}(\Delta_{y_1})}{1.83} = \frac{\mathrm{std}(\Delta_{y_2})}{1.25} = \frac{\mathrm{std}(\Delta_{y_3})}{3.95}. \tag{3.9}$$

The results of this analysis method are presented in Fig. 3.9. The top row shows the distributions of the measured and predicted positions using Eq. 3.7. The mean positions at each BPM have been subtracted from their respective distributions to account for the arbitrary offsets of the BPM movers.

The second row of Fig. 3.9 shows the distributions of scaled residuals, $\widetilde{\Delta_y}$. i.e. the Δ_y values of Eq. 3.9 normalised by the appropriate geometric factors. Each distribution from each BPM can be fitted with a Gaussian of the form,

$$\frac{\mathrm{d}N}{\mathrm{d}\widetilde{\Delta_y}} = \mathrm{A}_i \exp\left(\frac{\widetilde{\Delta_y}^2}{2\sigma^2_{\mathrm{BPM}}}\right), \tag{3.10}$$

where A_i is a normalisation factor.

The analysis yielded $\sigma_{\mathrm{BPM}} = 49 \pm 1$ nm. The error was propagated from the statistical uncertainty on the position residual and the uncertainties on the measured BPM separations. The statistical uncertainty was by far the dominant contribution. This result is consistent with past best single-sample geometric estimates for the resolution at the ATF2 IP system [83] at the same bunch charge.

3.4 The fitting method

Instead of constraining the position prediction to the known geometric separations, a linear fit can be applied to the measured positions and the fit coefficients determined using a least-squares approach:

$$\hat{y}_2 = \alpha_2 y_1 + \beta_2 y_3 + \gamma_2. \tag{3.11}$$

A constant fit parameter γ, allows for any relative position offsets due the BPM movers. Here the example of predicting positions at BPM 2 has been used again.

Following the same process as described previously for the geometric method, the variance of the residual can be determined,

$$\mathrm{std}(\Delta_{y_2})^2 = \sigma_{y_2}^2 + \alpha_2^2\sigma_{y_1}^2 + \beta_2^2\sigma_{y_3}^2. \tag{3.12}$$

The vertical position resolution at all three BPMs is again assumed to be the same:

$$\begin{aligned} \mathrm{std}(\Delta_{y_2})^2 &= \sigma_{\mathrm{BPM}}^2(\alpha_2^2 + 1 + \beta_2^2), \\ \sigma_{\mathrm{BPM}} &= \frac{\mathrm{std}(\Delta_{y_2})}{\sqrt{1 + (\alpha_2)^2 + (\beta_2)^2}}. \end{aligned} \tag{3.13}$$

Unlike the geometric method, fitting results in three different BPM vertical position resolution estimates depending on which BPM is used for predicting. The resolution, σ_{BPM} acquires a subscript to reflect this:

$$\sigma_{\mathrm{BPM}_1} = \frac{\mathrm{std}(\Delta_{y_1})}{\sqrt{1 + (\alpha_1)^2 + (\beta_1)^2}}, \quad \sigma_{\mathrm{BPM}_2} = \frac{\mathrm{std}(\Delta_{y_2})}{\sqrt{1 + (\alpha_2)^2 + (\beta_2)^2}}, \quad \sigma_{\mathrm{BPM}_3} = \frac{\mathrm{std}(\Delta_{y_3})}{\sqrt{1 + (\alpha_3)^2 + (\beta_3)^2}}. \tag{3.14}$$

It should be noted that these numerical subscripts do not indicate the resolution at any particular BPM, but just which combination of BPM measurements has been used.

The results of this fitting method analysis are shown in Fig. 3.10. This analysis estimated the resolution to be 49 ± 1 using IPA and IPB to predict, and 59 ± 1 using IPC. The poorer

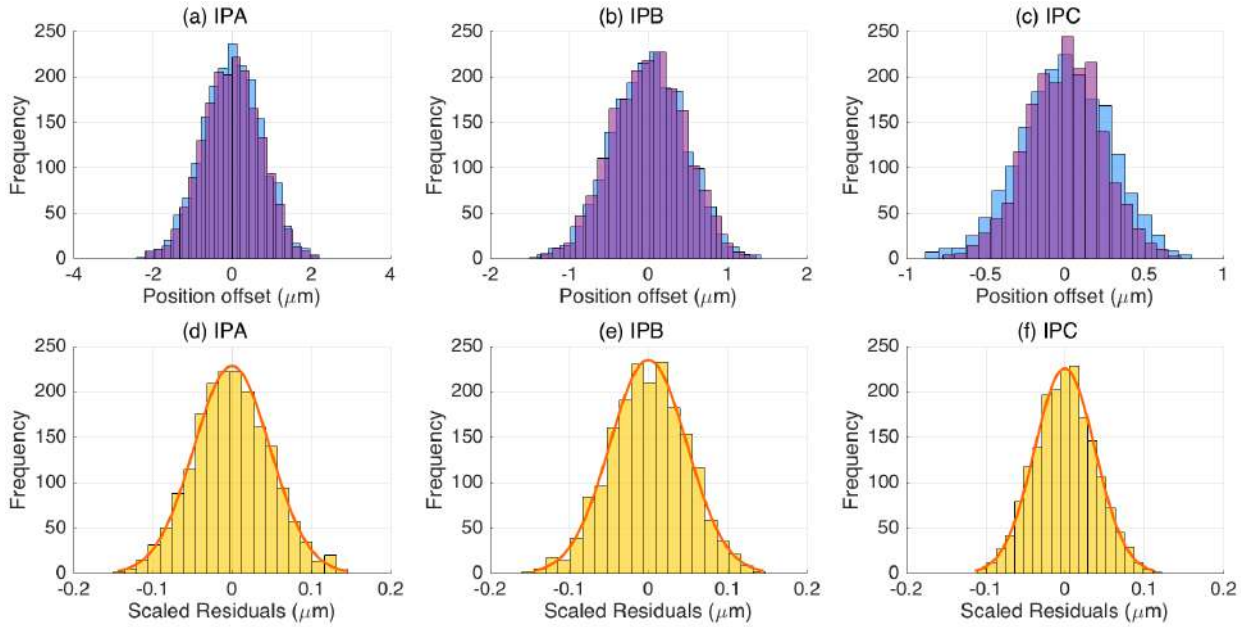

Figure 3.10: Distributions of the measured y positions (blue) and the predicted y positions obtained using the fitting method (purple) at BPMs (a) IPA, (b) IPB and (c) IPC; and distributions of the corresponding scaled position residuals at BPMs (d) IPA, (e) IPB and (f) IPC. The orange lines show Gaussian fits to the data.

resolution estimate using a prediction at IPC was likely due to IPC being further away from IPA and IPB than IPA and IPB are from each other. This difference in relative separations meant small position measurement errors at IPA and IPB resulted in larger errors in the prediction at IPC. This effect was exacerbated by the smaller position jitters at IPC compared to those at IPA and IPB (see measured jitters in Table 3.1), so signal-to-noise ratios were less favourable at IPC. For other resolution studies that featured comparable jitters at the three BPMs, this effect was less pronounced.

The geometric and fitting methods produced identical resolution estimates when IPA and IPB were used to predict positions, confirming the linear beam trajectory in the IP region. However, the three results for the fitting method on multiple repeat resolution data runs were found to vary ∼10 nm between themselves (in the way the IPC result does here), and from the geometric method estimates. One source of this discrepancy may be the individual BPM calibrations for the two BPMs used to predict position measurements. If beam conditions change between calibrating the BPMs and recording data for beam position measurements, the calibrations are no longer valid, and fitting out the calibration constants will result in more variation between the three resolution estimates.

3.5 Multi-parameter fit

The FONT group has used both the geometric and fitting methods previously and found them to be in good agreement for estimating the IP BPM resolution performance [8]. These models only make use of vertical position information in I', assuming the θ_{IQ} rotation has perfectly transferred all position information from the I and Q signals into I'. It also assumes there is no coupling between the x and y axes. However, the BPM mover system allows the roll of the BPMs to be adjusted relative to each other, which may mean a small amount of the x information could be coupled into the y-axis position information. Additionally, non-linearities in the system could result in a position dependence on, for example, the bunch charge.

This possibility can be addressed by adopting a multi-parameter fit method [59], which includes parameters such as the Q' signal, x-axis information, and the charge levels.

First, consider the vertical position, y, in terms of the raw I and Q signals,

$$y = \frac{I'}{kq} = \frac{(I\cos\theta_{IQ} + Q\sin\theta_{IQ})}{kq}.$$

This can be substituted into Eq. 3.11 for the predicted position:

$$\begin{aligned}\hat{y}_2 &= \alpha_2 y_1 + \beta_2 y_3 + \gamma_2, \\ &= \alpha_2 \frac{1}{k_1 q}(I_1\cos\theta_{IQ_1} + Q_1\sin\theta_{IQ_1}) + \beta_2 \frac{1}{k_3 q}(I_3\cos\theta_{IQ_3} + Q_3\sin\theta_{IQ_3}) + \gamma_2.\end{aligned} \tag{3.15}$$

All the calibration scale factors and rotation angles are constant terms in this equation, so it is possible to recombine all the pre-factors as

$$A_2 = \alpha_2 \frac{1}{k_1}\cos\theta_{IQ_1}, \quad B_2 = \alpha_2 \frac{1}{k_1}\sin\theta_{IQ_1},$$

$$C_2 = \beta_2 \frac{1}{k_3}\cos\theta_{IQ_3}, \quad D_2 = \beta_2 \frac{1}{k_3}\sin\theta_{IQ_3}, \quad E_2 = \gamma_2,$$

so the fit can be rewritten to incorporate all constants in single terms in the form:

$$\hat{y}_2 = A_2\frac{I_1}{q} + B_2\frac{Q_1}{q} + C_2\frac{I_3}{q} + D_2\frac{Q_3}{q} + E_2. \tag{3.16}$$

In this way a fit to the charge normalised I and Q information can be used to predict the $\hat{y}$ signal at a given BPM. Including Q information means any residual position information not effectively transferred to I' through rotation is addressed by a term in the fit.

In practice, the I and Q signals themselves are difficult to interpret without rotation into I' and Q' where, as discussed in Chapter 2, they can be read as proportional to position and

angle. Since I' and Q' are themselves linear combinations of I and Q, it is more informative to apply the multi-parameter fit to I' and Q' values using:

$$\hat{y_2} = A'_2\frac{I'_1}{q} + B'_2\frac{Q'_1}{q} + C'_2\frac{I'_3}{q} + D'_2\frac{Q'_3}{q} + E'_2, \tag{3.17}$$

as the final predicted $\hat{y}$ values would be identical to those calculated using Eq. 3.16, but the relative sizes of the coefficients will be more indicative of position and angle contributions to the final result, and thus may illuminate how successful the rotation has been.

There is also the potential to include other parameters that may be contributing position information in a multi-parameter fit, such as the bunch charge using the charge-dependent q term, and x-axis data. However, the mathematical justification for incorporating these new terms cannot be traced through derivation, as it was for I' and Q'. They can be assumed on first approach to contribute linearly, as shown in Table 3.2.

Table 3.2: Equations for different multi-parameter fits incorporating different subsets of BPM information as fit parameters. The i, j, k subscripts depend on which of the three BPMs are being used to measure positions.

Number of fit parameters	Multi-parameter fit equation
5	$\hat{y}_i = A'_i\frac{I'_{j_y}}{q_y} + B'_i\frac{Q'_{j_y}}{q_y} + C'_i\frac{I'_{k_y}}{q_y} + D'_i\frac{Q'_{k_y}}{q_y} + E'_i$
6	$\hat{y}_i = F'_i\frac{I'_{j_y}}{q_y} + G'_i\frac{Q'_{j_y}}{q_y} + H'_i\frac{I'_{k_y}}{q_y} + J'_i\frac{Q'_{k_y}}{q_y} + K'_i q_y + L'_i$
11	$\hat{y}_i = M'_i\frac{I'_{j_y}}{q_y} + N'_i\frac{Q'_{j_y}}{q_y} + O'_i\frac{I'_{k_y}}{q_y} + P'_i\frac{Q'_{k_y}}{q_y} + R'_i q_y$ $+S'_i\frac{I'_{j_x}}{q_x} + T'_i\frac{Q'_{j_x}}{q_x} + U'_i\frac{I'_{k_x}}{q_x} + V_i\frac{Q'_{k_x}}{q_x} + W_i q_x + X_i$

The standard deviation of the residuals, std(Δ_y), can be calculated using one of the equations in Table 3.2, and then be substituted into Eq. 3.9, using normalisation factors determined from the geometric separations to estimate the resolution [84]:

$$\sigma_{\text{BPM}} = \frac{\text{std}(\Delta_{y_1})}{1.83} = \frac{\text{std}(\Delta_{y_2})}{1.25} = \frac{\text{std}(\Delta_{y_3})}{3.95}. \tag{3.18}$$

The results of this analysis using the different multi-parameter fits are shown in Table 3.3, along with the three-parameter position fitting results from Section 3.4. Again, the freedom of the fits applied here means these methods resulted in three different estimates of the vertical position resolution.

Table 3.3: Vertical position resolution estimates using different numbers of fitted parameters. The 3-parameter fit corresponds to using a fit to positions (see Eq. 3.11). The other fits correspond to the fitting methods presented in Table 3.2. The statistical uncertainty on all of these resolution estimates is ±1 nm.

Number of fit parameters	Vertical position resolution (nm)		
	Predicting at IPA	Predicting at IPB	Predicting at IPC
3	49	49	59
5	43	38	35
6	43	38	34
11	42	37	33

Inclusion of Q' terms in the 5-parameter fit caused the largest reduction in the resolution estimate, compared to the 3-parameter fits. For example, including Q' reduced the resolution estimate from 49 ± 1 nm to 38 ± 1 nm in the instance when IPB was used to predict. This scale of reduction was consistently found to be the case across repeat data runs, suggesting the phase rotation to divide the signals into position and angle-dependent terms is not perfect and there is residual position information left in the Q' signals.

The charge-dependent term, q, had very little impact when it was included in the 6-parameter fit. Horizontal x information, similarly, made a difference of no more than a nanometre to the resolution estimate when included in the 11-parameter fit.

It is notable that the resolution estimates when predicting at IPC were always lower than those predicting at IPA and IPB, with the lowest estimate of 33 ± 1 nm with an 11-parameter fit. This was consistently the case in analysis of many data runs. It is possible the phase rotations for IPC were systematically less accurate than those at IPA and IPB. But with so many parameters left unconstrained, the three estimated results were likely to be in disagreement with each other; this is an unavoidable side-effect of fitting.

Even though the multi-parameter fits consistently provided lower resolution estimates, it would not be practical to include them in a position calculation to enter into a low-latency feedback system. Therefore, although this approach is of interest as a tool to compare with geometric or 3-parameter position fitting results and isolate unused position information or position dependences, they do not represent a “useable” vertical position resolution for input into feedback at the ATF2.

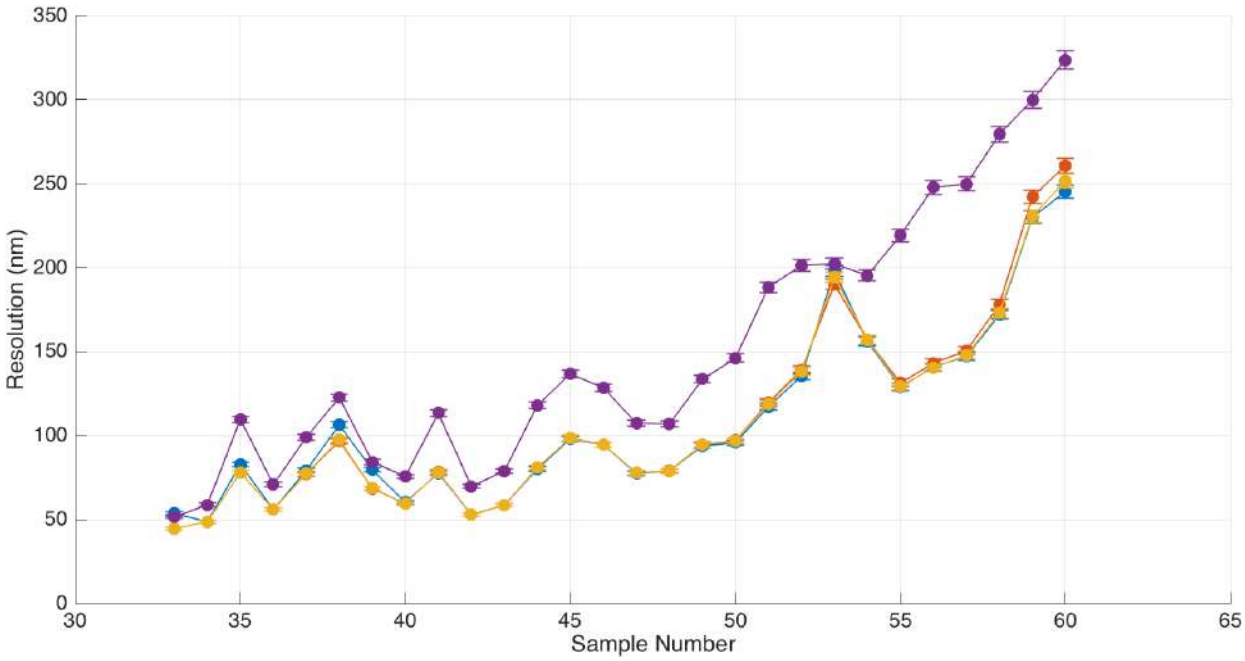

Figure 3.11: The estimated resolution performance versus sample number calculated using the geometric method (blue), and the 3-parameter fitting method predicting at IPA (red), IPB (yellow) and IPC (purple). The lines connect the data points. The error bars indicate the statistical uncertainty on the resolutions.

3.6 Sample number dependence

The I and Q waveforms from the cavities display features that dictate where within the digitised window it might be optimal to sample for best resolution performance. The pulse has an exponentially decaying envelope, with sample numbers early in the waveform offering the best signal-to-noise ratio. However, this picture is complicated by the sinusoidal feature. It was therefore of interest to look at how the resolution varies along the pulse.

Fig. 3.11 shows the resolution estimated at different sample numbers, using both geometric and 3-parameter fitting methods. The shape reflects the degradation of resolution as the signal-to-noise worsens with the pulse's decay, as expected. It is, again, notable that the 3-parameter fitting result using IPC is worse. The geometric and fitting using IPA and IPB are in good agreement.

The sinusoidal features of the cavity signal output are also visible in the shape of the resolution performance using both methods of analysis; this was to be expected, as the oscillation inevitably results in lower signal levels at some sample points, degrading the resolution. This sample-number dependence motivated consideration of how sampling methods might improve the resolution.

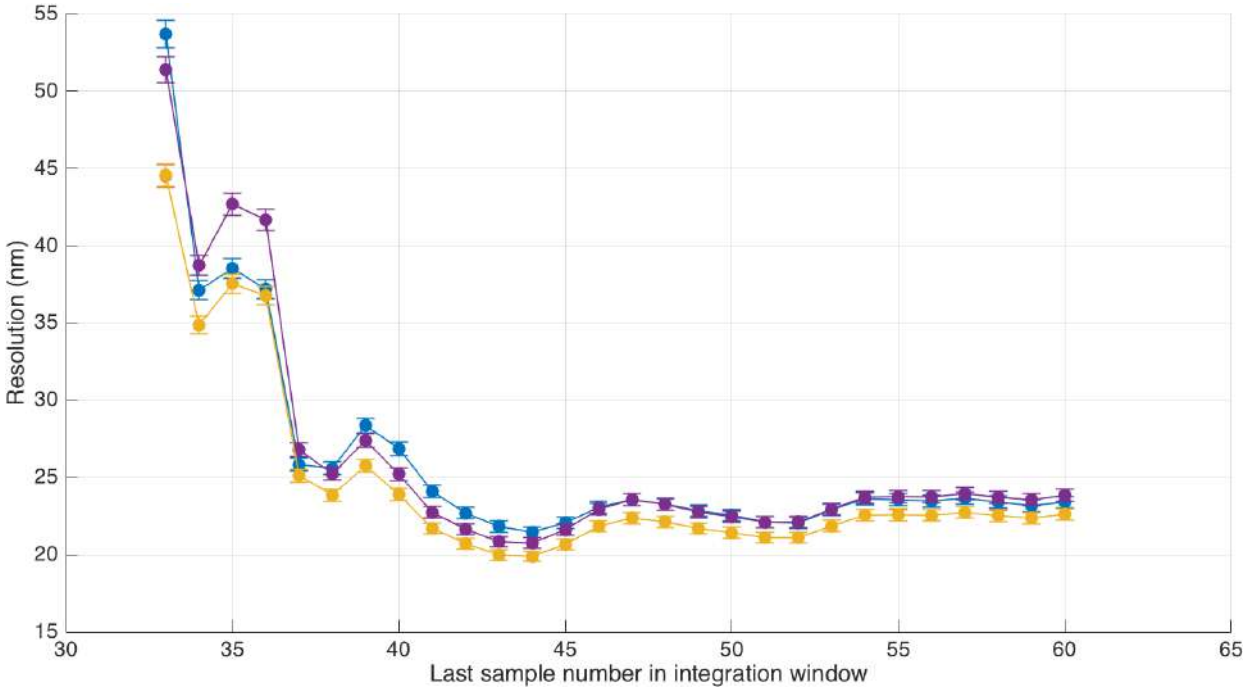

Figure 3.12: Resolution versus last sample number in the integrated sampling window using geometric method (blue) and the 3-parameter fitting method predicting at IPA (red), IPB (yellow) and IPC (purple). The data points for IPA are not visible at they are overlapped by the IPB data. The lines connect the data points. The error bars indicate the statistical uncertainty on the resolutions.

3.7 Integrated sampling

Past FONT studies investigated a multi-sample averaging approach for improving resolution [8]. The analysis presented now took this approach further using direct resolution measurements and a new approach of integrating across the waveform for each BPM. This method summed the I and Q signal levels across multiple samples. The calibration was performed in the same way, using the same range of sample numbers.

Fig. 3.12 shows the resolution for a cumulatively increasing sample window using both the geometric and 3-parameter fitting methods. Sample number 33 was chosen as a starting point, as this marks the beginning of the waveform (Fig. 3.5). The first point in Fig. 3.12 at sample 33 corresponds to a single sample. The next point at sample 34 indicates that samples 33 to 34 have been integrated, and so on, increasing the window to a maximum of 33 to 60, i.e., 28 samples. The resolution estimates were ∼1µm at samples earlier than 33, as this portion of the data was noise dominated.

This integration method improved the resolution estimate significantly. The best result (Fig. 3.12) was 21.5 ± 0.4 nm using the geometric method and 20.0 ± 0.4 nm using fitting,

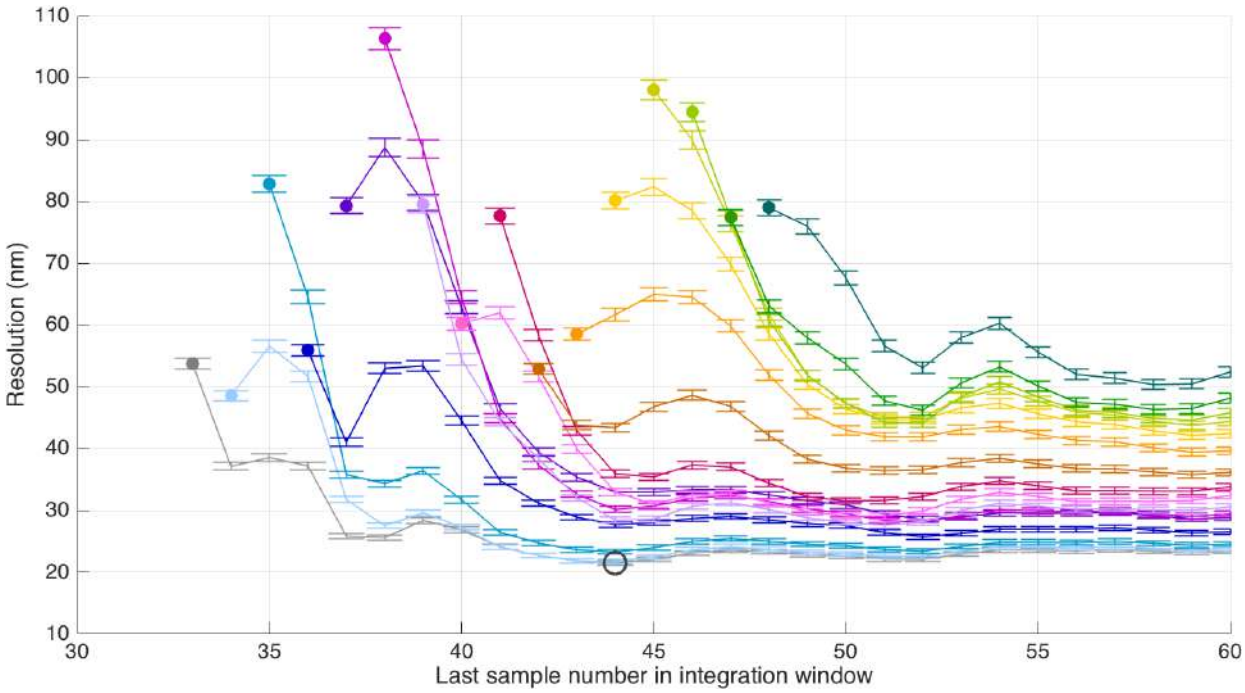

Figure 3.13: Geometric resolution versus the last sample number in the integrated sampling window. Each colour represents a different starting sample for the integration, defined by the solid points at the start of each line, for which the resolutions have been calculated using a single sample. The lines connect the data points. The error bars indicate the statistical uncertainty on the resolutions. The black circle indicates the minimum resolution, 21.5 ± 0.4 nm, integrating between samples 33 and 44.

both calculated by integrating from samples 33 to 44. This result is to be compared with the best estimates in previous sections of 49 ± 1 nm using a single sample. The oscillation observed in Fig. 3.11 for single sample was still in evidence here, but was smoothed by the integration to be less prominent as the window size increased. The resolution did not improve by extending the window much beyond ∼10 samples, as the signals had decayed away significantly by that point in the waveform.

Fig. 3.13 shows the geometric resolutions obtained by shifting the starting sample of the integration window, as well as changing the window length. There was always a significant improvement in integrating, as opposed to using a single sample. The overall best resolution estimate was still 21.5 ± 0.4 nm using an integration between samples 33 and 44.

The data set was re-analysed for all the different resolution estimate methods discussed, using an integration approach. The results are presented in Table 3.4 alongside the single sample results. Adding more fitting parameters did not make more than a few nanometers difference to the best resolution estimates, compared to switching from single sample to integration sampling, which improves results by ∼30 nm.

Table 3.4: Vertical position resolution estimates using geometric and fitting methods and using both a single sample (sample 34) and an integration window (samples 33 to 44). The uncertainty on all single sample resolution estimates is ±1 nm. The uncertainty on all integration resolution estimates is ±0.4 nm.

		Single sample resolution (nm)			Integration resolution (nm)		
Resolution method	Number of fit parameters	Predicting at IPA	IPB	IPC	Predicting at IPA	IPB	IPC
Geometric	-	49	49	49	21.5	21.5	21.5
Fitting	3	49	49	59	19.9	19.9	20.7
Multi-parameter	5	43	38	35	19.5	20.0	17.8
Multi-parameter	6	43	38	34	19.5	20.0	17.8
Multi-parameter	11	42	37	33	19.2	19.6	17.5

Integrating in firmware is something that could be implemented in future for the FONT feedback system at the ATF2 IP. This upgrade would result in a best useable vertical position resolution estimate of ∼20 nm. This would be a substantial improvement on the current useable resolution estimate of ∼50 nm using just one sample of the waveform.

3.8 Resolution versus attenuation

The amplitude of the I and Q signals should scale with the input signal levels from the dipole cavity. To check for a linear response, the variable attenuators immediately after the cavity hybrids and before the first stage mixer (Fig.3.2) could be used to attenuate signal levels. Ideally, the calibration scale factor, k, should scale linearly as the signals are attenuated. In the context of resolution studies, signal-to-noise ratios should be more favourable with larger signals, i.e.:

$$\sigma_{\mathrm{BPM}} \propto \frac{1}{q}. \tag{3.19}$$

For these measurements, the dipole cavity signal was attenuated by 0 to 50 dB in 10 dB increments. The charge was kept constant at $\sim 0.15 \times 10^{10}$ electrons per bunch. This charge was lower than typical for FONT operation but was chosen to avoid saturation at the 0 dB setting, where it was often impossible to operate with higher charges. A calibration was performed at each setting to calculate k for the three IP BPMs. The range of AQD0FF settings used for the calibrations was scaled at each attenuation to reflect the signals levels.

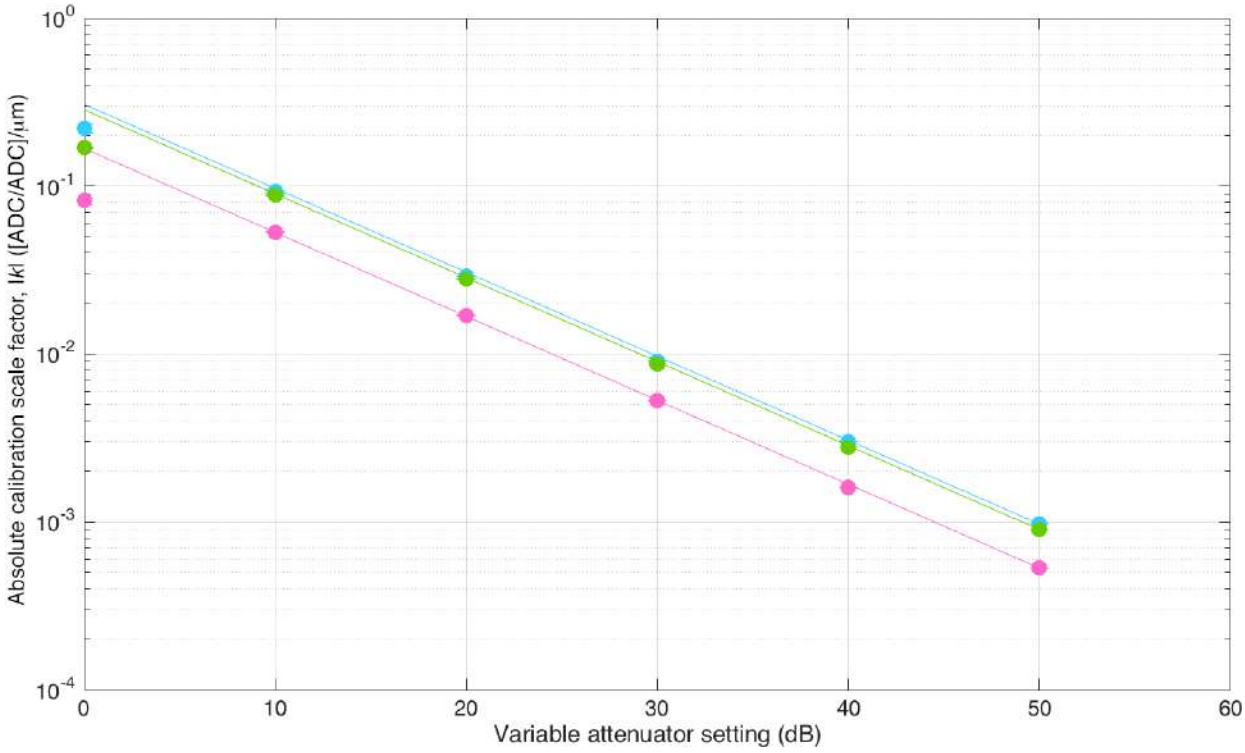

Figure 3.14: Absolute calibration scale factor, $|k|$, measured at IPA (blue), IPB (green), and IPC (pink) versus attenuation. Each line represents a linear scaling of the respective calibration scale factors at 50 dB to lower attenuation settings.

Fig. 3.14 shows $|k|$ for each BPM plotted against the attenuation setting used. The 50 dB result should have scaled to lower attenuations if the system were behaving linearly. For attenuations between 10 and 50 dB $|k|$ scaled well. However, the measured values at 0 dB deviated from the expected values. This may indicate that some component of the electronics was saturating when signal levels were large.

The calibration scale factors calculated were used to calculate the respective resolution. The results are detailed in Table 3.5 and plotted for the geometric method in Fig. 3.15, using both single sample and integration methods. The resolution estimates here were worse than those presented previously for 10 dB, as these data were gathered at a lower charge, where signal levels were lower, so the resolution was degraded. All the integration results demonstrated better performance than single sample, with a best single sample resolution estimate of 97 $\pm$ 7 nm, and a best integrated estimate of 70 $\pm$ 5 nm.

Between 20 and 50 dB, the resolution using both single sample and integration scaled well with attenuator setting. However, at 0 and 10 dB the resolution estimates ceased to scale. This was expected at 0 dB from the calibration scale factor analysis, but saturation may have been occurring at 10 dB also. One possible reason this showed up here, but not

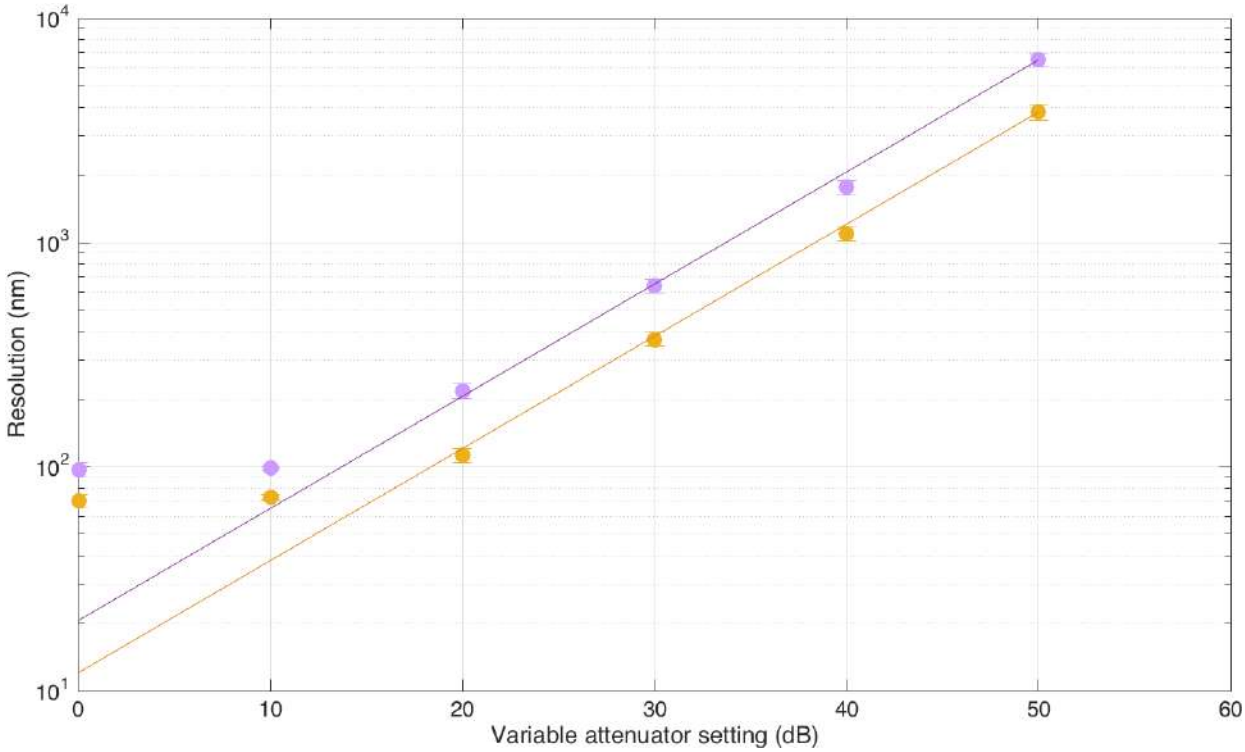

Figure 3.15: Geometric resolution versus attenuation, using single sampling (lilac) and integration (orange). The lines represents a linear scaling of the resolution at 50 dB. The error bars indicate the statistical uncertainty on the resolutions.

Table 3.5: Geometric resolution estimates using single sample and integration methods at different variable attenuator settings. The 50 dB geometric resolution results scaled to lower attenuations are also quoted for the single sample and integration results. Error bars indicate the statistical uncertainty on the resolutions.

	Measured resolution (nm)		50dB Predicted Resolution (nm)	
Attenuation (dB)	Single-sample	Integration	Single-sample	Integration
0	97 ± 7	70 ± 5	21 ± 2	12 ± 1
10	98.7 ± 2	73 ± 2	65 ± 5	38 ± 3
20	218 ± 16	112 ± 8	206 ± 15	121 ± 9
30	640 ± 46	369 ± 26	651 ± 49	381 ± 30
40	1760 ± 132	1090 ± 80	2060 ± 150	1200 ± 95
50	6510 ± 485	3810 ± 300	-	-

in calibration scale factor analysis, is that k is calculated using mean signal levels, whereas the resolution depends on a standard deviation. If saturation is occurring symmetrically on either side of a distribution, the mean levels will likely still be representative of the data, whereas the spread will be negatively impacted. If the system had not been saturating, these scalings suggest a resolution of 21 ± 2 nm should have been achievable at 0 dB attenuation and single sampling, and 12 ± 1 nm when integrating.

3.9 Resolution versus charge

Another means of changing the signal levels entering the IP system is to adjust the bunch charge. In this instance, the I and Q signal levels should scale, but k is a charge normalised constant, and should remain unchanged. The charge was varied from $\sim 0.15 \times 10^{10}$ to $\sim 0.5 \times 10^{10}$ electrons per bunch in steps of $\sim 0.05 \times 10^{10}$. The dipole cavity variable attenuators were set at 10 dB throughout.

The Integrating Current Transformers (ICTs) installed in the ATF2 beamline extraction line were used as a charge measurement. The ICT integrates the current induced in a set of coils by the magnetic field of the bunch, which is then calibrated into a charge measurement of electrons per bunch [85]. The ATF2 ICT signal was digitised synchronously with the reference cavity and dipole cavity information for these tests. The I and Q signals were charge normalised in the usual way using the reference cavity q signal in ADC counts. The reference cavity charge readings in ADCs track the ICT ATF2 charge readings in electrons per bunch very well (see Fig. 4.10 in Section 4.3.1).

Calibrations to determine k were performed at every charge step for each of the three BPMs, using a single sample at the peak of a calibration scale factor versus sample number plot, i.e., at the point of maximum cavity output. These results, shown in Fig. 3.16, demonstrated a pronounced dependence of $|k|$ on the bunch charge. Such a dependence should not exist, as k should be charge independent, but this dependence has consistently been observed [8]. This dependence could originate from electronic components saturating with higher signal levels. It is also feasible that the dipole cavity signal itself is not perfectly proportional to charge. This has implications for resolution estimates, as it means the positions calculated using these k calibration scale factors are not charge-independent.

The calibration scale factors were used to calculate the respective resolution for each step. The results are detailed in Table 3.6 and Fig. 3.17, demonstrating a clear dependence on the bunch charge. However, the results do not follow the inverse relationship expected (Eq. 3.19) if the resolution was a function of signal levels alone. This suggests resolution may have been limited by something else as charge levels were increased.

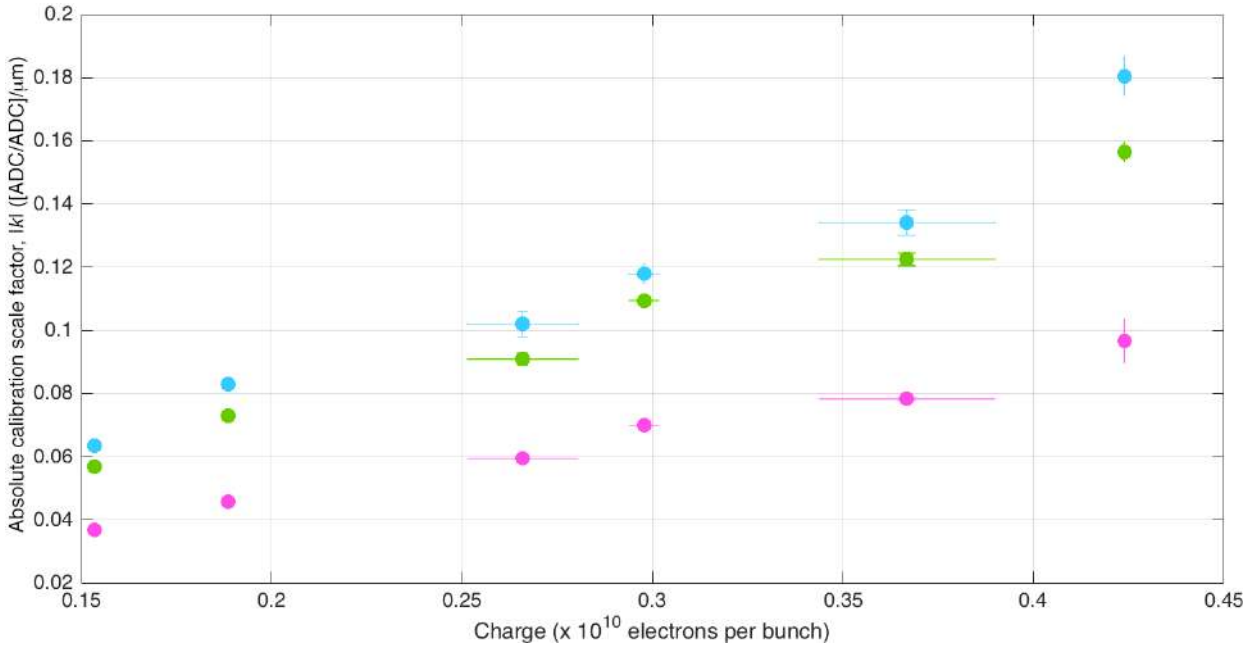

Figure 3.16: Absolute calibration scale factor, $|k|$, at IPA (blue), IPB (green), and IPC (pink) versus the mean bunch charge measured using the calibrated ATF2 ICT. Vertical error bars indicate the statistical uncertainties on $|k|$. Horizontal error bars indicate the standard deviation of the bunch charge.

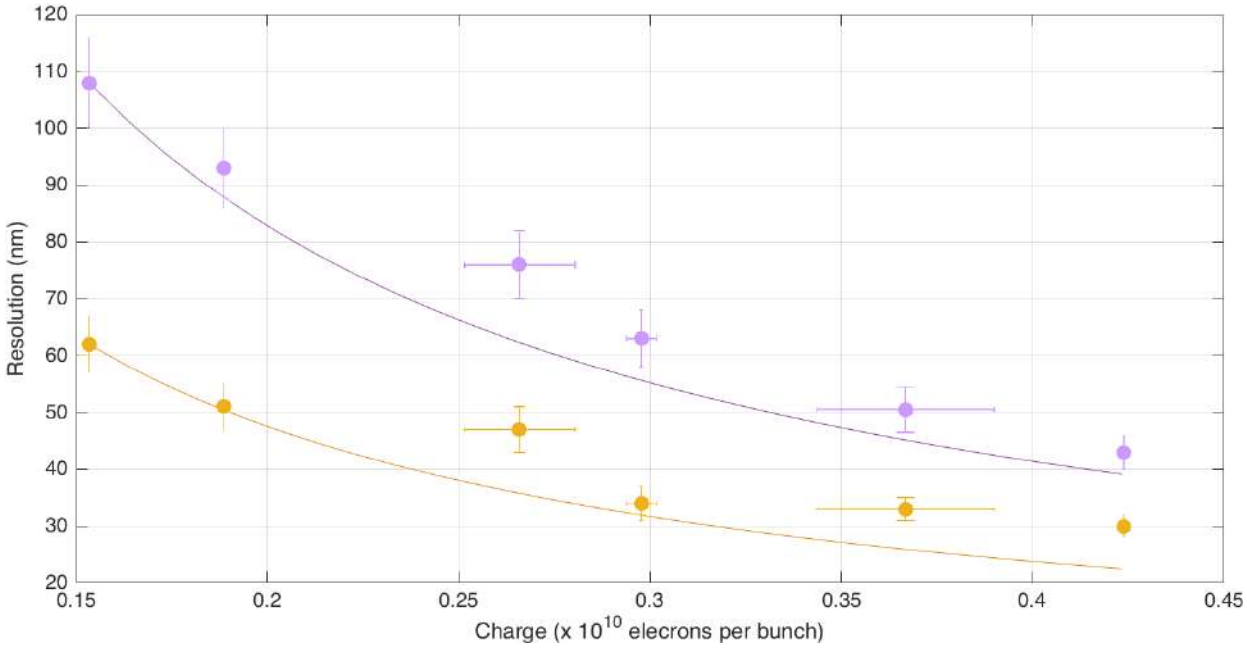

Figure 3.17: Geometric resolution versus mean bunch charge, calculated using single sampling (lilac) and integration (orange). The charge is measured using the calibrated ATF2 ICT. Vertical error bars indicate the statistical uncertainties on the resolutions. Horizontal error bars indicate the standard deviation of the bunch charge. The lines represent an inverse scaling of the resolution at 0.15×10^{10} electrons per bunch.

Table 3.6: Geometric resolution estimates using single sample and integration methods at different charge settings. Errors on the charge values indicate the errors on the mean. Errors on the resolutions indicate the statistical uncertainty.

Charge ($\times 10^{10}$ electrons per bunch)	Resolution (nm) Single-sample	Resolution (nm) Integration
0.1534 ± 0.0003	108 ± 8	62 ± 5
0.1886 ± 0.0011	93 ± 7	51 ± 4
0.2659 ± 0.0145	76 ± 6	47 ± 4
0.2978 ± 0.0039	63 ± 5	34 ± 3
0.3668 ± 0.0231	51 ± 4	33 ± 2
0.4239 ± 0.0008	43 ± 3	30 ± 2

Typical operating conditions at the ATF2 do not involve charge variations of anything like the magnitude studied in this charge scan. However, consistent resolution performance would clearly be aided by ensuring the charge levels are stable and that there are not significant charge fluctuations between data runs and their associated BPM calibrations.

3.10 Resolution versus position

If the beam is aligned within the linear operating range of the IP BPMs, the resolution performance should have no dependence on the beam position within the cavity. This was tested during a study of the effect of the ATF2 octupoles [86] in which the beam was systematically moved by small amounts in the x and y axes. Data for resolution calculations were gathered for 54 different x and y position combinations. The variable attenuators were set at 10 dB on the dipole cavity y-output signals, and 20 dB on the x-output signals.

Fig. 3.18 shows the geometric resolution results as a function of the mean offset position measured at the three BPMs in the x and y axes, integrating across 10 samples. They show no observable dependence of resolution on position. They do, however, demonstrate a large range of resolution results, varying here between ∼25 and ∼45 nm. This is representative of the typical variation observed on repeat measurements. Other possible causes of these inconsistencies in performance that make resolution results difficult to reproduce will be explored in Section 3.12.

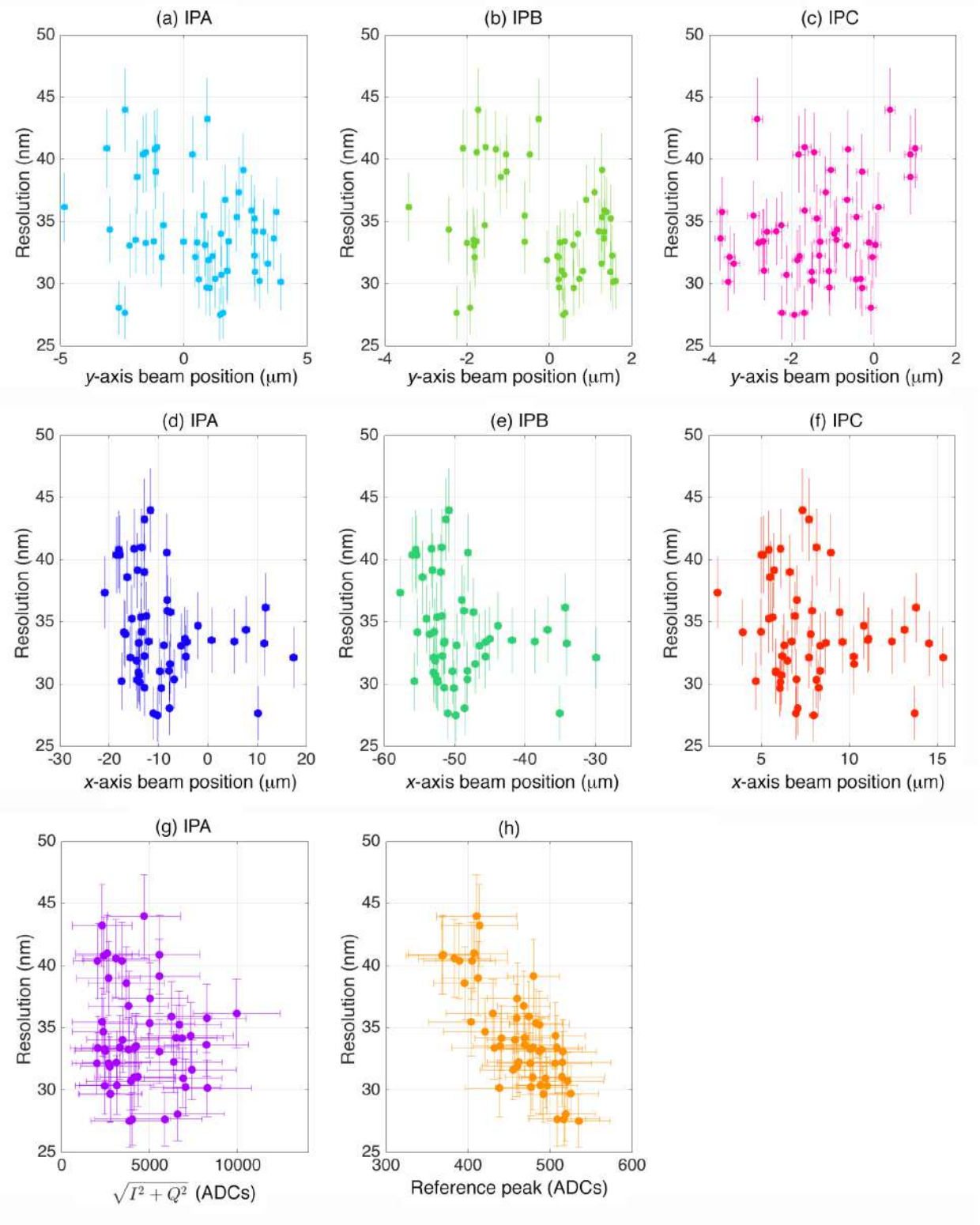

Figure 3.18: Resolution versus mean beam position measured at (a) IPA, (b) IPB, (c) IPC, in the y axis, and at (d) IPA, (e) IPB, (f) IPC, in the x axis; (g) Resolution versus the mean quadrature sum of the IPA I and Q signals, and (h) the mean reference cavity signal level. The vertical error bars indicate the statistical uncertainties on the resolutions. The horizontal error bars indicate the standard deviations of the respective x-axis parameters.

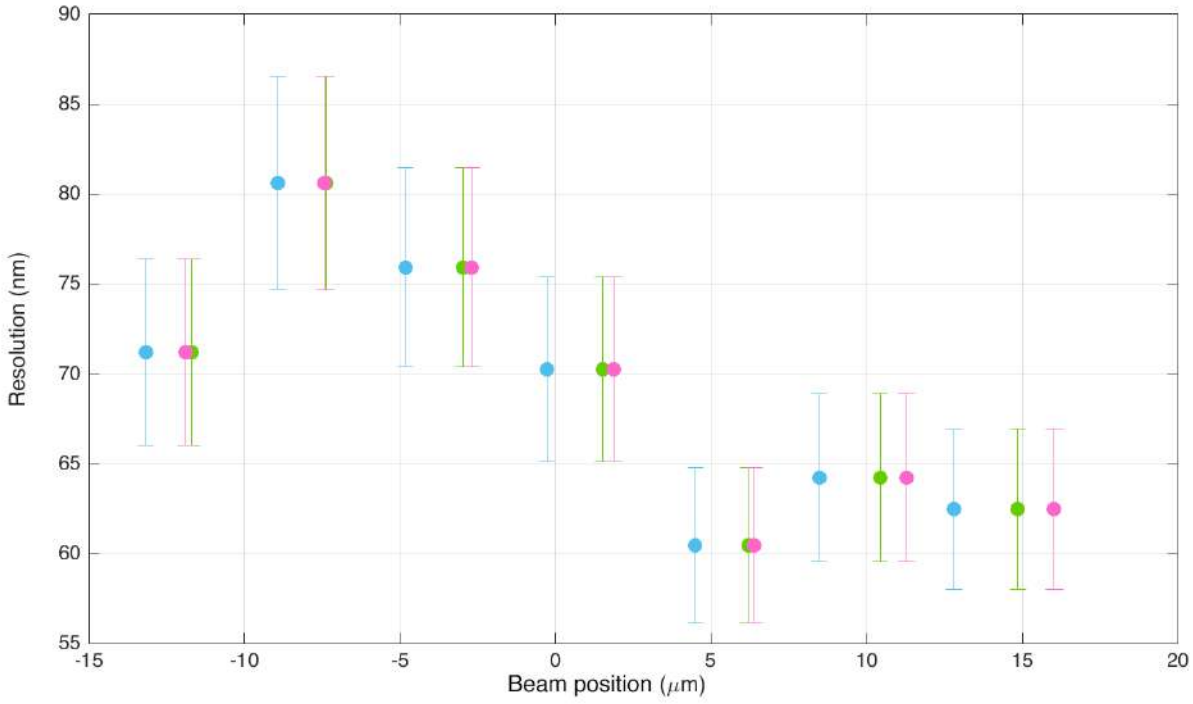

Figure 3.19: Geometric resolution versus beam position in the y-axis with 20dB attenuation on the dipole cavities measured at IPA (blue), IPB (green), and IPC (pink). The error bars indicate the statistical uncertainties on the resolutions.

A measure of the signal amplitude was calculated using the quadrature sum of the I and Q signals at IPA, shown in Fig. 3.18.g, where no clear effect on resolution is visible. Similar analysis using IPB and IPC also showed no clear dependence. Fig. 3.18.h shows the resolution versus the reference cavity signal peak, reiterating the results of Section 3.9, with the resolution estimate decreasing with increasing bunch charge. This suggests that the resolution dependence on bunch charge could be a likely cause of the variations observed across the 54 data sets.

The resolution dependence on position was also studied over a wider spread of vertical beam positions by analysing the individual steps of an AQD0FF calibration taken with 100 data points per step. 20 dB attenuation was placed on the dipole signal to keep the beam in a linear operating range, which reduced the resolution performance. The geometric resolution was calculated at each step and calibrated into positions using a fit to the overall calibration scan. Fig. 3.19 shows the resolution versus position results, again, demonstrating no conclusive position dependence. Fig. 3.20 shows the same experiment repeated at 50 dB, where the changes in position are very large. However, at attenuation levels this high, the uncertainty on the resolution makes the results indistinguishable.

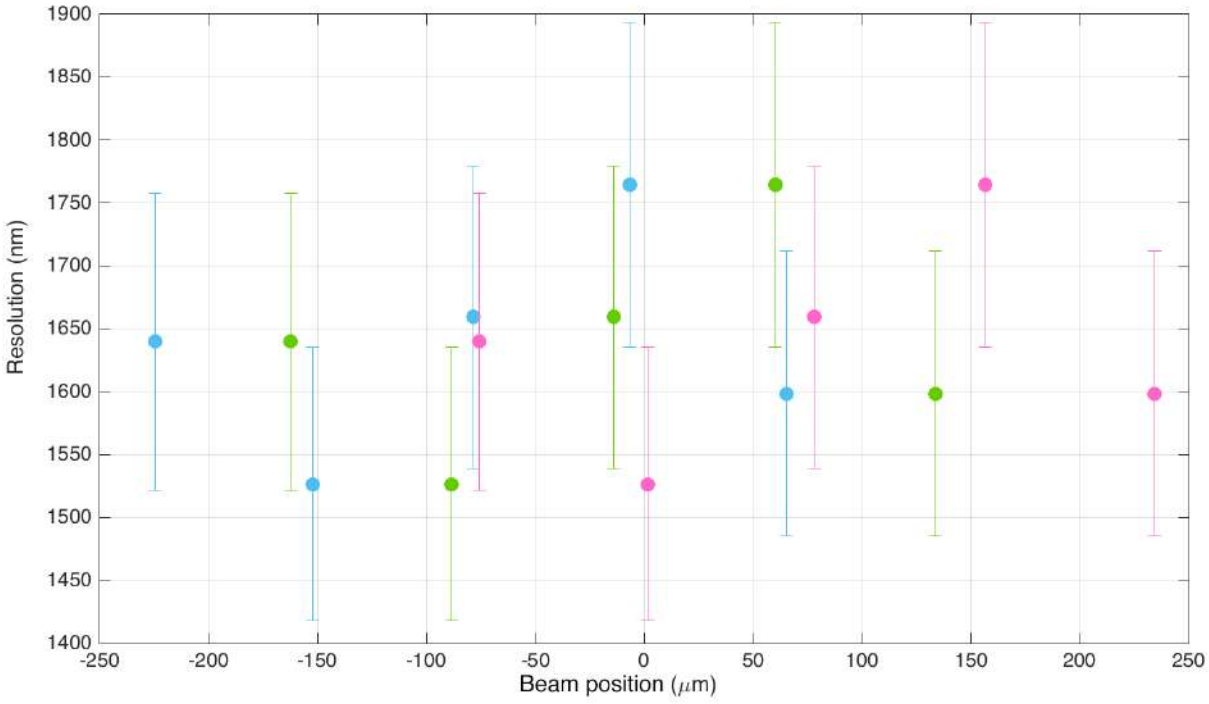

Figure 3.20: Geometric resolution versus beam position in the y-axis with 50dB attenuation on the dipole cavities measured at IPA (blue), IPB (green), and IPC (pink). The error bars indicate the statistical uncertainties on the resolutions.

3.11 Resolution with filtering

Narrow BPFs were placed on the AFT2 IP dipole cavity outputs (see Section 2.10) to mitigate the effects of the oscillatory waveform in the I and Q signals. The smoothing of the waveform reduced the likelihood of saturation, making it feasible to operate at higher bunch charges and lower attenuations where resolution performance was improved. A cleaner pulse shape also made it easier to identify the peak of the waveforms by eye. However, it was important to quantify the effect this filtering had on the resolution.

The I and Q waveforms with filters are shown in Fig. 3.21. These data were gathered with 10 dB attenuation at a charge of $\sim 0.45 \times 10^{10}$ electrons per bunch to be comparable to studies without filtering. Fig. 3.22 shows the calibration scale factor, k, as a function of sample number. The peak k corresponds to sample 52, motivating this sample as optimal for the best signal-to-noise ratio. This optimal sample is $\sim$12 samples after the pulse begins. This is in contrast to the filter-free data (Fig. 3.6), where the optimal sample was $\sim$4 samples after the pulse began. This is a consequence of the filtering smearing out the waveform.

Fig. 3.23 shows the resolution along the pulse using a single sample and geometric and 3-parameter fitting methods. The shape reflects the degradation of resolution as the signal-

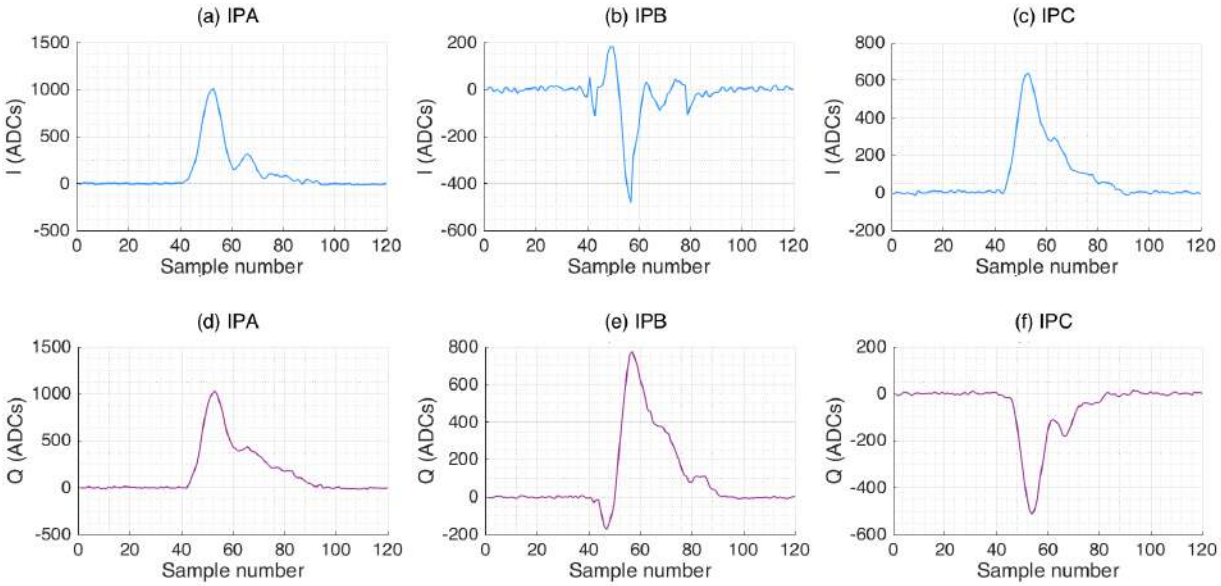

Figure 3.21: IP BPM signals in ADCs versus sample number for one example waveform in y with BPFs installed on the dipole cavity outputs; (a) IPA I, (b) IPB I, (c) IPC I, (d) IPA Q, (e) IPB Q, (f) IPC Q.

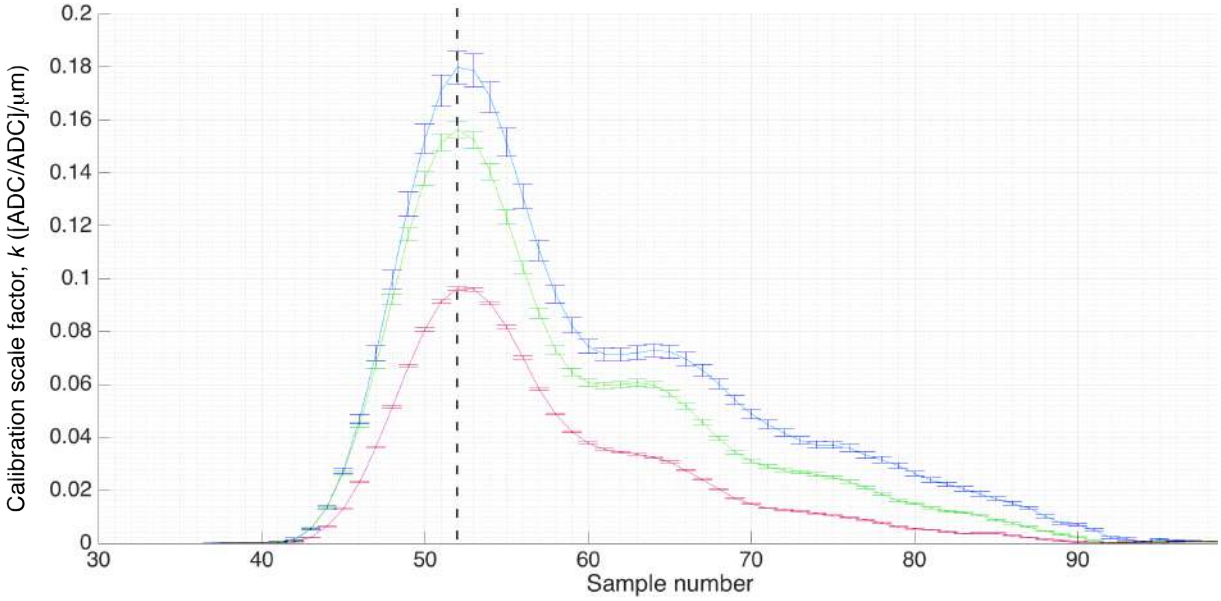

Figure 3.22: Calibration scale factor, k, versus sample number, measured at IPA (blue), IPB (green) and IPC (pink). The lines join the data points, with error bars indicating the statistical uncertainties on k. Optimal sample 52 is indicated by the dashed line.

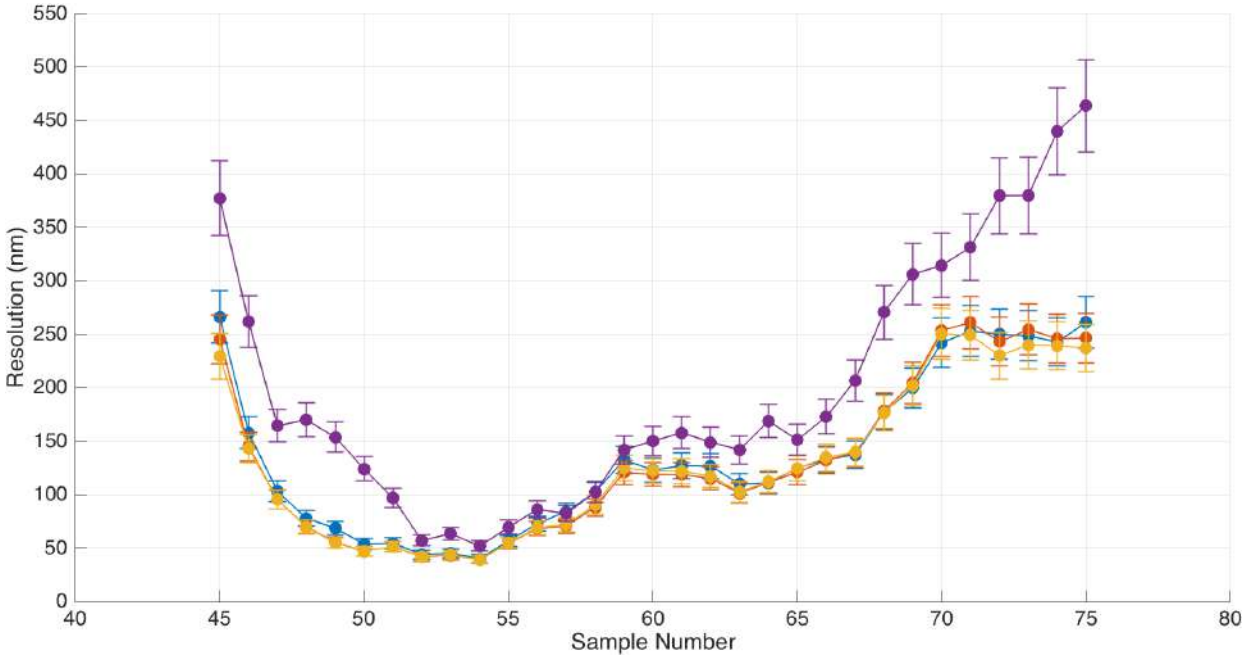

Figure 3.23: The estimated resolution performance versus sample number calculated using the geometric method (blue), and the 3-parameter fitting method predicting at IPA (red), IPB (yellow) and IPC (purple). The lines connect the data points. The error bars indicate the statistical uncertainty on the resolutions.

to-noise worsens with the pulse's decay. It also indicates a worse resolution using samples anywhere before the peak of k, which is as expected, as the signal is all noise before the peak. Fig. 3.24 shows the geometric resolution results for different integration windows. There is always a significant reduction in the resolution by integrating, with the lowest resolution of 27 $\pm$ 2 nm integrating between samples 49 and 58.

Table 3.7 details resolution estimates using all the methods of resolution analysis discussed in this chapter, and both single sample and integration. Like previously presented no-filtering data analysis (Table 3.4), integration had the biggest impact in lowering the resolution estimate. Multi-parameter fits reduced the resolution estimate further; particularly the inclusion of Q' information with the 5-parameter fit. The overall best results with an 11-parameter fit are very similar to those found without filtering at ∼20 nm.

Despite these data being taken at a similar bunch charge, the best "useable for feedback" single-sample geometric resolution estimates of ∼40 nm were better than the equivalent ∼50 nm results without filtering. This improvement may be a consequence of the signals being effectively integrated in hardware by the filtering, as demonstrated by the smoothing of the waveform. This makes filtering a good way to improve resolution for feedback with the current FONT firmware, which only allows single sample points to be utilised.

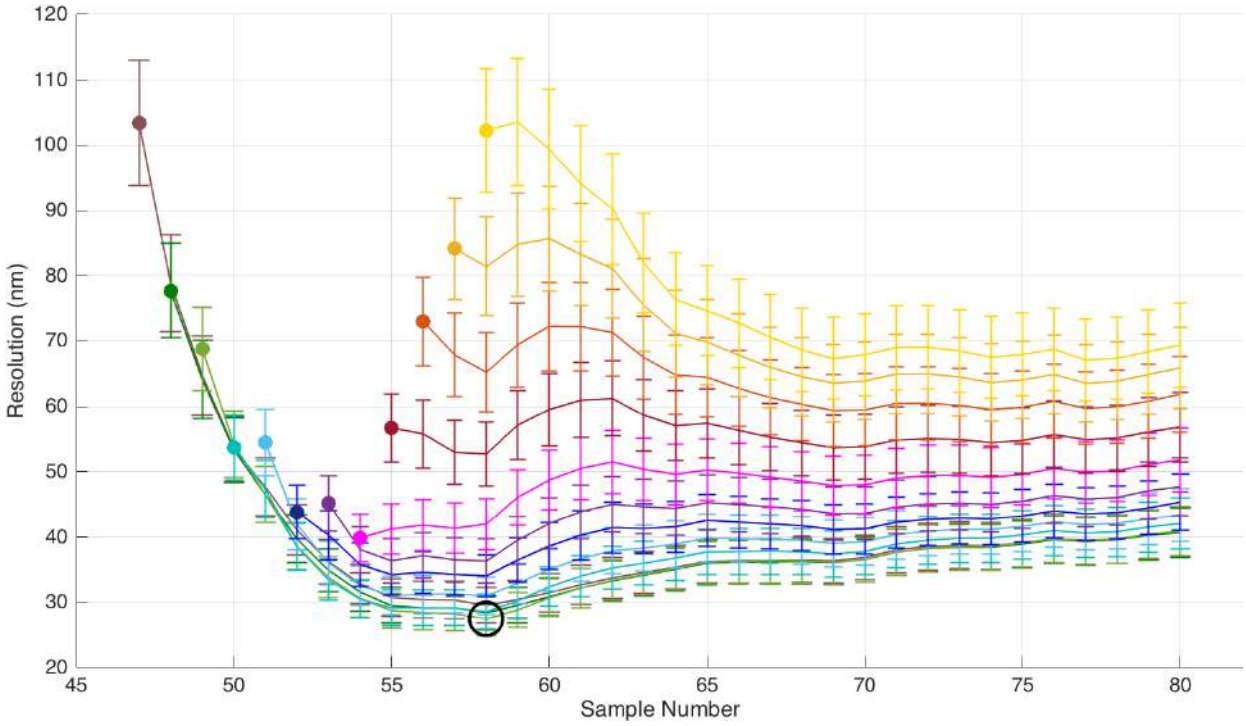

Figure 3.24: Geometric resolution versus the last sample number in the integrated sampling window. Each colour represents a different starting sample for the integration, defined by the solid points at the start of each line, for which the resolutions have been calculated using that single sample. The lines connect the data points. The error bars indicate the statistical uncertainty on the resolutions. The black circle indicates the minimum resolution, 27 ± 2 nm, integrating between samples 49 and 58.

Table 3.7: Vertical position resolution estimates using geometric and fitting methods and using both a single sample (sample 54) and an integration window (samples 49 to 58). The uncertainty on all single sample resolution estimates is ±3 nm. The uncertainty on all integration resolution estimates is ±2 nm.

		Single sample resolution (nm)			Integration sample resolution (nm)		
Resolution method	Number of fit parameters	Predicting at IPA	IPB	IPC	Predicting at IPA	IPB	IPC
Geometric	-	40	40	40	27	27	27
Fitting	3	39	39	52	26	26	30
Multi-parameter	5	38	38	26	23	22	20
Multi-parameter	6	37	38	26	23	22	20
Multi-parameter	11	35	35	23	20	21	15

3.12 Rolling resolution studies

It is important for resolution estimates to be reproducible. The results in the previous sections are representative of the best-observed performance, but geometric integrated resolution estimates have been observed to vary between ∼25 nm and ∼45 nm with no operator changes (Fig. 3.18). All data runs can ultimately be reduced to the ∼20 nm level by utilising multi-parameter fits. But some resolution data runs have demonstrated ∼20 nm resolution with just an integrated geometric method, the addition of more complicated fits having very little impact (see Table 3.4).

To isolate the source of these inconsistencies, a detailed resolution study was performed on a 3400-trigger data set compiled from three successive data runs; a 400-trigger, 2000-trigger, and 1000-trigger run. There was a 67-second gap between the first two runs and an 8-minute gap between the last two. The dipole attenuation was 20 dB and the charge was $\sim 0.5 \times 10^{10}$ electrons per bunch. No changes were made to the accelerator set-up, the BPM alignment, attenuation or signal digitisation process. These conditions did not rule out the possibility of beam position drift, charge drifts, charge jumps, or other machine-based instabilities. However, it provided the cleanest foundation for studying resolution estimate variations over time.

Fig. 3.25 shows the geometric resolution calculated using shifting 200-trigger subsets of the data. The resolution was calculated by integrating across 12 samples. Results range from 18 ± 1 nm to 35 ± 2 nm. The biggest deviation occurs for 200-trigger blocks that overlap between the second and third subsets, suggesting some significant difference between the two. There are also smaller oscillations and a slight mean degradation of the resolution with time.

Variations in charge

Fig. 3.26 shows the reference cavity signal, q, level for all 3400 triggers. A jump is visible at around trigger 2400. This corresponds to the intersection of the second and third subsets of the data, suggesting a charge drift in the 8 minutes between those two data sets being recorded. A significant disjunction in charge levels will result in highly non-linear behaviour, which is reflected in the spike in the resolution estimate for analysis subsets that include it. It was shown in Section 3.9 that the resolution and calibration scale factors demonstrate a dependence on charge levels. This may explain the slightly higher mean resolution estimates after the transition at trigger 2400, and the gradual worsening in resolution across the data set as the charge levels gradually drift down.

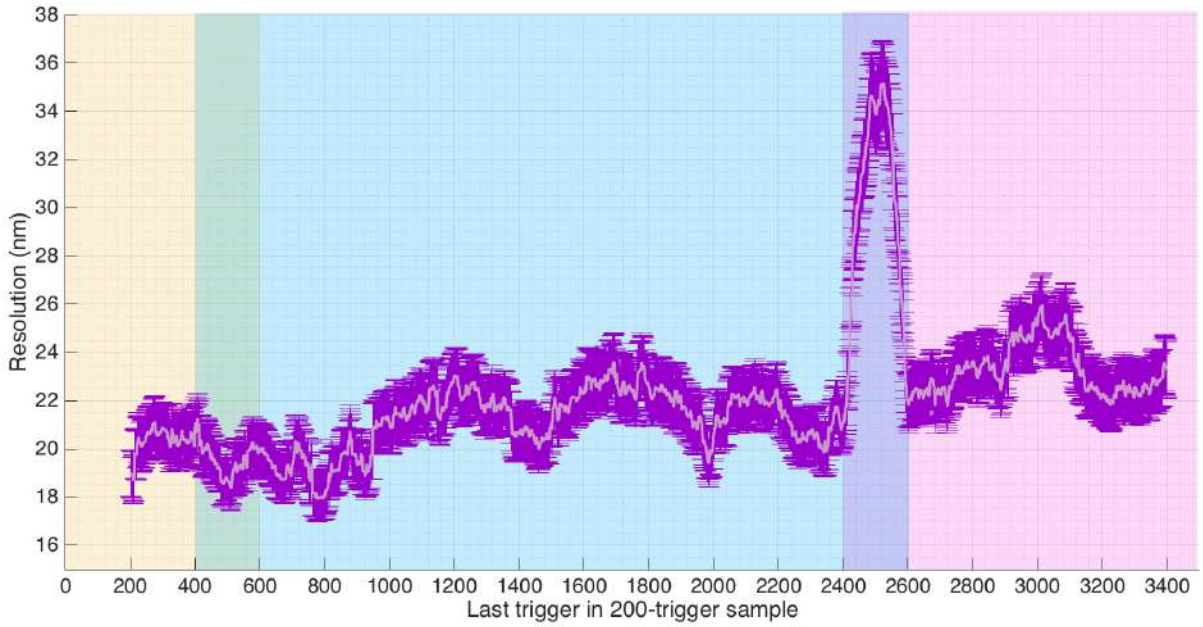

Figure 3.25: Geometric resolution versus the last trigger in the 200-trigger subset of a 3400-trigger data set used to calculate the resolution. The error bars in dark purple indicate the statistical uncertainties on the resolutions. The complete data set is a combination of three smaller data runs taken sequentially, indicated by the different coloured regions: data run 1 (yellow), data run 2 (blue), and data run 3 (pink). Green and lilac regions represent analysis subsets that traverse data runs.

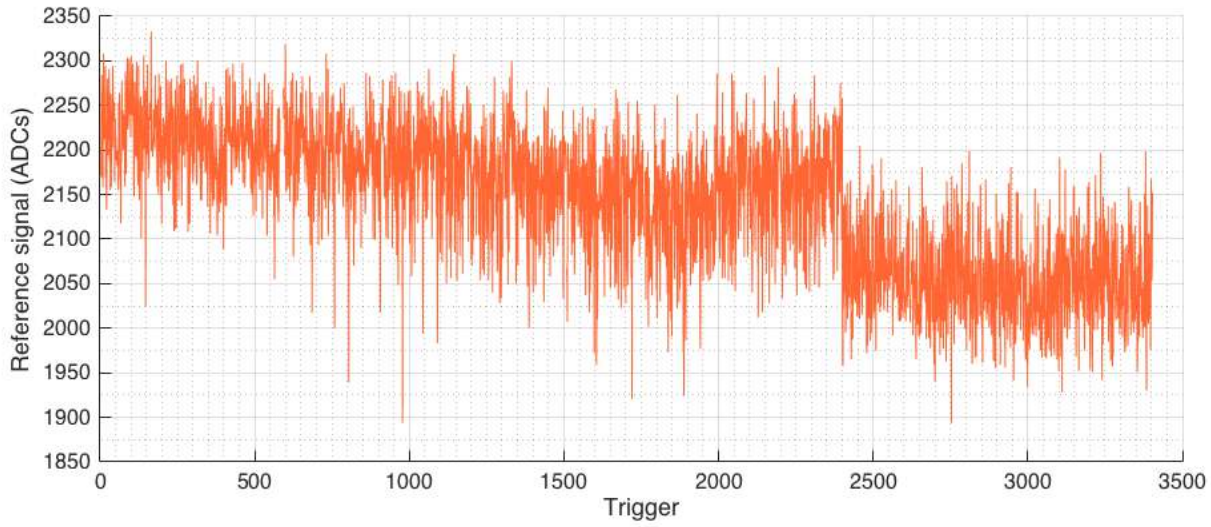

Figure 3.26: Reference cavity signal, q, versus trigger across 3400 sequential triggers.

Variations in θ_{IQ}

The same BPM calibrations were used for all the resolution analysis in Fig. 3.25. If the phase angle θ_{IQ} has changed since the calibration was performed, position information may not be perfectly rotated into I'. To check, θ_{IQ} was calculated for the subsets of data in this study. For an ordinary data run the spread in I and Q is due to the natural beam jitter, so the values will traverse a much smaller range than they do for a calibration, where the beam is intentionally moved using the upstream magnet QD0FF. But a fit can still be applied to determine θ_{IQ} (see Section 2.6). Differing θ_{IQ} values between the data and calibration indicate the calibration may no longer be valid.

Fig. 3.27 shows the θ_{IQ} calculated for every 200-trigger subset. There is some θ_{IQ} jitter and deviation from the calibration θ_{IQ}, with a maximum phase difference of $\sim$0.04 radians (approximately 2 degrees) at all three BPMs. The θ_{IQ} jitter for IPC in Fig. 3.27.c is noisier, because the position jitter was smaller at IPC, so results were more adversely affected. The transition between the second and third sub-sets of data at trigger 2400 is visible as a step, with the average θ_{IQ} level increasing $\sim$0.02 radians at all three BPMs. These drifts and steps in θ_{IQ} will contribute to variations in resolution performance.

Fitting out variations

If the different fitting methods in sections 3.4 and 3.5 are indeed addressing errors in the calibration scale factor, θ_{IQ} rotation, charge variation, etc., then the inconsistencies presented in this rolling resolution study should disappear when these methods are applied.

Fig. 3.28 shows the results of the rolling resolution study using different fits. The transitional peak due to the charge jump at trigger 2400 is reduced by an initial 3-parameter fit. Charge changes would result in incorrect calibration scale factors, which are fitted out with this method. The fitting of Q' values in the 5-parameter fit smoothes results further at all three BPMs by incorporating position information that has not been successfully rotated into I'. The final inclusion of charge with the 6-parameter fit removes the peak at trigger 2400 entirely, along with reducing the overall degradation of the resolution with time, likely due to the charge drift. More complex fits including x-information are not presented, as they made no substantial difference.

The final 6-parameter fit is replotted in Fig. 3.29 with the original geometric resolution method in Fig. 3.29.a to compare. The resolution at all three BPMs are now in good agreement, regardless of which 200-trigger subset is selected. Using IPC to predict still results in a lower overall result with the multi-parameter fit, but the geometric, IPA and IPB fitting results all estimate a resolution of $\sim$20 nm.

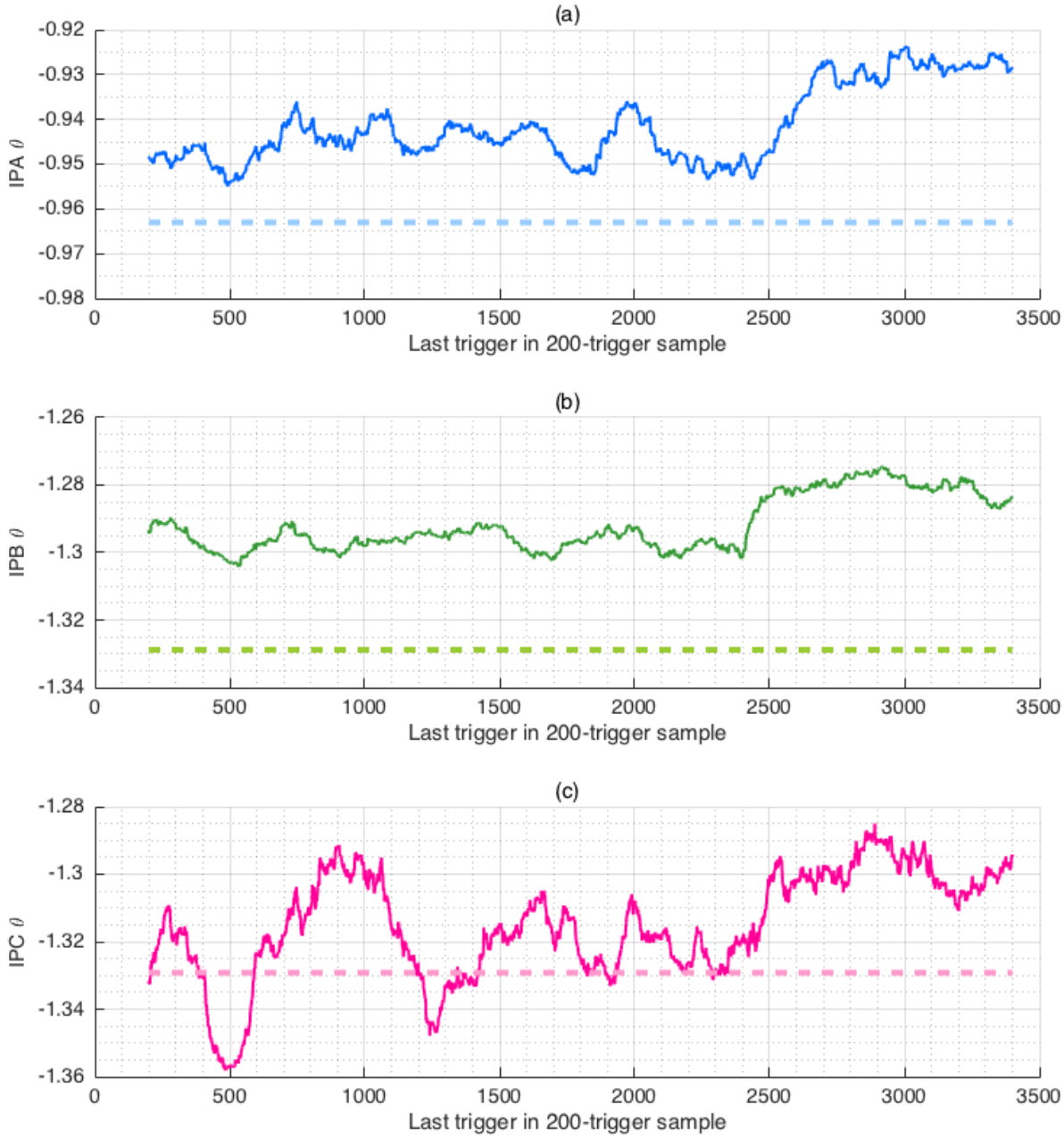

Figure 3.27: θ_{IQ} versus the last trigger in the 200-trigger subset of a 3400-trigger data set used for calculating θ_{IQ}. Measured at (a) IPA, (b) IPB, and (c) IPC. The θ_{IQ} values calculated from the respective BPM calibrations are plotted as dashed lines.

This study has demonstrated that variations observed in the geometric resolution estimates can be attributed to inaccurate calibrations, charge drifts and charge jumps. These inconsistencies are addressed by different multi-parameter fits, reducing the resolution estimates to a common level. In the absence of these non-linearities, the geometric and fitting methods should agree.

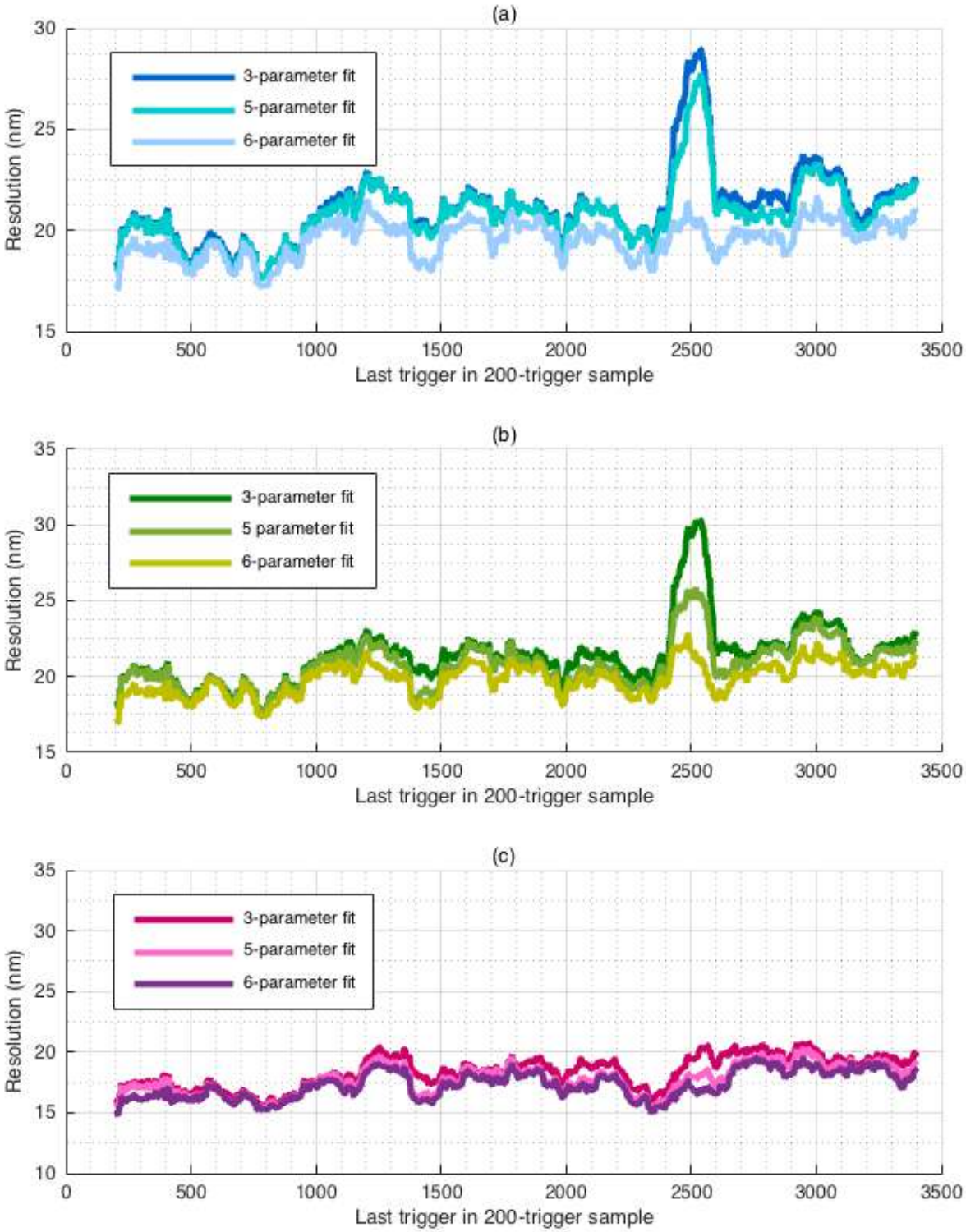

Figure 3.28: Resolution versus the last trigger in the 200-trigger subset of a 3400-trigger data set used for calculating the resolution. Measured at (a) IPA, (b) IPB, and (c) IPC. Legends indicate the number of parameters in the different fits used (see Table 3.2 for specific parameters).

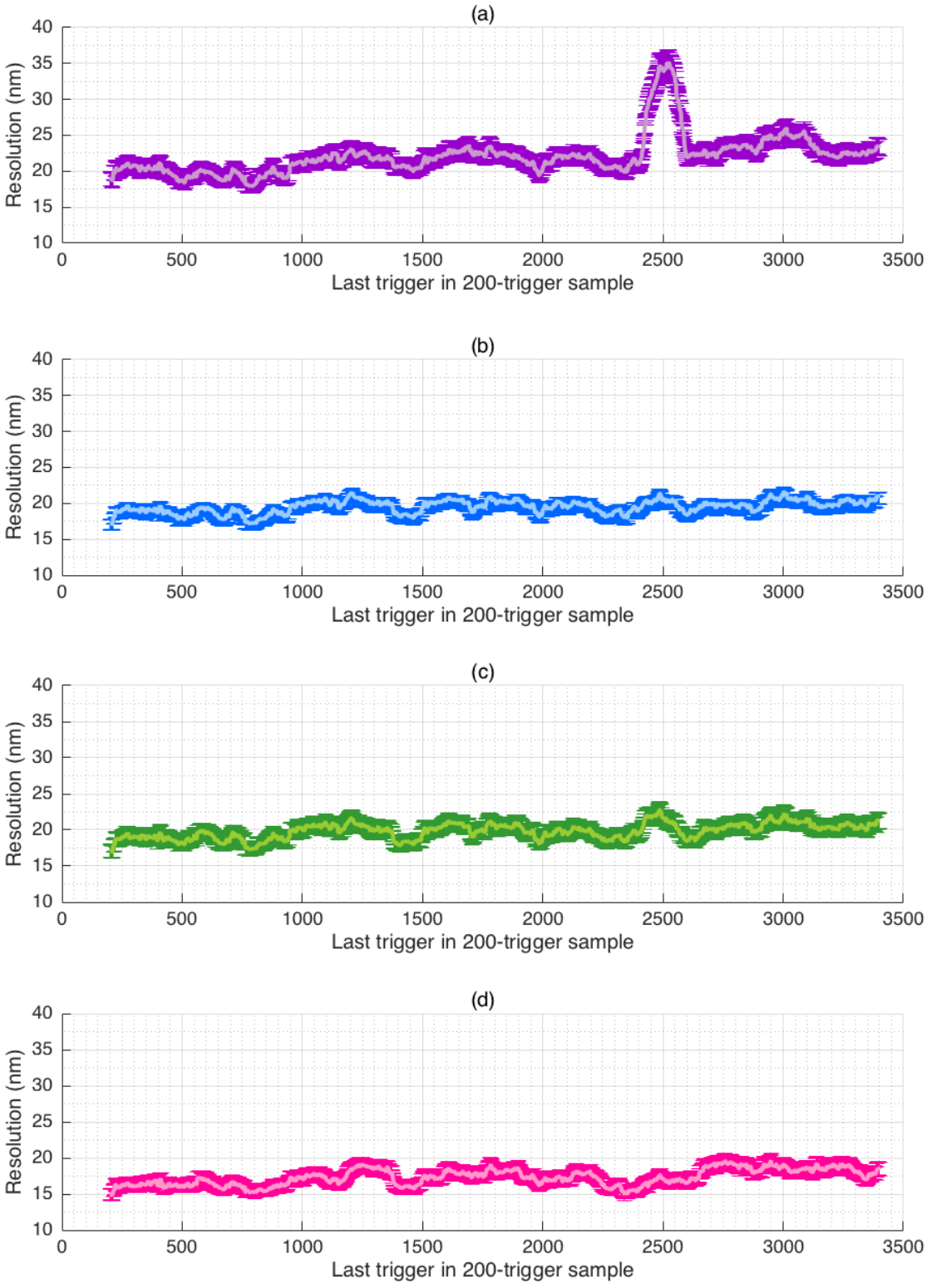

Figure 3.29: Resolution versus the last trigger in a 200-trigger subset of a 3400-trigger data set used for calculating the resolution. Calculated using (a) a geometric method, and (b) 6-parameter fitting method predicting at IPA, (c) IPB, and (d) IPC. The error bars in darker shades indicate the statistical uncertainties on the resolutions.

3.13 Summary

This chapter explored the resolution performance of the three ATF2 IP BPMs. The experimental set-up involved operating with a high-beta optics beam at a typical charge of $\sim 0.5 \times 10^{10}$ electrons per bunch to pass the beam through the linear operating range of all the BPMs simultaneously. Two FONT boards were utilised to digitise both vertical and horizontal information from the cavity BPMs.

A geometric analysis method using the known BPM separations estimated a vertical position resolution of 49 ± 1 nm. This result was reduced by ∼10 nm by applying multi-parameter fits to determine the resolution, incorporating Q', charge, and x-axis information in addition to fitting for calibration scale factors. The addition of Q' information was found to make the largest difference, suggesting the θ_{IQ} rotation is not successfully transferring all the position information into I', which is then used to calculate positions.

Resolution performance was found to have a strong dependence on which sample number within the digitised waveform was used, with earlier samples producing the best results. Integrating across the waveform instead of using a single sample point resulted in a significant improvement in resolution estimates. A best geometric method resolution estimate of 21.5 ± 0.4 nm was calculated by integrating across 12 samples. This was reduced to 17.5 ± 0.4 nm using integration sampling and an 11-parameter fit.

The resolution and calibration scale factor were found to scale linearly with dipole cavity attenuation between 20 and 50 dB settings. Non-linear behaviour was observed at both 0 and 10 dB, indicating electronic components in the signal processing may be saturating when signal levels are high. The calibration scale factor was also found to scale with the charge, despite the charge-normalising analysis process, which should result in no dependence. Consequently, the resolution was also found to have a strong reliance on the bunch charge. No resolution dependence on beam position was observed.

BPFs were installed in the IP processing electronics with the hopes of mitigating the unwanted oscillatory waveform in the dipole cavity pulses. This smoothed the waveform out and resulted in an optimal sampling location later in the pulse. The single-sample resolution results were also improved ∼10 nm on results without filtering, due to the filtering effectively integrating the waveform in hardware. This suggests BPF-operation to be useful for improving resolution for feedback operation, where FONT firmware is currently only able to make use of a single digitised sample point.

Finally, the resolution reproducibility was investigated using a rolling resolution study on an extended data set, during which user-controllable conditions were kept constant. The

geometric analysis results demonstrated a variation in resolution estimate of between 18 ± 1 nm and 35 ± 2 nm, depending on which subsets of triggers were used for analysis. Jumps in the bunch charge and drifts in θ_{IQ} were isolated as potential sources of degradation to resolution performance. These inconsistencies across the data run were removed by applying a 6-parameter fitting method, confirming the multi-parameter fits are indeed addressing inaccurate calibrations and charge-dependences in the data. In the absence of these non-linearities the geometric resolution estimate is in agreement with multi-parameter fitting methods.

Chapter 4

IP BPM sensitivity to phase jitter

Any mechanism - whether beam-based or hardware based - that results in trigger-to-trigger variations in the relative phase delay of different signals could compromise optimal performance for beam position measurements using the IP BPM system. Sensitivity to phase was previously found to cause resolution limitations in the stripline BPM-based FONT feedback system upstream in the extraction line at the ATF2 [53]. It was therefore deemed valuable to check the IP BPM set-up for similar phase-related sensitivities. This chapter will describe these studies, including a test of position sensitivity to beam-based bunch phase and detailed studies of the reference limiter as a source of unwanted phase jitter.

4.1 Bunch-phase jitter

Synchrotron oscillations in the damping ring at the ATF2 caused jitter in the arrival time of bunches with respect to the 714 MHz master oscillator. This could have manifested in the IP system as a phase jitter in the GHz-level cavity BPM signals relative to the local oscillator (LO) used to down-mix them in the first stage of the processing electronics. Consequently there would have been a bunch-to-bunch phase difference, ϕ_{LO}, presented in Eq. 2.10 and 2.11, between the LO signals and the cavity signals. The IP BPM signal processing system at the ATF2 was designed to be insensitive to jitter in the bunch phase (see Section 2.4). However, if phase sensitivity was somehow coupled into the processing output signals, it could have degraded position resolution.

4.1.1 Experimental set-up

To test for position sensitivity to the bunch phase with regard to the LO, the LO phase was varied relative to the BPM cavity output signals using a variable phase shifter placed on the 714 MHz signal (Fig. 4.1). With a test signal, the phase shifter was measured to generate

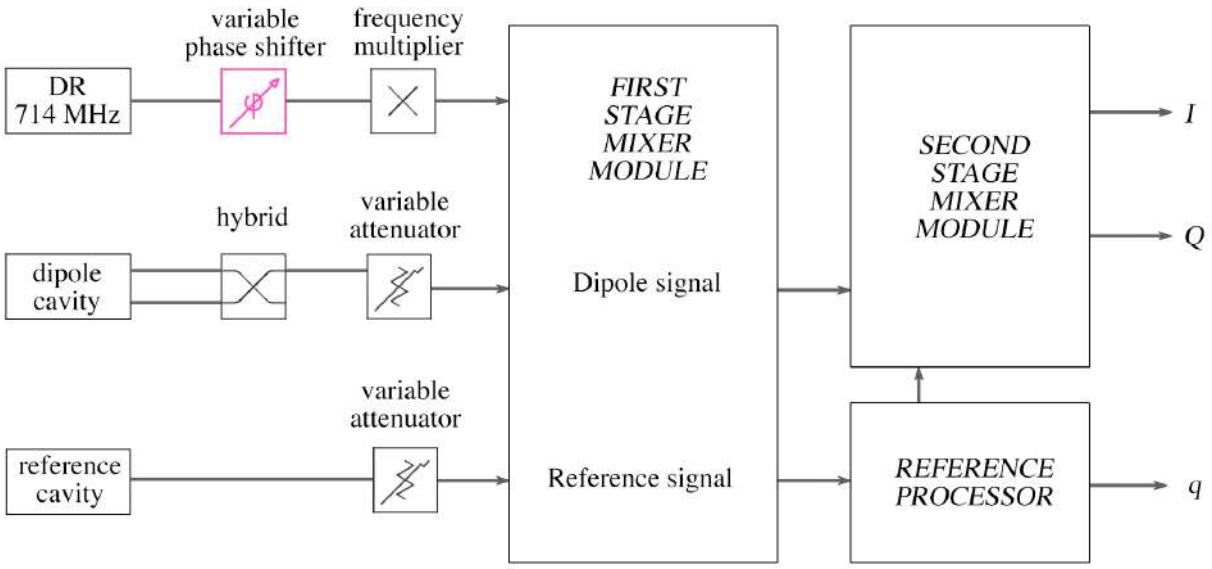

Figure 4.1: Block diagram of the IP BPM electronic processing system, with a variable phase shifter introduced to alter the 714 MHz damping ring LO phase relative to the bunch phase.

a 15° phase shift at 714 MHz over 16 turns. For down-mixing the y-plane cavity signals at ∼6.426 GHz, the LO 714 MHz was frequency multiplied eight times to be 5.712 GHz, i.e. 714 MHz away from the cavity signal resonant frequency. At this frequency, the phase shift on the LO signal corresponded to 7.5° per turn of the phase shifters in the set-up.

The beam position was measured at IPB at a charge of 0.47×10^{10} electrons per bunch with single-bunch trains, recording 100 triggers per measurement. A high dipole cavity attenuation of 30 dB was used to make sure phase shift-related changes in the position measurement would not be obscured by the natural beam jitter, which for this study was ∼200 nm with 0 dB attenuation at IPB. The BPM was calibrated, and jitter runs were taken in which the phase was shifted successively in increments between 0 and 120°. The experiment was repeated using a 50 dB dipole cavity attenuation to increase the dynamic range so the scan could traverse a wider phase shift range up to 240°.

4.1.2 Calculating maximum position sensitivity to phase

Mean positions were calculated for each phase setting for the 30 dB study (Fig. 4.2.a) and the 50 dB study (Fig. 4.2.b). Each data set was fitted with an equation of the form:

$$y = a\cos(bx + c) + d. \tag{4.1}$$

The maximum gradient of the fit in nanometres per degree was then used to estimate the maximum apparent position variation that could be due to phase jitter (Table 4.1),

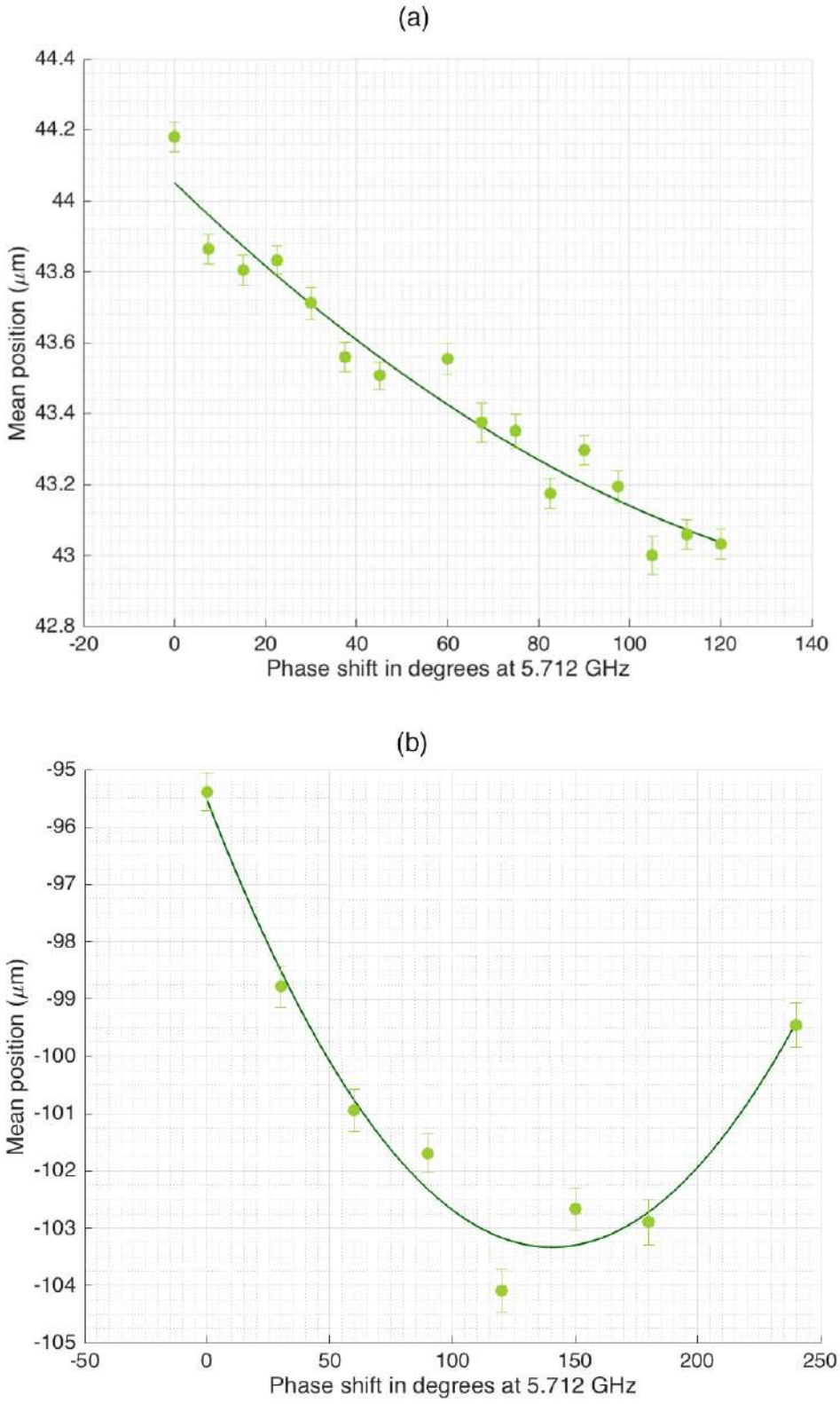

Figure 4.2: Mean position versus phase shift of the LO signal relative to the bunch phase measured at IPB with (a) 30dB dipole attenuation, and (b) 50 dB dipole attenuation. A fit of the form detailed in Eq. 4.1 is plotted as a solid line.

Table 4.1: Waveform equation fits to the 30 and 50 dB data shown in Fig. 4.2. The maximum position sensitivity on phase and that result extrapolated to 0 dB attenuation. Errors are propagated from uncertainties on the fit parameters.

Dipole cavity signal attenuation (dB)	30	50
Wave equation fits	$y = 43\cos(-0.0012x + 35) + 86$	$y = 640\cos(0.0011x + 22) + 530$
Maximum position sensitivity on phase (nm/degree)	50 ± 10	710 ± 30
Maximum position sensitivity on phase at 0 dB attenuation (nm/degree)	1.7 ± 0.4	2.2 ± 0.1

demonstrating a maximum sensitivity of 2.2 ± 0.1 nm per degree using the 50 dB study extrapolated to at 0 dB. This result is in agreement with the result at 30 dB.

4.1.3 The ATF2 bunch phase variation

The RMS train-to-train bunch phase variation at the ATF2 was previously measured to be 0.49° of 714 MHz [53]. This phase jitter corresponds to 3.92° at 5.712 GHz. It is therefore possible, using the larger phase-sensitivity estimate from the 50 dB data set in Table 4.1, that up to 8.6 ± 0.4 nm of apparent position jitter measured in the IP BPM system could be due to bunch phase jitter. This sensitivity to bunch phase jitter at the IP will become significant in the future as the ATF2 IP system pushes towards achieving nanometre-level resolution capabilities.

4.2 Reference limiter phase jitter

The limited reference signal followed a different route through the processing electronics compared with the reference diode and the dipole cavity signals (Fig. 4.3), and as such was slightly delayed relative to them on entering the second stage mixer module. This phase delay was accounted for by a $\Delta\phi$ term in the reference processor output in Eq. 2.14, which contributed, along with other phase and frequency-dependent terms to the θ_{IQ} phase angle (defined in Eq. 2.18) between the final output I and Q signals.

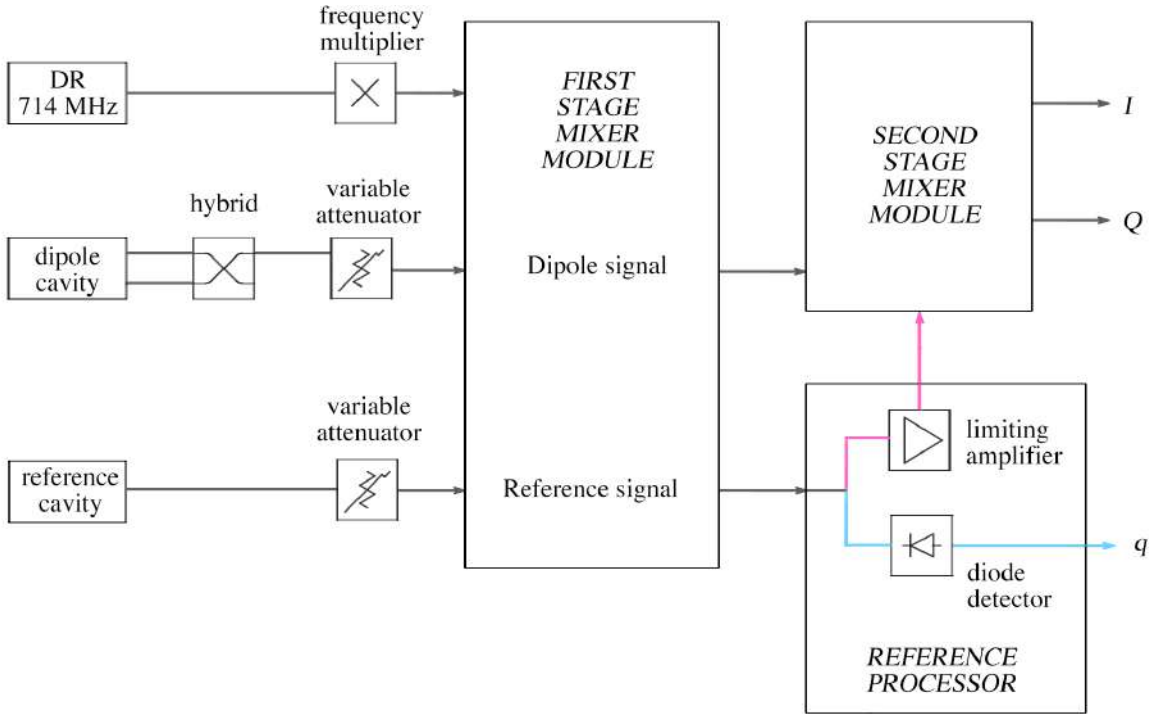

Figure 4.3: Block diagram of the IP BPM processing system. The different paths of the charge diode signal q (blue) and limited reference signal (pink) into the second stage mixer module are highlighted within the reference processor.

If the delay introduced by the limiting amplifier in the reference processor (Fig. 4.3) varied trigger to trigger, there would be a phase jitter between the down-mixed dipole and reference cavities mixed in the second stage. This would be visible as a rotational spread of the data points in the θ_{IQ} angle calibration plot and could be incorporated as a phase delay term, $\delta_{\theta_{IQ}}$ in the I' and Q' analysis:

$$\begin{aligned} I' &= I\cos(\theta_{IQ}+\delta_{\theta_{IQ}}) + Q\sin(\theta_{IQ}+\delta_{\theta_{IQ}}), \\ &\propto q\,y. \end{aligned} \tag{4.2}$$

$$Q' = -I\sin(\theta_{IQ}+\delta_{\theta_{IQ}}) + Q\cos(\theta_{IQ}+\delta_{\theta_{IQ}}). \tag{4.3}$$

The final measurement of the beam position offset, y, defined in Eq. 2.27, would then have a dependence on this additional phase delay:

$$y \propto \frac{I}{q}\cos(\theta_{IQ}+\delta_{\theta_{IQ}}) + \frac{Q}{q}\sin(\theta_{IQ}+\delta_{\theta_{IQ}}). \tag{4.4}$$

Using the small angle approximations $\sin\delta_{\theta_{IQ}} \sim \delta_{\theta_{IQ}}$ and $\cos\delta_{\theta_{IQ}} \sim 1$,

$$y \propto \frac{I'}{q} + \frac{Q'}{q}\delta_{\theta_{IQ}}. \tag{4.5}$$

Thus if the limiting amplifier in the reference processor was introducing varying amounts of phase delay, it could be coupled into position through the Q' signal. Without this additional Q' term, calculated positions would have a jitter characterised by the standard deviation of the distribution of limiting amplifier phase noise.

4.2.1 BPM calibration phase distributions

The purpose of this study was to test for the existence of a significant limiter phase jitter, which would be discernible as a rotational distribution in a $\frac{Q}{q}$ versus $\frac{I}{q}$ calibration plot used to determine θ_{IQ}. Phase jitter is distinguishable from beam position jitter and angular beam jitter, all illustrated in Fig. 4.4. Beam position jitter causes data distributions along the I' axis, which runs parallel to a global fit to the data. Angular beam jitter causes a spread along the Q' axis, and could most easily be confused with phase jitter in a calibration. However, angular jitter distributions would be independent of location in IQ space, and would not form the distinctive bow tie-like shape caused by phase jitter.

Fig. 4.5 shows an example IPB calibration $\frac{Q}{q}$ versus $\frac{I}{q}$ plot demonstrating clear phase jitter, with a rotational distribution in the data points, becoming smaller close to the centre of rotation. These data were taken with 30 dB attenuation on the dipole signal and at a charge of 0.7×10^{10} electrons per bunch. For this study the IP mover system was fully operational, so the calibration was performed by moving the IP BPM mover, rather than steering the beam. The calibration consisted of nine mover steps with 30 triggers recorded per step.

A large number of calibration runs under different beam conditions and at all three IP BPMs were found to display this characteristic θ_{IQ} spread to different extents. The IPB calibration presented here was chosen for preliminary analysis because the effect was particularly pronounced.

4.2.2 Calculating the local phase angle

The θ_{IQ} for a calibration was determined from a global fit to all the data, as described in Chapter 2. For this study, a "local" θ_{IQ} was also determined for each data point individually. The phase jitter was then estimated using the standard deviation of the local θ_{IQ} values at each step in the calibration. The local θ_{IQ} was calculated using:

$$\text{local}\,\theta_{IQ} = tan^{-1}\Big(\frac{Q - Q_0}{I - I_0}\Big), \tag{4.6}$$

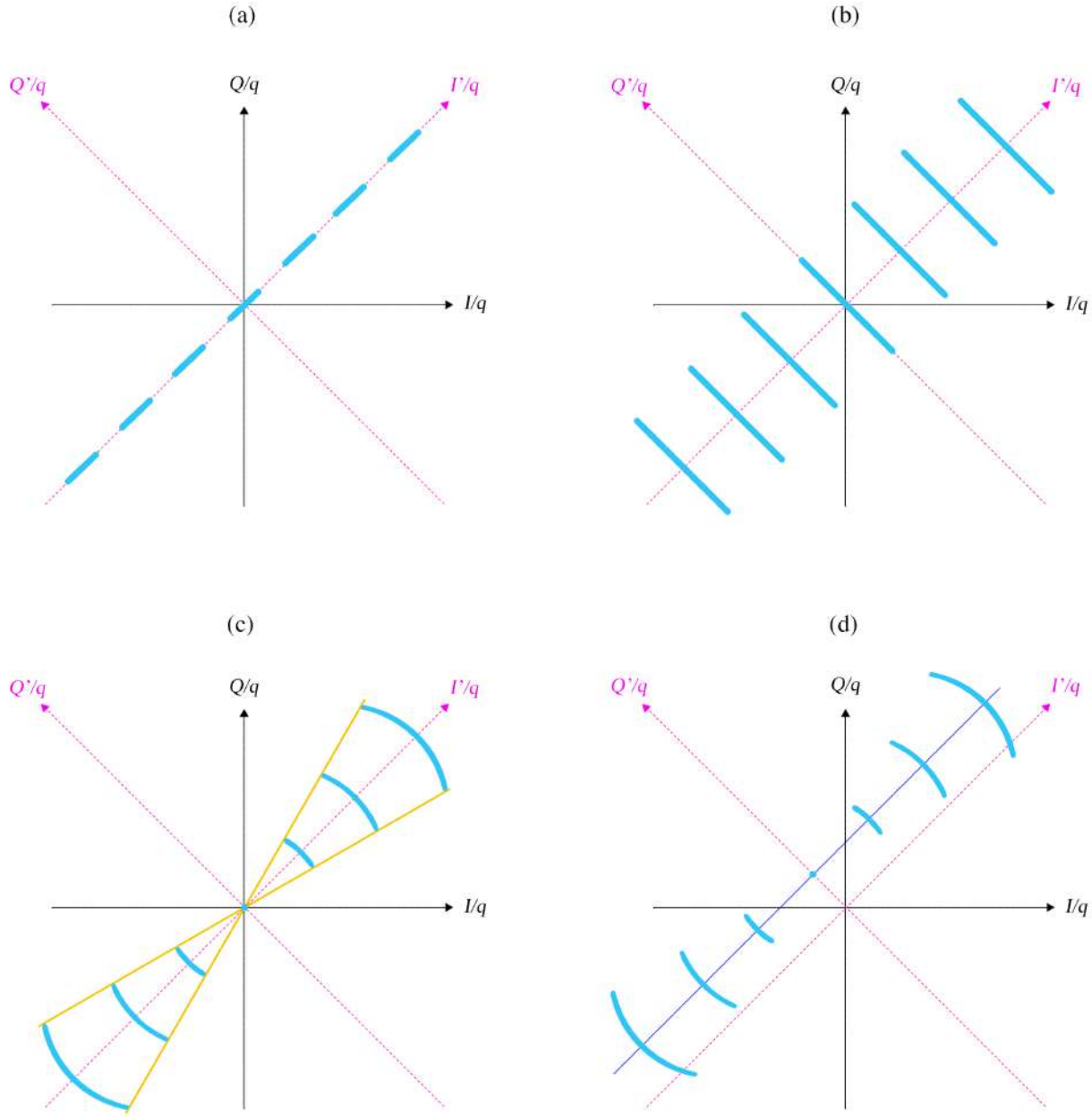

Figure 4.4: A simulation of a $\frac{Q}{q}$ versus $\frac{I}{q}$ for a BPM calibration to determine θ_{IQ}. Blue areas indicate data clusters at different calibration steps. Pink dashed lines indicate the $\frac{Q'}{q}$ and $\frac{I'}{q}$ axis determined from a global fit to the data. Sub plots show examples of (a) beam position jitter with distributions along the I' axis, (b) beam angular jitter with distributions along the Q' axis, (c) phase jitter with a rotational θ_{IQ} distribution indicated by yellow lines, and (d) phase jitter with a Q' offset in the origin of phase rotation and the global fit indicated by a blue line.

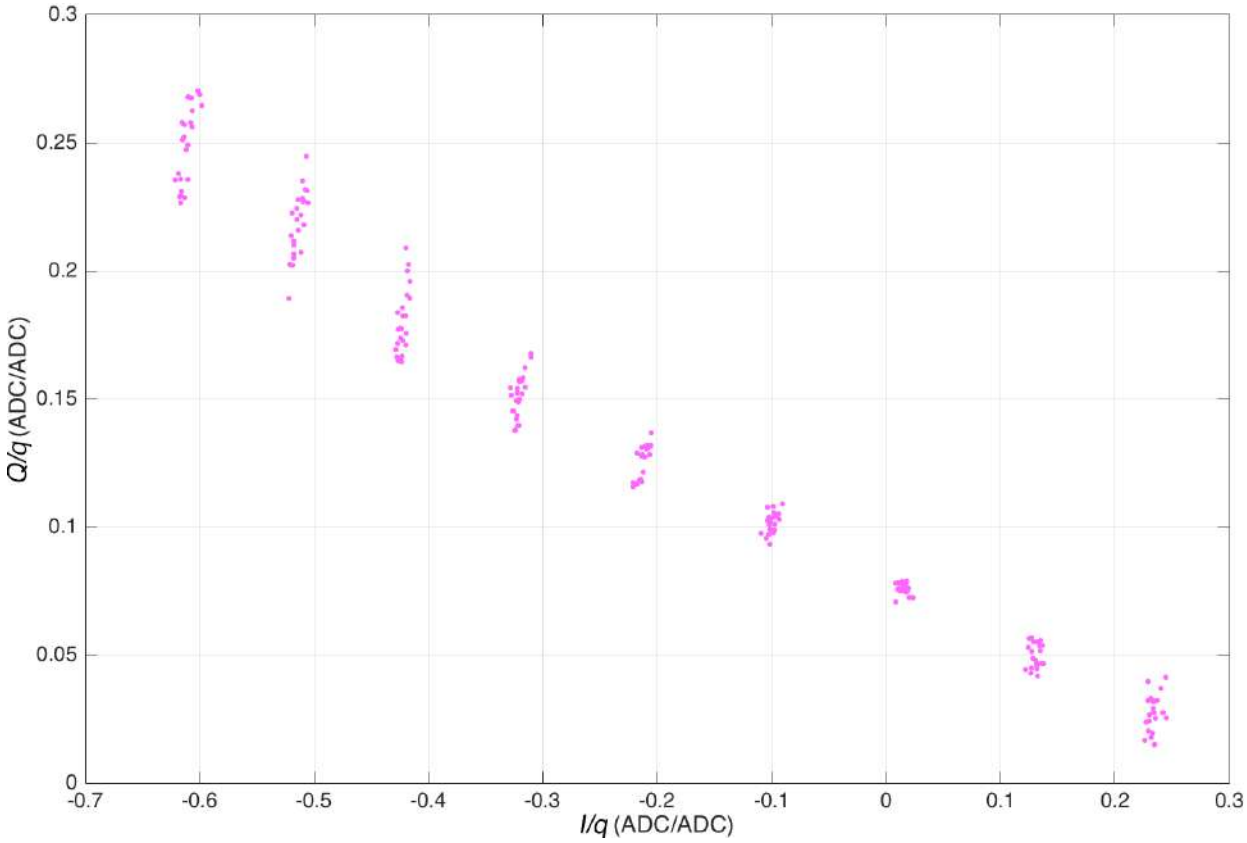

Figure 4.5: $\frac{Q}{q}$ versus $\frac{I}{q}$ for a calibration at IPB.

for each data point, where Q_0 and I_0 were the coordinates of the centre of rotation. Ideally, the centre of rotation would also be the origin on the Q versus I plot, but it is apparent from the calibration in Fig. 4.5 that this was not the case.

When the BPMs were moved to calibrate, rather than the beam itself, the position of the beam within the cavity changed at each mover step, while the angular trajectory remained constant. The BPMs themselves may also have had some intrinsic angle relative to the beam trajectory. These factors resulted in an offset in the centre of rotation along the Q' axis. To account for this all local θ_{IQ} values were calculated using the intersection of a linear fit to the global data set (the I' axis) and the Q' axis passing through the origin, as illustrated in Fig. 4.4.d.

4.2.3 Phase jitter estimate

The results of this analysis on the BPM calibration are shown in Fig. 4.6. The phase jitter should be constant, regardless of which calibration step was examined. However, the jitter appears to increase nearer the origin of rotation, where the local θ_{IQ} values are more difficult to estimate accurately and cannot be easily discerned from angular jitter. For this reason, the standard deviation of local θ_{IQ} values for calibration steps furthest

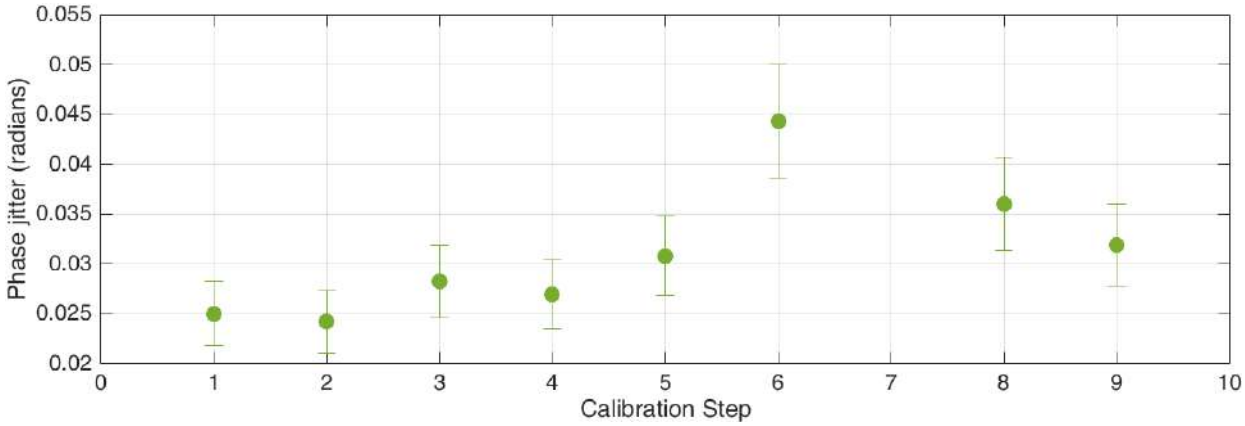

Figure 4.6: Local phase jitter versus calibration step, measured at IPB using the data from Fig. 4.5. Error bars indicate the error on the standard deviation. Calibration step 7 closest to the centre of rotation has been excluded from the plot, as the local θ_{IQ} could not be well estimated.

from the origin should provide the most realistic estimate of the phase jitter, which for this analysis is ∼0.025 radians. Calibrations at the other two BPMs also produced estimates of ∼0.025 radians using steps furthest from the origin of rotation. This should, therefore, be considered the best estimate of limiter phase jitter this analysis can provide.

4.2.4 Phase delay dependence on charge

Bench-tests of the limiting amplifier in the reference processing system have shown the delay to the output signal is dependent on the input amplitude [87], shown in Fig. 4.7. The input power to the reference processor would vary with the bunch charge, the cavities producing larger signal levels for higher charges. Consequently, the characteristic phase jitter distribution observed in calibration $\frac{Q}{q}$ versus $\frac{I}{q}$ plots could have been caused by charge jitter during calibration data taking.

To test this the charge level for the calibration shown in Fig. 4.5 was plotted for all triggers in Fig. 4.8.a, using the amplitude of the charge-normalising reference signal, q. Fig. 4.8.b shows the calibration replotted with the same reference charge level colour-coding scheme. It does not indicate any clear charge dependence within each mover step. The correlation between phase and charge was studied in detail for many calibration runs at different BPMs, different attenuations and different charge settings. The analysis demonstrated no consistent or significant correlation. This indicates that even if the source of the rotational spread in the phase does have some charge dependence, it is not the dominant effect.

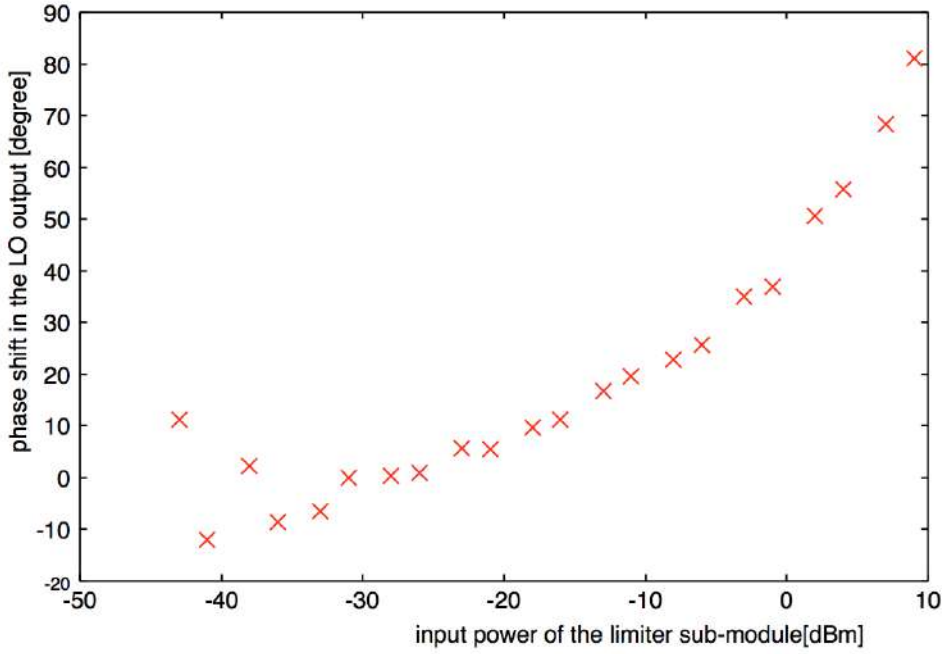

Figure 4.7: Phase shift in the output of the reference limiter versus the power of the input signal, indicative of the phase delay dependence on charge [87].

4.3 Direct measurement of limiter phase delay

4.3.1 Experimental set-up

A study was devised to measure the limiter phase delay directly trigger by trigger. Fig. 4.9 shows a simplified block diagram of the set-up with the reference signal split before the limiting amplifier. The intermediate frequency reference was mixed with a limited version of itself in a second stage processor borrowed from the dipole cavity x-signal processing. This mixing resulted in two outputs:

$$I_{\mathrm{REF}} = k_{\mathrm{REF}}\, q \cos(\Delta\phi + \delta_{\theta_{IQ}}), \tag{4.7}$$

$$Q_{\mathrm{REF}} = k_{\mathrm{REF}}\, q \sin(\Delta\phi + \delta_{\theta_{IQ}}), \tag{4.8}$$

where $\Delta\phi$ is the constant phase delay due to the different routes the reference and limited reference signals take through the processing, $\delta_{\theta_{IQ}}$ is the instantaneous phase delay on each trigger recorded due to limiter phase jitter, k_{REF} is a coefficient, and q is the bunch charge. Combining these two simultaneous equations in the form:

$$Q_{\mathrm{REF}} = I_{\mathrm{REF}} \tan(\Delta\phi + \delta_{\theta_{IQ}}), \tag{4.9}$$

the $(\Delta\phi + \delta_{\theta_{IQ}})$ could be determined from the inverse tangent of a gradient fit to a Q_{REF} versus I_{REF} plot. Assuming the limiter phase delay noise formed a normal distribution, the

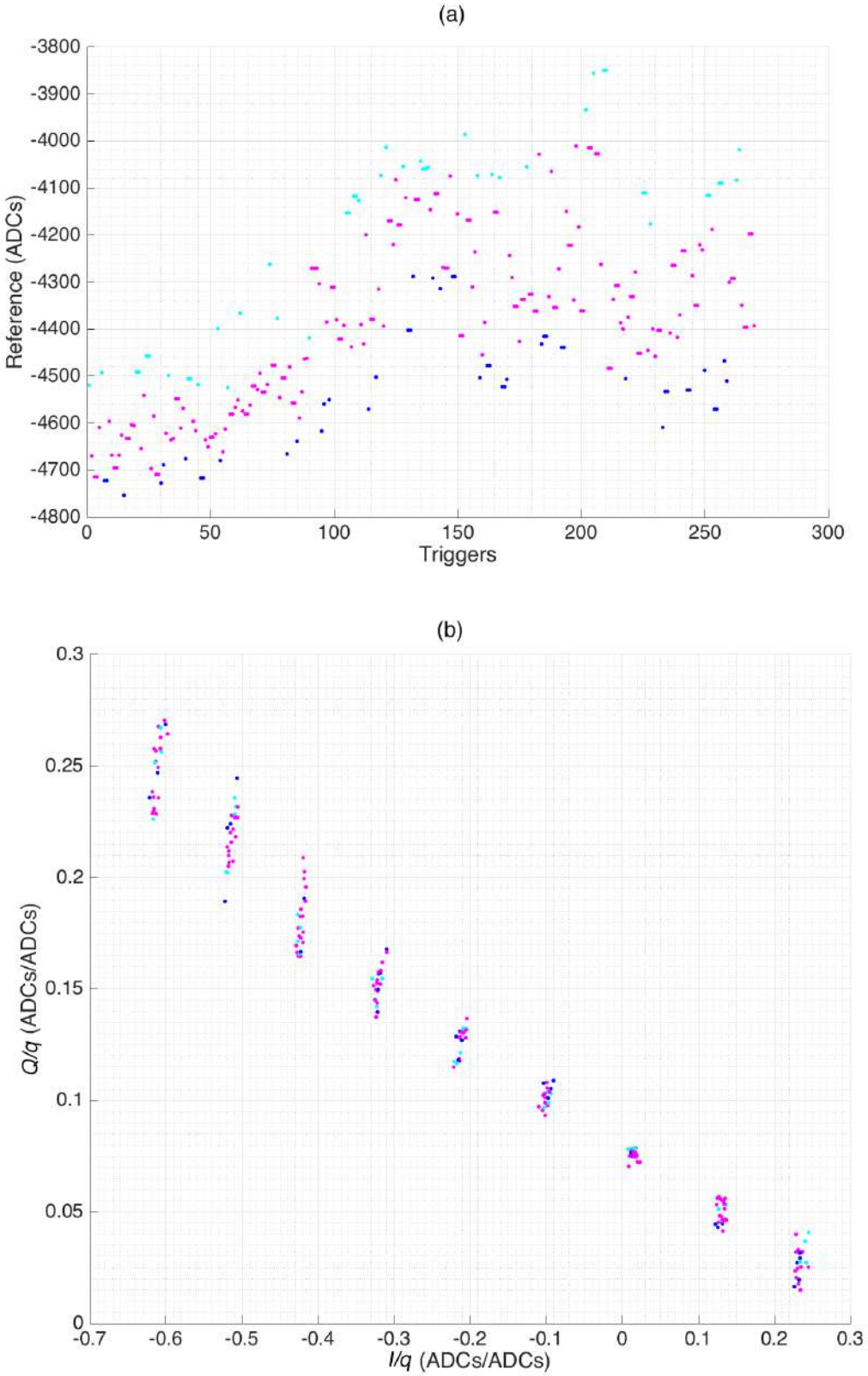

Figure 4.8: (a) Reference cavity signal amplitude in ADCs versus sequential triggers for an IPB calibration data set at 30 dB. The data points further than one sigma from the mean within each 30-trigger calibration step have been colour-coded to highlight the high and low ends of the charge distributions. (b) The $\frac{Q}{q}$ versus $\frac{I}{q}$ plot for the same calibration with the same colour coding for charge levels.

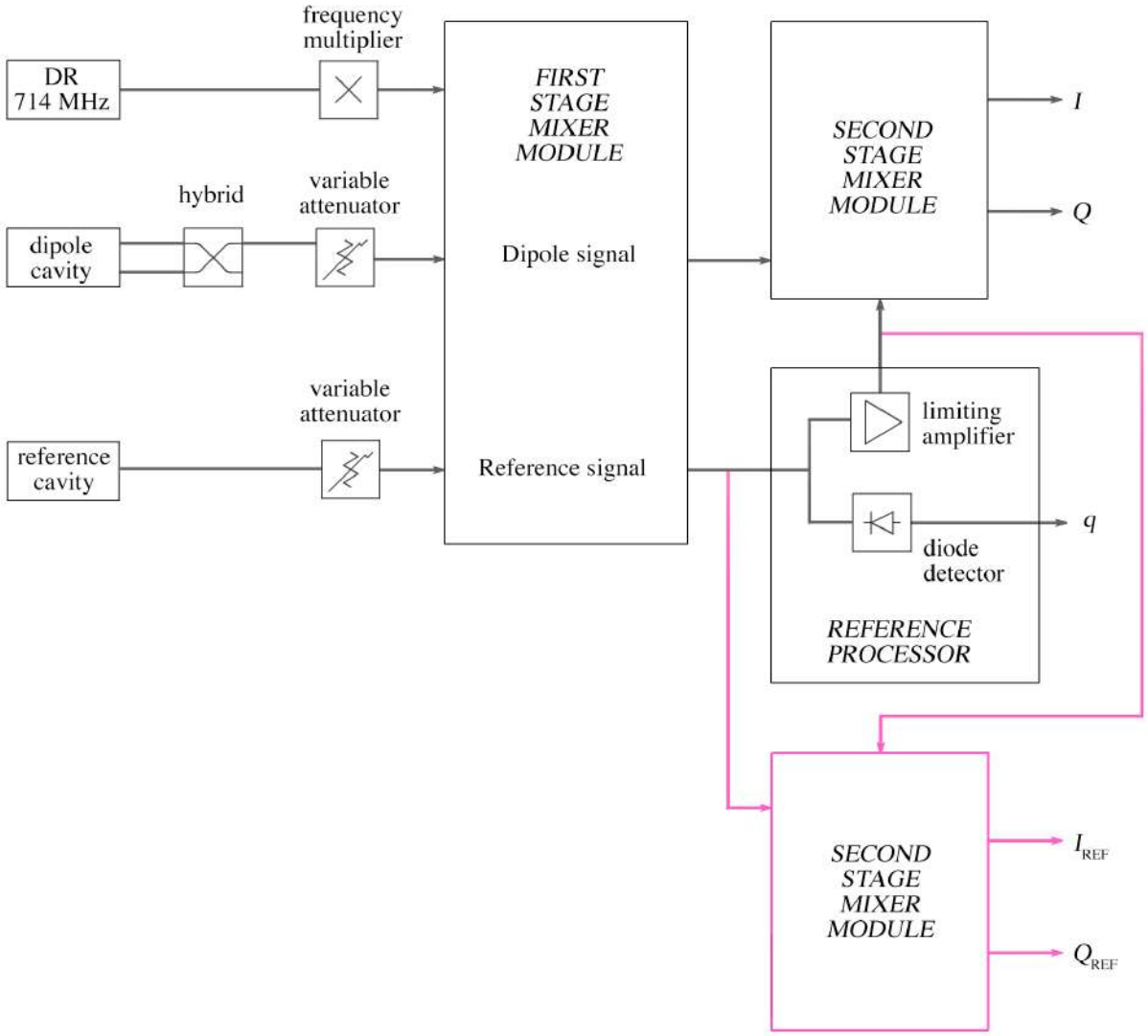

Figure 4.9: Block diagram of the IP BPM processing system with the first stage reference signal output split before the second stage and mixed with the limited version of itself in a second stage mixer module.

standard deviation of this angle across many bunch trains provided a direct measurement of the limiter phase delay jitter.

Dipole cavity I and Q signals were recorded simultaneously, using the identical limited reference signal (as shown in Fig. 4.9) to down-mix to baseband. This meant the reference limiter delay could be accounted for in analysis and incorporated into position measurements through the additional Q' term derived in Eq. 4.5.

The reference diode signal, q, could not be used to normalise with respect to charge, as it was not independent of the Q_{REF} and I_{REF} signals. For this study, the ICT in the ATF2 extraction line was used to provide an independent charge measurement for normalisation

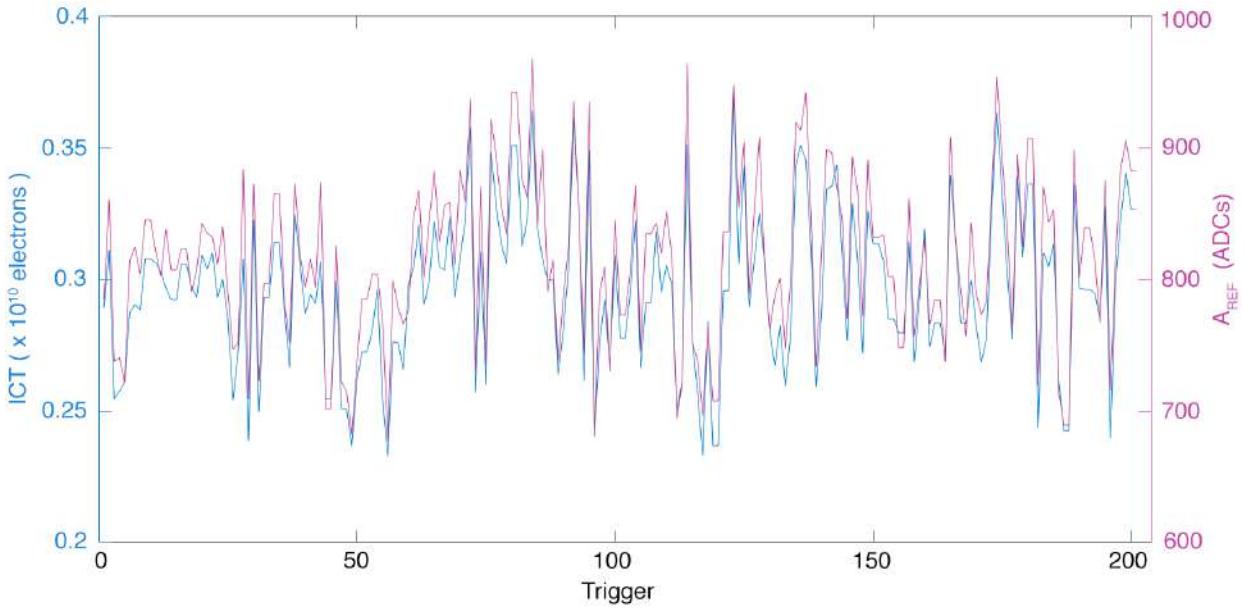

Figure 4.10: ICT charge monitor and A_{REF} versus sequential triggers for a 200-trigger data set at a single laser intensity setting.

[85]. For these tests, the ATF2 ICT signal was digitised synchronously with the reference cavity and dipole cavity information.

Fig. 4.10 shows the ICT and self-mixed reference signal level amplitude, A_{REF}:

$$A_{\mathrm{REF}} = \sqrt{Q_{\mathrm{REF}}^2 + I_{\mathrm{REF}}^2}, \tag{4.10}$$

plotted in sequential triggers for the data run at a laser intensity setting to achieve $\sim 0.3 \times 10^{10}$ electrons per bunch. The ICT and A_{REF} track each other very well.

Data were recorded for 200 trains at different charge settings between ~ 0.1 and $\sim 0.6 \times 10^{10}$ electrons per bunch. The dipole cavity signals were attenuated by 10 dB, and the reference cavity signals by 50 dB. The charge normalised Q_{REF} and I_{REF} signals are shown in Fig. 4.11, from which the limiter phase was then calculated.

4.3.2 Calculating the limiter phase jitter

The limiter phase ($\Delta\phi + \delta_{\theta_{IQ}}$) was determined (Eq. 4.9) and the $\delta_{\theta_{IQ}}$ was calculated trigger by trigger from the deviation of each limiter phase from the mean limiter phase ($\Delta\phi$) within each 200-trigger ensemble of data at different ICT settings. The standard deviation of the $\delta_{\theta_{IQ}}$ values was calculated as a measure of the limiter phase jitter.

The results of this analysis in Fig. 4.12 show an apparent limiter phase jitter dependence at lower charges, with the results levelling off above a mean ICT charge of 0.4×10^{10} electrons

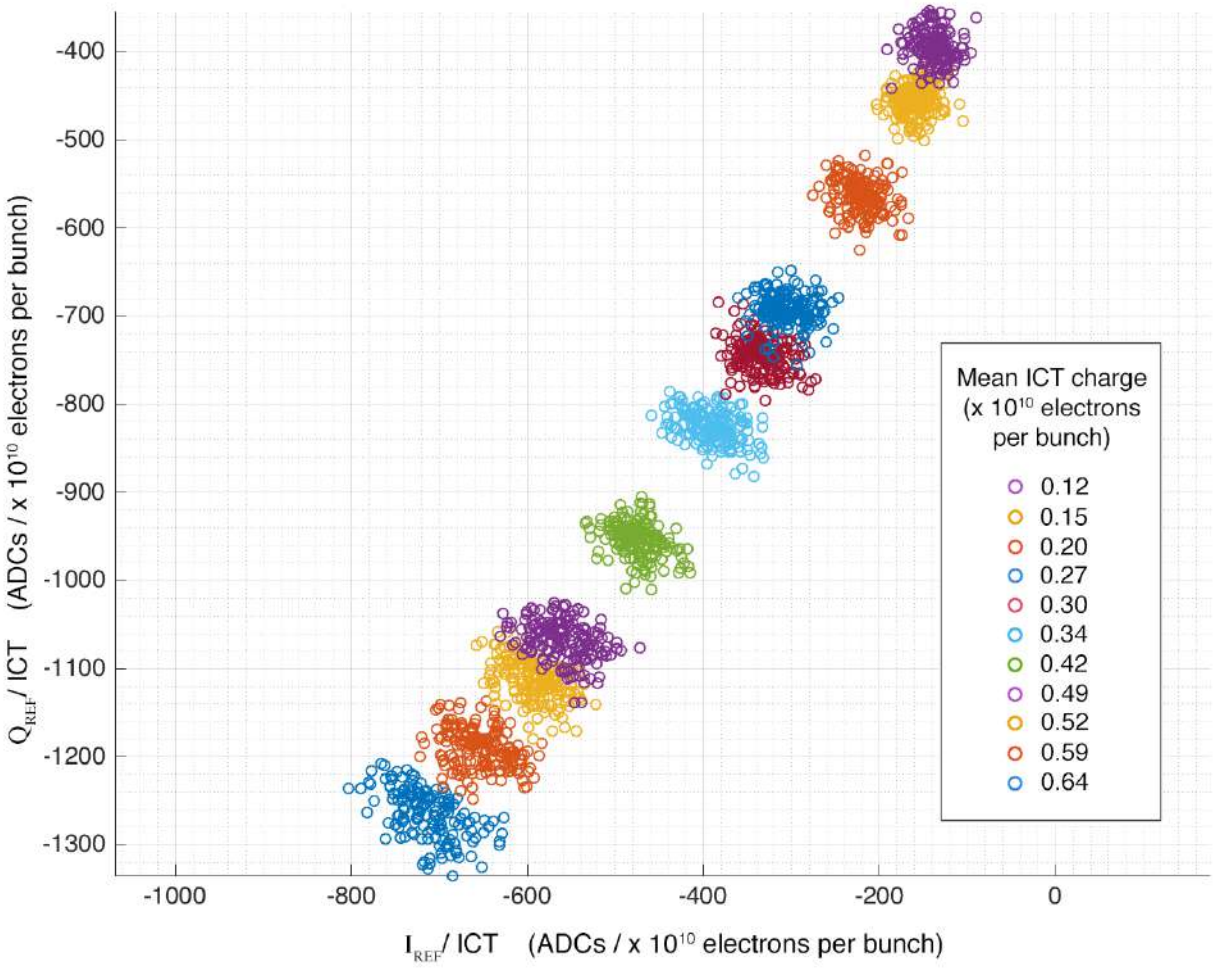

Figure 4.11: Q_{REF}/ICT versus I_{REF}/ICT. Different colours indicate data sets taken at different charges.

per bunch at ∼0.025 radians. This direct measurement of the limiter phase jitter is in agreement with the calibration analysis estimate presented in Section 4.2.3.

The deviation from the estimated phase jitter value of ∼0.025 radians at lower charge values is likely indicative of a regime where lower input signal levels due to lower bunch charges mean the system noise is becoming comparable to the phase jitter and disguising its effects. This becomes more apparent if the results shown in Fig. 4.11 are rotated into a Q'_{REF} versus I'_{REF} axis, shown in Fig. 4.13. The horizontal distribution of each calibration step should be a function of the system noise if all charge correlation is removed. The vertical distribution will be a function of system noise and phase jitter. At lower charge settings the horizontal and perpendicular jitters become comparable, which makes the phase jitter impossible to measure with confidence.

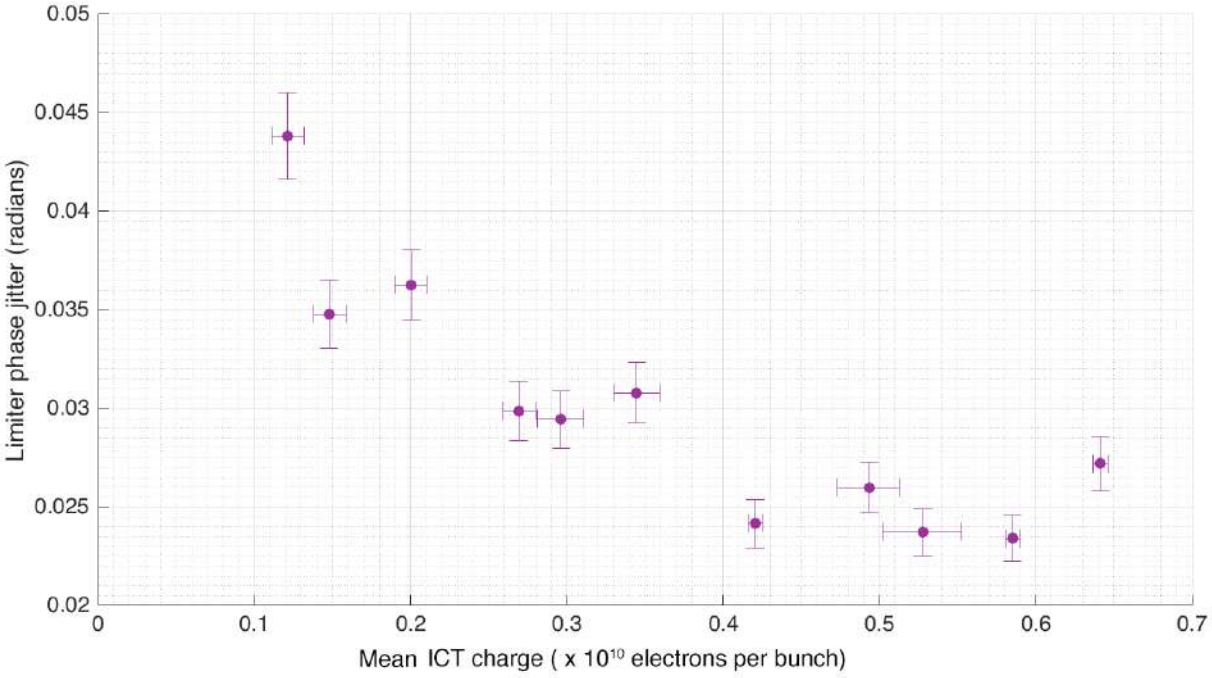

Figure 4.12: The limiter phase jitter versus mean ICT charge. The errors on the limiter phase jitter indicate the error on the standard deviation. The errors on the mean ICT indicate the standard deviation of the ICT distributions.

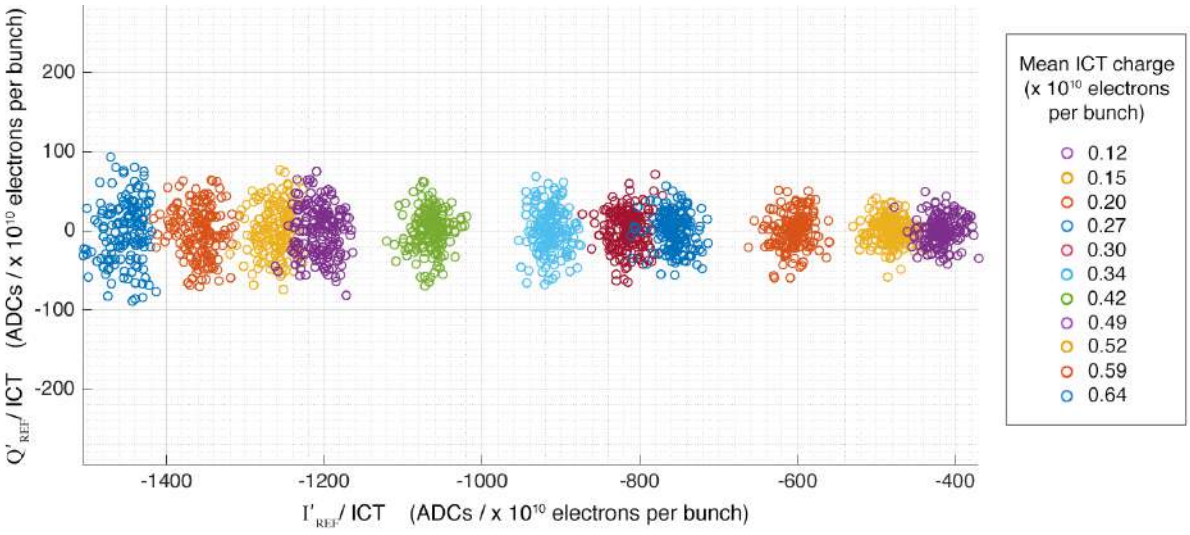

Figure 4.13: Q_{REF}'/ICT versus I_{REF}'/ICT. Different colours indicate data sets taken at different charges.

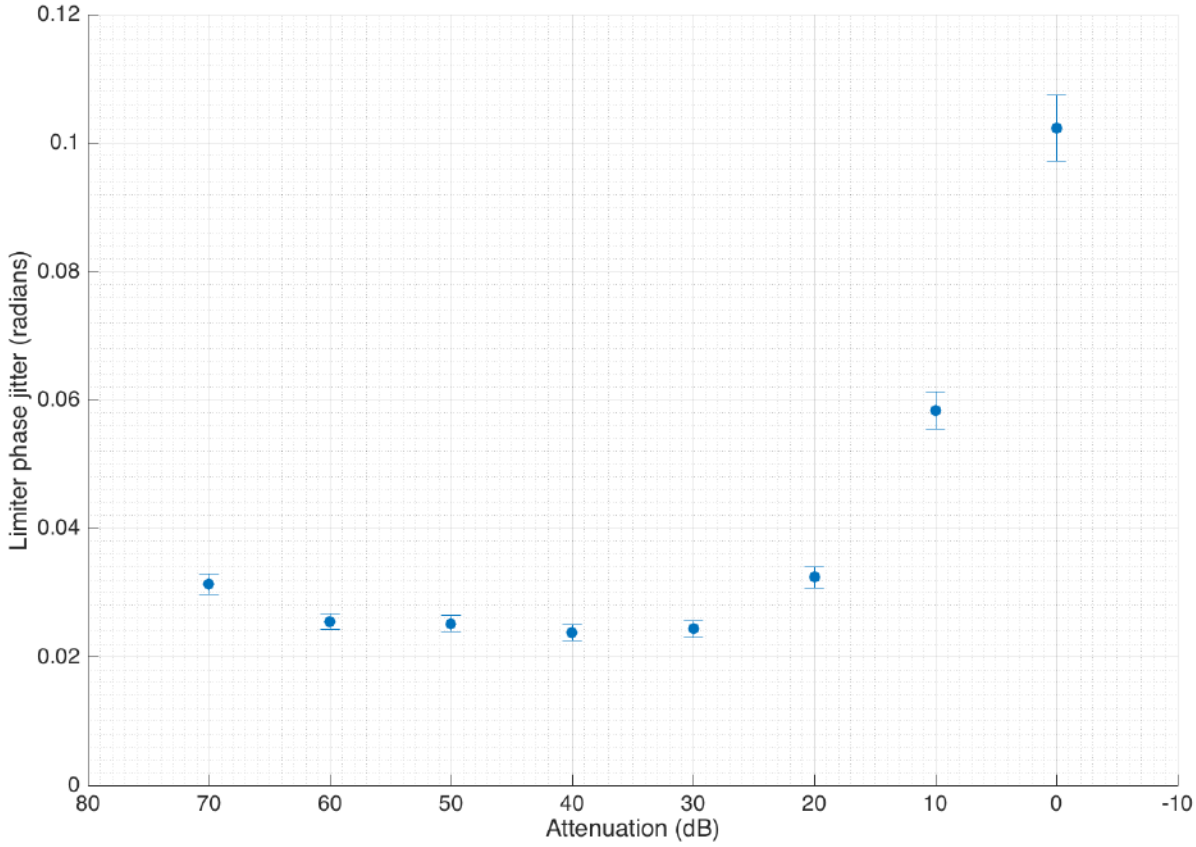

Figure 4.14: The limiter phase jitter in radians versus the reference cavity attenuation. The errors indicate the error on the standard deviation.

4.3.3 Attenuation scan

The previous charge scan study for direct measurement of the limiter phase jitter was performed with a constant reference cavity signal attenuation of 50 dB (set using the reference variable attenuator, see Fig. 4.9). This is typical for operation of the IP system. To check the phase jitter at different input powers, an attenuation scan was performed at a constant charge setting of $\sim 0.6 \times 10^{10}$ electrons per bunch. Identical analysis and ICT charge normalisation were applied from the previous sections to calculate the phase jitter for different data sets. The results are presented in Fig. 4.14. It is clear that the optimal working range is between 30 to 60 dB, where the phase jitter is, again, measured to be $\sim$0.025 radians.

4.3.4 Position sensitivity to phase jitter

To study the position sensitivity to limiter phase jitter, the $\delta_{\theta_{IQ}}$ values were calculated trigger-by-trigger while positions were measured at IPB with 10 dB attenuation on the dipole cavity signals, and 50 dB on the reference. The results (Fig. 4.15) demonstrate a position jitter of 370 $\pm$ 10 nm. It was then possible to correct the positions to remove the

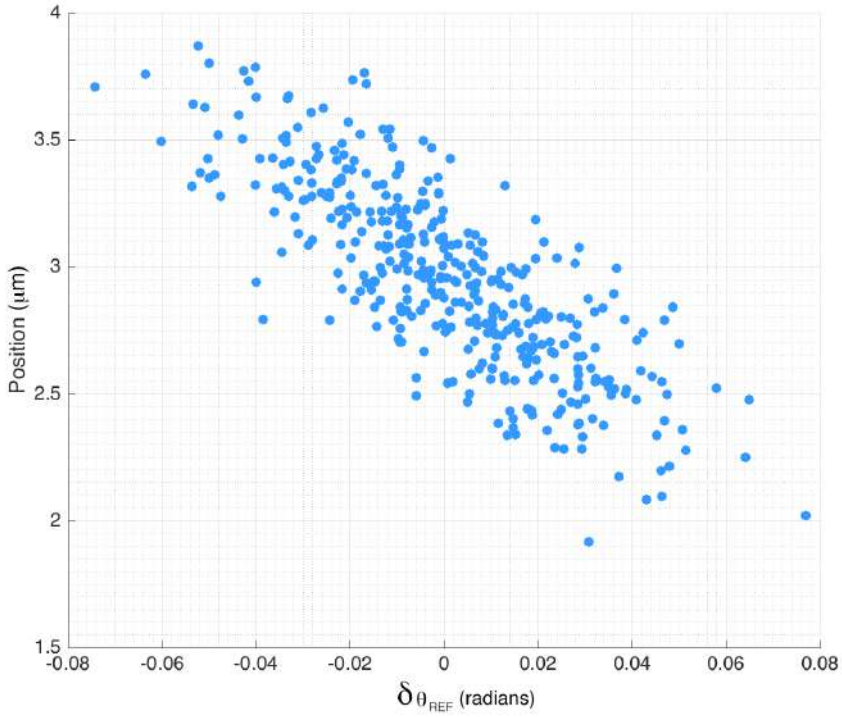

Figure 4.15: Position versus the limiter phase delay for a 200-trigger data set. Positions measured at IPB at 10 dB dipole attenuation. The correlation is 81%.

phase dependence using Eq. 4.5. Fig. 4.16 shows the same data with positions recalculated by incorporating the $\delta_{\theta_{IQ}}$ terms. This analysis has removed correlation between position and phase and reduced the position jitter to 230 ± 10 nm. This is a dramatic reduction, confirming the limiter phase jitter coupling into position through the angular Q' component is a significant effect.

It follows from this result that one way to mitigate the impact of phase jitter is to reduce the size of Q'. This was confirmed by tracking the amplitude of the Q' signal and the correlation between position and $\delta_{\theta_{IQ}}$ using different samples in the digitised waveform. The results are shown in Fig. 4.17. It can be seen that when Q' is smaller, position phase sensitivity is reduced.

In practice, phase sensitivity can be minimised by reducing the Q' component at the ATF2 IP BPMs through steering the beam or adjusting the BPM movers to minimise the angular trajectory of the beam through the cavities. If Q' minimisation proves insufficient, it may be necessary to correct for the phase using the approach demonstrated in this Chapter. Alternatively, the reference processor's limiting amplifier could be investigated for potential upgrades to reduce the phase jitter it generates.

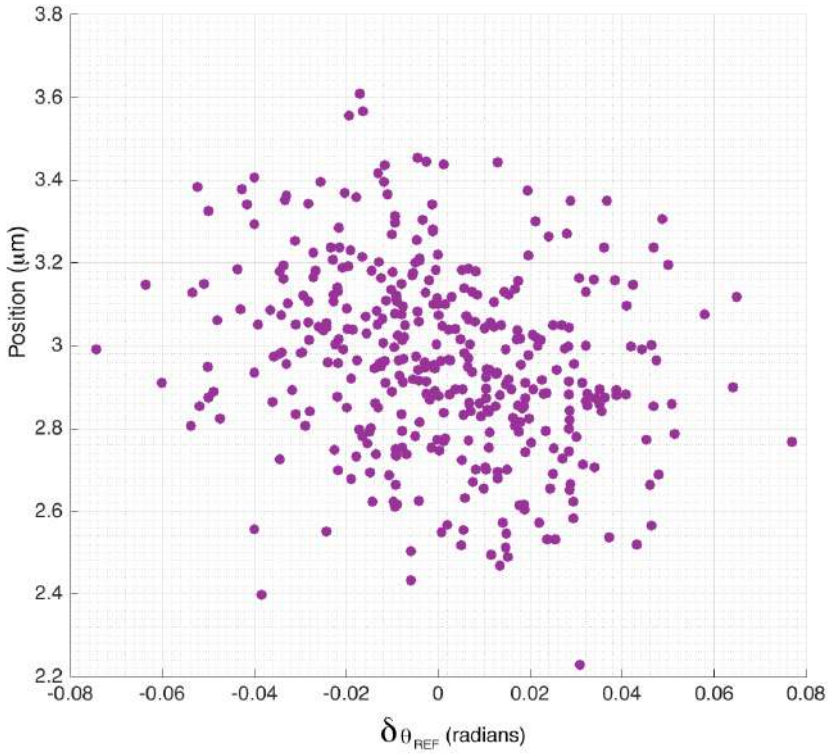

Figure 4.16: Position (phase-corrected using Eq.4.5) versus the limiter phase delay for the same 200 trigger data set as Fig. 4.15. The correlation is reduced to ∼0%.

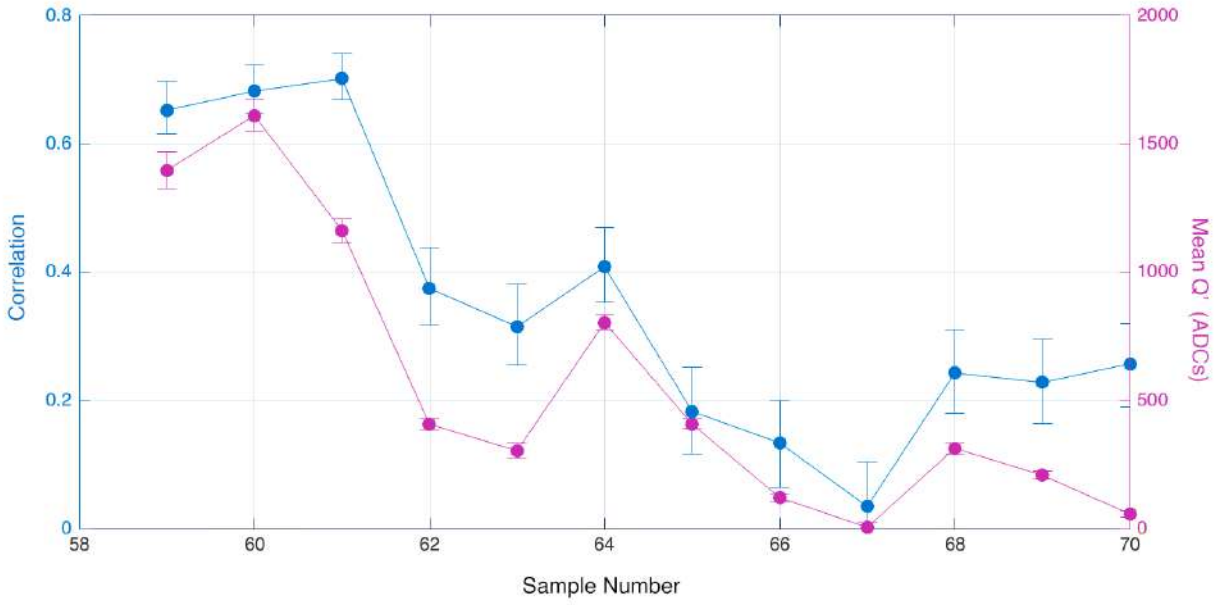

Figure 4.17: Correlation (left scale, blue) between position and limiter phase delay and mean Q' (right scale, purple) versus sample number. The lines connect the data points. Errors on the correlation indicate one sigma confidence interval. Errors on the mean indicate the standard deviation.

4.4 Summary

The IP BPM system's position measurement sensitivity to bunch phase jitter was investigated by varying the LO signal in controlled steps relative to the BPM cavity output signals using a variable phase shifter. A maximum position sensitivity at 0.71 ± 0.03 µm per degree was measured with 50 dB attenuation. This scales to 2.2 ± 0.1 nm per degree at 0 dB attenuation. Given the measured bunch phase jitter of the beam, up to 8.6 ± 0.4 nm of apparent position jitter measured at the IP at 0 dB could actually be due to bunch phase jitter. It is unclear how this phase would be leaking into the final position-dependent processor signals, as the system is designed to be insensitive to bunch-to-LO phase differences. But as the resolution of the IP BPM system pushes towards nanometre-level position resolution, this may become a significant concern.

The limiting amplifier in the reference processor of the IP down-mixing electronics was then tested as a source of phase jitter. Measurements of this rotational distribution estimated a potential phase jitter source on the order of 0.025 radians. In regimes where the data distributions were not dominated by system noise, i.e. at higher bunch charges, a limiter phase jitter of 0.025 radians was again measured, with the operationally typical 50 dB attenuation on the reference cavity signal. An attenuation scan was also performed, and again demonstrated a minimum limiter phase jitter of 0.025 radians between the attenuations of 30 and 60 dB.

Finally, the position sensitivity to phase was tested. Utilising Eq. 4.5 a position-to-phase sensitivity of 81% was completely removed, and the apparent position jitter reduced from 370 nm to 230 nm. The position sensitivity was found to track very well with the amplitude of the Q' signal. Phase sensitivity can be minimised operationally by reducing the angular trajectory of the beam through the cavities to minimise the Q' component of the signals.

Chapter 5

Two-BPM IP feedback

The FONT group has had many successes with feedback studies at the ATF2, including a coupled-loop feedback system using two stripline BPMs and two kickers to correct both position and angle in the extraction line and stabilising the beam along the final focus [88]. These results have demonstrated a latency and beam position stabilisation capacity more than sufficient for the ILC requirements [52]. Subsequent FONT studies have shifted to the ATF2 IP region (detailed in the previous chapters), in an attempt to achieve the ambitious goal of stabilising the beam to the nanometre level [32]. Previous feedback studies at the IP have included detailed tests of a single-BPM system utilising position information from one cavity BPM to stabilise to a minimum beam position jitter of 74 $\pm$ 5 nm [8].

The study presented here takes a novel approach to beam stabilisation, utilising beam position information from two cavity BPMs as input to the feedback to correct the beam at a third, intermediate cavity BPM. In addition to stabilising the beam at a location other than the BPMs providing input to the feedback, this mode has the potential to improve stabilisation capability by using the position information from two BPMs. This method also provides the first independent measurement of the IP feedback performance via a witness BPM; unexpected esoteric effects internal to the cavity BPM system are not excluded if the position information entered into the feedback and measurements of the correction originate from the same BPM, as in a single-BPM feedback mode.

In practice, it is very difficult to use all three of the ATF2 cavity BPMs simultaneously in a way that optimises their performance. The challenges of experiments with this new mode of feedback are presented in this chapter, starting with the experimental conditions and set-up required. The results of initial test trials are detailed, along with diagnostic studies to test proof of principle and problems encountered in optimising performance. The subsequent best-achieved results in this mode will then be presented.

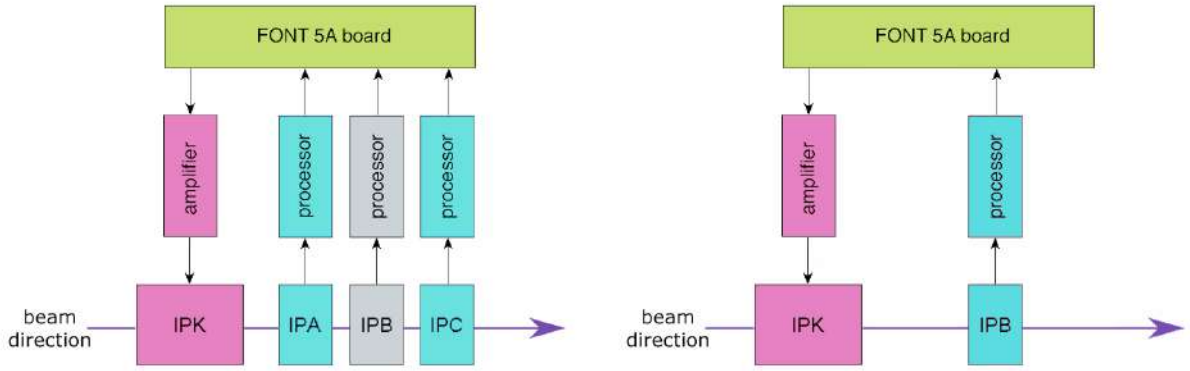

(a) Two-BPM IP feedback

(b) Single BPM IP feedback

Figure 5.1: Block diagram of the IP feedback system for (a) the two-BPM feedback configuration, where IPA and IPC are used as inputs to the feedback, and IPB is used as an independent witness of the correction; and (b) single-BPM feedback, where information from IPB is used as input to the feedback and for measuring the correction.

5.1 Experimental Set-up

The two-BPM feedback studies were performed using a two-bunch train with a bunch spacing of 280 ns. A FONT board was used to digitise the IP BPM y-axis signals, as shown in Fig. 5.1.a. The set-up utilised all three dipole cavity BPMs to measure the beam position. The bunch 1 signals from IPA and IPC were used by the FONT board to calculate the necessary corrective kick signal, which was applied to bunch 2 using the kicker, IPK. The position information from IPB was digitised synchronously but was only used to monitor the correction. This arrangement contrasts with the single-BPM feedback previously used for IP feedback, shown in Fig. 5.1.b, which made use of only one IP BPM as both input to the feedback and to measure the subsequent correction. A detailed diagram of the IP electronics set-up for two-BPM feedback is shown in Fig. 5.2.

With nominal IP optics, the jitter either side of the tuned waist was larger than the dynamic range at the BPMs furthest from the IP (i.e., IPA and IPC). With a single-BPM study set-up, this problem was mitigated by moving the beam waist closer to the BPM. A simple longitudinal waist adjustment was not sufficient for two-BPM feedback, as it was necessary to have useable beam jitters at all three BPMs simultaneously. As detailed in Chapter 3, this can be achieved using a beam with a β_y^* 1000 times larger than the ATF2 nominal optics. This set-up resulted in a much lower divergence of the beam around the IP and smaller jitters at the BPMs.

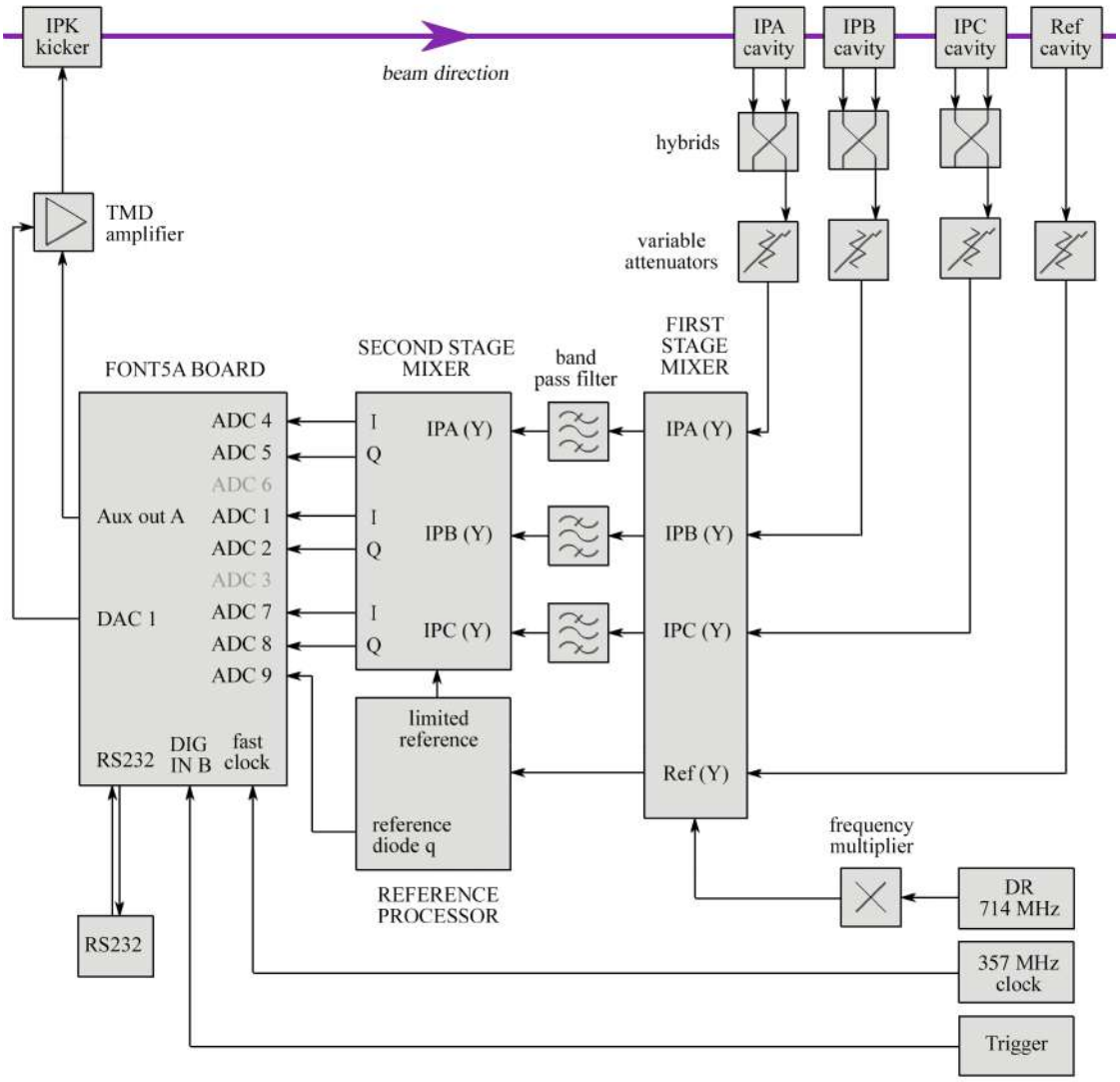

Figure 5.2: Detailed block diagram of the hardware and two-stage processing electronics set-up for the two-BPM IP feedback system.

Fig. 5.3 shows the beam path interpolated in the y axis between IPA and IPC for 100 sequential measurements of bunch 1 in the train. This plot shows there is a discernible waist around -35 mm from the nominal IP, but it has been significantly diminished by the high-beta optics tuning. The beam position jitter as a function of the longitudinal distance from the nominal IP location is shown in Fig. 5.4, with the jitter at all three BPMs reduced, in particular to ∼0.5 µm at IPA and IPC.

Fig. 5.5 shows example I and Q waveforms. The data were taken with 0 dB attenuation on the dipole signals, and with narrow BPFs on the dipole cavity outputs to smooth the unwanted oscillatory features (see Section 2.10). The mixer DC baseline offset (see Section 2.7) is visible at the beginning of the waveforms. This baseline can be removed in analysis,

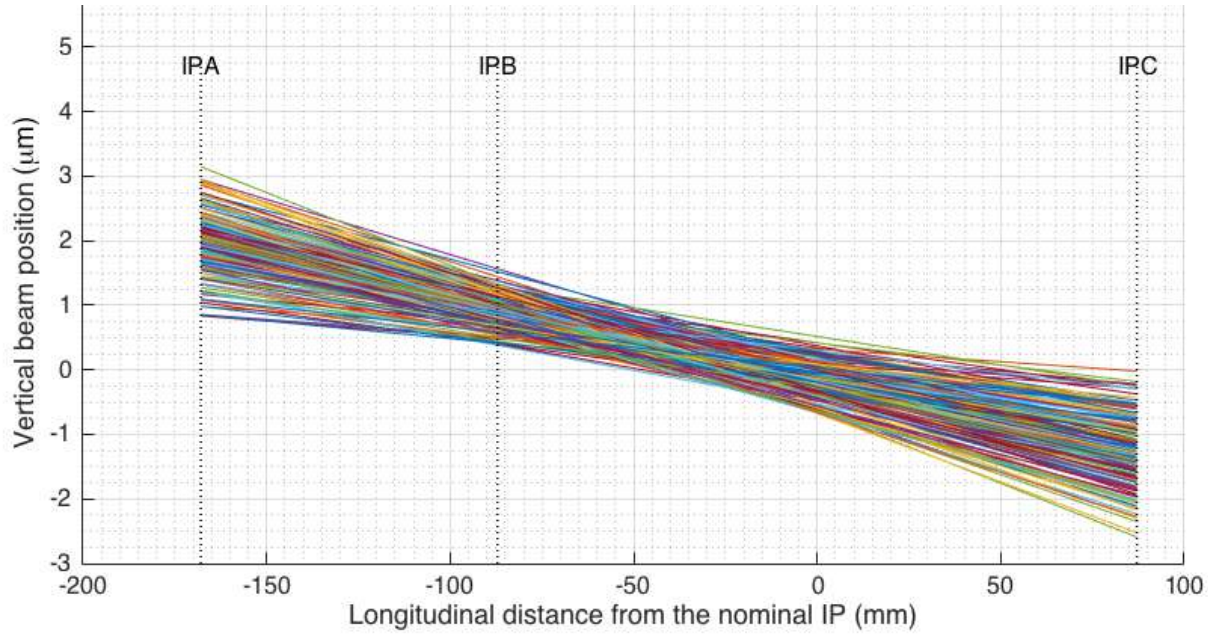

Figure 5.3: Vertical beam position versus longitudinal distance from the nominal IP for 100 sequential triggers. Each coloured line represents the beam path of a different trigger. The locations of IPA, IPB, and IPC BPMs are indicated. The beam paths are obtained from a linear interpolation of the measured positions at IPA and IPC.

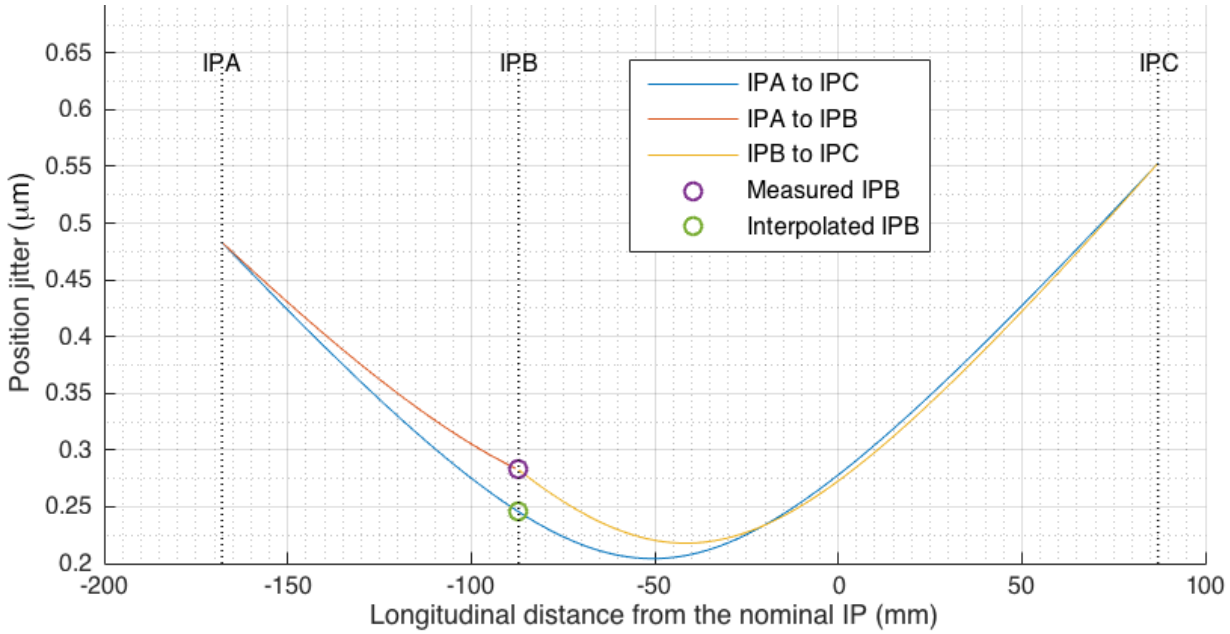

Figure 5.4: Vertical beam position jitter versus longitudinal distance from the nominal IP. Separate interpolations between IPA and IPC (blue), IPA and IPB (red) and between IPB and IPC (yellow) are plotted. The purple circle indicates the jitter measured at IPB, and the green circle the jitter interpolated at IPB.

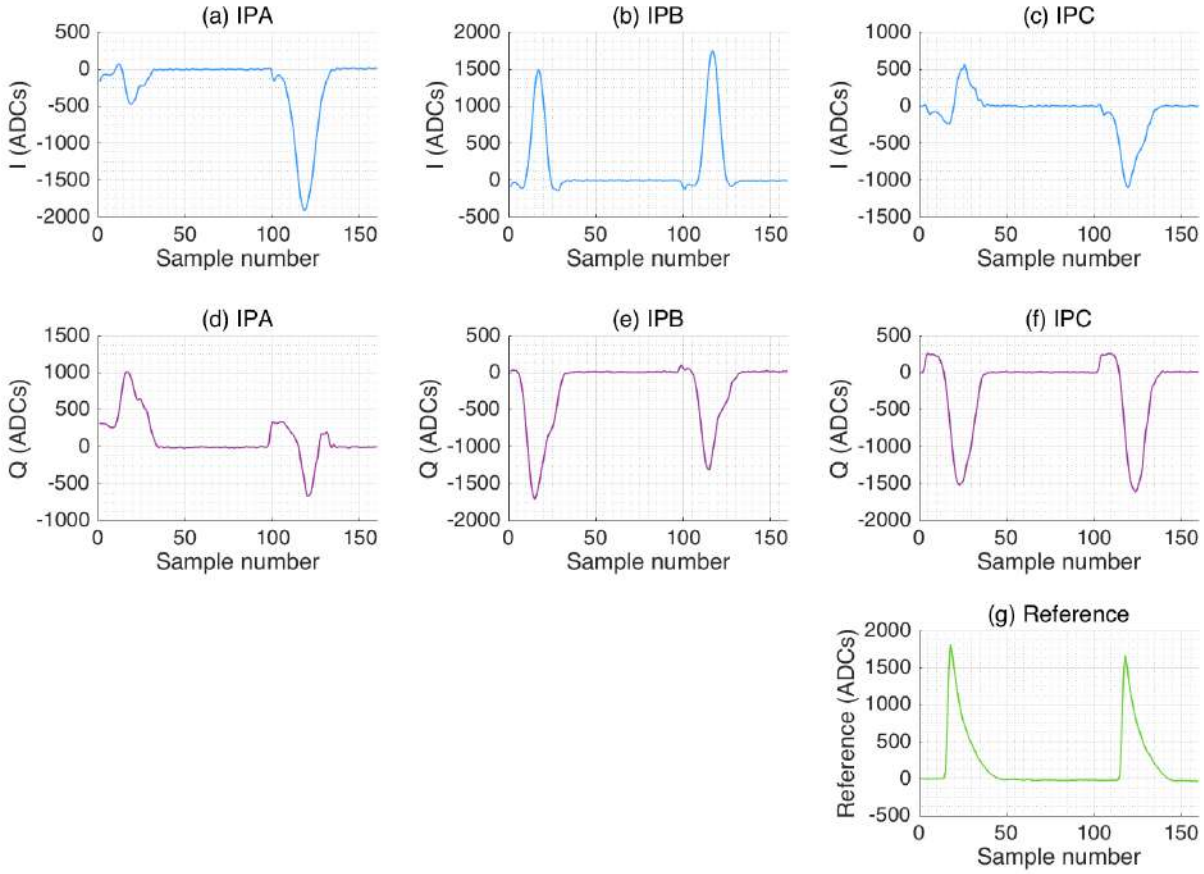

Figure 5.5: Waveform signals in ADCs versus sample number in the digitiser window for all of the FONT board ADC channels being utilised in this setup; (a) IPA I, (b) IPB I, (c) IPC I, (d) IPA Q, (e) IPB Q, (f) IPC A, and (g) the reference cavity.

and future firmware development plans include incorporating a baseline subtraction in the feedback algorithm.

The FONT board firmware utilises single samples within the digitised window, which can be set independently for each of the three ADC banks in the LabVIEW DAQ [50] but not for each channel individually. Sample numbers were selected to correspond to the maximum of the calibration scale factor, k. Sample 16 was chosen for bunch 1 at IPA and IPB on banks one and two, and sample 21 for IPC and the reference cavity signal on bank three. Bunch 2 was sampled 100 samples later (at 116 and 121), corresponding to the bunch-to-bunch separation of 280 ns at a sampling rate of 2.8 ns.

The five-sample delay on the third ADC bank (channels seven, eight and nine) relative to the first two banks was an artefact of upstream feedback firmware development and is not indicative of the signals arriving at IPC and the reference five samples later.

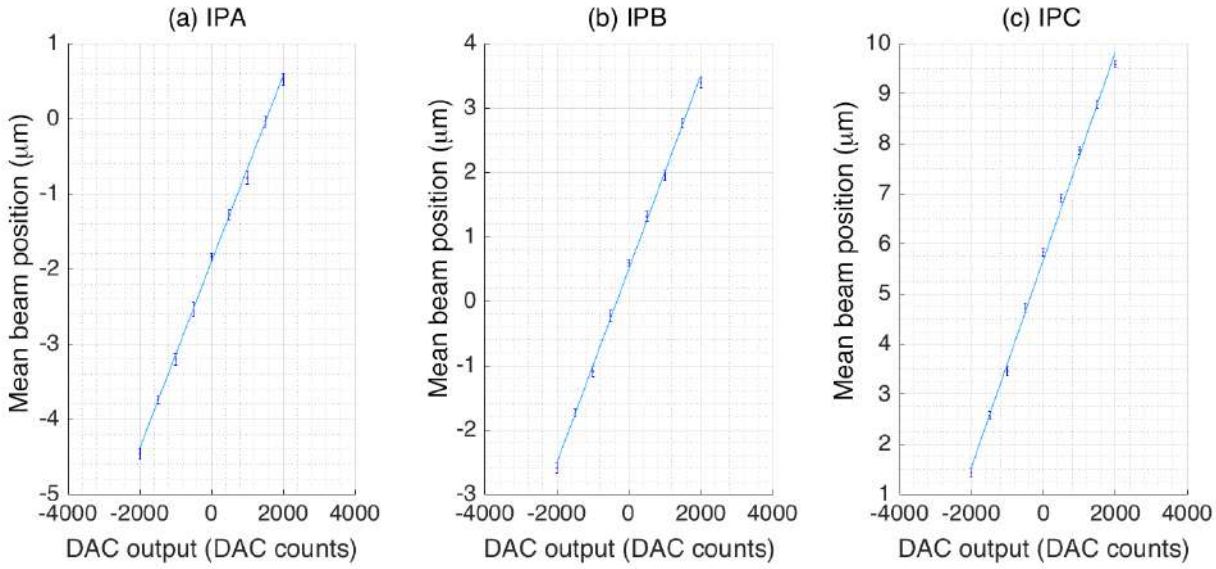

Figure 5.6: Mean bunch 2 position versus constant DAC output setting applied to IPK at (a) IPA, (b) IPB and (c) IPC. The line indicates the results of a linear fit to the data.

5.2 Feedback gain calculation

Before implementing feedback, it was necessary to calibrate the effect of the kick applied by the stripline kicker in terms of beam position at the IP BPMs. This calibration was achieved by sending a constant DAC output from the FONT board to the kicker amplifier. This output was then varied between -2000 and +2000 DAC counts in steps of 500 counts and the response of the I and Q signals in the train were monitored and used to calculate the beam position at different DAC settings.

The results of this kicker scan are shown in Fig. 5.6. The linear fit to these plots provides kicker calibration constants, H, in units of nm/DAC for a given sample number from the gradients. Table 5.1 details these results.

The purpose of this experiment was to stabilise the beam in the y axis at the witness BPM, IPB, but without using the position measurements at IPB. Instead, the vertical position measurements at IPA, y_{A}, and IPC, y_{C}, were weighted according to their longitudinal distances from IPB (see Table 2.1) assuming a straight-line trajectory to interpolate the position at IPB:

$$y_{B_{\mathrm{interp}}} = \left(\frac{174.2}{174.2+80.8}\right) y_A + \left(\frac{80.8}{174.2+80.8}\right) y_C = 0.68 y_A + 0.32 y_C. \qquad (5.1)$$

Table 5.1: Kicker calibration constants, H, for the three IP BPMs. Errors determined from the statistical uncertainties on the fits.

BPM	Sample Number	H (nm/DAC)
A	16	1.24 ± 0.02
B	16	1.50 ± 0.02
C	21	2.07 ± 0.02

In terms of the raw I, Q and q signals digitised on the FONT board the equation is:

$$y_{B_{\text{interp}}} = \left(0.68\frac{\cos\theta_{AIQ}}{k_A}\right)\frac{I_A}{q} + \left(0.68\frac{\sin\theta_{AIQ}}{k_A}\right)\frac{Q_A}{q} + \left(0.32\frac{\cos\theta_{CIQ}}{k_C}\right)\frac{I_C}{q} + \left(0.32\frac{\sin\theta_{CIQ}}{k_C}\right)\frac{Q_C}{q}. \tag{5.2}$$

Assuming the position of the next bunch in the train will be identical to the first (i.e. high bunch-to-bunch position correlation), the necessary corrective position kick, V_k, to remove the position offset measured at the first bunch needs to be equal to $-y$. The kicker calibrations, H, are used to calculate the corrective kick signal that needs to be sent to the kicker via the FONT board in units of DAC counts,

$$V_k = \frac{-y}{H}, \tag{5.3}$$

which for this set-up must incorporate values to correct at IPB using $y_{B_{\text{interp}}}$ and H_B:

$$V_k = \left(0.68\frac{\cos\theta_{AIQ}}{H_B\,k_A}\right)\frac{I_A}{q} + \left(0.68\frac{\sin\theta_{AIQ}}{H_B\,k_A}\right)\frac{Q_A}{q} + \left(0.32\frac{\cos\theta_{CIQ}}{H_B\,k_C}\right)\frac{I_C}{q} + \left(0.32\frac{\sin\theta_{CIQ}}{H_B\,k_C}\right)\frac{Q_C}{q}. \tag{5.4}$$

For use in the on-board firmware feedback algorithm, this equation can be simplified to

$$V_k = G_1\frac{I_A}{q} + G_2\frac{Q_A}{q} + G_3\frac{I_C}{q} + G_4\frac{Q_C}{q}, \tag{5.5}$$

where G_1, G_2, G_3 and G_4 are the feedback gains entered into the FONT DAQ and sent to the FONT board. These gains were calculated manually for each new experimental set-up using the kicker and BPM calibration scan constants:

$$G_1 = 0.68\frac{\cos\theta_{AIQ}}{H_B k_A}, \quad G_2 = 0.68\frac{\sin\theta_{AIQ}}{H_B k_A}, \quad G_3 = 0.32\frac{\cos\theta_{CIQ}}{H_B k_C}, \quad G_4 = 0.32\frac{\sin\theta_{CIQ}}{H_B k_C}. \tag{5.6}$$

Table 5.2: Example firmware feedback gain values used for initial tests in two-BPM feedback mode in units of DAC(ADC/ADC).

G1	G2	G3	G4
-1245	-775	1002	380

Example gains used in the initial feedback results presented here are listed in Table 5.2. These values were re-calculated and re-entered into the DAQ from new kicker and BPM calibrations every time the set-up was changed e.g. for data taken with different attenuations, using different waveform sampling numbers, or with slightly different optics.

5.3 Initial feedback trials

The FONT board was set to perform interleaved feedback; this meant the feedback was switched on for every other train. Interleaving allows any slow beam position drift to be tracked. The drift would otherwise make it difficult to compare results from two separate feedback-on and feedback-off data sets. Fig. 5.7 shows the y positions measured at IPB for bunch 1 and bunch 2 for 200 sequential triggers, which have been separated into two 100-trigger data sets with feedback-off and feedback-on. No alterations were made to bunch 1 in each train, regardless of whether the feedback was on or off; it was just measured. But the bunch 2 position was corrected when the feedback was turned on.

The feedback acted to stabilise the bunch position to a single location; in this case, at around -2.5 µm offset. Because the orbit of bunch 1's interpolated IPB position was positive (Fig. 5.3) for this test, the feedback was shifting the already negative bunch 2 at IPB to be further negative. If the feedback experiment required the bunch to be stabilised at a specific position, that could be set using a constant kick offset. At IPB there was a clear position offset between the two bunches (see feedback off data in Fig. 5.7). This offset was a result of the bunches following different orbits through the accelerator, likely due to variations in the damping ring extraction kicker pulse. This orbit difference between the two bunches in the train is not problematic for feedback purposes, as long as the difference is a constant trigger to trigger, and the separation is not so large that it becomes impossible to centre both bunches within the dynamic range of the BPMs.

The beam stabilisation was quantified in the standard deviation of the position, i.e. position jitter, best visualised in a histogram of vertical position distributions (Fig. 5.8). Table 5.3 details the mean positions and position jitters with their respective uncertainties. The feedback reduced the bunch 2 position jitter from 263 ± 19 nm jitter to 132 ± 10 nm.

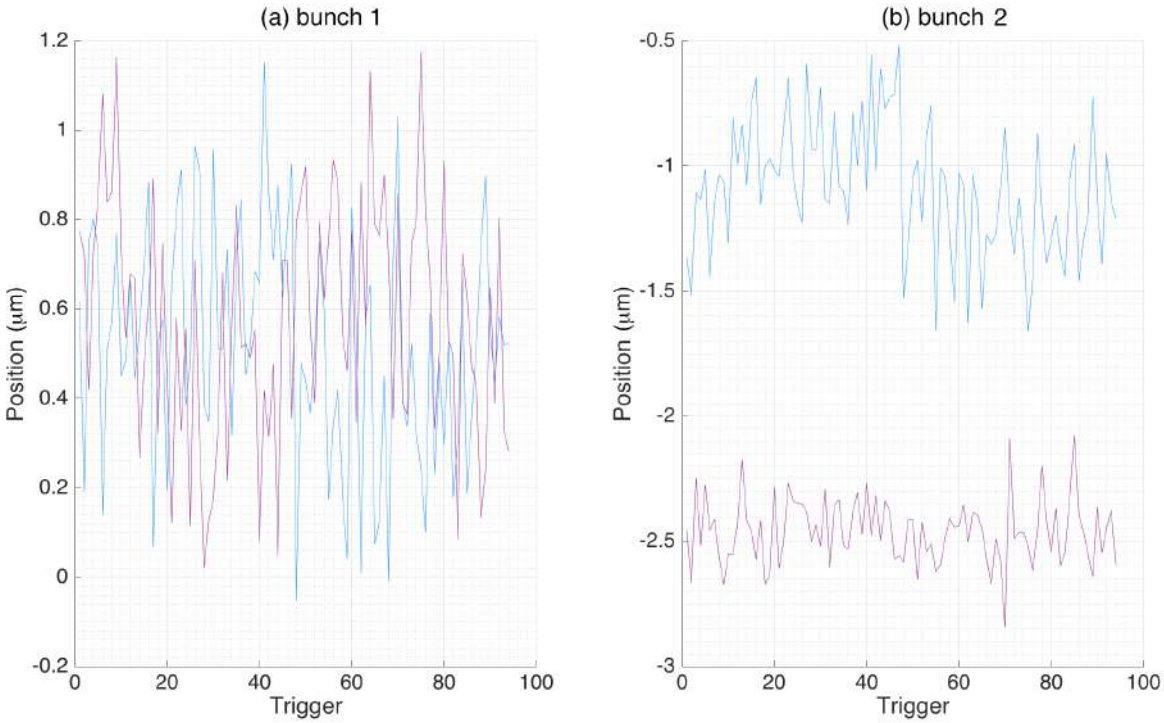

Figure 5.7: The measured vertical beam position at IPB versus trigger number for (a) bunch 1, and (b) bunch 2, with feedback off (blue) and feedback on (purple).

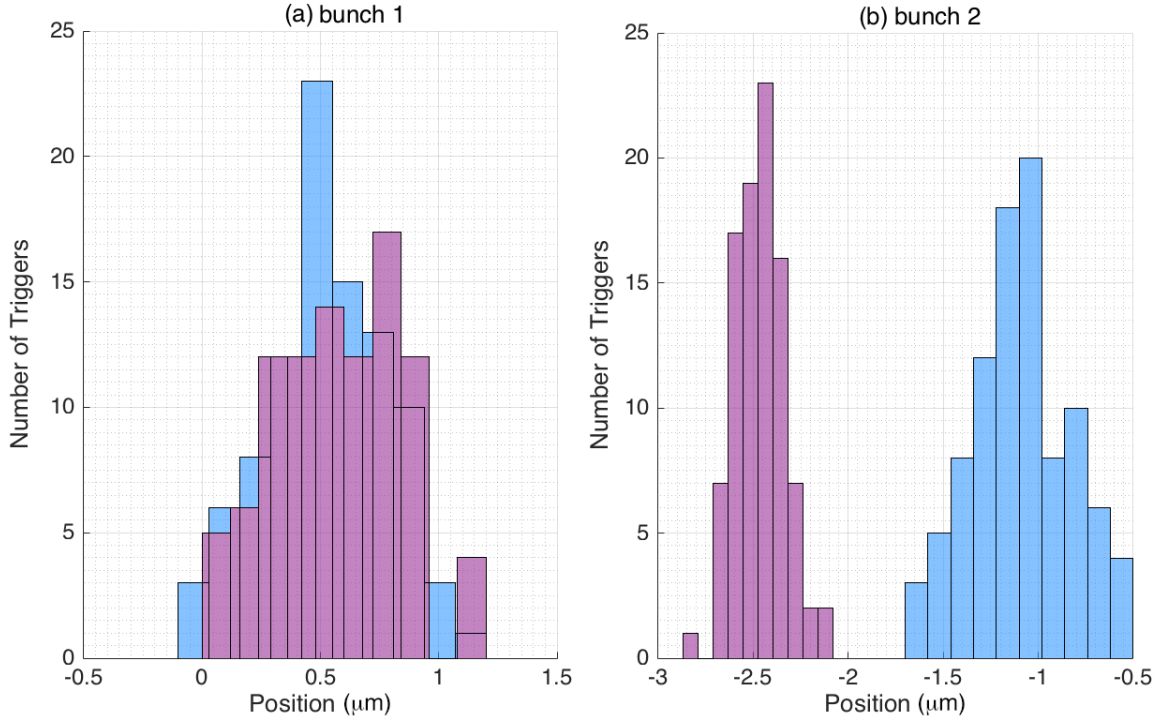

Figure 5.8: Distribution of vertical positions measured at IPB for (a) bunch 1 and (b) bunch 2, with feedback off (blue) and on (purple)

Table 5.3: Measured mean y positions and position jitters (standard deviations) at IPB for bunch 1 and bunch 2 for the cases of feedback off and feedback on. The quoted uncertainties represent standard errors on the mean and standard deviation.

	Mean position (nm)		Position jitter (nm)	
Bunch	Feedback off	Feedback on	Feedback off	Feedback on
1	520 ± 30	580 ± 30	261 ± 19	267 ± 19
2	-1090 ± 30	-2460 ± 10	263 ± 19	132 ± 10

This result was a positive step as a first demonstration of the two-BPM feedback operating successfully. However, the 132 nm correction falls short of the 74 ± 5 nm beam stabilisation previously achieved with single-BPM feedback at the IP [8]. To understand the performance on this first two-BPM feedback run, it was important to look at the bunch-to-bunch position correlation; a high degree of correlation is vital for successful feedback.

Bunch 2 position versus bunch 1 position is plotted in Fig. 5.9. Table 5.4 lists the calculated correlation between the two positions. The first thing to note is that ideally the feedback process should remove the bunch-to-bunch position correlation at IPB. A reduction in the correlation is not expected at IPA or IPC, and indeed this is not the case. However, focussing on the feedback-off plots, it is vital to see a high correlation, particularly at IPA and IPC, as they provide inputs to the feedback. The correlation at IPA was very high at 98%. However, correlation was significantly lower at IPC, 86%, and also, incidentally, at IPB, 69%. This poor correlation at IPC was particularly problematic for optimal feedback performance.

Table 5.4: Correlation between bunch 1 and bunch 2 positions at the three IP BPMs with feedback off and feedback on. The errors are a one-sigma confidence level.

	Bunch-to-bunch position correlation	
BPM	Feedback off	Feedback on
IPA	98 ± 1 %	95 ± 1 %
IPB	69 ± 5 %	-23 ± 10 %
IPC	86 ± 3 %	81 ± 3 %

Many attempts were made to improve bunch-to-bunch correlations at IPC (and IPB) on shift, such as moving the beam waist by changing the QD0FF current, adjusting the

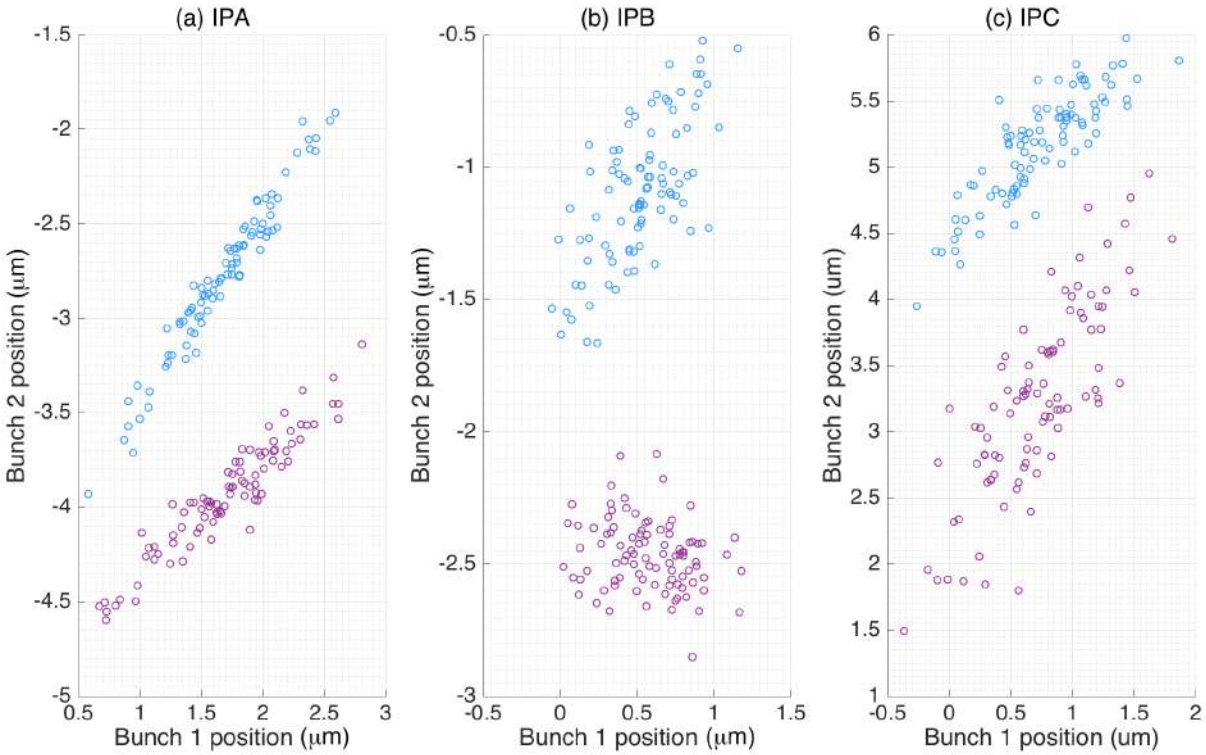

Figure 5.9: Bunch 2 position versus Bunch 1 position measured at (a) IPA, (b) IPB and (c) IPC, with feedback off (blue) and feedback on (purple).

damping ring extraction kicker timing, and re-centring the BPMs. Offline analysis has identified the reason for this disparity in the observed bunch-to-bunch correlation measured at the different BPMs (see Section 5.7). However, for the initial trial runs, this was the best-achieved correlation, and consequently, the best-measured feedback correction.

5.4 Mathematical treatment of feedback corrections

It is useful to compare the measured corrected position jitter to a theoretical estimate of the expected performance. The predicted corrected bunch 2 position, Y_2, can be modelled based on the feedback-off information gathered in interleaved feedback mode,

$$Y_2 = y_2 - g y_1 - \delta_2, \tag{5.7}$$

where y_1 is the bunch 1 feedback-off position, y_2 the bunch 2 feedback-off position, g is the gain (which is assumed equal to 1 if the two bunches have similar position jitters and are highly correlated), and δ_2 is any constant kick offset, which for this study was 0. For two-BPM feedback, the predicted corrected bunch 2 position, Y_2, was calculated using the interpolated feedback-off positions at the correction location. So, for this study, y_1 and y_2 at IPB were calculated by interpolating the feedback-off positions at IPA and IPC (Eq. 5.1).

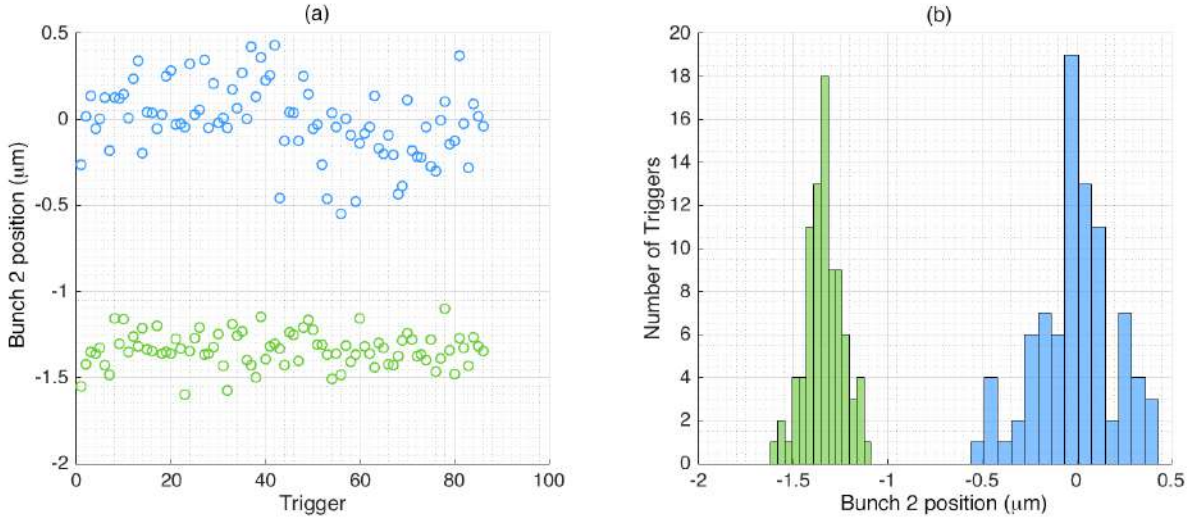

Figure 5.10: (a) IPB bunch 2 position versus trigger ; (b) the distribution of IPB bunch 2 positions. Interpolated feedback-off, y_2, (blue), and predicted feedback-on, Y_2 (green).

The predicted corrected bunch 2 jitter, i.e. the standard deviation of the positions, can then be calculated by subtracting correlated variances:

$$\sigma_{Y_2}^2 = \sigma_{y_2}^2 - g^2\sigma_{y_1}^2 - 2\rho_{12}\sigma_{y_1}\sigma_{y2}, \tag{5.8}$$

where σ_{Y_2}, σ_{y_1} and σ_{y_2} are position jitters and ρ_{12} is the bunch-to-bunch correlation.

The interpolated IPB feedback-off bunch 2 positions, y_2, and the predicted feedback-on corrected positions, Y_2 are shown in Fig. 5.10 for this two-BPM feedback study. The jitters of these distributions are detailed in the first two columns of Table 5.5.

To compare the measured corrected beam jitter of 132 ± 10 nm (from Table 5.3) with the predicted corrected beam jitter, the resolution of the BPM must be accounted for. Measurements of position jitter, σ_m, will be a combination of the true position jitter, σ_T, and the resolution of the BPM system used to measure the jitter, σ_R:

$$\sigma_m = \sqrt{\sigma_T^2 + \sigma_R^2}, \tag{5.9}$$

where the smallest measurable jitter is the resolution. Here the covariance terms are not considered, assuming the true beam position and the system noise that determines the resolution are uncorrelated.

The resolution for these data sets were estimated using a geometric method and single sample to be 59 ± 3 nm. This suggest an achievable corrected position jitter measurement of 115 ± 7 nm, quoted in the third column of Table 5.5. This interpolated result is consistent

with the measured result of 132 ± 10 given the assumptions involved in predicting (such as having calculated perfect gain settings with $g = 1$). With the given beam conditions and experimental set-up the feedback system was concluded to be behaving as it should.

Table 5.5: Mathematically predicted position jitters at IPB. The quoted uncertainties are the standard errors. The measurable result is calculated using the predicted corrected result added in quadrature to the BPM resolution.

Bunch 2 position jitter (nm)		
Interpolated feedback-off	Predicted corrected	Measurable corrected
σ_{y_2}	σ_{Y_2}	σ_m
211 ± 16	99 ± 8	115 ± 7 nm

5.5 Random jitter source scan

The robustness of the feedback in this mode of operation was tested by inducing large vertical orbit beam jitters in the ATF2 beamline. This jitter generation was performed using two air-core steering magnets installed upstream in the extraction line [89]. The two magnets were supplied with Gaussian-distributed currents, so the standard deviation of the current distributions could be scaled to change the magnitude of the jitter.

Fig. 5.11 shows the measured mean positions and jitters of bunch 2 at IPA, IPB, and IPC with a range of jitter source strengths. Even at large incoming jitters, the feedback was still correcting the position jitter at IPB reasonably well. Fig. 5.11.g and Fig. 5.11.h show the interpolated second-bunch positions and jitters alongside the predicted feedback performance calculated as in the previous section. These plots show that as incoming position jitters approached 2 µm the system is not correcting as well as predicted. This reduced performance was likely due to saturation in the electronics. The mean position may still have been valid in this scenario if the bunch was well centred, and indeed in Fig. 5.11.g the interpolated position results agree well with the predicted.

It is also noticeable that as incoming jitters increased (Fig. 5.11), the bunch position jitter was reduced at IPA (Fig. 5.11.b), and increased at IPC (Fig. 5.11.f). This effect was observed because in correcting to reduce the second-bunch position jitter at IPB, the jitter waist of the second-bunch beam trajectory was shifted towards IPB. With the uncorrected beam waist lying between IPB and IPC, this movement towards IPB inevitably resulted in a slight reduction in the jitter at IPA and an increase in the jitter at IPC, as observed.

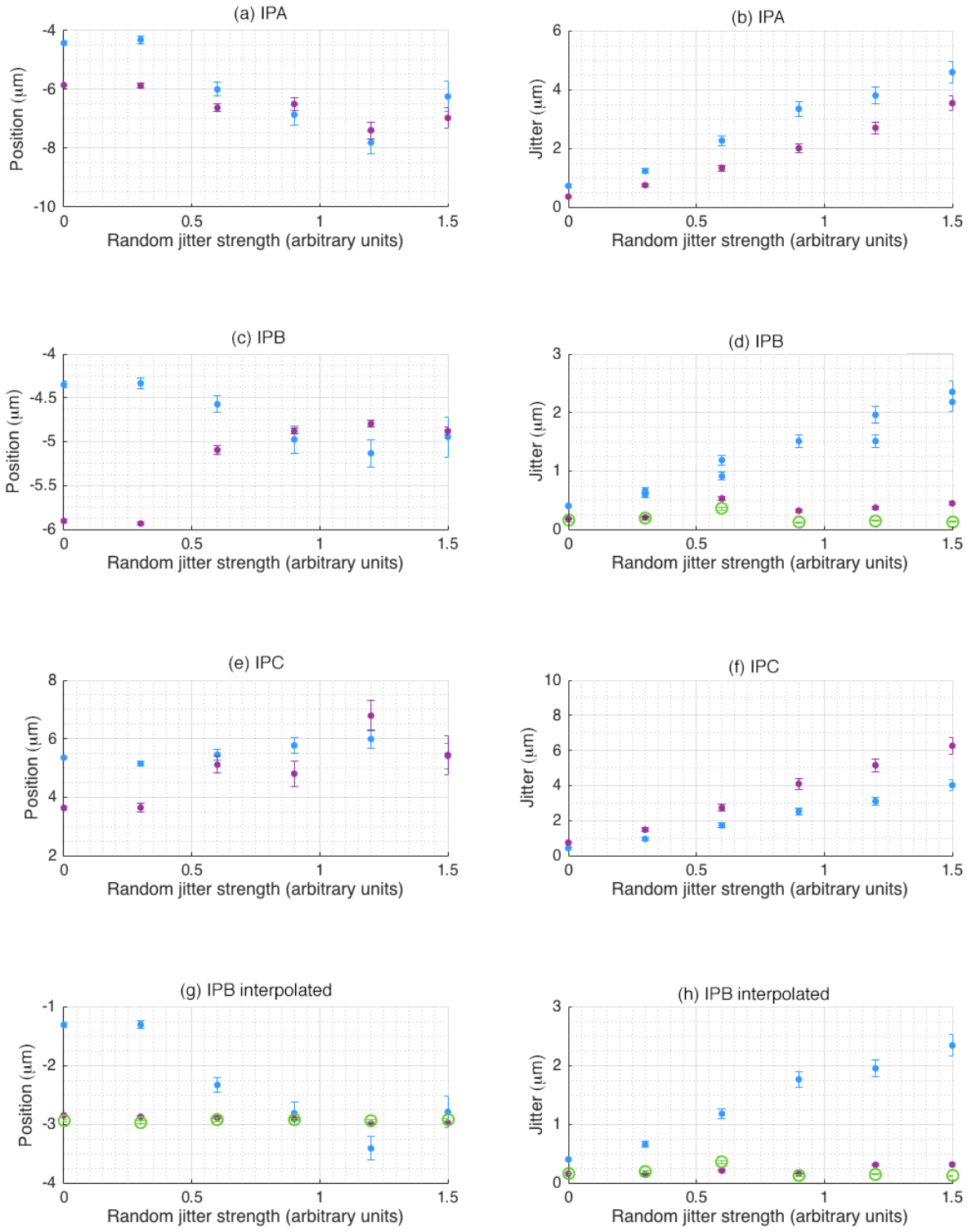

Figure 5.11: Mean position and jitter of bunch 2 versus random jitter source strength measured at (a)-(b) IPA, (c)-(d) IPB, (e)-(f) IPC, and (g)-(h) interpolated at IPB. Feedback off (blue), feedback on (purple), and predicted at IPB (green). Error bars indicate the standard errors on the mean and standard deviation.

5.6 Gain ratio scan

The gains for the feedback algorithm were calculated as described in Section 5.2. These calculations use the separations of the BPMs to weight contributions to the corrective kick (Eq. 5.5). To confirm the gain weighting ratios were optimal, a gain scan was performed by systematically altering the weightings of the four gain parameters (Eq. 5.6). For example, for a gain ratio of 1 in this scan, the IPA-derived gains were calculated with a weighting of 1 and the IPC-derived gains with a weighting of 0, i.e.:

$$G_1 = 1\,\frac{cos\theta_{AIQ}}{H_{B_{\rm interp}} k_A}, \quad G_2 = 1\,\frac{sin\theta_{AIQ}}{H_{B_{\rm interp}} k_A}, \quad G_3 = 0, \quad G_4 = 0, \tag{5.10}$$

and hence,

$$V_k = G_1 \frac{I_A}{q} + G_2 \frac{Q_A}{q}. \tag{5.11}$$

At the opposite end of the scan for a gain ratio of 0 the IPA-derived gains were weighted by 0, and the IPC-derived gains were weighted by 1. Intermediate ratios included the weighting of 0.7 (i.e., 0.7 weighting to IPA-derived gains, and 0.3 weighting to the IPC-derived gains), which most closely corresponds to the theoretical optimal set-up of Eq. 5.6.

Fig. 5.12 shows the results of this scan, demonstrating that as the weightings of IPA and IPC shifted, the location of the corrected position shifted also. The optimal correction at IPB occurred at a ratio around 0.7 (Fig. 5.12.h). This agrees with the nominal gain ratios of 0.68 and 0.32 derived from the known BPM separations.

With a gain ratio of 1 the feedback correction algorithm was effectively reduced to single-BPM feedback at IPA (although with slightly incorrect kicker calibrations derived using interpolation for correction at IPB), and indeed, the best feedback correction at IPA was observed to occur with this ratio. Similarly, at a gain ratio of 0, the feedback was effectively performing single-BPM feedback at IPC, and thus the best bunch 2 corrected jitter at IPC was observed there at that gain setting. To confirm this, predicted positions and jitters are included in Fig. 5.12.b and Fig. 5.12.f for IPA and IPC assuming single BPM feedback where, as expected, they agree with measurements at the extremes of the gain ratio scan.

5.7 Bunch correlation as a function of sample number

Poor bunch-to-bunch position correlation (<90%) was measured at IPC (and IPB) for these initial two-BPM feedback trials, despite excellent correlation measured at IPA. Given that a high correlation is vital for successful feedback, it was necessary to try and identify the

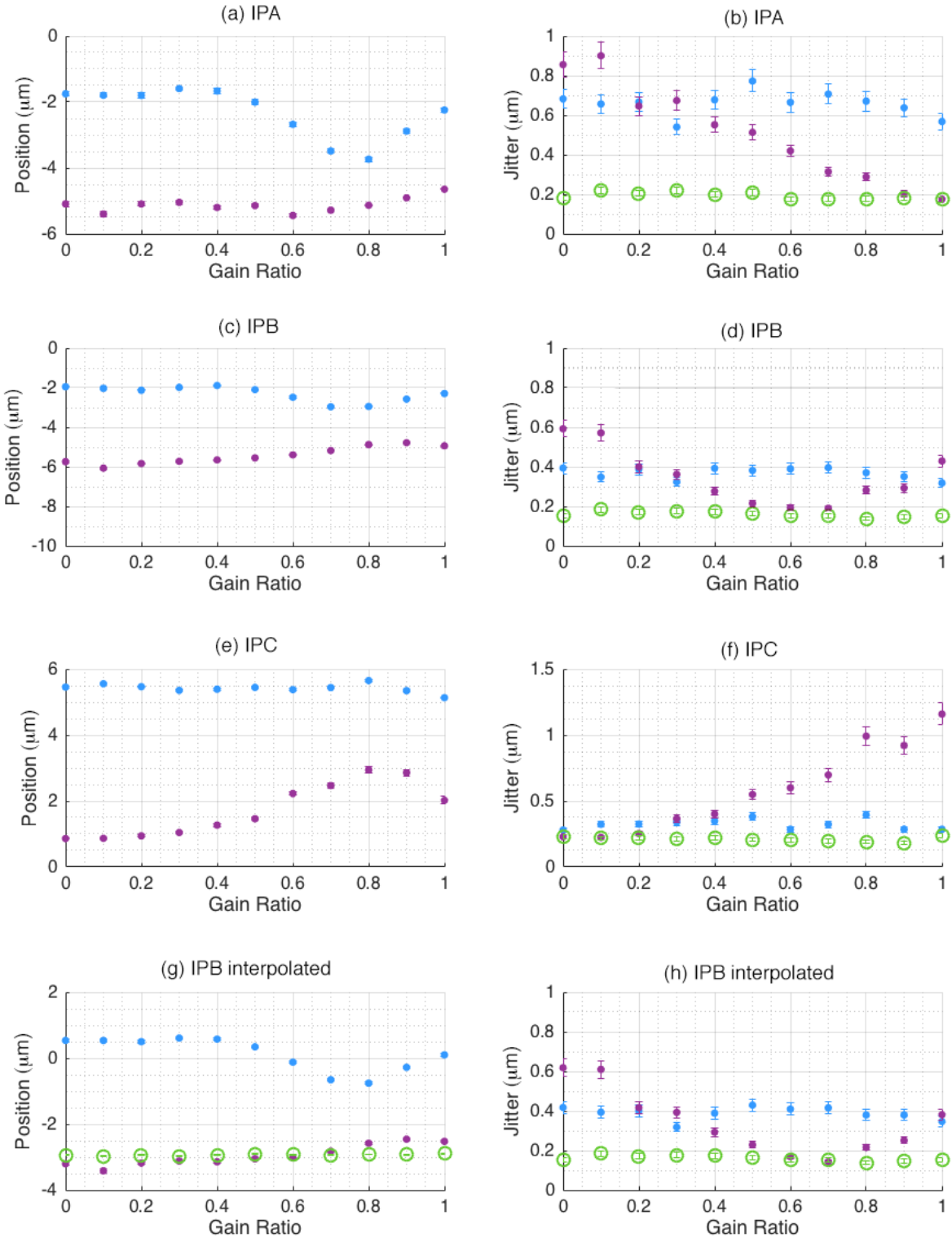

Figure 5.12: Mean position and jitter of bunch 2 versus the feedback gain ratio at (a)-(b) IPA, (c)-(d) IPB, (e)-(f) IPC and (g)-(h) interpolated at IPB. Feedback off (blue), feedback on (purple), predicted performance (green) using single-BPM feedback at that BPM on plots (b) and (f), and using two-BPM feedback on plots (d), (g) and (h).

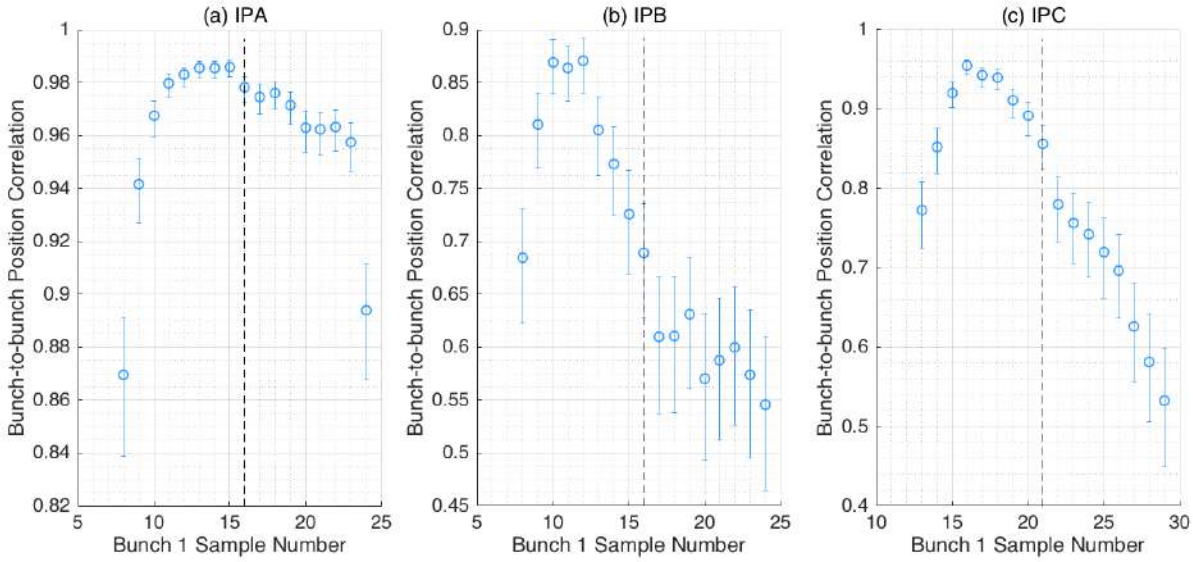

Figure 5.13: Bunch-to-bunch position correlation versus bunch 1 sample at (a) IPA, (b) IPB and (c) IPC. The error bars indicate a one-sigma confidence level. The samples used for feedback are indicated by the dashed lines.

source of this discrepancy to improve conditions for future experiments. The correlation was studied as a function of many variables and was found to have a high dependence on which sample number within the digitiser window was being used.

Fig. 5.13 shows bunch-to-bunch correlation analysis as a function of sample number. A reference sample of 21 for bunch 1 and 121 for bunch 2 was used throughout, and as the bunch 1 sample number was adjusted, bunch 2 was also changed to be 100 more than bunch 1. The correlation at IPB and IPC falls rapidly across the course of the pulse, with sample 21 for IPC which was used for feedback proving far from optimal. Higher correlation could have been achieved by sampling earlier in the digitised waveform at IPC, and would likely have resulted in a better feedback correction.

An improved predicted feedback performance was calculated using Eq. 5.8 and re-sampling the feedback-off data from IPA and IPC at sample numbers with improved bunch-to-bunch position correlation. The combination of sample 12 at IPA and sample 17 at IPC was found to be optimal. Fig. 5.14 shows the interpolated IPB positions and position jitter, with the results summarised in Table 5.6. This analysis predicts a corrected jitter of 81 ± 3 nm should have been measurable if these correlation-optimal sample numbers had been used instead as inputs to the feedback. The importance of optimising sample number selection for the best bunch-to-bunch correlation is clear, and all subsequent feedback runs in this mode incorporated this step in the set-up.

Table 5.6: Mathematically predicted position jitters at IPB, calculated from the standard deviations, using sample 12 at IPA and sample 17 at IPC for highest bunch-to-bunch correlation. The quoted uncertainties are the standard errors.

Bunch 2 position jitter (nm)		
Interpolated feedback-off	Predicted corrected	Measurable corrected
σ_{y_2}	σ_{Y_2}	σ_m
190 ± 15	55 ± 4	81 ± 3

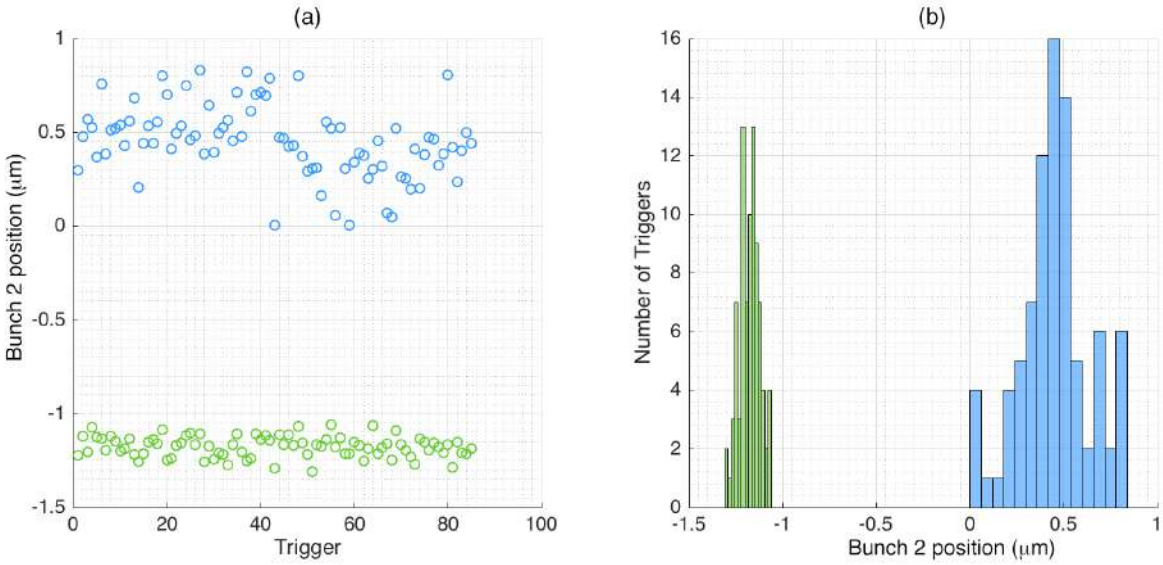

Figure 5.14: (a) IPB bunch 2 position versus trigger; (b) the distribution of IPB bunch 2 positions. Interpolated feedback-off, y_2, (blue), and predicted feedback-on, Y_2 (green). Interpolations calculated using samples to optimise bunch correlation.

One hypothesis for the bunch-to-bunch correlation varying this way across the pulse is saturation. The sample numbers chosen for feedback matched the peak of the calibration scale factor, corresponding to the largest cavity output. If the processing systems were saturated on peak, that could explain the degradation in correlation observed. These data were gathered with 0 dB attenuation to operate with the highest possible position sensitivity for feedback but may have made the system more vulnerable to saturation effects if the beam was not sufficiently centred within the dynamic operating range at all three BPMs.

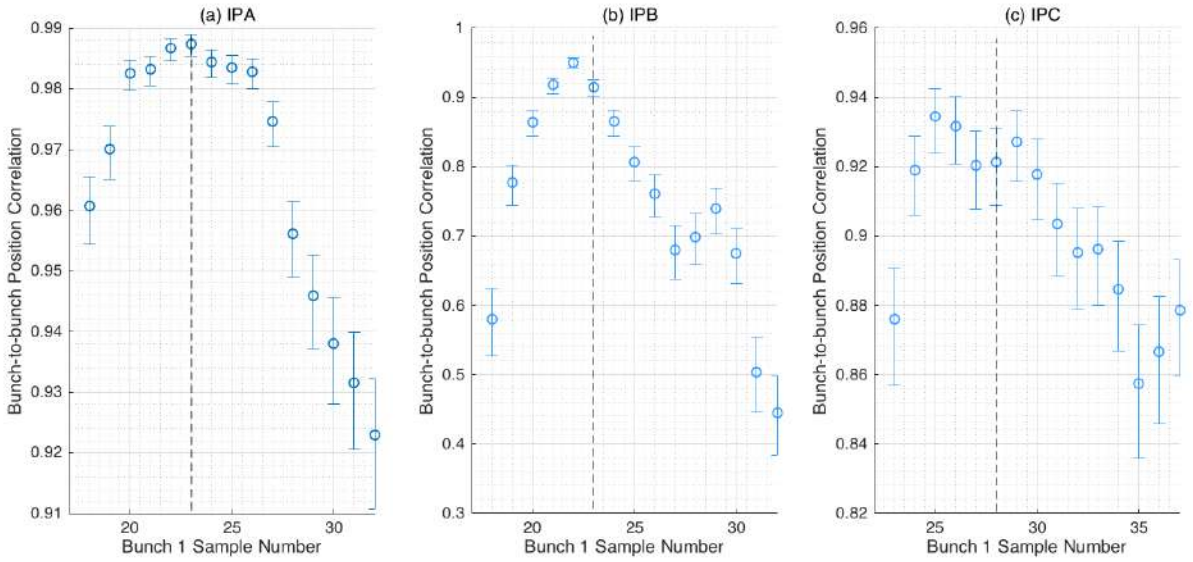

Figure 5.15: Bunch-to-bunch position correlation versus bunch-one sample number at (a) IPA, (b) IPB and (c) IPC. The error bars indicate a one-sigma confidence level. Sample numbers used for feedback are shown by dashed lines and were selected for optimal bunch-to-bunch position correlation.

5.8 Best two-BPM performance results

The two-BPM feedback study was repeated, again operating in a two-bunch mode with a bunch spacing of 280 ns and high-beta optics. The beam waist was moved away from its nominal position to produce comparable jitters ∼0.5 µm at IPA and IPC. The dipole attenuation was still 0 dB, but more time was dedicated to centring the beam in all three BPMs using the IP BPM movers and beam steering to mitigate the saturation effects observed in previous studies. The plots in Fig. 5.15 show the high bunch-to-bunch correlations and the sample numbers used for feedback.

Fig. 5.16 shows the positions measured at IPB for bunch 1 and bunch 2. This feedback run again consisted of 200 sequential triggers separated into two 100-trigger data sets of feedback-off and feedback-on. The bunch 2 position was being corrected by the feedback, stabilising the bunch position to a single location, in this case, at around -2.2 µm offset in the IPB cavity BPM. The vertical beam position distributions are shown in Fig. 5.17, with the mean positions and position jitters detailed in Table 5.7. The feedback has reduced the bunch 2 position jitter from 218 ± 16 to 57 ± 4 nm. This is the best-ever recorded FONT IP feedback stabilisation.

The IPB bunch 2 verses bunch 1 positions are shown in Fig. 5.18, demonstrating that the feedback process was successfully removing the position correlation between the two

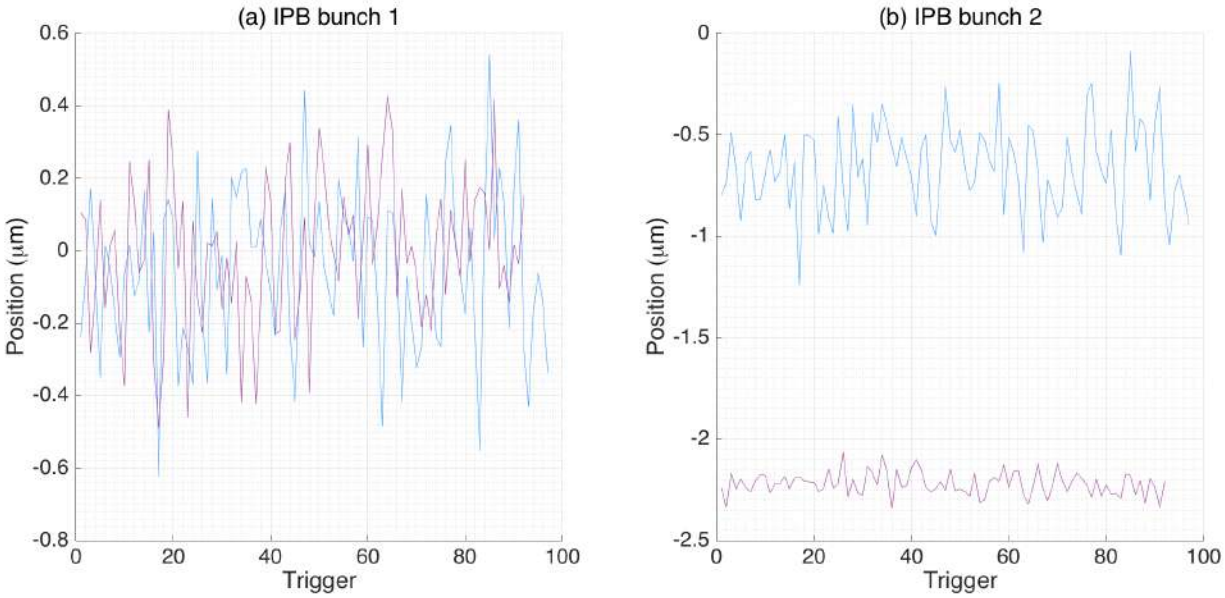

Figure 5.16: The measured vertical position at IPB versus trigger number for (a) bunch 1 in the train, and (b) bunch 2 in the train, with feedback off (blue) and feedback on (purple).

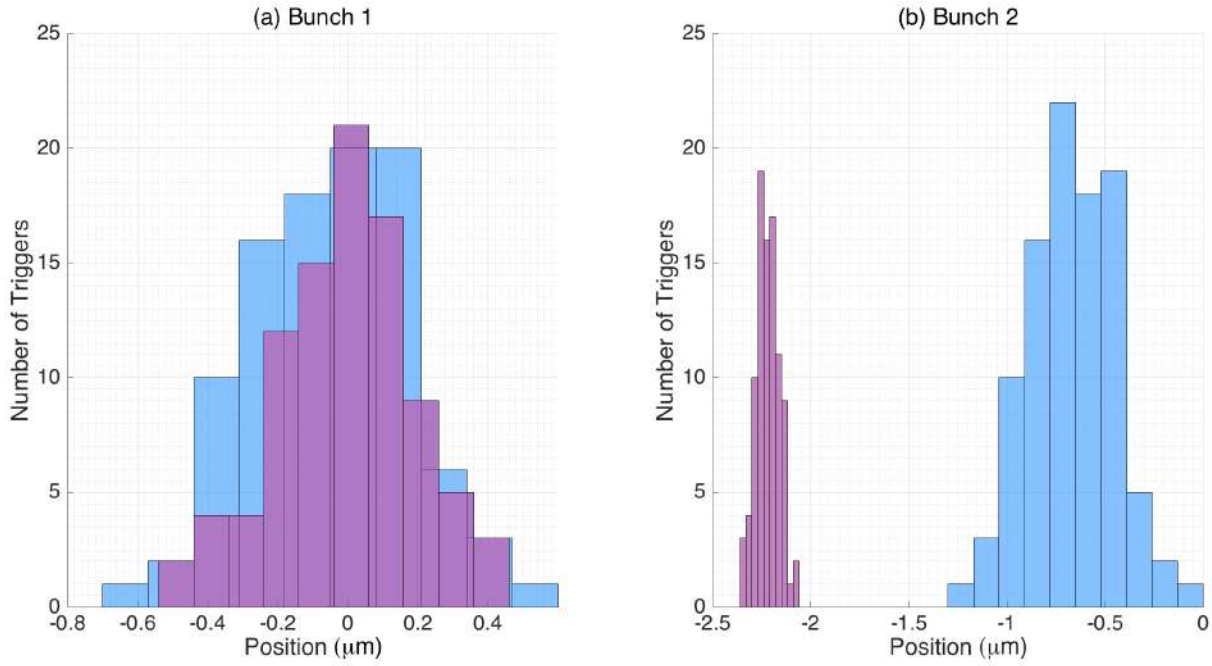

Figure 5.17: Distribution of vertical positions measured at IPB for (a) bunch 1 and (b) bunch 2, with feedback off (blue) and on (purple)

Table 5.7: Measured mean y positions and position jitters (standard deviations) at IPB for bunch 1 and bunch 2 for the cases of feedback off and feedback on. The quoted uncertainties represent standard errors on the mean and standard deviation.

	Mean position (µm)		Position jitter (nm)	
Bunch	Feedback off	Feedback on	Feedback off	Feedback on
1	-0.053 ± 0.022	0.004 ± 0.021	223 ± 16	202 ± 15
2	-0.667 ± 0.022	-2.220 ± 0.006	218 ± 16	57 ± 4

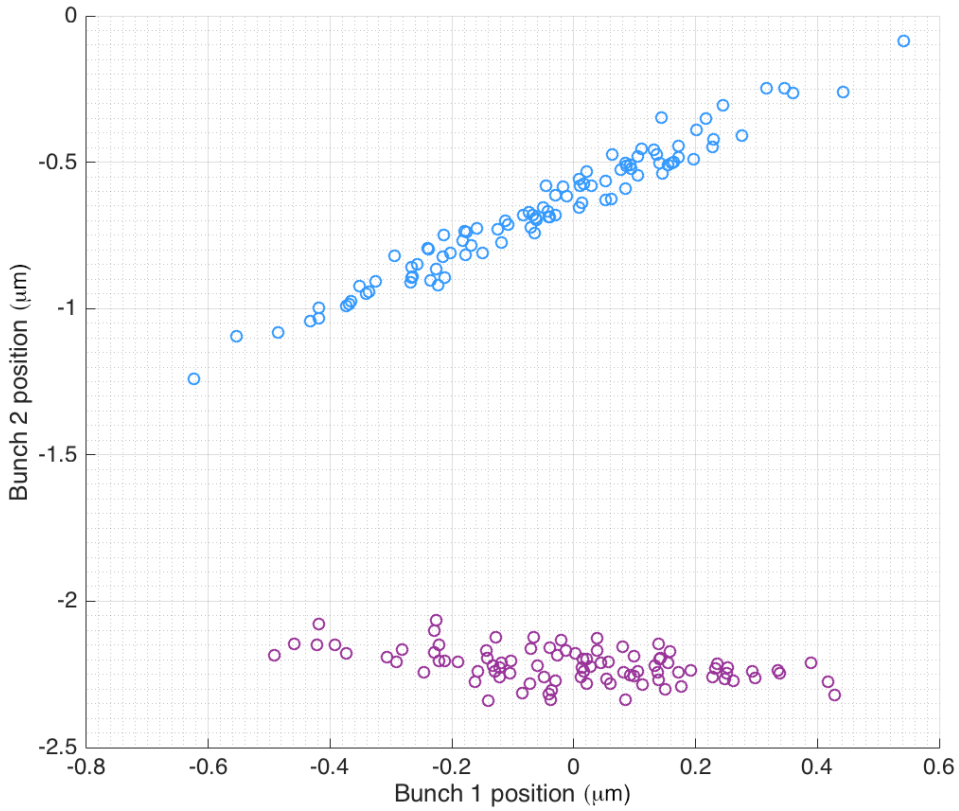

Figure 5.18: Bunch 2 position versus bunch 1 position measured at IPB with feedback off (blue) and feedback on (purple).

Table 5.8: Correlation between the bunch 1 and bunch 2 positions at IPB with feedback off and feedback on. The error bars indicate a one-sigma confidence level of the correlation coefficient.

Bunch-to-bunch position correlation	
Feedback off	Feedback on
0.981 ± 0.003	-0.43 ± 0.08

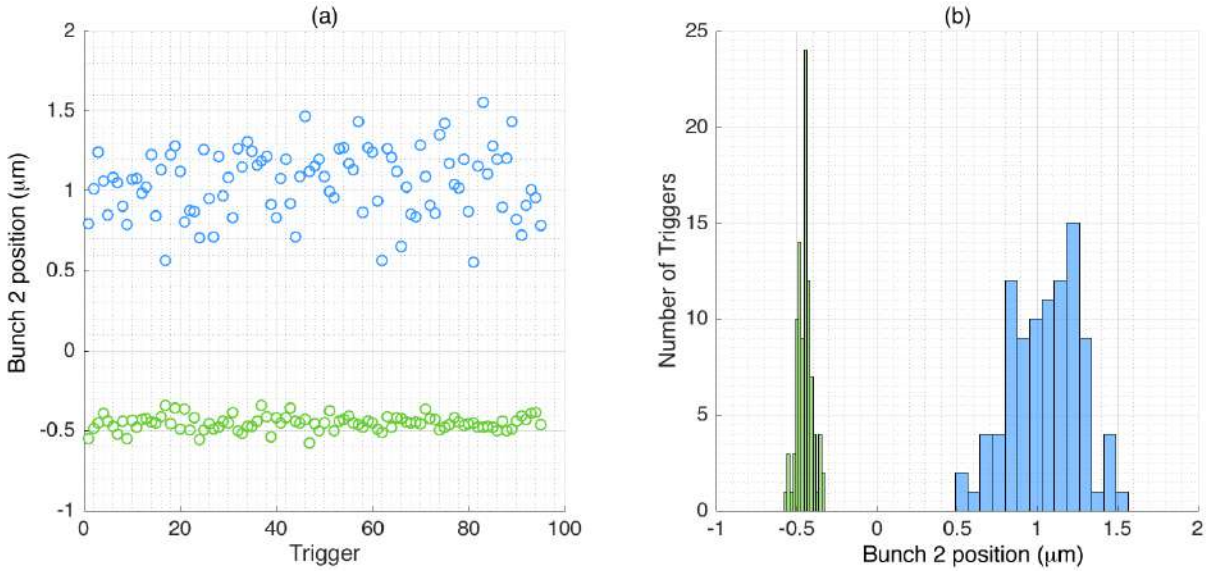

Figure 5.19: (a) Interpolated IPB feedback-off second-bunch positions (blue) and predicted IPB feedback-on positions (green) versus trigger number, (b) the distribution of interpolated feedback-off and predicted feedback-on positions.

Table 5.9: Mathematically predicted position jitters at IPB. The quoted uncertainties are the standard errors. The measurable result is calculated using the predicted corrected result added in quadrature to the BPM resolution.

Bunch 2 position jitter (nm)		
Interpolated feedback-off	Predicted corrected	Measurable corrected
σ_{y_2}	σ_{Y_2}	σ_m
211 ± 15	46 ± 3	58 ± 3 nm

bunches. Table 5.8 details the calculated correlation estimates for each data set, and suggests the feedback may have been over-correcting slightly, as the feedback-on correlation was -0.43 rather than ∼0. For future feedback it would be advisable to perform a sensitive gain scan around the calculated values to optimise the correction.

The measured feedback correction was compared to a theoretically-calculated estimate of the expected performance if everything is functioning as expected, using the methods derived in Section 5.4. Fig. 5.19 shows the result of this analysis, with the calculated jitters from the plot listed in Table 5.9, demonstrating a predicted interpolated result of 46 ± 3 nm. Added in quadrature to the BPM resolution (estimated to be 35 ± 2 nm using a geometric method), the analysis suggests an achievable corrected position jitter measurement of 58 ± 3 nm, which agrees with the measured 57 ± 4 nm feedback correction.

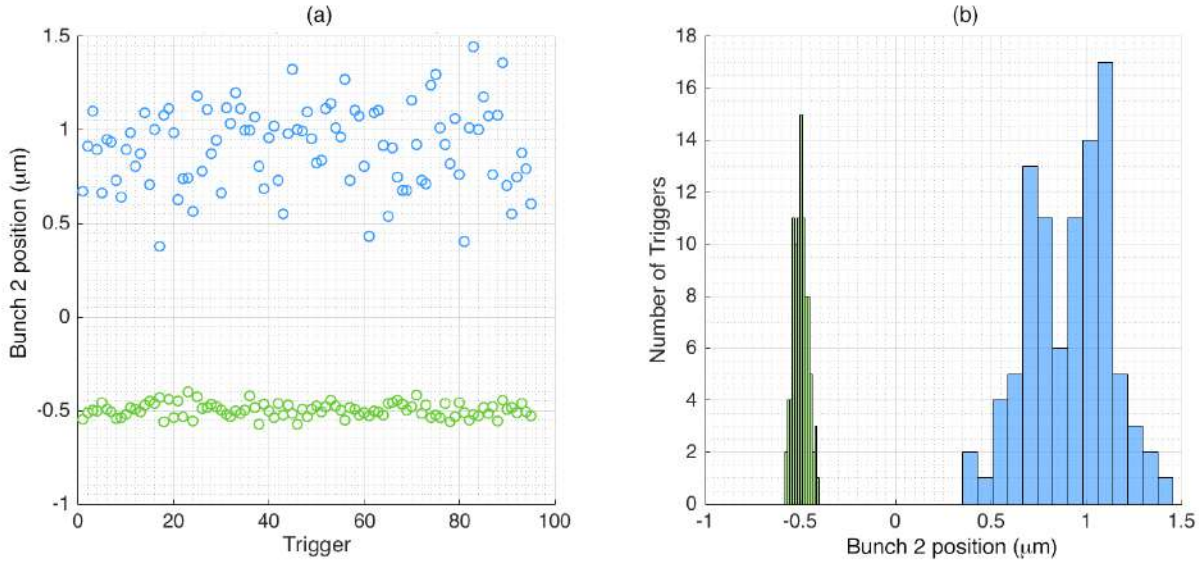

Figure 5.20: (a) Interpolated IPB feedback-off second-bunch positions (blue) and predicted IPB feedback-on positions (green) versus trigger number, (b) the distribution of interpolated feedback-off and predicted feedback-on positions. Interpolations calculated using positions measured at IPA and IPC using ten-sample integration analysis.

The analysis in Chapter 3 suggested that the resolution of the feedback system could be further improved by enabling integrated waveform sampling in the feedback firmware. This sampling method was applied to the best-performing data set in this mode of feedback. Fig. 5.20 and Table 5.10 detail the IPB interpolated predicted performance using integration across 10 samples, suggesting the beam jitter at IPB could be stabilised to 37 ± 3 nm. With an estimated ten-sample integrated resolution for these data-sets of 23 ± 2 nm, this corresponds to a measurable jitter correction of 44 ± 3 nm at IPB. This enhancement would represent a notable improvement in feedback performance and provides another motivation for future FONT studies to pursue this avenue of firmware development.

Table 5.10: Mathematically predicted position jitters at IPB. The quoted uncertainties are the standard errors. The measurable result is calculated using the predicted corrected result added in quadrature to the BPM resolution.

Bunch 2 position jitter (nm)		
Interpolated feedback-off	Predicted corrected	Measurable corrected
σ_{y_2}	σ_{Y_2}	σ_m
220 ± 16	37 ± 3	44 ± 3 nm

5.9 Summary

A novel mode of beam-based feedback was successfully operated in the ATF2 IP region for bunch position stabilisation, utilising information from two cavity BPMs (IPA and IPC) as inputs to the feedback to correct at an intermediate cavity BPM (IPB). This study was the first demonstration of the stabilisation of beam jitter at a location other than the BPMs providing input to the feedback. It also enabled the first independent measurement of the FONT IP feedback performance via a separate witness BPM. It was hoped this mode would improve the stabilisation capability in utilising information from two BPMs, improving the resolution of the feedback system. The best-measured reduction in the position jitter in this mode of feedback operation was from 218 ± 16 to 57 ± 4 nm.

In practice, it proved very challenging to use all three of the ATF2 cavity BPMs simultaneously in a way that optimised their performance. Initial studies in this feedback mode were hindered by poor bunch-to-bunch correlation at IPC, despite good correlation at IPA. This low correlation was subsequently found to be a consequence of saturation on the waveform peak at 0 dB, resulting in less-than-optimal bunch-to-bunch position correlation. However, mathematical simulations of the feedback process predicted that with sample numbers earlier in the pulse the feedback could have been improved, as was subsequently demonstrated (and surpassed) in the best-performance feedback run where sample numbers were chosen to optimise bunch correlation.

Saturation effects were mitigated in best-performing tests while operating with 0 dB attenuation by spending considerable time before feedback runs ensuring the signals were well centred in the BPMs and, as mentioned, selecting optimal-correlation sample numbers. An alternative option for future studies, if optimal beam centring proves impossible given the limitations of the BPM movers, is to introduce attenuation on the dipole cavities to prevent the peak signals saturating. However, using 10 dB attenuation to reduce signal sizes will worsen the BPM resolutions. The variable attenuators before the first stage processing electronics can only be set in steps of 10 dB, but it may be desirable to introduce smaller-step attenuation capabilities in future to combat saturation effects when beam conditions are poor without compromising resolution excessively.

Detailed scans introducing an artificially-large jitter using an upstream jitter source were used to test the strength of the feedback system. A reasonable level of correction was observed at IPB, although the feedback struggled to perform as well as predicted when the incoming uncorrected jitter exceeded 2 µm RMS, likely due to resolution limitations with signals this large. A gain ratio scan confirmed the gain weightings were set correctly and validated the theory motivating the design of the feedback firmware algorithm, with

contributions to the interpolated positions weighted by the distances between the IP BPMs. In future it may be useful to perform more sensitive gain scans to refine this feedback mode, perhaps incorporating a two-dimensional approach during which the IPA-derived and IPC-derived gains are altered independently and in smaller steps.

A mathematical interpolation of data from IPA and IPC using an integration sampling method suggests an on-board sample-integrating firmware to enhance the system resolution would be an excellent next step in improving the FONT feedback performance. Analysis of the best-performing two-BPM feedback data integrating the waveforms across ten samples predicts we could achieve a measurable correction of $\sim$40 nm with the capacity to integrate in firmware, which is very promising. Indeed, sample integrating in firmware would have the potential to improve performance in all modes of feedback operation, and will, therefore, be a primary focus of future FONT developments in attempting to achieve nanometre stabilisation at the ATF2.

Chapter 6

Conclusions and Outlook

6.1 Summary

The ATF2 is an accelerator test facility designed to test technologies and beam dynamics for future electron-positron linear colliders. The studies in this thesis contribute towards the ATF2 goal 2 of demonstrating nanometre level beam stabilisation at the IP using a beam position feedback system. The ATF2 IP set-up includes three high-resolution cavity BPMs which are used to measure the transverse position of the beam. A FONT digital feedback board digitises the BPM measurements of the first bunch in a multi-bunch train, calculates the required correction, then applies a corrective kick to the next bunch using an upstream kicker. The standard deviation of the corrected bunch position, i.e. the position jitter, over an ensemble of bunch trains is used to quantify the position stabilisation.

The resolution of the cavity BPMs is the dominant limitation for feedback in the ATF2 IP. Therefore, a lot of work has been put into optimising the resolution of the IP system and quantifying its performance. This included ensuring the signal arrival times from the dipole and reference cavities coincided correctly within the processing electronics. A mixer pedestal subtraction was introduced to regular operation to remove unwanted DC outputs. The electronic noise floor of the IP system was quantified as $\sim$11 ADC counts. Calibrated into nanometers using IPA measurements at a charge of 0.44×10^{10} electrons per bunch, this corresponded to 21 ± 2 nm using a single sample, and 13 ± 1 nm using an 8-sample integration. These results are representative of the resolution limit for position measurements with the IP BPM system.

Having three cavity BPMs deployed in the IP region with no intermediary magnetic components meant it was possible to estimate the resolution directly. The measured position at two BPMs was used to predict the position at the third using a linear transport model.

The residual difference between the predicted and measured results at the third BPM for an ensemble of data was then used to estimate the resolution of the BPM system, assuming all three BPMs are the same. The resolution was found to have a strong dependence on which sample numbers within the digitised waveform were used. The previous best estimate of the geometric method resolution performance of ∼50 nm using a single sample of the waveform was reduced to ∼20 nm by integrating across 12 samples.

The geometric resolution analysis demonstrated varying resolution estimates depending on which subsets of triggers were used for calculating positions. Jumps in the bunch charge and drifts in the θ_{IQ} calibration angle were isolated as potential sources of degradation to resolution performance. These variations were corrected by applying a multi-parameter fitting method, which addressed changes in calibrations and charge-dependence in the resolution calculation. The geometric resolution estimate is expected to be in agreement with multi-parameter fitting methods in the absence of these effects. The best resolution result was then further reduced to 17.5 ± 0.4 nm using wave form integration and a multi-parameter fit to raw BPM signals.

An unwanted parasitic waveform in the dipole cavity BPM pulses was studied and found to be ∼60 MHz in frequency, bunch charge-dependent and stable in the IQ-space. This necessitated that the unwanted pulse features were beam generated. To mitigate the impact on the operation of the IP BPMs, two narrow BPFs were installed on the dipole cavity outputs to smooth the waveform. This improved single sample resolution estimates by ∼10 nm, due to the filtering effectively integrating the waveform in hardware. Given that the FONT feedback firmware was only able to make use of a single digitised sample point, the BPF-operation proved an excellent means of slightly improving resolution for feedback operation.

The BPM resolution estimate and calibration scale factor were found to scale linearly with dipole cavity attenuation between 20 and 50 dB settings. Non-linear behaviour was observed at both 0 and 10 dB, indicating electronic components in the signal processing may be saturating when signal levels are high. The calibration scale factor was also found to scale with the charge, despite the charge-normalising analysis process, which should mean there is no dependence. Consequently, the resolution was also found to have a strong reliance on the bunch charge. No resolution dependence on beam position was observed.

Synchrotron oscillations in the damping ring at the ATF2 cause jitter in the arrival time of bunches with respect to the 714 MHz master oscillator. This manifested itself in the IP system as a phase jitter in the GHz-level cavity BPM signals relative to the LO used to down-mix them in the first stage of the processing electronics. The IP BPM system was

found to display a maximum position sensitivity to bunch phase jitter of 2.2 ± 0.1 nm per degree of 5.712 GHz at 0 dB attenuation. Given the measured bunch phase jitter of the beam, up to 8.6 ± 0.4 nm of apparent position jitter measured at the IP at 0 dB could actually be due to bunch phase jitter.

The limiting amplifier in the reference processor of the IP down-mixing electronics was also tested as a source of phase jitter. A jitter of 0.025 radians was measured directly by splitting the reference signal before the processor and mixing it with the limited version of itself. The phase sensitivity was found to couple strongly to the amplitude of the Q' signal, enabling the position-to-phase sensitivity to be effectively removed in the analysis by including Q' as a term in the position calculation. For one example data set that demonstrated 81% correlation between position and phase, the apparent position jitter measurement was reduced from 370 nm to 230 nm by accounting for the phase through a coupled Q' term.

Finally, a novel approach to beam stabilisation was presented, utilising beam position information from two cavity BPMs as input to the feedback to correct the beam at a third, intermediate cavity BPM. In addition to stabilising the beam at a location other than the BPMs providing input to the feedback, this method provided the first independent measurement of the IP feedback performance via a witness BPM. The improved stabilisation capability using the position information from two BPMs, and carefully selecting sample numbers to optimise bunch-to-bunch correlation resulted in a best-ever measured feedback position stabilisation of 57 ± 4 nm. A mathematical interpolation of data from IPA and IPC using an integration sampling method suggests an on-board sample-integrating firmware to enhance the system resolution could achieve a measurable correction of ∼40 nm in future.

Any future accelerators, including linear colliders like the ILC and CLIC, and x-ray free electron lasers, will require BPMs for diagnostic purposes and orbit feedback to enable very precise beam handling. High-resolution beam position measurements and low-latency feedback systems capable of nanometre-level position stabilisation will be vital to realise this precise beam handling [59]. It is hoped the work presented in this thesis will contribute towards the advancement of these future endeavours.

6.2 Further studies

The dramatic improvement in resolution estimates by integrating in the analysis indicates that an updated feedback firmware that enables waveform integration could make a significant improvement to feedback performance. It may also be beneficial to implement a mixer baseline subtraction in firmware. With these enhancements, it would be worthwhile

returning to both the two-BPM and one-BPM feedback modes and repeating feedback studies in the ATF2 IP region[1]. A more sensitive gain study in the two-BPM feedback mode with the four gains altered independently could also have the potential to improve optimal performance in this mode, as the best studies presented in this thesis were clearly over-correcting.

Following the success of the two BPM feedback mode, it would be of interest to try a feedback correction where the information from two BPMs is still used as input to the feedback, but the correction location is placed at one of those two BPMs, instead of at an intermediate location. This set-up could utilise a nominal optics beam, with the waist placed near the correction location BPM. In a regime where the jitter is comparable to resolution, the beam stabilisation performance should only be limited by the resolution. The signals from the second input BPM would need to be attenuated to account for large jitters off waist at the IP in nominal optics, but with the correction location at the other BPM, this information would be predominantly angular in nature.

The position sensitivity to phase in the IP system needs to be addressed. Operationally, this could be accounted for by incorporating a direct phase measurement into all studies so the dependence can be removed in the analysis. Another possibility is upgrading the limiting amplifier in the reference processor, which appears to be the dominant source of unwanted phase jitter. For now, the effect can be mitigated by always trying to ensure the Q' signals are minimised in the digitiser output.

The unwanted parasitic waveform in the dipole cavity pulses has been diagnosed as definitively beam-generated, being both charge dependent and stable in the IQ-space. The source is, as yet, unknown. Remaining possibilities yet to be ruled out include transient effects from strong unsuppressed modes, such as the second monopole mode of the dipole cavities, or unwanted reference cavity modes. One of the best ways to investigate this experimentally would be to check the cavity outputs directly with an oscilloscope. This has not be checked to date due to lacking access to a GHz-frequency scope.

It would also be valuable to return to the baseline noise studies with 70 dB attenuation on the dipole cavity signals. The I signal outputs in Fig. 2.14 have a distinct shape with a large initial transient. The step function of the Q signal outputs is closer to what would be expected from a DC diode output. The difference between these channels should be investigated and may illuminate ways to reduce the $\sim$11 ADC noise floor of the IP processing electronics. This would hopefully bring the ATF2 collaboration closer to achieving the resolution required to stabilise the beam position to the nanometre-level.

[1] These studies have now been performed and preliminary results are presented in [90].

Bibliography

[1] M. Herrero, The Standard model. *NATO Sci.Ser.C* **534**, 1-59 (1999).

[2] P. W. Higgs, Broken symmetries and the masses of gauge bosons. *Physical Review Letters* **13**, 508-509 (1964).

[3] G. Aad, et al., Observation of a new particle in the search for the standard model Higgs boson with the ATLAS detector at the LHC. *Physical Review Letters* **B 716 (1)**, 1-29 (2012).

[4] S. Chatrchyan, et al., Observation of a new boson at a mass of 125 GeV with the CMS experiment at the LHC. *Physical Review Letters* **B 716 (1)**, 30-61 (2012).

[5] K. Steffen, Basic course on accelerator optics. *Lectures of the CAS CERN accelerator school: General Accelerator Physics* **CERN 85-19**, 25-63 (1985).

[6] E. Wilson, Transverse beam dynamics. *Lectures of the CAS CERN accelerator school: General Accelerator Physics* **CERN 85-19**, 64-95 (1985).

[7] K. Kim, Characteristics of synchrotron radiation. *AIP Conference Proceedings* **184**, 565-632 (1989).

[8] N. Blaskovic Kraljevic, *Development of a high-precision low-latency position feedback system for single-pass beamlines using stripline and cavity beam position monitors*, D.Phil. thesis, University of Oxford (2015).

[9] E. Wilson, *An Introduction to Particle Accelerators*. (Oxford University Press, 2001).

[10] R. Hellborg, Industrial accelerators. *Handbook of Accelerator Physics and Engineering 2nd edition*, 27-31 (World Scientific, 2013).

[11] O. S. Bruning, et al., *LHC design report* **CERN-2004-003-V-1** (2004).

[12] K.K. Gan, Physics with low-energy e+e- and e-e- collisions at tau charm factory. *Tau-Charm Factory Workshop* **SLAC-R-343**, 576-588 (1989).

[13] LEP Collaboration, *LEP design report*, **CERN-LEP-84-01 2** (1984).

[14] The ATLAS Collaboration, Measurement of the SM Higgs boson mass in the diphoton and 4l decay channels using the ATLAS detector. *2017 European Physical Society Conference on High Energy Physics* **ATL-PHYS-PROC-2018-013** (2018).

[15] CMS Collaboration, Measurement of the top quark mass using proton-proton data at $\sqrt{s} = 7$ and 8 TeV. *Physical Review* **D93**, 072004 (2016).

[16] F. Borzumati, E. Kato, The Higgs boson and the International Linear Collider. *Frontiers in Physics* **2:32** (2014).

[17] T. Teubner, Physics of the top quark at future lepton colliders. *Journal of Physics: Conference Series* **452**, 012043 (2013).

[18] M. Aicheler, et al., *A multi-TeV linear collider based on CLIC technology: CLIC Conceptual Design Report* **CERN-2012-007** (2012).

[19] T. Behnke, et al., *The International Linear Collider Technical Design Report Volume 1: Executive Summary*, **ILC-REPORT-2013-040** (2013).

[20] M. J. Boland et al., *Updated baseline for a staged Compact Linear Collider*, **CERN-2016-004** (2016).

[21] C. Rossi, Summary from the CLIC main linac hardware baselining WG. *CLIC Workshop 2018*, 26 January 2018. URL: https://indico.cern.ch/event/656356/contributions/2826073/attachments/1590021/2515932/MLHW_Baselining_summary260118.pdf

[22] L. Evans, S. Michizono, *The International Linear Collider Machine Staging Report 2017* **CERN-ACC-2017-0097** (2017).

[23] V. Balakin et al., Focusing of submicron beams for TeV-scale e+e- linear colliders. *Physical Review Letters* **74**, 2479-2482 (1995).

[24] D. Burke, Results from the Final Focus Test Beam. *Fourth European Particle Accelerator Conference* (1994).

[25] CLIC Collaboration, Experimental verification of the CLIC two-beam scheme, status and outlook. *International Particle Accelerator Conference* **TUOBC01**, 1101 (2012).

[26] R. Ruber, et al., The CTF3 two-beam test stand. *NIM* **A 729**, 546-553 (2013).

[27] KEK: High Energy Accelerator Research Organisation.
URL: http://www.kek.jp/en/

[28] C. Swinson, *Development of beam position monitors for final focus systems at the International Linear Collider*, D.Phil. thesis, University of Oxford (2010).

[29] F. Hinode, et al., ATF Accelerator Test Facility: design and study report. *KEK Internal* **95-4**, internal report (1995).

[30] K. Kubo, et al., Extremely Low Vertical-Emittance Beam in the Accelerator Test Facility at KEK. *Physical Review Letters* **88** 194801 (2002).

[31] Y. Honda, et al., Achievement of Ultralow Emittance Beam in the Accelerator Test Facility Damping Ring. *Physical Review Letters* **92** 054802 (2004).

[32] B. Grishanov, et al., ATF2 Proposal. *KEK Report 2005-9*, internal report (2005).

[33] P. Raimondi, A. Seryi, Novel final focus design for future linear colliders. *Physical Review Letters* **86** 3779 (2001).

[34] ATF2 collaboration, *Aiming for nanobeams: Accelerator Test Facility* **ATF-E1227**, ATF2 online resource. URL: http://www-atf.kek.jp/atf/files/ATF-E1227.pdf

[35] G. White, et al., Experimental validation of a novel compact focusing scheme for future energy-frontier linear lepton colliders. *Physical Review Letters* **112** 034802 (2014).

[36] C. Adolphsen, et al., *The International Linear Collider Technical Design Report - Volume 3.I: R&D in the technical design phase* **CERN-ATS-2013-037** (2013).

[37] S. Sakanaka, et al., Design of an RF system for the ATF damping ring. *Particle Accelerator Conference* **3**, 1791, (1995).

[38] M. Patecki, *Optimisation analysis and improvement of the effective beam sizes in Accelerator Test Facility 2*, PhD thesis, Warsaw University of Technology (2016).

[39] J. Urakawa, ATF Results and ATF II Plans. *Particle Accelerator Conference* **A03**, 1950-1954 (2007).

[40] M. N. Nguyen, J. Krzaszczak, *Trip report for the installation and commission of the double extraction-kicker system at KEK - ATF.* **ATF06-04**, internal report (2006).

[41] T. Okugi et al., *ICFA Beam Dynamics Newsline* **61** 24-69 (2013).
URL: http://icfa-usa.jlab.org/archive/newsletter/icfa_bd_nl_61.pdf

[42] A. Faus-Golfe, et al., Upgrade and systematic measurement campaign of the ATF2 multi-OTR system. *International Particle Accelerator Conference*, **MOPWO023**, 933-935 (2013).

[43] T. Okugi, ATF International Collaboration, Achievement of Small Beam Size at ATF2 Beamline. *Linear Accelerator Conference* **MO3A02**, 27-31 (2016).

[44] D. Schulte, Beam-Beam Effects in Linear Colliders. *Proceedings of the CAS-CERN Accelerator School*, CERN-2017-006-SP (2017).

[45] A. Seryi, L. Hendrickson, G. White, Issues of Stability and Ground Motion in ILC. *36th ICFA Advanced Beam Dynamics Workshop NANOBEAM 2015*, SLAC-PUB-11661 (2005).

[46] R. Amirikas, et al., Ground motion & comparison of various sites, *EUROTeV: European Design Study Towards a Global TeV Linear Collider* **EUROTeV-Report-2005-023-1**, report (2005).

[47] P. N. Burrows, Feedback on nanosecond timescales (FONT): Results from first beam tests at the NLCTA at SLAC. *Particle Accelerator Conference 2003*, 687-689 (2003).

[48] P. N. Burrows, et al., The FONT4 ILC intra-train beam-based digital feedback system prototype. *Particle Accelerator Conference 2007*, 416-418 (2007).

[49] P. N. Burrows, et al., Tests of the FONT3 linear collider intra-train beam feedback system at the ATF. *Particle Accelerator Conference 2005*, 1359-1361 (2005).

[50] D. Bett, *The development of a fast intra-train beam-based feedback system capable of operating on the bunch trains of the international linear collider*, D.Phil. thesis, University of Oxford, (2013).

[51] C. Adolphsen, et al., *The International Linear Collider Technical Design Report - Volume 3.II: Accelerator baseline design* **CERN-ATS-2013-037** (2013).

[52] R. Apsimon, et al., The FONT5 bunch-by-bunch position and angle feedback system at ATF2. *Technology and Instrumentation in Particle Physics* **37**, 2063-2071 (2011).

[53] M. Davis, *The development of intra-train beam stabilisation system prototypes for a future linear collider*, D.Phil. thesis, University of Oxford (2014).

[54] R. Lorenz, Cavity beam position monitors. *American Institute of Physics Conference Proceedings* **451**, 53-73 (1998).

[55] D. Pozar, *Microwave Engineering*. (Wiley, 2011).

[56] Z. Li, et al., Cavity BPM with dipole-mode-selective coupler. *Particle Accelerator Conference 2003* SLAC-PUB-11913 (2003).

[57] T. Shintake, Proposal of a nanometer beam size monitor for e+e linear colliders. *NIM* **A 311**:3, 453-464 (1992).

[58] J. Yan, et al., Measurement of nanometer electron beam sizes with laser interference using shintake monitor. *NIM* **A 740**, 131-137 (2014).

[59] Y. Inoue, et al., Development of a high-resolution cavity-beam position monitor. *Physical Review Special Topics Accelerators and Beams*, **11**:6, 062801, (2008).

[60] S. Jang, et al., Development of a cavity-type beam position monitors with high resolution for ATF2. *International Particle Accelerator Conference 2013* **MOPME058**, 604-606 (2013).

[61] O. Blanco, *ATF2 IP chamber: BPMs Displacement System w/ BPMs*, ATF2 internal technical drawings (2013). URL: http://atf.kek.jp/twiki/pub/ATF/IP-IPBPM-Movers/BPMs_displacement_system_with_BPMs_(spots_for_3D_machine_shown).pdf

[62] S.H. Kim, *Reference cavity BPM layout*, KNU-RCB-0000, ATF2 internal technical drawings (2013).
URL: http://atf.kek.jp/twiki/pub/ATF/IPBPMbyKNU/Ref._BPM_layout.pdf

[63] The GdfidL Electromagnetic Field simulator. URL: http://www.gdfidl.de/

[64] S. Jang, The KNU electronics repair schedule and new IPBPM fabrication schedule. *ATF2 IP BPM meeting*, 22 April 2014.
URL: http://atf.kek.jp/twiki/bin/view/ATF/IPBPMmeetings2

[65] O. Blanco, *BPMs Positioning System: Revision 08*, ATF2 internal technical instructions (2014). URL: http://atf.kek.jp/twiki/pub/ATF/IP-IPBPM-Movers/user_manual.pdf

[66] C. Perry, Proposed Changes to IP-BPMs. *ATF2 Project Meeting*, 14 March 2017. URL: https://indico.cern.ch/event/614198/contributions/2489219/attachments/1427273/2190411/IP-BPM_Proposed_Changes.pdf

[67] T. Tauchi, Data of dipole resonant frequencies of previous IPBPMs. *ATF2 IP BPM meeting*, 3 February 2015.
URL: http://atf.kek.jp/twiki/bin/view/ATF/IPBPMmeetings2

[68] S. Jang, KNU IP-BPM and reference cavity, *ATF2 IP BPM meeting*, 7 October 2013.
URL: http://atf.kek.jp/twiki/bin/view/ATFlogbook/IPBPMMeeting20131007

[69] A. Aryshev, T. Tauchi, IPBPM RF measurements. *ATF2 meeting*, May 2017. URL: http://atf.kek.jp/twiki/pub/ATF/IPBPMmeetings2/17_05_12_IPBMP_RF_AA.pdf

[70] S. Wallon, The Cedrat mover-3 issue. *ATF2 meeting*, 23 May 2017. URL: http://atf.kek.jp/twiki/pub/ATF/IPBPMmeetings2/2017.05.23_Big_issues_with_Cedrat_electronics_and_one_mover.docx

[71] M. Ross, et al., RF cavity BPMs as beam angle and beam correlation monitors. *Particle Accelerator Conference 2003*, 2548-2550 (2003).

[72] S. Walston et al., Performance of a high resolution cavity beam position monitor system, *NIM* **A 578**, 1-22 (2007).

[73] Xilinx, *Virtex-5 FPGA User Guide v5.4 Edition*, 16 March 2012. URL: http://www.xilinx.com/support/documentation/user_guides/ug190.pdf

[74] TMD Technologies Limited. URL: http://www.tmd.co.uk/

[75] CERN BE/ABP Accelerator Beam Physics Group, MAD - Methodical Accelerator Design. URL: http://mad.web.cern.ch/mad/

[76] S. Jang, C-band BPF for IPBPM. *ATF2 IPBPM meeting*, June 2015. URL: http://atf.kek.jp/twiki/pub/ATF/IPBPMmeetings2/C-band_BPF_for_IPBPM.pptx

[77] B. Constance, *Design and beam testing of a fast, digital intra-train feedback system and its potential for application at the International Linear Collider*, D.Phil. thesis, University of Oxford (2011).

[78] S. Wallon, ATF2 IP-BPM - piezo movers calibration. *ATF2 Project Meeting*, 14 March 2017. URL: https://indico.cern.ch/event/614198/contributions/2489218/attachments/1427397/2191592/2017.03.14_ATF2_IP-BPM_-_piezo_movers_calibration.pdf

[79] N. Blaskovic, et al., Status of IPBPM performance and resolution studies. *ATF2 Project Meeting*, 14 March 2017. URL: https://indico.cern.ch/event/614198/contributions/2489212/attachments/1427337/2190538/FONT_IPBPMs_-_Talitha_-_2017_ATF_Project_Meeting.pdf

[80] T. Okugi, *Instructions for loading High Beta Optics*, internal technical instructions (2017). URL: http://atf.kek.jp/twiki/bin/view/Main/HighBetaOptics

[81] Y. I. Kim,*Cavity beam position monitor system for the beam delivery and interaction point of the Accelerator Test Facility 2 and future linear collider*, Ph.D. thesis, Kyungpook National University (2012).

[82] O. Blanco, *Beam dynamics in the final focus section of the future linear collider*, PhD thesis, Laboratoire de L'accelerateur Lineaire, (2015).

[83] N. Blaskovic Kraljevic, et al., Progress towards electron-beam feedback at the nanometre level at the Accelerator Test Facility (ATF2) at KEK. *6th International Particle Accelerator Conference*, 1133-1135 (2015).

[84] T. Nakamura, *Development of beam-position monitors with high position resolution*, Master Thesis, The University of Tokyo, (2008).

[85] P. Strehl, *Beam Instrumentation and Diagnostics*. (Springer, 2006).

[86] F. Plassard, Ultra-low β_y^* tuning study at ATF2. *ATF2 Project Meeting*, 21 March 2018. URL: https://agenda.linearcollider.org/event/7869/contributions/41087/attachments/32885/50041/atf2-project-meeting2018.pdf

[87] Y. Honda, *Bench test of limiter/int detector module*, ATF2 internal report (2006). URL: http://atf.kek.jp/twiki/pub/ATF/IPBPMmeetings2/limiter_module_test_0.pdf

[88] R. Apsimon, et al., Design and performance of a high resolution, low latency stripline beam position monitor system. *Physical Review Special Topics Accelerators and Beams* **18** 032803 (2015).

[89] Y. Kano, IP-BSM 2-bunch operation. *ATF2 Project Meeting*, 14 Jan, 2016. URL: https://agenda.linearcollider.org/event/6939/contributions/34157/attachments/28156/42605/IPBSM-2_bunch_operation_Kano.pdf

[90] R. Ramjiawan, Status of FONT IP Feedback. *ATF2 Project Meeting*, 22 March 2018. URL: https://agenda.linearcollider.org/event/7869/contributions/41090/attachments/32887/50047/Ramjiawan_ATF2Workshop2018.pdf